Fracture Mechanics Investigation of Structures with Defects

By

Yong Li

Supervised by

Prof. Erasmo Viola

Dissertation

Submitted to the University of Bologna

in partial fulfillment of the requirements for the degree of

DOCTOR OF PHILOSOPHY

in

Structural Engineering and Hydraulics

April, 2013

Alma Mater Studiorum — Università di Bologna

Dottorato di Ricerca in Ingegneria Strutturale ed Idraulica

XXV Ciclo

Settore scientifico disciplinare — ICAR/08

Settore concorsuale — 08/B2

Fracture Mechanics Investigation of Structures with Defects

da

Yong Li

Relatore

Prof. Erasmo Viola

Coordinatore del Dottorato

Prof. Erasmo Viola

Esame finale anno 2013

Alma Mater Studiorum — University of Bologna

Doctoral in Structural Engineering and Hydraulics

XXV Cycle

Settore scientifico disciplinare — ICAR/08

Settore concorsuale — 08/B2

Fracture Mechanics Investigation of Structures with Defects

by

Yong Li

Supervisor

Prof. Erasmo Viola

Coordinator of Doctoral

Prof. Erasmo Viola

Final examination in 2013

ABSTRACT

Fracture mechanics plays an important role in the material science, structure design and industrial production due to the failure of materials and structures are paid high attention in human activities. This dissertation, concentrates on some of the fractural aspects of shaft and composite which have being increasingly used in modern structures, consists four chapters within two parts.

Chapters 1 to 4 are included in part 1. In the first chapter, the basic knowledge about the stress and displacement fields in the vicinity of a crack tip is introduced. A review involves the general methods of calculating stress intensity factors are presented. In Chapter 2, two simple engineering methods for a fast and close approximation of stress intensity factors of cracked or notched beams under tension, bending moment, shear force, as well as torque are presented. New formulae for calculating the stress intensity factors are proposed. One of the methods named Section Method is improved and applied to the three dimensional analysis of cracked circular section for calculating stress intensity factors. The comparisons between the present results and the solutions calculated by ABAQUS for single mode and mixed mode are studied. In chapter 3, fracture criteria for a crack subjected to mixed mode loading of two-dimension and three-dimension are reviewed. The crack extension angle for single mode and mixed mode, and the critical loading domain obtained by SEDF and MTS are compared. The effects of the crack depth and the applied force ratio on the crack propagation angle and the critical loading are investigated. Three different methods calculating the crack initiation angle for three-dimension analysis of various crack depth and crack position are compared. It should be noted that the stress intensity factors used in the criteria are calculated in section 2.1. In Chapter 4, to reveal the accuracy and effectiveness of the stress intensity factors calculated in section 2.2, a number of numerical examples are given for dynamic characteristics of free vibration of Timoshenko beams with transverse non-propagating open cracks. The coupling between tension and bending is considered for circular cross section beams subjected to bending moment - axial force - shear force and bending moment - shear force - torque. The non-dimensional bending modes, rotational modes, tension modes, as well as torsion modes as functions of crack depth ratio and crack location ratio are graphically researched.

Chapter 5 to 8 included in Part II dealing with the fractural properties of composite materials. Chapter 5 focuses on the fractural process connected with a finite central crack along the plane interface between two bonded dissimilar materials under biaxial loading. The analytical solution, based upon the complex potential technique, stemmed from the boundary value problem formulated for the interfacial crack model subjected to biaxial loading at infinity. Numerical solutions of the in-

terfacial crack problem, based on a Finite Element Method (FEM) formulation, are worked out with reference to external loadings applied at the boundary of a bonded finite plate with the same interfacial crack. The non-linear stress-strain response of this model is investigated. Models of different material properties, interface crack lengths, biaxial loading conditions and interfacial fracture strengths are investigated. In Chapter 6, the geometry model used in Chapter 5 subjected to the in-plane general loading is analyzed. The elastic solution is obtained by the application of the complex variable technique coupled with the principle of the superposition. The normalized circumferential stress, the normalized maximum shear stress, as well as the strain energy density factor near the crack tip are described. The influence of the shear-tension force ratio, biaxial factor and the distance ahead of the crack tip are investigated. In Chapter 7, two popular and simple fracture criteria for interfacial crack proposed by He and Hutchinson (HH-criterion), Piva and Viola (PV-criterion) are introduced. The critical value of applied tensile stress of a function of the biaxial factor, the force ratio and material combination according to the PV-criterion is studied. Crack propagation angle in several situations of bi-material systems or homogeneous materials are calculated. The main work is focused on the improvement of PV-criterion by introducing the interface toughness. In the last chapter, the aspects of Extended Finite Element Method (XFEM), such as crack discontinuous enrichment, crack tip enrichment, level set method, are introduced. Specially, for the interfacial crack, a special enrichment function which can be spanned the near-tip displacement field are realized. The fracture criterion proposed in section 2.6 is used to track the crack propagation trajectory of interfacial crack. Several numerical examples for stress intensity factor of interface crack and the crack extension trajectory are given by MATLAB codes.

ACKNOWLEGEMENTS

This thesis cannot be done without the support of my supervisor Prof. Erasmo Viola. I am grateful for his guidance, support, motivation, enthusiasm and commitment. The most important thing I learned from him is his rigorous attitude toward research. His patience and positive evaluation have provided me a lot of impetus for moving forward in my research area.

I thank Dr. Nicholas Fantuzzi for his excellent advice and unstinted support. I have thoroughly enjoyed the study life with my colleagues: Ilaria Ricci, Rosario Miletta, Alessandro De Rosis, Matteo Mazzotti, Alejandro Gutierrez, Marco Miniaci. I'm grateful that I could work with Dr. Camilla Colla, Dr. Ferretti Elena. I would like to thank Assistant Prof. Francesco Tornabene and Alessandro Marzani for their precious suggestions on my article. Many thanks to Chiara Brighenti for her technological supports. I thank Prof. Francesco Ubertini, Prof. Stefano De Miranda and the Department of Civil Engineering at University for their help.

My entire PhD study is financially supported by Erasmus Mundus CONNEC project, I would dedicate my profound gratitude for this project.

Finally, I would express my sincere thanks to my parents Mr. Li Shitao and Mrs. Long Shurong for their unconditional support and mentoring throughout my life. Special thanks to my girlfriend Dr. Mao Yanhui for her encourage and accompany. Thanks to my brother Mr Li Qiang and sister-in-law Chang Fang, as well as my little nephew Li Zhexi. I would not have completed my PhD if not for my family's love, affection and care. I dedicate this dissertation to my family.

Li Yong

Bologna, Italy

12.04.2013

This page intentionally left blank

CONTENTS

Chapter 1

Introduction and basic knowledge

1.1 Introduction

Fracture mechanics in the broad sense of this concept includes the part of science of strength of material and structures which relates to a study of the carrying capacity of a body with or without consideration of initial cracks and also to a study of various laws governing crack development.

Omitting a historical review of the subject matter, the present report is concerned with a study of the equilibrium and growth of macroscopic cracks within the framework of continuum mechanics. Nature and the practical activity of human permitted of observing various modes of fracture. A special case is perfectly brittle or elastic fracture, which is not encountered in practice among metallic materials. The fracture of such materials is accompanied by plastic deformation. There is simply a possibility of introducing into consideration a small (compared with the characteristic dimension of a crack) plastic zone due to stress concentration at the crack edge. According to Irwin, the size of this plastic zone is proportional to the square of the ratio of the stress intensity factor to the yield strength [1]. This zone is surrounded by the field of elastic strain whose value is related directly to the stress intensity factors calculated from the solution of the elastic problem. If the plastic zone must be taken into account, its length artificially increases the extent of the crack. This formal action enables an easy analytic transition from the description of elastic fracture to that of elastic-plastic fracture. Thus, the determination of the stress intensity factor and its critical value includes both the above modes of fracture.

1.2 Stress and displacement fields in the vicinity of a crack tip

Before proceeding to the solution of the problem indicated in the above section, it's necessary to recapitulate some basic relations of the theory of elasticity which will be needed in what follows.

Considerable mathematical difficulties involved in solving general equations of elasticity call for the construction of solutions for more or less wide classes of special cases. Such as, the class of "plane elasticity problems" which incorporates two practically important case: (a) the deformation of a long cylinder by force, the same in all planes, applied to its lateral surface and lying in planes perpendicular to the generators of the cylinder; (b) the deformation of a plate by force lying in its plane and applied to its perimeter.

Every elementary course in elasticity gives the derivation of the equilibrium equations for the plane elasticity problem (in this case we have three equilibrium equations, with neglect of body forces and inertial terms). We present the complete system which is closed by Hooke's law for an isotropic body in plane strain

$$\frac{\partial \sigma_x}{\partial x} + \frac{\partial \tau_{xy}}{\partial y} = 0, \qquad \frac{\partial \sigma_y}{\partial y} + \frac{\partial \tau_{xy}}{\partial x} = 0 \tag{1.1}$$

$$\sigma_x = \lambda\theta + 2\mu\varepsilon_x, \qquad \sigma_y = \lambda\theta + 2\mu\varepsilon_y, \qquad \tau_{xy} = \tau_{yx} = \mu\gamma_{xy} \tag{1.2}$$

$$\varepsilon_x = \frac{\partial u}{\partial x}, \qquad \varepsilon_y = \frac{\partial v}{\partial y}, \qquad \gamma_{xy} = \frac{\partial u}{\partial y} + \frac{\partial v}{\partial x} \tag{1.3}$$

$$\left(\theta = \varepsilon_x + \varepsilon_y = \frac{\partial u}{\partial x} + \frac{\partial v}{\partial y}\right)$$

The relations in eq. (1.3) are obtained on the assumption of "small strains", i.e., such changes in a body when the derivatives of the displacement components with respect to x and y are so small that their square and products may be neglected.

The system of five equations (1.1-1.3) with first-order partial derivatives in five unknown functions σ_x, σ_y, τ_{xy}, u, v is the system of basic equations in plane elasticity.

By using the set of formulas (1.1-1.3), it is easy to derive both a system of equations containing only displacements

$$(\lambda + \mu)\frac{\partial \theta}{\partial x} + \mu\Delta u = 0, \qquad (\lambda + \mu)\frac{\partial \theta}{\partial y} + \mu\Delta v = 0 \tag{1.4}$$

and equations involving only stresses, for which purpose to the relations of eq. (1.1) and eq. (1.2) must be added one more equation

$$\Delta(\sigma_x + \sigma_y) = 0 \tag{1.5}$$

If use is made of the representations of stress and displacement components in terms of the stress function $U(x, y)$ introduced in 1862 by the English astronomer G. B. Airy

$$\sigma_x = \frac{\partial^2 U}{\partial y^2}, \qquad \sigma_y = \frac{\partial^2 U}{\partial x^2}, \qquad \tau_{xy} = -\frac{\partial^2 U}{\partial x \partial y} \tag{1.6}$$

then from eq. (1.5) it follows that $U(x, y)$ is a bi-harmonic function

$$\Delta^2 U = 0 \tag{1.7}$$

Back as far as to 1898, E. Goursat proved that every bi-harmonic function might be expressed in terms of analytic functions of a complex variable [1]. In particular, he suggested the following rep-

resentation of a bi-harmonic function in terms of two analytic functions φ and χ of a complex variable as

$$\mathrm{U} = \frac{1}{2}(\bar{z}\varphi + z\bar{\varphi} + \chi + \bar{\chi}) \tag{1.8}$$

From the foregoing relations and eq. (1.8), one obtains the complex representation of solutions of the plane elasticity problem, which underlies the methods of application of complex function theory in elasticity developed by G. V. Kolosov and N. I. Muskhelishvili.

Omitting rather simple computations, we present the expressions for the complex representation of displacements and stresses obtained by G. V. Kolosov in 1909 [2]

$$\sigma_x + \sigma_y = 2\left[\Phi(z) + \overline{\Phi(z)}\right] \tag{1.9}$$

$$\sigma_y - \sigma_x + 2i\tau_{xy} = 2[\bar{z}\Phi'(z) + \Psi(z)] \tag{1.10}$$

$$2\mu D = \kappa\varphi(z) - \overline{z\varphi'(z)} - \overline{\psi(z)} \tag{1.11}$$

where

$$\varphi(z) = \chi'(z) = \int \Phi(z)dz\,, \qquad \psi(z) = \int \Psi(z)dz \tag{1.12}$$

$$D = u + iv \tag{1.13}$$

and $\kappa = 3 - 4\nu$ is for plane strain, $\kappa = (3-\nu)/(1+\nu)$ is for plane stress.

It may be shown that for any values of $\varphi(z)$ and $\psi(z)$ the functions σ_x, σ_y τ_{xy}, u and v as determined from eqs. (1.9-1.11) satisfy the basic equations (1.1-1.3). In other words, eqs. (1.9-1.11) are the general solutions of the plane problem eqs. (1.1-1.3) of the theory of elasticity. In solving practically important problems, however, we have to impose some additional conditions on the quantities into consideration on the boundary of the region, which leads to the so-called boundary values problems, and relations (1.9-1.11), in spite of their generality, are not the specific solution of these boundary value problems.

Two special cases of relations (1.9-1.11) are associated with the name of H. M. Westergaard [1]. Assuming, for example, that

$$\Phi(z) = \frac{1}{2}Z_1(z), \qquad \Psi(z) = -\frac{1}{2}zZ_1'(z) \tag{1.14}$$

from relations (1.9-1.11), we obtain

$$\sigma_x + \sigma_y = 2ReZ_1 \tag{1.15}$$

$$\sigma_y - \sigma_x = 2yImZ_1^{'} \tag{1.16}$$

$$\tau_{xy} = -yReZ_1^{'} \tag{1.17}$$

The solution furnished by these equations possesses the property that when $y = 0$, $\tau_{xy} = 0$ and $\sigma_x = \sigma_y$.

By using Hook's law and expressing the displacements, v from eqs. (1.1-1.3) in terms of the stresses determined by relations (1.15-1.17), the following expressions for the case of plane strain ($\varepsilon_z = 0$) are obtained.

$$u = \frac{1+\nu}{E}[(1-2\nu)ReZ_1^0 - yImZ_1], \ \left(Z_1 = \frac{dZ_1^0}{dz}\right) \tag{1.18}$$

$$v = \frac{1+\nu}{E}[2(1-\nu)ImZ_1^0 - yReZ_1] \tag{1.19}$$

Let now

$$\Phi(z) = -\frac{1}{2}iZ_2(z), \qquad \Psi(z) = \frac{1}{2}izZ_2^{'}(z) + iZ_2(z) \tag{1.20}$$

From the same relations (1.9-1.11), then we have

$$\sigma_x + \sigma_y = 2ImZ_2 \tag{1.21}$$

$$\sigma_y - \sigma_x = -2ImZ_2 - 2yReZ_2^{'} \tag{1.22}$$

$$\tau_{xy} = ReZ_2 - yImZ_2^{'} \tag{1.23}$$

This solution possesses the property that $\sigma_y = 0$ along the line $y = 0$.

In a similar way, the displacements can be determined.

$$u = \frac{1+\nu}{E}[2(1-\nu)ImZ_2^0 + yReZ_2], \ \left(Z_2 = \frac{dZ_2^0}{dz}\right) \tag{1.24}$$

$$v = \frac{1+\nu}{E}[-(1-2\nu)ReZ_2^0 - yImZ_2] \tag{1.25}$$

One of the most important features in the design of structural elements with cracks is the consideration of stress redistribution resulting from the formation of slits and cracks under the action of external loads. The crack tip is then the location of the highest stress concentration and the origin of the likeliest further fracture. The analysis of the state of stress at the crack tip therefore assumes a special importance. The most general case of strain and stress fields at the crack tip can be obtained by superimposing the stresses due to the following three particular modes of deformation (Fig. 1.1).

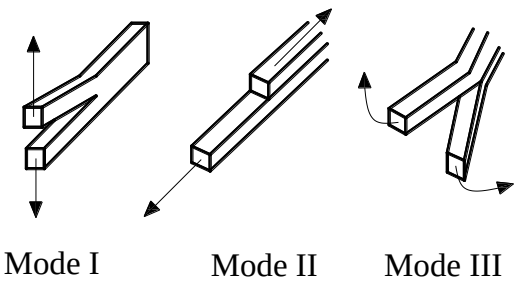

Fig. 1.1. Basic modes of deformation of crack surfaces.

The first mode is associated with an opening displacement in which the crack surfaces move directly apart in opposite directions (symmetrically about the xy and xz planes). The second mode corresponds to displacements in which the crack surfaces slide over one another (symmetrically about the xy plane, but skew-symmetrically about the xz plane). The third mode is connected with anti-plane strain (cutting with the scissors) in which one surface slides over the other parallel to the leading edge of the crack (skew-symmetric strain about the xy and xz planes).

We now revert to Westergaard's solutions and choose the function Z_1, analytic in the entire region with the exception of some segments of the real axis, in the following form

$$Z_1 = \frac{g(z)}{\sqrt{(z-a)(z-b)}} \tag{1.26}$$

If $g(z)$ is a reasonably smooth function, this expression will furnish the solution of the problem of a crack situated along the real axis, $a < x < b$, $y = 0$, since $\sigma_y = \tau_{xy} = 0$ in this interval. From this it follows that

$$Img(z) = 0 \ \ (a < x < b) \tag{1.27}$$

For example, this function giving the solution of the problem of a crack subjected to uniaxial tension p at infinity and free from stress in the interval $-l < x < l$, $y = 0$ is of the form

$$Z_1 = \frac{pz}{\sqrt{z^2 - l^2}} \tag{1.28}$$

By making a change of the variable $\xi = z - b$ in expression (1.26), then

$$Z_1 = f(\xi)\xi^{-1/2} \tag{1.29}$$

In the vicinity of the crack tip $x = b$, i.e., for small value of $|\xi|$, from (1.26) and (1.27) it follows that the function $f(\xi)$ is sufficiently smooth and then $|\xi| \to 0$, it may be replaced by a real constant

$$Z_1|_{|\xi|\to 0} = \frac{K_I}{\sqrt{2\pi\xi}} \ or \ K_I = \lim_{|\xi|\to 0} \sqrt{2\pi\xi}\, Z_1 \tag{1.30}$$

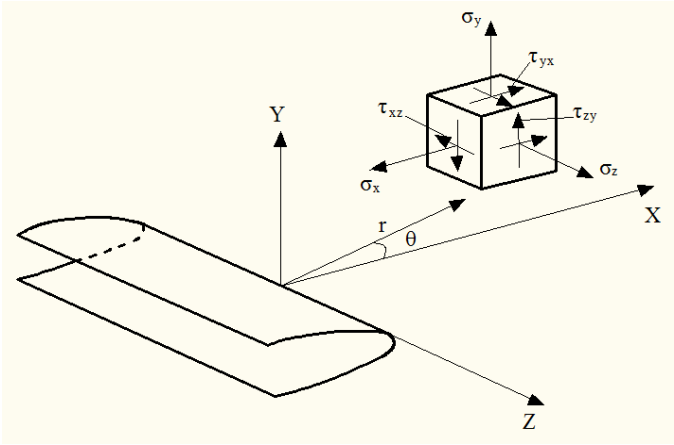

Fig. 1.2 Coordinate system and stress components at a crack tip.

Eq. (1.30) is substituted in eqs. (1.15-1.17) and transformed to polar coordinates $\xi = re^{i\theta}$ in these relations (Fig. 1.2). By rejecting terms of higher order that r, easily, formulas for stress fields are obtained giving a good approximation in a region where r is small compared, for example, with the crack length

$$\sigma_x = \frac{K_I}{\sqrt{2\pi r}}\cos\frac{\theta}{2}\left(1 - \sin\frac{\theta}{2}\sin\frac{3\theta}{2}\right)$$

$$\sigma_y = \frac{K_I}{\sqrt{2\pi r}}\cos\frac{\theta}{2}\left(1 + \sin\frac{\theta}{2}\sin\frac{3\theta}{2}\right)$$

$$\sigma_z = \nu(\sigma_x + \sigma_y) \tag{1.31}$$

$$\tau_{xy} = \frac{K_I}{\sqrt{2\pi r}}\sin\frac{\theta}{2}\cos\frac{\theta}{2}\cos\frac{3\theta}{2}$$

$$\tau_{xz} = \tau_{yz} = 0$$

The displacements in the vicinity of the crack tip are obtained by substituting eq. (1.30) in eqs. (1.18-1.19) and transforming to polar coordinates

$$u = \frac{K_I}{G}\sqrt{\frac{r}{2\pi}}\cos\frac{\theta}{2}\left(1 - 2\nu + \sin^2\frac{\theta}{2}\right)$$

$$v = \frac{K_I}{G}\sqrt{\frac{r}{2\pi}}\sin\frac{\theta}{2}\left(2 - 2\nu - \cos^2\frac{\theta}{2}\right) \tag{1.32}$$

Relations (1.30), (1.31) and (1.32) represent asymptotic expressions for the stress and displacement fields in the vicinity of the crack tip for the first mode of deformation associated with an opening displacement.

We now proceed to the second mode of deformation in which the crack surfaces slide over one another. Similarly from the above it can be concluded that as $|\xi| \to 0$ in the vicinity of the crack tip

$$Z_2|_{|\xi|\to 0} = \frac{K_{II}}{\sqrt{2\pi\xi}} \; or \; K_{II} = \lim_{|\xi|\to 0} \sqrt{2\pi\xi}\, Z_2 \tag{1.33}$$

Substituting eq. (1.33) into eqs. (1.21-1.25), it can be obtained that the following asymptotic representations in polar coordinates for this case of deformation

$$\begin{aligned}
\sigma_x &= -\frac{K_{II}}{\sqrt{2\pi r}} \sin\frac{\theta}{2}\left(2 + \cos\frac{\theta}{2}\cos\frac{3\theta}{2}\right) \\
\sigma_y &= \frac{K_{II}}{\sqrt{2\pi r}} \cos\frac{\theta}{2}\sin\frac{\theta}{2}\cos\frac{3\theta}{2} \\
\sigma_z &= \nu\left(\sigma_x + \sigma_y\right) \qquad (1.34) \\
\tau_{xy} &= \frac{K_{II}}{\sqrt{2\pi r}} \cos\frac{\theta}{2}\left(1 - \sin\frac{\theta}{2}\sin\frac{3\theta}{2}\right) \\
\tau_{xz} &= \tau_{yz} = 0
\end{aligned}$$

$$\begin{aligned}
u &= \frac{K_{II}}{G}\sqrt{\frac{r}{2\pi}} \sin\frac{\theta}{2}\left(2 - 2\nu + \cos^2\frac{\theta}{2}\right) \\
v &= \frac{K_{II}}{G}\sqrt{\frac{r}{2\pi}} \cos\frac{\theta}{2}\left(1 - 2\nu + \sin^2\frac{\theta}{2}\right) \qquad (1.35) \\
\omega &= 0
\end{aligned}$$

The last of the above-mentioned special cases is connected with anti-plane strain in which one surface slides over the other parallel to the leading edge of the crack. In this case $\omega = \omega(x, y)$ is the only non-zero displacement component ($u = v = 0$), and the equilibrium equations and Hooke's law assume the following form

$$\frac{\partial \tau_{xz}}{\partial x} + \frac{\partial \tau_{yz}}{\partial y} = 0 \tag{1.36}$$

$$\tau_{xz} = G\gamma_{xz} = G\frac{\partial \omega}{\partial x}, \tau_{yz} = G\gamma_{yz} = G\frac{\partial \omega}{\partial y} \tag{1.37}$$

from which it follows that, upon substitution of eq. (1.37) in eq. (1.36), the displacement satisfies Laplace's equation

$$\Delta\omega = 0 \tag{1.38}$$

If $\omega = \omega(x, y)$ is chosen in the form

$$\omega = \frac{1}{G} Im Z_3 \tag{1.39}$$

then from (1.37) it will be obtained

$$\tau_{xz} = ImZ_3', \tau_{yz} = ReZ_3' \tag{1.40}$$

In the vicinity of the tip of a crack ($y = 0, x < 0$) with head at the point $y = 0, x = 0$, the stress function Z_3 is of the form

$$Z_3|_{|\xi|\to 0} = \frac{K_{III}}{\sqrt{2\pi\xi}} \; or \; K_{III} = \lim_{|\xi|\to 0} \sqrt{2\pi\xi}\, Z_3 \tag{1.41}$$

Substituting eq. (1.41) in eq. (1.39) and eq. (1.40), expressions for displacements and stresses at the crack tip in the case of anti-plane strain can be obtained

$$\tau_{xz} = -\frac{K_{III}}{\sqrt{2\pi r}} \sin\frac{\theta}{2}$$

$$\tau_{yz} = \frac{K_{III}}{\sqrt{2\pi r}} \cos\frac{\theta}{2}$$

$$\sigma_x = \sigma_y = \sigma_z = \tau_{xy} = 0 \tag{1.42}$$

$$u = v = 0$$

$$\omega = \frac{K_{III}}{G}\sqrt{\frac{2r}{\pi}} sin\frac{\theta}{2} \tag{1.43}$$

The relations obtained involve three quantities K_I, K_{II} and K_{III}, termed the stress intensity factors for the three modes of deformation discussed above. These factors play extremely important roles in the mechanics of brittle fracture.

The stress intensity factors are often designated by the symbol K without a suffix implying that either the mode of deformation is clear from the problem or the factor may apply to any mode.

1.3 Stress intensity factors

1.3.1 Stress intensity factors

The design of a body for strength is closely related to the determination of its state of stress. This is necessary not only for the purpose of finding a dangerous point and the components of stress at it but also for assessing the strength of material at this point since most criteria for the occurrence of a dangerous state are expressed in terms of the components of stress. For many practically important shapes of bodies and loading conditions the determination of the state of stress concentration factors. These factors represent the ratio of the maximum value of any component of the stress tensor

to the corresponding nominal value and are thus expressed by non-dimensional numbers. The determination of the state of stress and hence of stress concentration is a subject to which entire branches of continuum mechanics are devoted, such as elasticity theory and plasticity theory, which are presently thoroughly studied.

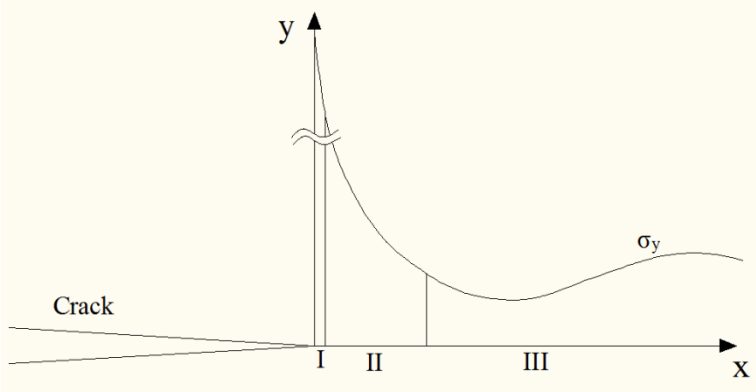

Fig. 1.3 Distribution of stress σ_y ahead of the tip of a brittle crack. I, Region of non-linear strains and of realization of fracture mechanism; II, region of validity of asymptotic formulas, $\sigma_y = K/\sqrt{2\pi x}$; III, region of nominal stresses.

The problem of determining the state of stress near the crack tip differs from the usual problems of determining stress concentration in that the geometrically linearized formulation of boundary conditions and the physically linear theory of elasticity lead to infinite stresses and infinite stress gradients at the end of a thin cut. The concept of the stress concentration factor becomes meaningless. However, it is sufficient to know the nature and intensity of the state of stress in a region surrounding the end of cut together with a small volume where the fracture mechanism is concentrated (Fig 1.3). This means a rejection of the stress concentration factor in favor of the asymptotic representation of the state of stress at the end of the cut. The radial and angular distribution for the asymptotic representation of the state of stress is independent of the crack length, the body shape and the loading conditions. The intensity of this distribution, however, is depends only on a single factor K which, in contrast, is independent from the coordinates of points near the end of the cut. Consequently, all fracture processes in materials are initiated and governed by the intensity of the stress field (surrounding the crack end) through the stress intensity factor K. In contrast to the concentration factor, the stress intensity factor is dimensional quantity (with the dimension kgf/mm$^{3/2}$ in engineering). From the above discussion one can see the dominant role of the stress intensity factor in fracture mechanics, a fact which accounts for the consideration of the stress intensity factor as the subject of analytic or experimental investigation.

The concept of stress intensity factor is a result of the bi-dimensional analysis of the stress field at the crack tip. This analysis was carried out by Williams [3], taking into account Westergaard's work [4]. Using coordinate system centered in the crack tip and according to Williams' analysis, the

stress field components near the crack tip are proportional to $\sqrt{K}/r$, where r is the radial distance from the tip. For each node, the stress field in the crack tip region can be expressed using stress intensity factor from eq. (1.31) and eq. (1.34) as

$$\lim_{r\to 0}\sigma_{ij}^{I} = \frac{K_I}{\sqrt{2\pi r}} f_{ij}^{I}(\theta)$$

$$\lim_{r\to 0}\sigma_{ij}^{II} = \frac{K_{II}}{\sqrt{2\pi r}} f_{ij}^{II}(\theta) \tag{1.44}$$

$$\lim_{r\to 0}\sigma_{ij}^{III} = \frac{K_{III}}{\sqrt{2\pi r}} f_{ij}^{III}(\theta)$$

where r and θ are the polar coordinates in the system of axes having the origin at the crack tip Fig. 1.4. According to Williams' analysis, the components of the stress field can be written as a series of expressions, from this expansion, the stress intensity factor can be calculated from the stress field in the crack tip.

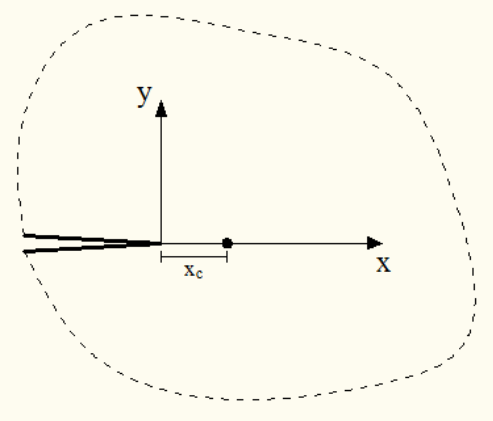

Fig. 1.4 Cracked plate and the local coordinate system.

1.3.2 Calculating the stress intensity factors

Generically there are two kinds of methods for evaluating the stress intensity factors: the analytical methods and the numerical methods. The analytical methods have been the basis for the development of fracture mechanics. They have delivered the basic equations for the crack tip stress and displacement field, which still serve as the starting point for many other solutions. The knowledge that these fields for either fracture mode always take the same from offering the possibility to determine the stress intensity factor in an indirect way. However, these methods are the least interesting from an engineering point of view, because in general they try to satisfy the boundary conditions exactly and it is possible in case of infinite plate only. Basically, the analytical solution tries to find an Airy stress function that for Mode I stress problems takes the form of Westergaard stress function [4].

Other forms of complex stress functions are developed. One of them is developed by Muskhelishvili [5] as mentioned in the Section 1.2.

If a straightforward solution of the equations is not possible, numerical procedures can be applied to obtain approximate figures. Various numerical methods have been developed to derive stress intensity factor. For instance a conformal mapping technique can be used [6] to treat the important technical problem of a crack emanating from a hole. Boundary collocation method starts off a set of linear algebraic equations and replaces the elastic differential equations. The series expansion is adapted to satisfy the boundary conditions. This method has been used to solve many crack problems of plate with finite size [7, 8]. The method mentioned above is a combination of conformal mapping and boundary collocation method [9].

Boundary collocation method starts off a set of linear algebraic equations and replaces the elastic differential equations. The series expansion is adapted to satisfy the boundary conditions. This method has been used to solve many crack problems of plate with finite size [10, 11].

1.3.3 Numerical methods

In this section, some numerical methods for calculating stress intensity factor will be presented.

1.3.3.1 Compounding method

The compounding method, proposed by Cartwright and Rooke [12], is used for stress intensity factor determination in complex structures, starting form available solutions for simper problems. This method consists of decomposing a cracked structure with N boundaries into N ancillary configurations, each one containing one boundary and for which stress intensity factor solutions are available. The stress intensity factor for a crack tip can be expressed as a function of N ancillary stress intensity factor values

$$K_{IN} = K_0 + \sum_{n=1}^{N} (K_n - K_0) \tag{1.45}$$

where K_0 is the stress intensity factor for the same body without boundaries and K_n is the stress intensity factor for the body with the boundary n. When boundaries interact one with another, stresses at the location of these boundaries will be different, leading to an increase or decrease of stress intensity factor values. Due to this effect, another term K_e, corresponding to the boundary-to-boundary interaction is added in eq. (1.45)

$$K_{IN} = K_0 + \sum_{n=1}^{N} (K_n - K_0) + K_e \tag{1.46}$$

If a crack crosses a boundary, a modification in equations (1.45) and (1.46) will be required in order to account for the effect of the stress originated by this boundary at the crack tip. This effect is not taken into account in the preceding considerations, but must be considered because of the change in stress and displacement fields at the crack tip due to the boundary. In these circumstances, the structure with a crack length $2a$, containing a boundary crossed by the crack, is converted into an equivalent structure without the boundary but with an equivalent crack length $2a'$. The stress intensity factor calculation takes into account the other boundaries interacting with the crack length $2a'$. Taking into account that $K_{0n} = Q_0 K_n$, where K_n is the stress intensity factor for configuration n containing a crack of length $2a$, the stress intensity factor can be rewritten in non-dimensional form, dividing all terms by $\sigma\sqrt{\pi a}$, obtaining

$$Q_{IN} = Q_0 \left(1 + \sum_{n=1}^{N} (Q_n - 1)\right) \tag{1.47}$$

1.3.3.2 Displacement extrapolation method

The displacement extrapolation method was developed in order to obtain crack tip singular and stress intensity factors using only nodal displacements of elements around the crack [13]. The near crack tip displacement field may be expressed as a series in function of the stress intensity factors, distance to the crack tip and the angle with the propagation directions. For $\theta = \pi$ (along the crack line) and using the first term of this series, the displacements are given by

$$\begin{aligned} u_x &= \frac{K_{II}}{2G}\sqrt{\frac{r}{2\pi}}(1+\kappa) \\ u_y &= \frac{K_I}{4G}\sqrt{\frac{r}{2\pi}}(1+\kappa) \\ u_z &= \frac{2K_{III}}{G}\sqrt{\frac{r}{2\pi}} \end{aligned} \tag{1.48}$$

where $\kappa = 3 - 4\nu$ in plane stress and $\kappa = (3-\nu)/(1+\nu)$ in plane strain. From these equations, a relationship between displacements and the apparent stress intensity factor K_0 is obtained. Using a linear extrapolation to $r = 0$, the stress intensity factor at the crack tip can be estimated with high accuracy. This technique can be more accurate using the quarter node point or collapsed elements, when finite elements are used. Furthermore, for these situations modifications are required in the equations in [14].

1.3.3.3 Force method

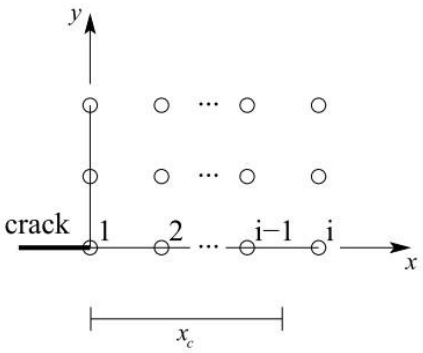

Fig. 1.5 Definition of the distance x_c for a generic grid.

The force method is an alternative to the displacement method, using nodal reactions obtained in a finite element model which proposed by Raju and Newman in 1977. A recent publication by Morais[15] applying this method to isotropic center-cracked infinite plates and orthotropic beam specimens showed good results.

Considering an orthotropic body subjected to mixed mode loading (Mode I and Mode II) under plane stress or plane strain conditions, the crack is assumed to be oriented along one of the material symmetry axis. Therefore, stresses along the x-axis and in the vicinity of the crack tip are

$$\tau_{xy} = \frac{K_{II}}{\sqrt{2\pi x}}$$

$$\sigma_y = \frac{K_I}{\sqrt{2\pi x}} \tag{1.50}$$

The total forces over the $x_c - sized$ ligament can be expressed as

$$F_y = t\int_0^{x_c} \sigma_y dx = K_I\sqrt{\frac{2x_c}{\pi}}, \qquad F_x = t\int_0^{x_c} \tau_{xy} dx = K_{II}\sqrt{\frac{2x_c}{\pi}} \tag{1.51}$$

where t is the plate's thickness, and their values can be evaluated from nodal forces in FE models. Moreover, as in the displacement extrapolation method, the linear relation between F_y, F_x and $\sqrt{x_c}$ allows a similar stress intensity evaluation procedure based on K_I and K_{II} versus x_c plots. It is worth noting that eq. (1.51) demand finite element meshes that contain element faces along the crack $y = 0$ plane (see Fig. 1.5). Nevertheless, more general meshes can also be used with appropriate force direction corrections [16]. It is also convenient that the element length is kept constant in the vicinity of the crack tip. So far the stress intensity factor has been calculated in the following examples by using an extrapolation technique [15].

It is worth notice that definition of x_c and nodal forces need to be considered. In fact x_c is taken in the middle of the positions of the last grid point of the sub-domain element whose force will be con-

sidered and the next grid point. As far as the solution which concern a displacement field is obtained from the static analysis and the internal stresses are derived from the plate displacement, the stress intensity factor estimation can be done as follows

$$K_I' = \sqrt{\frac{\pi}{2x_c}} \sum_{i=1}^{n} F_{y,i}, \quad K_{II}' = \sqrt{\frac{\pi}{2x_c}} \sum_{i=1}^{n} F_{x,i} \tag{1.52}$$

and K_I, K_{II} are subsequently calculated by extrapolating to $x_c = 0$, the linear approximation to K_I' versus x_c and K_{II}' versus x_c plots, respectively. One advantage over the displacement extrapolation method is obvious: there is no need to know the frequently complicated stress intensity factors - displacements relations. Secondly, force summations which take over a properly chosen x_c - distances are likely to be more accurate than point measurements of displacement jumps.

1.3.3.4 Singularity subtraction technique

The Singularity Subtraction Technique (SST) uses a singular solution of the stress field in order to calculate the stress intensity factor. From Williams' series expansion, giving the stress field, and the equations from statics, stress tensor components in any location close to the crack tip are known, and may be used for calculating stresses in any direction. If a point *P* close to the crack tip where the stress components are known is selected, the stress σ_P calculated in *P*, at a distance ε from the crack tip, is related with the new t_I and t_{II} components that are obtained using the following equations

$$K_I = t_I\sqrt{2\pi r}, \qquad K_{II} = t_{II}\sqrt{2\pi r} \tag{1.53}$$

where for the stress intensity factor determination the value of r is independent from ε and it is calibrated from known stress intensity factor solutions.

1.3.3.5 J-integral

One of the most accurate methods consists in calculating strain energy release rates and using their relations with stress intensity factors, which are quite simple for isotropic materials.

The J-integral is a contour integral characterizing the strain energy release rate for an elastic non-linear material. The stress field is related to the strain energy density as

$$\sigma_{ij} = \frac{\partial \Phi}{\partial \varepsilon_{ij}} \tag{1.54}$$

where Φ is the strain energy. From the definition of potential energy along a contour, work theorem and the previous equation, Rice [17] defined an integral independent of integration contour Γ around the crack tip as

$$\mathrm{J} = \int_{\Gamma} \left(\phi \mathrm{dy} - \mathrm{T} \frac{\partial \mathrm{u}}{\partial \mathrm{x}} \mathrm{ds} \right) \tag{1.55}$$

where ϕ is strain energy density per unit volume, T is the traction vector $\mathrm{T} = \sigma \mathbf{n}$, u is the displacement vector and y is the direction perpendicular to the crack line. For linear or non-linear elastic materials, the strain energy release rate is equal to the strain energy release rate along a contour at crack tip vicinity ($\mathrm{J} = \mathcal{G}$); this parameter is related to the stress intensity factor as $\mathcal{G} = \mathrm{K}^2/\mathrm{E}$ in plane stress or $\mathcal{G} = 2\mathrm{K}^2/\mathrm{E}(1-\nu^2)$ in plane strain.

1.3.3.6 Virtual crack closure technique

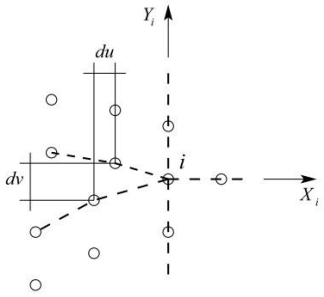

Fig.1.6. Modified virtual crack closure technique

The Virtual Crack Closure Technique (VCCT) is based on energy release rate when the crack grows with an infinitesimal increment. It is based on the calculation of the strain energy release rate, using the energy variation when an extension of crack length is imposed

$$\mathcal{G} = \frac{\partial U}{\partial a} \approx \frac{\mathrm{U_{a+\Delta a}} - \mathrm{U_a}}{\Delta \mathrm{a}} \tag{1.56}$$

This technique was proposed by Rybicki and Kanninen in 1977 [18], however it requires two analysis in order to calculate the strain energy release rate for a specific crack length. Some other reviews of VCCT can be found in literature [19, 20]. A modified version is proposed where only one model is needed to calculate the energy release rate which is based on the same assumptions as VCCT in two steps, but in addition it is assumed that the conditions at the crack tip are significantly altered when the crack extends by an increment Δa, from a crack length $\mathrm{a} + \Delta\mathrm{a}$ to a length $\mathrm{a} + 2\Delta\mathrm{a}$. This implies that the displacements of a region close to the crack tip, when the tip is at specific node i, are approximately the same as the displacements at the same location when the tip is at the previous node, at which the displacements are computed.

The energy variation $\Delta\varepsilon$ necessary to close the crack along a distance Δa is

$$\Delta\varepsilon = \frac{1}{2}\left(X_i du + Y_i dv\right) \tag{1.57}$$

Where X_i and Y_i are the nodal forces at point i, du and dv are the node displacements at the node beside i. Therefore, the information required for the calculation of the energy variation is obtained from a single numerical analysis. After obtaining the energy variation, the energy release rate is calculated as

$$\mathcal{G} = \frac{\Delta\varepsilon}{\Delta A} = \frac{\Delta\varepsilon}{\Delta a \cdot b} \tag{1.58}$$

where ΔA is the surface area created by a crack propagation of Δa; in the case of plates with a thickness b, this area is $\Delta a \cdot b$. The calculation of strain energy release rates for each mode is made using the displacements and nodal forces corresponding to the strain energy of that mode. Thus, for the case of Fig. 1.6, the energy release rate is

$$\begin{aligned} \mathcal{G}_I &= -\frac{1}{2\Delta a} Y_i dv \\ \mathcal{G}_{II} &= -\frac{1}{2\Delta a} X_i du \end{aligned} \tag{1.59}$$

References

[1] V.Z. Parton, E.M. Morozov. Elastic-plastic Fracture Mechanics. MIR Publishers, Moscow, 1978.

[2] G.V. Kolosov, On one application of complex function theory to the plane problem of the mathematical theory of elasticity, Ur'ev, 1909.

[3] M.L. Williams. On the stress distribution at the base of a stationary crack. Journal of Applied Mechanics, 1957, 24(1): 109-114.

[4] H.M. Westergaard. Bearing pressures and cracks. Journal of Applied Mechanics, 1939, 6(61): 49-53.

[5] G.C. Sih. Methods of analysis and solutions of crack problems: Recent developments in fracture mechanics. Mechanics of fracture. Noordhoff International Publishers. 1973.

[6] O.L. Bowie, C.E. Freese, Elastic analysis for a radial crack in a circular ring. Engng. Fract. Mech. 1972, 4(2): 315-321.

[7] O.L. Bowie, D.M. Neal. A modified mapping-collocation technique for accurate calculation of stress intensity factors: technical report. Theoretical & Applied Mechanics Research Laboratory Army Materials and Mechanics Research Center, 1969.

[8] S.K. Cheong, C.S. Hong. Analysis of cracks emanating from a circular hole in an orthotropic plate under mixed mode deformation. Engng. Fract. Mech. 1988, 31(2): 237-248.

[9] C.Y. Dong, S.H. Lo, Y.K. Cheung, et.al. Anisotropic thin plate bending problems by Trefftz boundary collocation method. Engineering Analysis with Boundary Elements, 2004, 28(9): 1017-1024.

[10] Y.H. Wang, Y.K. Cheung, Boundary collocation method for cracks emanating from a hole in an anisotropic plate. Engng. Fract. Mech. 1994, 48(1):53-62.

[11] Y.H. Wang, L.G. Tham, P.K.K. Lee, Y. Tsui, A boundary collocation method for cracked plates. Computers & Structures, 2003, 81(28-29):2621-2630.

[12]D.J. Cartwright, D.P. Rooke, Approximate stress intensity factors compounded from known solutions. Engng. Fract. Mech. 1974, 6(3): 563-571.

[13]Stress analysis of cracks. Fracture toughness testing and its applications, ASTM, 1965, 381:30-83.

[14]G. Guinea. Ki evaluation by the displacement extrapolation technique. Engng. Fract. Mech. 2000, 66(3): 243-255.

[15]A.B. de Morais. Calculation of stress intensity factors by the force method. Engng. Fract. Mech. 2007, 74(5): 739-750.

[16]J.P. Pereira, C.A. Duarte. Extraction of stress intensity factors from generalized finite element solutions. Engineering Analysis with Boundary Elements, 2005, 29(4): 397-413.

[17]J.R. Rice. Mathematical analysis in the mechanics of fracture. Chapter 3 of Fracture, An Advanced Treatise, Academic Press, N.Y., 1968, pp. 191-311.

[18]E.F. Rybicki, M.F. Kanninen. A finite element calculation of stress intensity factors by a modified crack closure integral. Engng. Fract. Mech. 1977, 9(4): 931-938.

[19]H. Okada, M. Higashi, M. Kikuchi, et. al., Three dimensional virtual crack closure integral method (vccm) with skewed and non-symmetric mesh arrangement at the crack front. Engng. Fract. Mech. 2005, 72(11): 1717-1737.

[20]A.C. Orifici, R. Krueger. Benchmark assessment of automated delamination propagation capabilities in finite element codes for static loading. Finite Elements in Analysis and Design, 2012, 54: 28-36.

Chapter 2

Calculation of stress intensity factors

2.1 Introduction

There is an important class of crack problems, involving surface damage in the form of part-through cracks in round bars or beams, where a three dimensional analysis becomes necessary. Valiente [1] numerically obtained two solutions by the finite element method, firstly, on the basis of the computation of the sample compliance and the energy release rate on the basis of the former, and secondly, using the stiffness derivative technique on the basis of the virtual crack extension to calculate the energy release rate. Levan, Royer and Couroneau[2, 3] calculated the SIFs in round bars with transverse circular cracks using the boundary integral equation method. Daoud and Cartwright [4, 5] computed SIFs in a circular bar with a straight-fronted crack under tension and bending using finite element numerical procedure. Ng and Fenner [6] built a three-dimensional finite element model with both straight and circular-arc crack fronts in an edge cracked circular bar to compute SIFs in tension and bending. Shin and Cai [7] applied experimental backtracking and finite element method on stress intensity factors of an elliptical surface crack in a circular shaft under tension and bending. Carpinteri [8] computed the dimensionless SIFs for straight-front and semi-elliptical cracks using the finite element method and 3D isoperimetric elements of 20 nodes. Si [9] presented normalized stress intensity factors as a function of crack depth for round bars under tension and bending based on reviews. Naik and Maiti [10] presented the formulation for analyzing the triply coupled free vibration of beams based on compliance approach in the open edge crack in an arbitrary angular orientation. Some reviews of the stress intensity factor solutions for surface cracks in round bars subjected to tension loading are introduced in Ref. [11, 12]. Some of these modeling techniques have already been overviewed in this introduction. Because of the complexities of the problems, exact solutions for edge cracks in round bars under tension and bending are obtained. For engineering estimations of the strength of cracked bodies, the use of procedures involving a smaller amount of computational works can be suitable, even if a lower accuracy is involved.

In this chapter, two simple engineering methods for a fast and close approximation of stress intensity factors of cracked or notched beams are presented. The first simple and convenient method proposed by Kienzler and Herrmann [13] is to estimate the stress intensity factors of circular section beams with notched crack. This method is based on an elementary beam theory assuming that the

strain energy release rate $\mathcal{G}$ for crack extension is equal to that for crack widening so that the well-known Irwin's $\mathcal{G} - K$ relation can be used to determine the stress intensity factors. Bazant [14] suggested that this hypothesis was approximately valid within a correction factor that can be determined only through optimum fiting of the exact solution as he claimed. Gao and Herrmann [15] showed, by contrast, that this correction factor could be obtained through simple asymptotic matching with standard limiting crack solution. Ricci and Viola [16] presented an extension of this method to T-section cracked beam and addressed the coupled bending-torsion vibration of cracked T-beams within the context of the dynamic stiffness matrix method of analyzing structures.

Another method, named section method, proposed by Parton and Morozov [17], and based on equilibrium condition for internal forces evaluated in the cross-section passing through the crack tip, t the stress singularity at the tip of an elastic crack into account. This method has been modified and applied by Nobile [18, 19]. An extension of this method has been presented by Ricci and Viola [16] to estimate the stress intensity factors of cracked T-beams.

2.2 Kienzler-Herrmann's method

A remarkably simple method for close approximation of K_I in notched beams was discovered by Kienzler and Herrmann (1986, [13]). The method was derived from a certain unproven hypothesis (postulate) regarding the energy release when the thickness of the fracture band was increased. A different derivation of this method (Bazant, 1988, [14]) is showed, that is simpler and at the same time indicating the hypothesis used by Herrmann et al. might not be exact but merely a good approximation. Also, Herrmann's method relies on more sophisticated concepts (material forces) that seem more complicated than necessary to obtain the results.

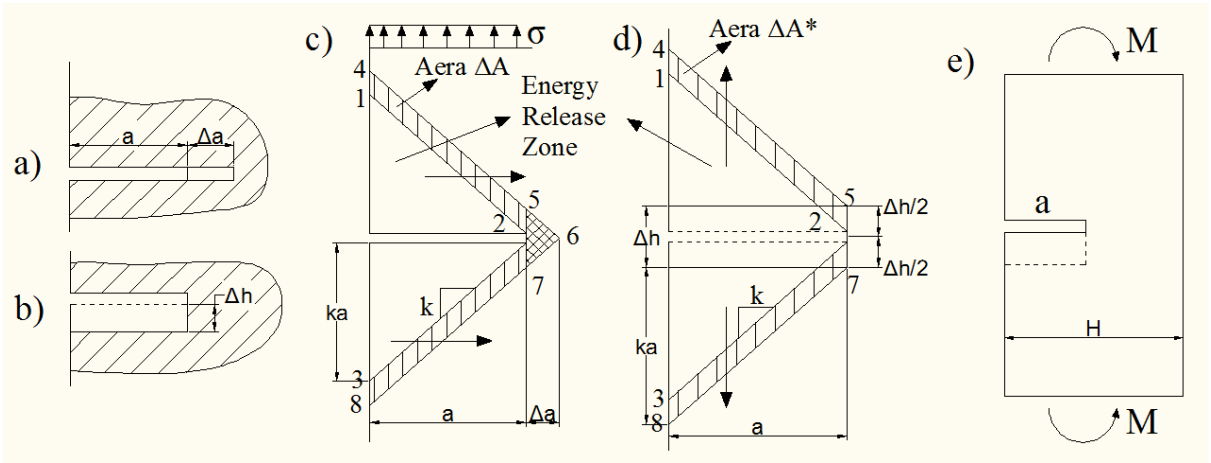

Fig.2.1 (a) Line crack advance; (b) crack band widening; (c, d) corresponding stress relief zones; (e) notched beam under constant bending moment

Let us estimate the energy release rate $\mathcal{G}$ by considering the expansion of the stress relief zone at crack extension Δa and employing the simplified "stress diffusion lines" of empirical slope β (k), see Figure 2.1 a, c. Considering now that instead of crack extension Δa the crack is widened into a crack band of width Δh, see Figure 2.1 b, d. This widens the stress relief zone from area 1231 to area 45784 as shown by arrows in Figure 2.1 d. Since the triangular area 56725 in Figure 2.1 c is second-order small if Δa was small, the increments of the stress relief zones 123876541 in Figure 2.1c and d are identical provided that $\frac{\Delta h}{2} = \beta \Delta a$. Therefore (at fixed boundary displacements, for which $\Pi = U$),

$$-b\mathcal{G} = \frac{\partial U}{\partial a} = 2\beta \frac{\partial U}{\partial h} \tag{2.1}$$

(Bazant, 1990 [14]), $b =$ thickness of body. The case $\beta = 1$ coincides with the hypothesis of Kienzler and Herrmann in 1986 [13]. However, there seems no reason to assume that $\beta = 1$, and numerical results in Bazant, show that more accurate results can be obtained if the empirical constant β is allowed to differ from 1.

The advantage of eq. (2.1) is that it can be used even in problems where the initial stress field before the appearance of the crack is non-uniform. The reason is that, approximately, the widening of the crack into a band has merely the effect of shifting the stress field as a rigid body along with the shift of the triangular stress relief zones as indicated by arrows in Fig. 2.1d, while the strain energy in the band can be easily estimated.

Following Kienzler and Herrmann, their method is best illustrated by considering a beam with a single edge crack subjected to a bending moment M in Fig. 2.1e. Assume that the beam has bending stiffness EI at the uncracked cross-section and EI^c at the cracked cross-section. Here, I and I^c denote the moments of inertia of uncracked and cracked section and E is the Young's modulus of the material. Then from the elementary beam theory of bending, the widening of the crack by Δh is effective to reduce the bending stiffness from EI to EI^c along the length Δh, and the corresponding change in energy of the beam is

$$\Delta U = \frac{M^2}{2}\left(\frac{1}{EI} - \frac{1}{EI^c}\right)\Delta h \tag{2.2}$$

where U is the potential energy available for crack growth. As $\Delta h \to 0$, the incremental strain energy gives

$$\frac{\partial U}{\partial h} = -\frac{M^2}{2E}\left(\frac{1}{I^c} - \frac{1}{I}\right) \tag{2.3}$$

The argument leading to eq. (2.3) may be extended to beams under axial force, torque and shearing force.

For bars and beams under tensile load N, the incremental strain energy as following is analogous to eq. (2.3),

$$\frac{\partial U}{\partial h} = -\frac{N^2}{2E}\left(\frac{1}{A^c} - \frac{1}{A}\right) \tag{2.4}$$

where EA denotes the tension stiffness, A, A^c being the cross-section area of uncracked and cracked beam portions, respectively.

For beams subject to a torque T, it also can be shown that

$$\frac{\partial U}{\partial h} = -\frac{T^2}{2\mu}\left(\frac{1}{J^c} - \frac{1}{J}\right) \tag{2.5}$$

where μJ denotes the torsion rigidity with $\mu = E/2(1-\nu)$ the shear modulus, and J, J^c being the polar moments of inertia of the uncracked and cracked portions, respectively.

According to the expressions by [15] for the loading conditions presented above, for beams subjected to a shear force Q, the following equation can be obtained

$$\frac{\partial U}{\partial h} = -\lambda\frac{Q^2}{2\mu}\left(\frac{1}{A^c} - \frac{1}{A}\right) \tag{2.6}$$

where λ is the shearing factor.

The strain energy release rate $\mathcal{G}$ is the energy dissipated during fracture per unit of newly created fracture surface area.

$$\mathcal{G} = -\frac{\partial U}{\partial A} \tag{2.7}$$

According to the well-known Irwin's G-K relation

$$\mathcal{G} = \frac{1}{E'}(K_I^2 + K_{II}^2) + \frac{1+\nu}{E}\,K_{III}^2 \tag{2.8}$$

where $E' = E/(1-\nu^2)$ is for plane strain, $E' = E$ is for plane stress, E is Young's modulus, and ν is Poisson's coefficient.

Therefore, the energy release rate due to crack extension is as following

$$\frac{\partial U}{\partial a} = -4R\frac{K^2}{E'}\sqrt{\eta - \eta^2} \tag{2.9}$$

where $\eta = a/(2R)$ is the dimensionless crack depth (crack ratio), a is the crack depth, R is the radius of the circular section, and K is the stress intensity factor.

The equations presented above allow one to calculate the stress intensity factors through eq. (2.1) once the factor β (slope of the stress diffusion lines) is determined. The stress intensity factors may be further evaluated through the following equations

$$K_{I_N} = \frac{N}{2}\sqrt{\frac{\beta'}{R(\eta-\eta^2)^{1/2}}\left(\frac{1}{A^c}-\frac{1}{A}\right)} \tag{2.10}$$

$$K_{I_M} = \frac{M}{2}\sqrt{\frac{\beta'}{R(\eta-\eta^2)^{1/2}}\left(\frac{1}{I^c}-\frac{1}{I}\right)} \tag{2.11}$$

$$K_{II_Q} = \frac{Q}{2}\sqrt{\frac{2\lambda\beta'(1+\nu)}{R(\eta-\eta^2)^{1/2}}\left(\frac{1}{A^c}-\frac{1}{A}\right)} \tag{2.12}$$

$$K_{III_T} = \frac{T}{2}\sqrt{\frac{2\beta}{R(\eta-\eta^2)^{1/2}}\left(\frac{1}{J^c}-\frac{1}{J}\right)} \tag{2.13}$$

where $\beta' = \beta E'/E$. In most of cases discussed in the literature, the slope factor β is $\beta = 1$. In plane stress, set $\beta' = 1$, one can obtain the following dimensionless formulas of stress intensity factors.

2.2.1 Beams under tension N

An axial tensile load N applied to a single-edge-notch circular section leads to a combined tension and bending moment, since the neutral axial of the ligament is shifted by e as following

$$e = \frac{16R^3(\eta-\eta^2)^{3/2}}{3A^c} \tag{2.14}$$

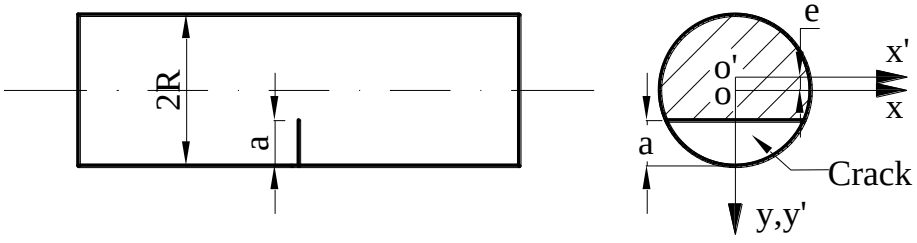

Fig. 2.2. Cracked beam and cracked circular cross-section.

which gives rise to a bending moment

$$M^N = eN \tag{2.15}$$

From eqs (2.10) and (2.11), when the circular section is subject to the tensile force N, the following relationship for the stress intensity factor K_{I_N} can be obtained

$$K_{I_N} = \frac{N}{2}\sqrt{\frac{\beta'}{R(\eta-\eta^2)^{1/2}}\left(\frac{1}{A^c}-\frac{1}{A}\right)} + \frac{M^N}{2}\sqrt{\frac{\beta'}{R(\eta-\eta^2)^{1/2}}\left(\frac{1}{I^c}-\frac{1}{I}\right)} \tag{2.16}$$

where the bending moment M^N in eq. (16) is derived from eq. (15). Substituting the expressions of A, A^c, I and I^c and setting $\beta' = 1$ in eq. (16), one can obtain

$$K_{I_N} = \frac{N}{R^{3/2}} F_N(\eta) \tag{2.17}$$

where $F_N(\eta)$ is the geometric function of crack ratio represented in the following

$$F_N(\eta) = \frac{1}{2}\sqrt{\frac{1}{\Delta}\left(\frac{1}{\Pi_1}-\frac{1}{\pi}\right)} + \frac{8\Delta^3}{3\Pi_1}\sqrt{\frac{1}{\Delta}\left[\left(\frac{\Pi_2}{4}+(1-2\eta)^3\Delta-\frac{256\Delta^6}{9\Pi_1}\right)^{-1}-\frac{4}{\pi}\right]} \tag{2.18}$$

with

$$\Pi_1 = \pi - \cos^{-1}(1-2\eta) + 2(1-2\eta)\sqrt{\eta-\eta^2}$$

$$\Pi_2 = \pi - \cos^{-1}(1-2\eta) - 2(1-2\eta)\sqrt{\eta-\eta^2}$$

$$\Delta = \sqrt{\eta-\eta^2} \tag{2.19}$$

2.2.2. Beams under bending moment M

For the circular section beams subjected to the bending moment M, the formula for the stress intensity factors K_{I_M} is given by eq. (2.11). Substituting the expressions of I, I^c and setting $\beta' = 1$, one can obtain the following expression

$$K_{I_M} = \frac{M}{2}\sqrt{\frac{\beta'}{R(\eta-\eta^2)^{1/2}}\left(\frac{1}{I^c}-\frac{1}{I}\right)} = \frac{M}{R^{5/2}} F_M(\eta) \tag{2.20}$$

where $F_M(\eta)$ is the geometric function of crack ratio expressed as

$$F_M(\eta) = \frac{1}{2}\sqrt{\frac{1}{\Delta}\left[\left(\frac{\Pi_2}{4}+(1-2\eta)^3\Delta-\frac{256\Delta^6}{9\Pi_1}\right)^{-1}-\frac{4}{\pi}\right]} \tag{2.21}$$

with Π_1, Π_2, Δ are already defined in eq. (2.19).

2.2.3. Beams under torque T

When a torque T is applied to the cracked circular section beam, substituting the expressions of J, J^c and setting $\beta = 1$ in eq. (2.13), one can obtain the following expression for the stress intensity factor

$$K_{III_T} = \frac{T}{2}\sqrt{\frac{2\beta}{R(\eta-\eta^2)^{1/2}}\left(\frac{1}{J^c}-\frac{1}{J}\right)} = \frac{T}{R^{5/2}}F_T(\eta) \tag{2.22}$$

where $F_T(\eta)$ is the geometric function of dimensionless crack depth expressed as

$$F_T(\eta) = \sqrt{\frac{1}{2\Delta}\left[\left(\frac{\Pi_1}{2}-\frac{8}{3}(1-2\eta)\Delta^3-\frac{256\Delta^6}{9\Pi_1}\right)^{-1}-\frac{2}{\pi}\right]} \tag{2.23}$$

with Π_1, Δ are already defined in eq. (2.19).

2.2.4. Beams under shear force Q

For the circular section beam under shear force Q, the formula of the stress intensity factors K_{II_S} is given by eq. (2.12), setting shearing factor $\lambda = 6/5$, $\beta' = 1$, Poisson's coefficient $\nu = 0.3$ and substituting the expressions of the cross-section area of uncracked and cracked beam portion A and A^c. One can obtain the following expression

$$K_{II_Q} = \frac{Q}{2}\sqrt{\frac{2\lambda\beta'(1+\nu)}{R(\eta-\eta^2)^{1/2}}\left(\frac{1}{A^c}-\frac{1}{A}\right)} = \frac{Q}{R^{3/2}}F_S(\eta) \tag{2.24}$$

where $F_S(\eta)$ is the geometric function of dimensionless crack depth is represented by eq. (2.25)

$$F_S(\eta) = 0.8832\sqrt{\frac{1}{\Delta}\left(\frac{1}{\Pi_1}-\frac{1}{\pi}\right)} \tag{2.25}$$

with Π_1, Δ are already defined in eq. (2.19).

2.3 Section method

In this section we shall show the possibility of applying the method of sections proposed by Parton and Morozov [14], a method well known in structural mechanics, to calculate the stress intensity factor. Considering a plane crack problem, we isolate a part of the body by an imaginary section (which may be a broken one) so that this section passes through the crack tip. We further write down the conditions for the equilibrium of external and internal forces exerted on the remaining part of the body. In setting up these conditions we take into account the asymptotic expressions for stress eq. (1.19).

The additional force arising at the crack tip from an increase in stresses is equal to

$$\int_0^b \sigma_s dr \tag{2.26}$$

where b can be determined from the condition that σ_s at $r = b$ is equal to the nominal stress.

Thus, the equilibrium condition expresses the fact that the force not transmitted through the crack line is compensated for by an additional force due to the stress concentration at the crack tip. Below is given example of the calculation of the intensity factor using the method of sections.

For example, the Griffith problem: an infinite plate with a single crack of length $2l$ is extended by a uniformly distributed stress σ perpendicular to the crack line. The force not transmitted through the crack is $2l\sigma$, and the increased stress at the ends of the crack produces an additional force equal to $2\int_0^b \sigma_s dr$. The value of b is found from the condition

$$\sigma_s(r = b) = \sigma \tag{2.27}$$

i.e.,

$$\frac{K}{\sqrt{2\pi b}} = \sigma \tag{2.28}$$

from which

$$b = \frac{K^2}{2\pi\sigma^2} \tag{2.29}$$

The equilibrium condition becomes

$$2l\sigma - 2\int_0^b \sigma_s dr = 0 \tag{2.30}$$

Substituting the value

$$\sigma_s = \frac{K}{\sqrt{2\pi r}} \tag{2.31}$$

we find the stress intensity factor

$$K = \sigma\sqrt{\pi l} \tag{2.32}$$

which coincides with its exact value.

The section method was modified by Nobile [7, 8] and applied to T-beams and curved beams. Consider a straight beam of constant circular-cross-section, the z-axis coincides with the geometrical axis while the x- and y-axis coincide with the principal axes of the cross-section. Loading involving

a couple bending moment M, tensile force N, shearing force Q are considered. Assume that a transverse crack of depth a would not alter the stress resultant on the cross-section passing through the crack tip, the singular stress distribution at the crack tip takes the form

$$\sigma_{ij}^{s} = \frac{K_i}{\sqrt{2\pi r}} \tag{2.33}$$

with the conditions that σ_{ij}^{s} acts at a distance $r = b$ from the crack tip. The nominal stress is evaluated by the well-known stress distribution of the reduced solid cross-section passing through the crack tip (ligament). The stress distribution does not take into account the presence of the crack. Then, the equivalent condition between singular stress and nominal stress resultant at the crack tip determines K_i approximately. Note that the approximation is better for b < a such that the elastic singular stresses are small as compared to geometric dimension of beam or crack length.

2.3.1. Pure bending

For pure bending, the normal stress acting on the reduced cross-section is evaluated by the well-known stress distribution of the reduced solid passing through the crack tip is given by

$$\sigma_z = \frac{M}{I^c} y' \tag{2.34}$$

where M is the bending moment and I^c is the moment of inertia of the crack section.

The force not transmitted through the crack section is equal to

$$F(y) = \frac{M}{I^c}\left[-\frac{2}{3}(R^2 - y^2)^{3/2} + ey(R^2 - y^2)^{1/2} + eR^2 \tan^{-1}\frac{y}{\sqrt{R^2 - y^2}}\right]\Bigg|_{R-a-b}^{R-a} \tag{2.35}$$

The singular stress component is related to the Model I stress intensity factor as

$$\sigma_z^{s} = \frac{K_{I_M}^{*}}{\sqrt{2\pi r}} \tag{2.36}$$

According to Fig. 2.3, the stress resultant arising at the crack tip is equal to

$$\begin{aligned} F^{s} &= \sum_{i=0}^{n-1} 2K_{I_M}^{*}\sqrt{\frac{2b}{\pi}}\xi\left(\sqrt{\frac{i+1}{n}} - \sqrt{\frac{i}{n}}\right), \quad \xi \le \zeta \\ F^{s} &= \sum_{i=0}^{n-1} 2K_{I_M}^{*}\sqrt{\frac{2b}{\pi}}\zeta\left(\sqrt{\frac{i+1}{n}} - \sqrt{\frac{i}{n}}\right), \quad \xi > \zeta \end{aligned} \tag{2.37}$$

where n is the number of divided strips.

$$\xi = \sqrt{R^2 - (R - a - \frac{i}{n}b)^2}$$

$$\zeta = \sqrt{R^2 - (R - a - \frac{i+1}{n}b)^2} \tag{2.38}$$

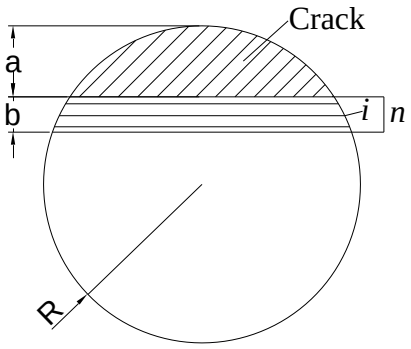

Fig. 2.3 The geometry of calculating stress resultant arising at the crack tip

The upper limit of integration is determined from the condition that σ_z^S is equal to the normal stress at $r = b$, which can be expressed as

$$\frac{K_{I_M}^*}{\sqrt{2\pi b}} = \frac{M}{I^c}(R + e - a - b) \tag{2.39}$$

Substituting eq. (2.39) to eq. (2.37), and following the hypothesis that $F^S = F$, the distance b can be solved by numerically method. Re-substituting b into eq. (2.39), the approximate stress intensity factor for mode I can be obtained as following

$$K_{I_M}^* = \frac{M}{R^{5/2}} F_M^*(\eta) \tag{2.40}$$

where $F_M^*(\eta)$ is the dimensionless geometric function of crack ratio.

2.3.2. Pure tension

Considering pure tension, as described in the foregoing section, a central axial tensile load applied to a transverse straight front crack beam gives rise to combined tension and bending since the neutral axis of the reduced crack section passing through the crack is shifted by an amount e as expressed in eq. (2.14).

The normal stress on this cross-section can be expressed as

$$\sigma_z = \frac{N}{A^c} + \frac{Ne}{I^c} y' \tag{2.41}$$

The force not transmitted through the crack section is as following

$$F = \left[-\frac{2}{3}\frac{Ne}{I^c}(R^2 - y^2)^{3/2} + \left(\frac{N}{A^c} + \frac{Ne^2}{I^c}\right)\left(y(R^2 - y^2)^{1/2} + R^2 \tan^{-1}\frac{y}{\sqrt{R^2 - y^2}} \right) \right] \Bigg|_{R-a-b}^{R-a} \tag{2.42}$$

The singular stress component σ_z^s and the stress resultant arising at the crack tip are the same to bending moment. The singular stress component is related to the Mode I stress intensity factors as in eq. (2.43).

$$\frac{K_{I_N}^*}{\sqrt{2\pi b}} = \frac{N}{A^c} + \frac{Ne}{I^c}(R + e - a - b) \tag{2.43}$$

The procedure for determining the approximate stress intensity factor is similar to that used for pure bending. The approximate stress intensity factor for mode I of pure tension can be expressed as

$$K_{I_N}^* = \frac{N}{R^{3/2}} F_N^*(\eta) \tag{2.44}$$

where $F_N^*(\eta)$ is the geometric function of dimensionless crack depth.

2.3.3. Shear force

When a shearing force Q is applied to cracked beam, the average shearing stress acting on the ligament cross section passing through the crack tip takes the form

$$\tau_{zy} = \frac{QQ_x^*}{I^c t} \tag{2.45}$$

where Q is the shearing force, Q_x^* is the first moment of area of the part of the reduced cross section bounded by t. I^c is the moment of inertia of ligament cross section. t is the width of the ligament cross section at the current calculation stress point. The shearing stress can be written as

$$\tau_{zy} = \frac{QQ_x^*}{2I^c\sqrt{R^2 - y^2}} \tag{2.46}$$

where,

$$Q_x^* = \left[-\frac{2}{3}(R^2 - y^2)^{3/2} + ey(R^2 - y^2)^{1/2} + eR^2 \tan^{-1}\frac{y}{\sqrt{R^2 - y^2}} \right]\Bigg|_{y}^{R-a} \tag{2.47}$$

The normal stress is evaluated by the well-known stress distribution of the reduced solid circular section passing through the crack tip (ligament). The force of the area before crack tip equals to

$$F = 2\int_{-\sqrt{R^2-y^2}}^{0} \left(\int_{R-a-b}^{R-a} \frac{SQ_x^*}{2I^c\sqrt{R^2 - y^2}} dy \right) dx = \int_{R-a-b}^{R-a} \frac{SQ_x^*}{I^c} dy \tag{2.48}$$

The singular stress component relating to Mode II stress intensity factor can be written as

$$\tau_{zy}^s = \frac{K_{II_s}^*}{\sqrt{2\pi r}} \tag{2.49}$$

The stress resultant arising at the crack tip is calculated

$$F^s = \sum_{i=0}^{n-1} 2K_{II_s}^* \sqrt{\frac{2b}{\pi}}\,\xi\left(\sqrt{\frac{i+1}{n}} - \sqrt{\frac{i}{n}}\right), \xi \le \zeta$$
$$F^s = \sum_{i=0}^{n-1} 2K_{II_s}^* \sqrt{\frac{2b}{\pi}}\,\zeta\left(\sqrt{\frac{i+1}{n}} - \sqrt{\frac{i}{n}}\right), \xi > \zeta \tag{2.50}$$

where ξ, ζ are defined in eq. (2.38).

The upper limit of integration is determined from the condition that τ_{zy}^s is equal to the normal stress at $r = b$, and it can be expressed as

$$\frac{K_{II_S}^*}{\sqrt{2\pi b}} = \frac{QQ_x^*}{2I^c\sqrt{R^2 - (R-a-b)^2}} \tag{2.51}$$

where

$$Q_x^* = \left[-\frac{2}{3}(R^2 - y^2)^{3/2} + ey(R^2 - y^2)^{1/2} + eR^2 \tan^{-1}\frac{y}{\sqrt{R^2 - y^2}}\right]\Bigg|_{R-a-b}^{R-a} \tag{2.52}$$

Substituting eq. (2.51) to eq. (2.52), and following the hypothesis that $F^s = F$, the distance b can be solved. Substituting b into eq. (2.51), the approximate stress intensity factor can be obtained as following

$$K_{II_S}^* = \frac{Q}{R^{3/2}} F_S^*(\eta) \tag{2.53}$$

where $F_S^*(\eta)$ is the geometric function of crack ratio.

The torsion problem of circular bars with a transverse crack is rather complicated. It can be obtained by harmonic function continuation technique. It will be investigated in the near future.

2.4 Numerical results and comparisons

The foregoing sections, derived for the geometric function are illustrated for a straight fronted edge cracked circular section beam subjected to bending moment, normal stress, shear force and torque. It is also considered here for the comparison and the agreement between the present results and those previous appear to be satisfactory.

In reference [1], Valiente proposed an experimental formula of Mode I stress intensity factor of tension as

$$K_{I_N}(\eta)/\sigma\sqrt{\pi a} = 1.4408 - 3.6364\eta + 19.35\eta^2 - 34.7849\eta^3 + 36.8446\eta^4 \tag{2.54}$$

Ng [6] listed the stress intensity factors of a transverse cracked circular section beam subjected to tension and bending moment. The details of the results are listed in Table 1.

Table.1. Results for the variation of the stress intensity factor along a straight crack front---tension and bending

a/D	0.1	0.159	0.217	0.257	0.297	0.353	0.407	0.453	0.500	0.547	0.594
Tension	0.98	1.07	1.17	1.24	1.35	1.57	1.84	2.14	2.54	3.10	3.77
Bending	0.87	0.84	0.85	0.87	0.89	0.93	1.00	1.10	1.23	1.40	1.59

For the straight-edged crack model, James and Mills [12] have concluded literature results and presented the dimensionless stress intensity factor of Mode I. In the following it is showed that the stress intensity factors versus crack depth ($0.01 < \eta < 0.65$) for a straight-edged crack subjected to axial loading and bending by using the polynomial approximation, are as follows

$$K_{I_N}(\eta)/\sigma\sqrt{\pi a} = 0.926 - 1.771\eta + 26.421\eta^2 - 78.481\eta^3 + 87.911\eta^4 \tag{2.55}$$

$$K_{I_M}(\eta)/\sigma_m\sqrt{\pi a} = 0.63 + 0.035\eta - 3.336\eta^2 + 13.406\eta^3 - 6.002\eta^4 \tag{2.56}$$

And they claimed that the solutions are only approximate and should be treated as an engineering estimate. They are based on other solutions, none of which are exact or rigorous, and engineering judgment is employed to synthesize them into a single closed form equation.

Daoud and Cartwright et al [4, 5] have also formulated the dimensionless stress intensity factors of the shaft under tension and bending moment from finite element results and shown as following respectively

$$K_{I_N}(\eta)/\sigma_n\sqrt{\pi a} = 1.11 - 3.59\eta + 24.87\eta^2 - 53.39\eta^3 + 57.23\eta^4, \quad 0.06 \le \eta \le 0.7 \tag{2.57}$$

$$K_{I_M}(\eta)/\sigma_m\sqrt{\pi a} = 1.04 - 3.64\eta + 16.86\eta^2 - 32.59\eta^3 + 28.41\eta^4, \quad 0.0625 \le \eta \le 0.625 \tag{2.58}$$

Shih and Chen [7] evaluated stress intensity factors by collapsed singular element with detailed mesh on crack front and appropriating adjacent area. The dimensionless formulas of stress intensity factors for bars under tension and bending cases as following

$$K_{I_N}(\eta)/\sigma\sqrt{\pi a} = -0.64 + 13.7\eta - 54.92\eta^2 + 78.39\eta^3 \tag{2.59}$$

$$K_{I_M}(\eta)/\sigma_m\sqrt{\pi a} = -0.17 + 5.13\eta - 19.266\eta^2 + 26.55\eta^3 \tag{2.60}$$

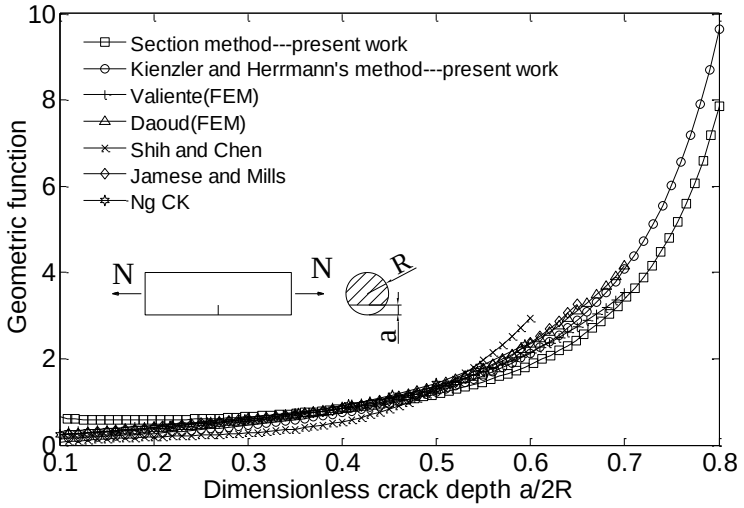

Fig.2.4. Geometric functions for circular section of beam under tension

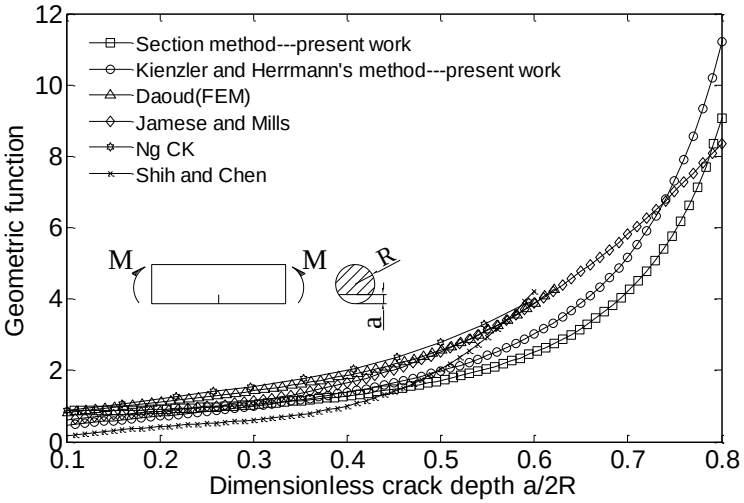

Fig.2.5. Geometric functions for circular section of beam under bending moment

From the Fig. 2.4, the great agreement between present works and the literature results can be obviously observed, except the result by Shih and Chen. Moreover, the geometric functions addressed in this paper are adequate and more broadly. Fig. 2.5 plots the geometric functions against non-dimension crack depth for straight-fronted cracks under bending moment, this plot is that of the maximum differences between all the solutions and thus the trend is the same. In the case of Shih and Chen, the trend is a little different.

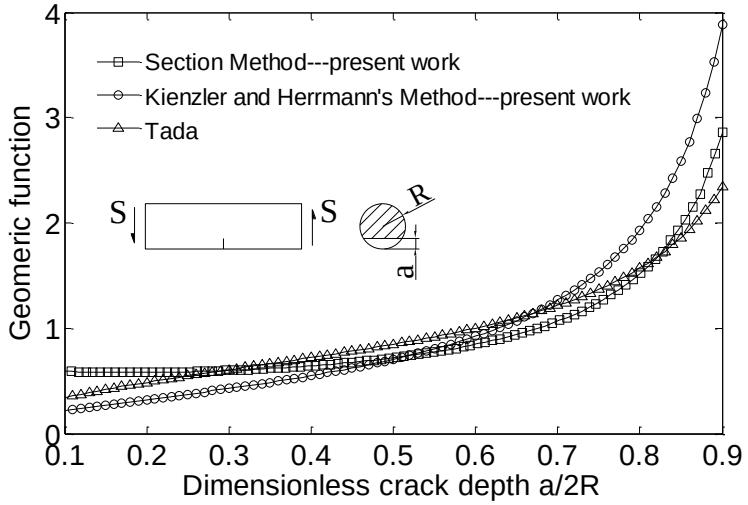

Fig.2.6. Geometric Function for circular section of a beam under a shear force

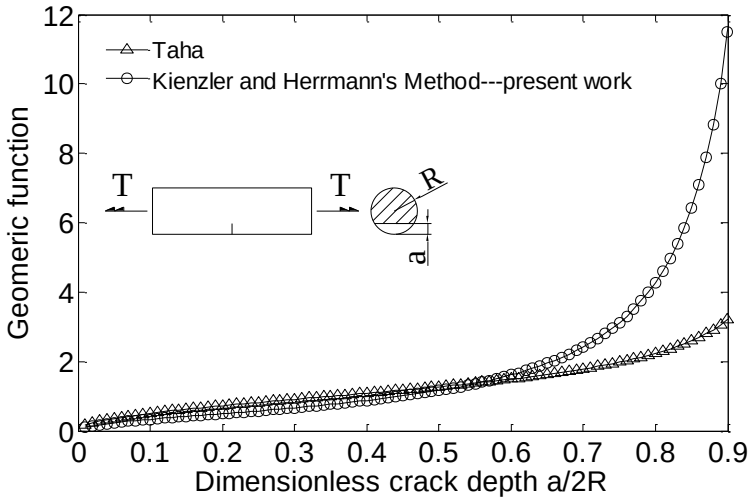

Fig. 2.7. Geometric Function for circular section of a beam under a torque

Figs. 2.6 and 2.7 show the comparisons of shear force and torque between the present researches and Tada's well-known results [20]. Hereby, the stress intensity factors of Tada are at the crack centre of straight-fronted cracks (the deepest crack point). The geometric functions given in the present investigation in Fig. 2.6 are good agreement with each other and that in the literature. Result of section method in Fig.2.6 of this paper shows an increase of stress intensity in the vicinity of the crack tip when the crack depth trends to zero. Fig. 2.7 shows that the agreement is good between the results for values of dimensionless crack depth from 0 to 0.7. However, the difference is obviously after the dimensionless crack depth exceeds 0.7, and the deeper the crack, the larger the difference. The present result is much larger than Tada's results.

2.5 Stress intensity factors for three-dimensional problems

The problem involving surface damage in the form of part-through cracks in round bars or beams, as solved in the last sections, is necessary to use a three dimensional analysis. Section method is applied again to the three dimensional analysis. The method proposed by Parton and Morozov [17], states that the additional force arising at the crack tip from an increase in stresses is equal to $\int_0^b \sigma_s dr$, where b can be determined from the condition that σ_z at $r = b$ is equal to the nominal stress. That is the distance b is the length of DK (or CJ), the force in the area of ABDCA equals to the force in the area of CFIKJC in Fig. 2.8 (a).

Nobile [18, 19] modified the section method that the additional stress due to crack, in the area of CFIGC in Fig. 2.8 (a), is equal to the force in the area of CEIGC. The distance b can be determined when singular stress equals to normal stress after neutral axis shifted, in the Fig. 2.8 (a) is CG. But from Fig.2.8 (a), it's clearly that, the force in area of CEIGC is less than that in area of CFIGC. Therefore, the modified suppose in [18, 19] is not accurate.

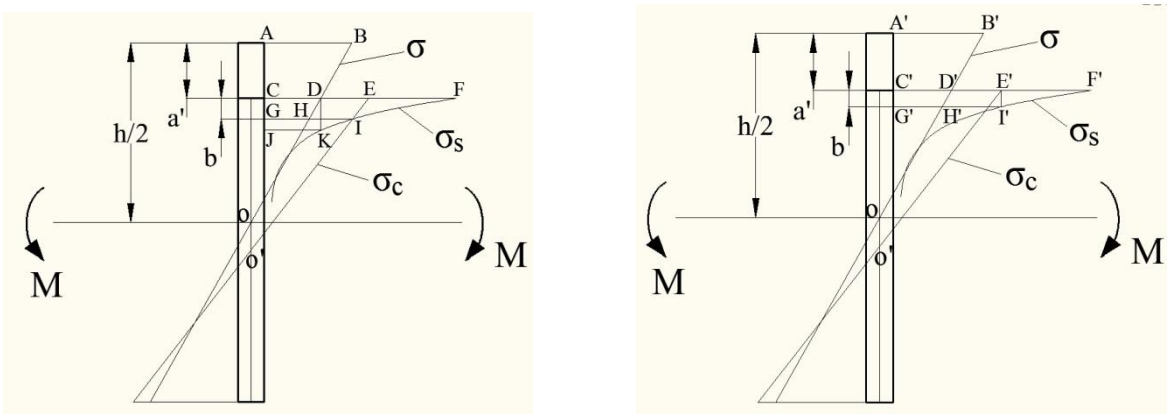

(a) (b)

Fig. 2.8 Section method

In this work, based on the original section method of Parton and Morozov and the modified method by Nobile, we improve the section method again. The additional force due to the stress concentration at the crack tip, in the area of C'D'E'F'I'H'G'C' in Fig. 2.8(b) equals to the force not transmitted the crack line, in the area of A'B'D'H'G'C'A'. The distance b can be determined from the condition that $\sigma_s|_{r=b} = \sigma_c|_{y'=\bar{y}}$. in Fig. 2.8(b) is at point I', where $\bar{y}$ is the distance from the neutral axis of the reduced cross section to the crack tip.

As a verified example, considering a rectangular section beam with an straight, opened and through transverse crack subjected to a bending moment M, the section is unit thickness and the height is h with crack depth a', the schematic diagram can be seen in Fig. 2.8(b).

The distribution of normal stresses on the integrated cross section is

$$\sigma = \frac{M}{I} y \tag{2.61}$$

The distribution of normal stresses on the reduced cross section passing through the crack tip is

$$\sigma_c = \frac{M}{I_c} y' \tag{2.62}$$

where I_c is the moment of inertia for the reduced part of the cross section, $y' = y + e$ is the longitudinal axis in the new coordinate, and $e = oo'$ is the shift of the neutral center.

The singular stress component relating to the mode I stress intensity factor is

$$\sigma_s = \frac{K_I}{\sqrt{2\pi r}} \tag{2.63}$$

The equation of equilibrium is

$$\int_{\frac{h}{2}-a'-b}^{h/2} \sigma \, dy = \int_0^b \sigma_s \, dr \tag{2.64}$$

The value of b is found from the equality

$$\frac{K_I}{\sqrt{2\pi b}} = \frac{M}{I_c} \bar{y} \tag{2.65}$$

After some necessary algebraically calculation, the stress intensity factor for mode I can be obtained as following

$$K_I = \frac{6M}{t h^{\frac{3}{2}}} F(\eta) \tag{2.66}$$

where t is thickness of rectangular section, $\eta = a'/h$ is crack depth ratio, $F(\eta) = \frac{\sqrt{2\pi\beta}}{(1-\eta)^2}$, with

$$\beta = \frac{1}{2} - \eta - \frac{1}{(1-\eta)^2} + \sqrt{\frac{1}{(1-\eta)^4} + \frac{2\eta-1}{(1-\eta)^2} + \frac{1}{4}} \quad \text{for } 0.5 - \eta - \beta \geq 0$$

$$\beta = \frac{1}{2} - \eta + \frac{1}{(1-\eta)^2} - \sqrt{\frac{1}{(1-\eta)^4} - \frac{2\eta-1}{(1-\eta)^2} - \frac{1}{4}} \quad \text{for others} \tag{2.67}$$

The geometric function $F(\eta)$ can be compared with the expressions given by Nobile [18, 19], Tada [21] and Brown [22].

Brown [22] examined the geometric function using least square fitting method. The formula shows the errors ratio less than 0.2% for $\eta \leq 0.6$.

$$F(\eta) = \sqrt{\pi\eta}(1.122 - 1.40\eta + 7.33\eta^2 - 13.08\eta^3 + 14.0\eta^4) \tag{2.68}$$

Tada [21] investigated the geometric function of this situation for any crack depth ratio η, the result shows better than 0.5% compared with experimental result. The formula is in Eq. (2.69).

$$F(\eta) = \sqrt{2tan\frac{\pi\eta}{2}}\frac{0.923 + 0.199(1 - sin\frac{\pi\eta}{2})^4}{cos\frac{\pi\eta}{2}} \tag{2.69}$$

Nobile [18, 19] proposed a formula by modified section method as following

$$F(\eta) = \frac{0.482}{\sqrt{(1-\eta)^3}} \tag{2.70}$$

For easy comparison, the four different results are graphically showed in Fig. 2.9. The comparison in Fig. 2.9 shows the results of Brown and Tada are in accordance very well. The presented result is better than that of Nobile, especially for $\eta \leq 0.6$ and agreement very well with the result of Brown and Tada.

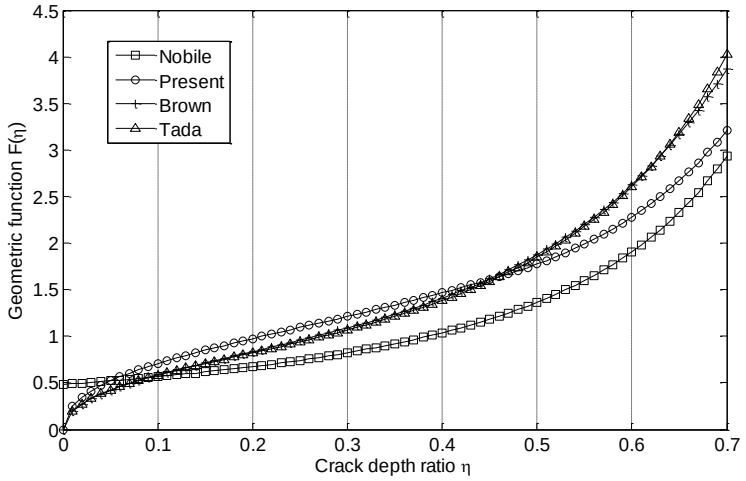

Fig. 2.9 Geometric function for rectangular section beam

As the result presented here is in well agreement with the well-known calculation in the literature. It is extended into a circular section as follows. Due to the symmetry (for bending and shear) or central symmetry (for torque), only the right half section is considered in the next presentation.

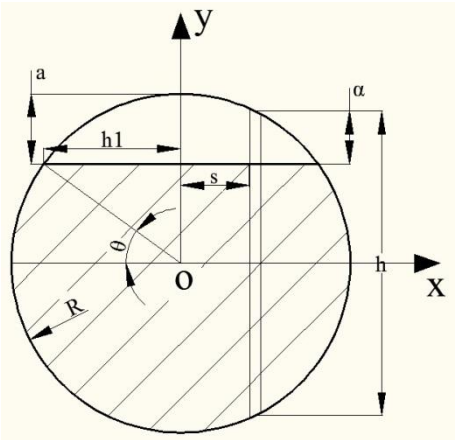

Fig. 2.10 Cracked circular section

The cracked circular section is considered to be divided into strips of width t that are independence from each other, i.e. there are no tractions between two successive strips, see Fig. 2.10. This is not true near the ends of the crack tip. In order to apply the method proposed in previews, every strip is regarded as a rectangular section.

For a given radius R and deepest crack depth a, the height h and the crack depth a' of each strip depending on the location point s, can be expressed as follows

$$h = 2\sqrt{R^2 - s^2},\ a' = \alpha = \frac{h}{2} - (R - a) \tag{2.71}$$

2.5.1 Beams subjected to bending moment

The distribution of normal stresses on the integrated cross section is

$$\sigma = \frac{M}{I} y \tag{2.72}$$

where I is the moment of inertia for the uncracked circular section.

The distribution of normal stresses on the reduced cross section passing through the crack tip is

$$\sigma_c = \frac{M}{I_c} y' \tag{2.73}$$

where I_c is the moment of inertia for the reduced part of the circular cross section.

The singular stress component is related to the mode I stress intensity factor is

$$\sigma_s = \frac{K_I}{\sqrt{2\pi r}} \tag{2.74}$$

The equation of equilibrium is

$$\int_{\frac{h}{2}-\alpha-b}^{h/2} \sigma\, dy = \int_0^b \sigma_s\, dr \tag{2.75}$$

The value of b is found from the equilibrium

$$\frac{K_I}{\sqrt{2\pi b}} = \frac{M}{I_c} y'|_{y'=\bar{y}=h/2-\alpha+e} \tag{2.76}$$

After some basic algebra calculation, the stress intensity factor can be obtained as following

$$K_I = \frac{M}{R^{2.5}} F(\eta) \tag{2.77}$$

where $F(\eta)$ is the geometric function of crack depth ratio η, can be expressed as following

$$F(\eta) = \frac{R^{2.5}\sqrt{2\pi b}}{I_c}\left(\frac{h}{2} - \alpha + e\right) \tag{2.78}$$

with $\eta = \alpha/h$ is crack depth ratio.

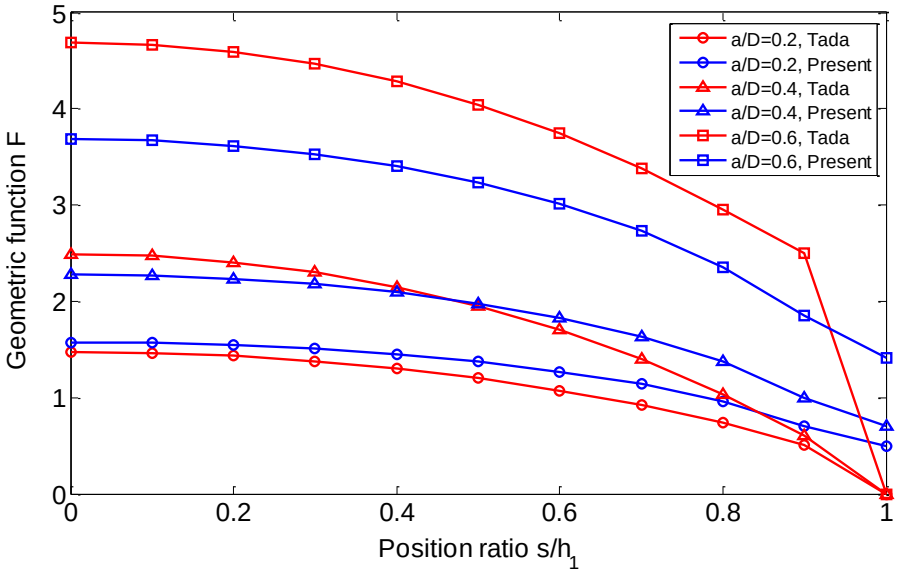

Fig. 2.11 Geometric function of bending

The geometric function of Eq. (2.78) is graphically compared with that in literature in the Fig. 2.11. It has been pointed out that the square root singularity does not in general exist at the surface point [22]. The usual meaning of stress intensity factor breaks down here. A plot of the geometric function against the place ratio shows typically that the results at the surface point deviate markedly from the trends indicated by the interior points. The stress intensity factors at the surface are deduced by extrapolating the trends exhibited by the interior points using a quadratic curve fitting [7].

2.5.2 Beams subjected to shear force

Consider the circular cross section in Fig. 2.12. We shall now argue that the direction of the transverse shear stress depends (in general) on the lateral location of interest at distance (R-a) from the neutral axis. We can no longer assume that all of the shear stresses act parallel to the y axis. Thus the direction of shear stress changes along (R-a). However, it can be easily demonstrated that at a point on the boundary of the cross-section, the shear stress τ acts tangent to the boundary. This conclusion follows from the fact that the outer surface of the beam is free of stress, and therefore the shear stress acting on the cross-section can have no component in the radial direction (because shear stresses acting on perpendicular planes must be equal in magnitude). This complication can invalidate the engineering mechanics expression for estimating the magnitude of the transverse shear stress. Accordingly, we restrict our analyses to situation where it is clear that the shear stress direc-

tion is parallel where $a = R$ for members with circular cross section, and the same with that rectangular cross section.

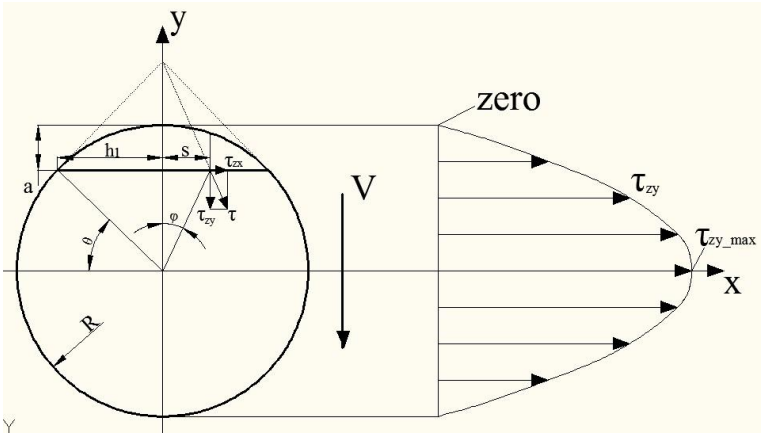

Fig. 2.12 Transverse shear stress direction and distribution in circular section

The stress due to shear force can be divided into two components. The vertical shear stress component is a constant along of the crack front, as the following

$$\tau_{zy} = \frac{4V\cos^2\theta}{3\pi R^2} = \frac{4V(R^2 - y^2)}{3\pi R^4} \tag{2.79}$$

where $\cos\theta = \frac{\sqrt{2Ra-a^2}}{R}$, $h_1 = \sqrt{R^2 - y^2}$.

At the neutral axis, $y = 0$, the vertical shear stress τ_{zy} is maximum and equals to

$$\tau_{zy\_max} = \frac{4V}{3\pi R^2} \tag{2.80}$$

The vertical shear stress contributes to mode II. As described in [19], assuming that the average shearing stress acting on the reduced cross-section passing through the crack tip may be approximated with the average shearing stress acting on un-cracked cross section, for the shear condition the method of computing stress intensity factor is not different from that of Parton and Morozov [17].

The singular stress due to crack relates to Mode II SIF as follows

$$\tau_{zy\_s} = \frac{K_{II\_V}}{\sqrt{2\pi r}} \tag{2.81}$$

The equation of equilibrium is

$$\int_{\frac{h}{2}-\alpha}^{h/2} \tau_{zy}\, dy = \int_0^b \tau_{zy\_s}\, dr \tag{2.82}$$

The upset integral limitation b is determined by the condition that

$$\tau_{zy\_s}|_{r=b} = \tau_{zy}|_{y=\frac{h}{2}-\alpha} \tag{2.83}$$

i.e.,

$$K_{II\_V} = \sqrt{2\pi b}\frac{4V\left(R^2 - (\frac{h}{2}-\alpha)^2\right)}{3\pi R^4} \tag{2.84}$$

Substituting Eq. (2.84) into Eq. (2.82) gives the value of b.

Inserting b into Eq. (2.84) it could be obtained

$$K_{II\_V} = \frac{V}{R^{1.5}}F(\eta) \tag{2.85}$$

where the geometric function is

$$F(\eta) = \sqrt{2\pi b}\frac{4\left(R^2 - \left(\frac{h}{2}-\alpha\right)^2\right)}{3\pi R^{2.5}} \tag{2.86}$$

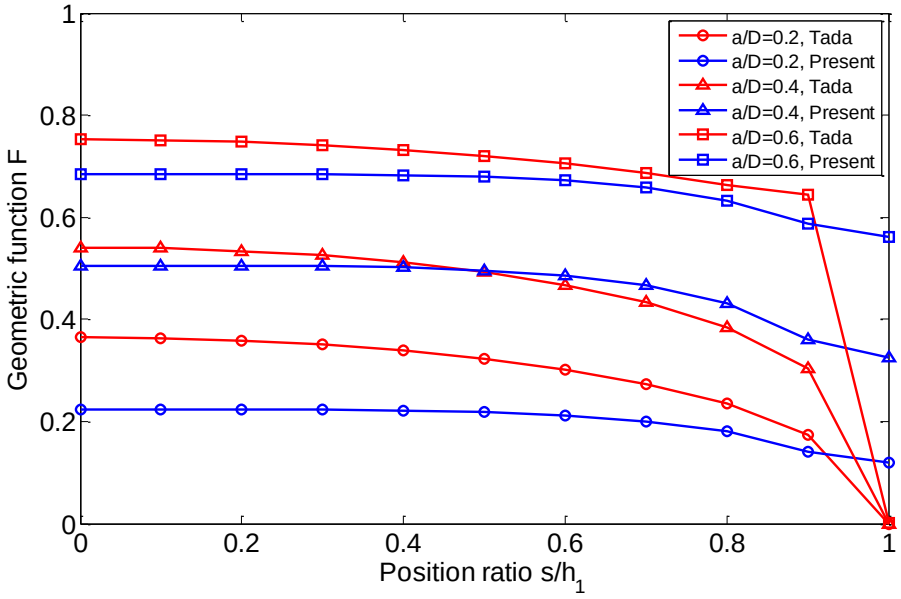

Fig. 2.13 Geometric function for K_{II} due to shear

Fig. 2.13 shows the comparison between the presented geometric function and the results in [20]. The shear coefficient is 9/10 in Tada's formulae [20].

As shown in Fig. 2.12, the shear stress has two components due to the shear stress directs to the intersect of the two tangential lines of the surface points. One is the vertical shear stress τ_{zy} which is contributes to Mode II, as described in Eq. (2.81). The other one is parallel shear stress τ_{zx} which is contributes to Mode III as follows (KIII due to shear)

$$\tau_{zx} = \frac{2x}{2h_1}\tau_{zy}tan\theta = \frac{4Vxsin\theta}{3\pi R^3} = \frac{4Vxy}{3\pi R^4} \tag{2.87}$$

The singular stress due to crack relates to Mode III SIF as follows

$$\tau_{zx\_s} = \frac{K_{III\_V}}{\sqrt{2\pi r}} \tag{2.88}$$

The equation of equilibrium is

$$\int_{\frac{h}{2}-\alpha}^{h/2} \tau_{zx}\, dy = \int_{0}^{b} \tau_{zx\_s}\, dr \tag{2.89}$$

The upset integral limitation b is determined by the condition that

$$\tau_{zx\_s}|_{r=b} = \tau_{zx}|_{y=\frac{h}{2}-\alpha} \tag{2.90}$$

i.e.,

$$K_{III\_V} = \frac{4Vs(\frac{h}{2}-\alpha)}{3\pi R^4}\sqrt{2\pi b} \tag{2.91}$$

Substituting Eq. (2.91) into Eq. (2.90) gives the value of b.

$$b = \frac{(h-\alpha)\alpha}{2(h-2\alpha)} \tag{2.92}$$

Inserting b into Eq. (2.91), one can obtain

$$K_{III\_V} = \frac{V}{R^{1.5}}F(\eta) \tag{2.93}$$

where the geometric function is

$$F(\eta) = \frac{4s(\frac{h}{2}-\alpha)}{3\pi R^{2.5}}\sqrt{2\pi b} \tag{2.94}$$

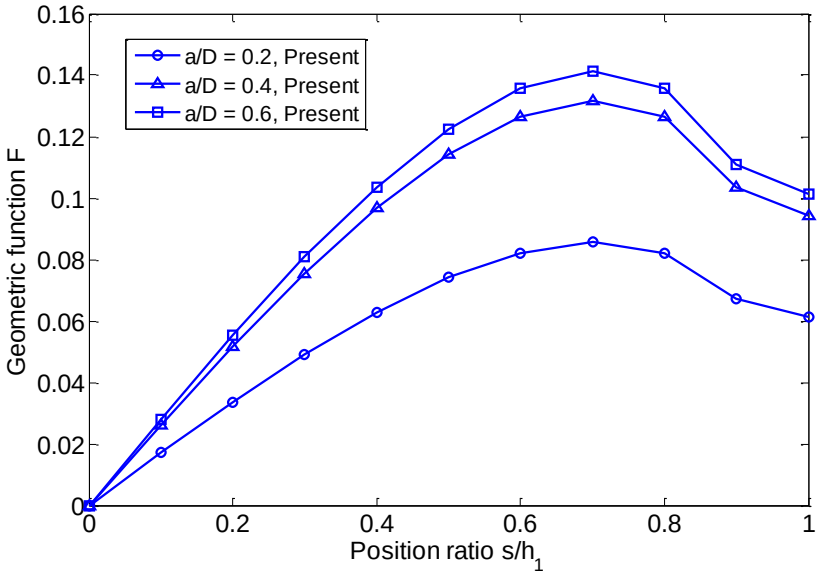

Fig. 2.14 Geometric function for K_{III} due to shear

2.5.3 Beams subjected to torque

The direction of the normal stresses on the integrated cross section due to torque is vertical to radius in circular section. The torsional shear stress component which parallel to the crack tip is related to Mode III, as follows

$$\tau'_{zx} = \frac{T}{J}\rho cos\varphi = \frac{T}{J}y \tag{2.95}$$

where J is the polar moment of inertia for circular section.

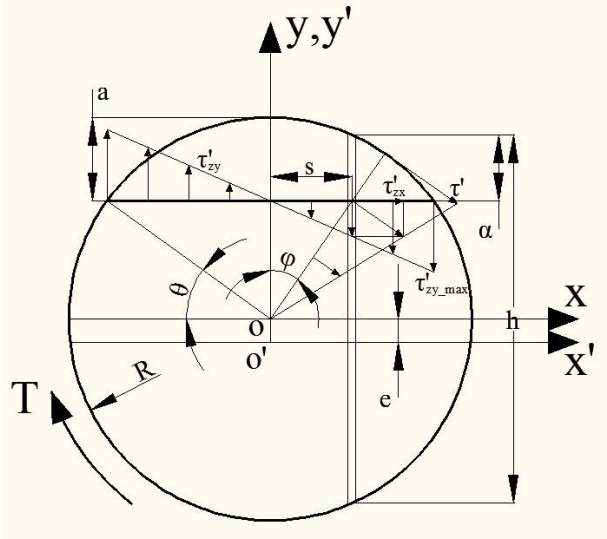

Fig. 2.15 Torsion stress direction and decomposition in circular section

Assume that torque distribution in the reduced cross section is like that in integrated circular section except the neutral axis shifted a distance e from the coordinate original. Therefore, the distribution of normal stresses on the reduced cross section passing through the crack tip is

$$\tau'_{zx\_c} = \frac{T}{J_c}y' \tag{2.96}$$

where J_c is the polar moment of inertia for the reduced part of the circular cross section.

The singular stress component relating to the mode III stress intensity factor is

$$\tau'_{zx\_s} = \frac{K_{III\_T}}{\sqrt{2\pi r}} \tag{2.97}$$

The equation of equilibrium is

$$\frac{K_{III\_T}}{\sqrt{2\pi b}} = \frac{T}{J_c}y'|_{y'=\bar{y}=\frac{h}{2}-\alpha+e} \tag{2.98}$$

The value of b is found from the equality

$$\int_{\frac{h}{2}-\alpha-b}^{h/2} \tau'_{zx}\, dy = \int_0^b \tau'_{zx\_s}\, dr \tag{2.99}$$

According to Eq. (2.98) and Eq. (2.99), the upset value b can be obtained. Instituting b into Eq. (2.98), the Mode III stress intensity factor due to torque is as following

$$K_{III\_T} = \frac{T}{R^{2.5}} F(\eta) \tag{2.100}$$

where the geometric function $F(\eta)$ is in the Eq. (2.101).

$$F(\eta) = \sqrt{2\pi b}\frac{R^{2.5}}{J_c}\left(\frac{h}{2} - \alpha + e\right) \tag{2.101}$$

The comparison of the geometric function with Tada's result is graphically showed in Fig. 2.16.

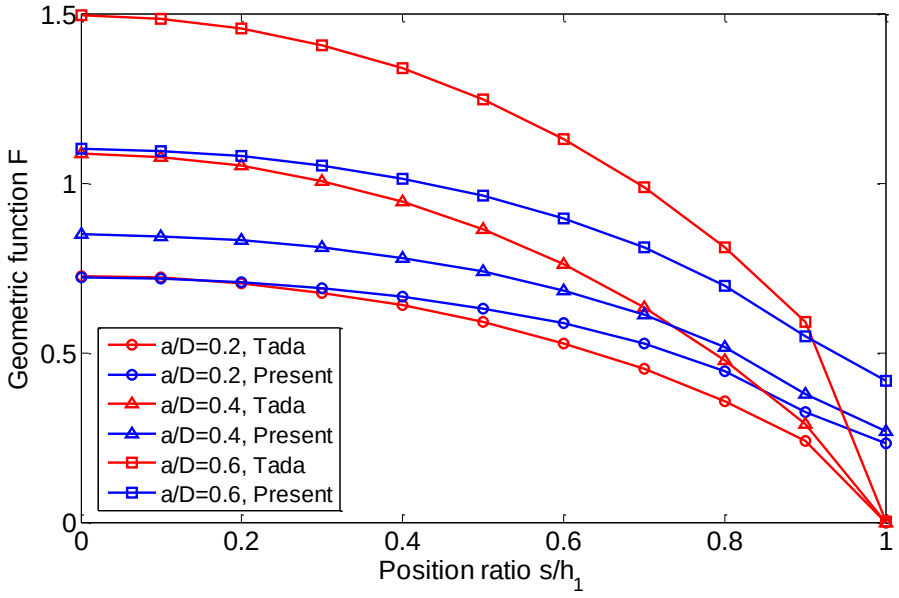

Fig. 2.16 Geometric function for K_{III} due to torque

The vertical shear stress due to torque is related to Mode II, equals to

$$\tau'_{zy} = \frac{T}{J}\rho sin\varphi = \frac{T}{J}x \tag{2.102}$$

This value is independent on the crack depth. In the middle of crack tip $x = 0$, it has minimum value $\tau'_{zy} = 0$, the maximum value is at $x = -Rcos\theta = -\sqrt{R^2 - y^2}$, $\tau'_{zy\_max} = \frac{T}{J}\sqrt{R^2 - y^2}$.

The same as that described in the foregoing section, the stress of beam under torque has two concepts. The concept relating to Mode II can be expressed as

$$\tau'_{zy\_c} = \frac{T}{J_c}s \tag{2.013}$$

and its singular form is

$$\tau'_{zy\_s} = \frac{K_{II\_T}}{\sqrt{2\pi r}} \tag{2.104}$$

According to the definition of the stress intensity factor

$$\frac{K_{II\_T}}{\sqrt{2\pi b}} = \frac{T}{J_c} s|_{y'=\bar{y}=\frac{h}{2}-\alpha+e} \tag{2.105}$$

$$K_{II\_T} = \frac{T}{J_c} s\sqrt{2\pi b} \tag{2.106}$$

The upset value b can be determined by the assumption of section method, as following

$$\int_{\frac{h}{2}-\alpha-b}^{h/2} \tau'_{zy}\, dy = \int_0^b \tau'_{zy\_s}\, dr \tag{2.107}$$

According to Eq. (2.106) and Eq. (2.107), the value b is obtained as

$$b = \frac{\alpha J_c}{2J - J_c} \tag{2.108}$$

Substituting Eq. (2.108) to Eq. (2.106), the Mode II stress intensity factor of torque is

$$K_{II\_T} = \frac{T}{R^{2.5}} F(\eta) \tag{2.109}$$

The geometric function $F(\eta)$ can be expressed as following

$$F(\eta) = \frac{R^{2.5}}{J_c} s\sqrt{2\pi b} \tag{2.110}$$

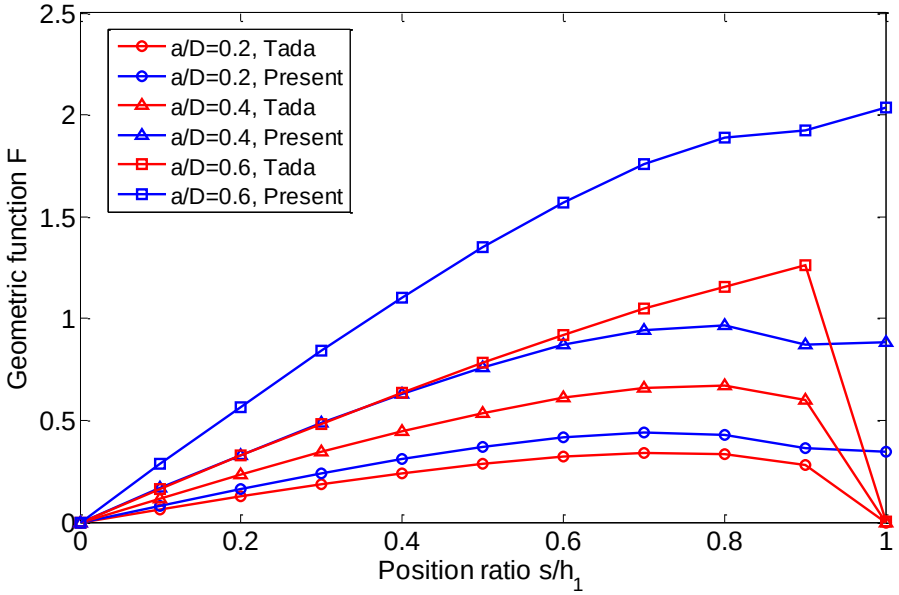

Fig. 2.17 Geometric function for K_{II} due to torque

2.6 Three-dimension numerical calculation of mixed mode stress intensity factors

In order to consider the general loading states, a structure with two perpendicular circular section beams subjected a vertical concentration load F at the end of the structure is considered here. The lengths of beams are L and $L/2$, respectively. The crack is located in the middle of the beam whose length is L. The radius of the section is R and the depth of the deepest point location of the crack is a. From the structure mechanics, it is easily to know that, on the crack section, the shearing force is $\mathrm{V} = \mathrm{F}$; the bending $\mathrm{M} = \mathrm{FL}/2$; the torque $\mathrm{T} = \mathrm{FL}/2$. It's a fracture mechanics problem of mixed-mode and three-dimensional.

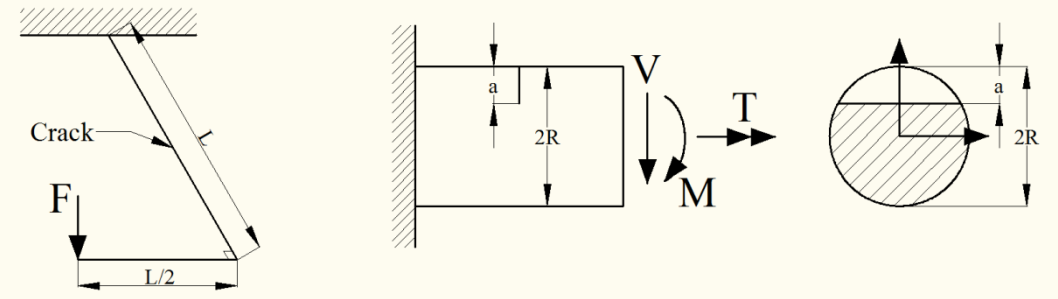

Fig. 2.18 The structure of beams

In generally, the totally stress intensity factor of each mode can be obtained by algebraically summing all the components of this mode. According to section 2.5, the geometric functions of the totally stress intensity factors about all the three Modes appear in Fig. 2.18 are calculated as following

$$K_I = \frac{M}{R^{2.5}} F_I(\eta) \tag{2.111}$$

$$K_{II} = K_{II\_V} + K_{II\_T} = \frac{V}{R^{1.5}} F_{II}(\eta) \tag{2.112}$$

$$K_{III} = K_{III\_V} + K_{III\_T} = \frac{T}{R^{2.5}} F_{III}(\eta) \tag{2.113}$$

The geometric function of the totally SIF for opening mode is the same as expressed in the section 2.5 due to only one component contributes to Mode I. Combining the second and the third stress intensity factors produced by shear and torque by algebraically summing, the geometric functions of all the stress intensity factors are compared with the results proposed in literature and obtained from ABAQUS using XFEM by an interaction integral method [23] in Figs. 2.19-2.21. For the ABAQUS result of 'XFEM (structure)' means that the model is exactly the same with that the first figure showed in Fig. 2.18, only a concentrated force F is applied. The model of 'XFEM (Single beam)' is like the second figure as showed in Fig. 2.18, a beam with length L and circular section with radius

R, a crack with depth a locates in the middle of the beam. For different modes, different forces are applied.

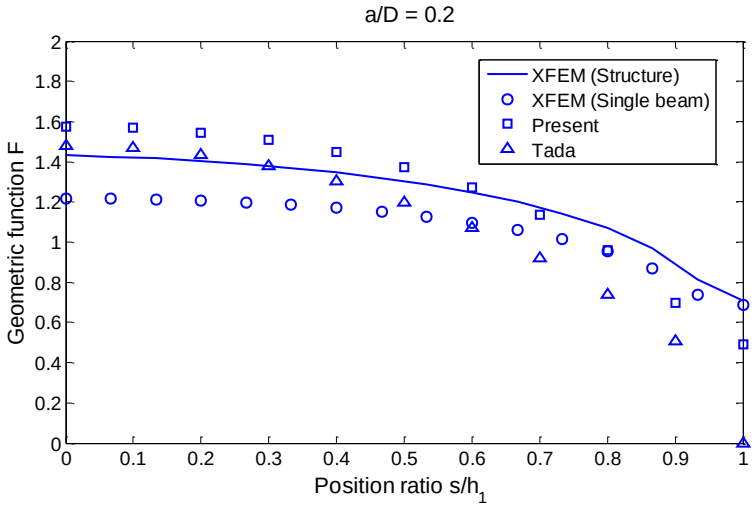

(a)

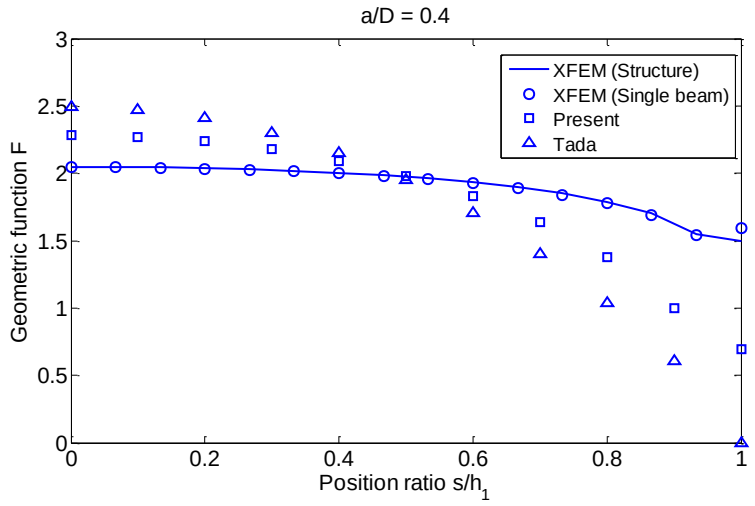

(b)

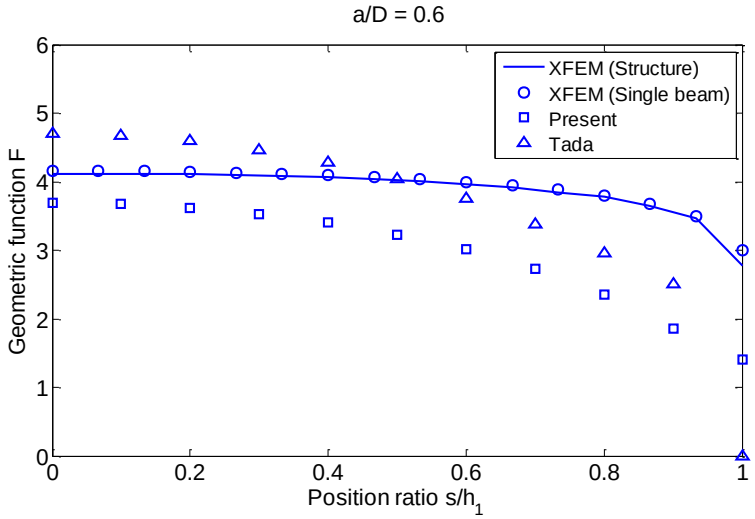

(c)

Fig. 2.19 Comparison of Mode I geometric function for different crack depth ratio (a) $\eta = 0.2$, (b) $\eta = 0.4$, (c) $\eta = 0.6$

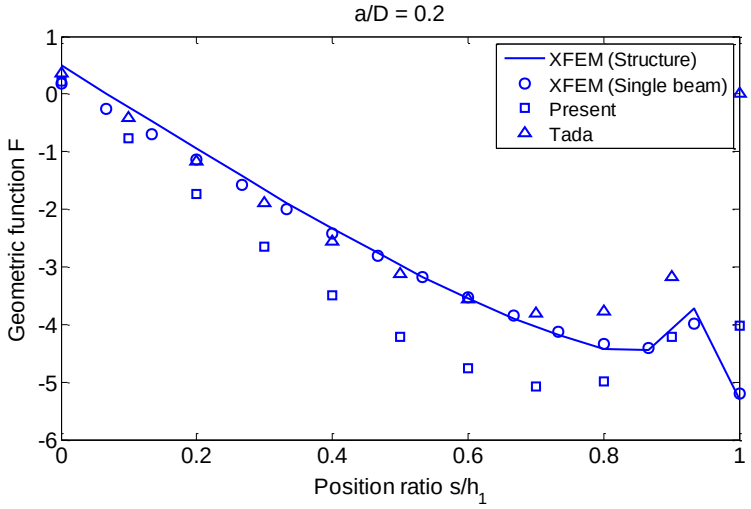

(a)

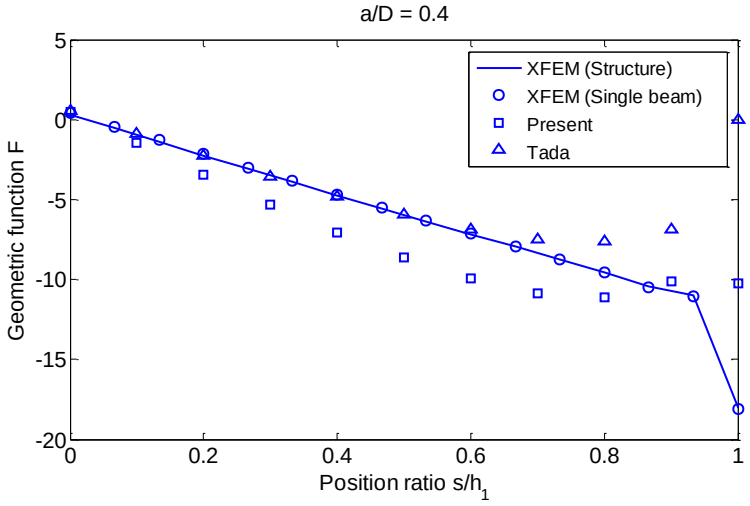

(b)

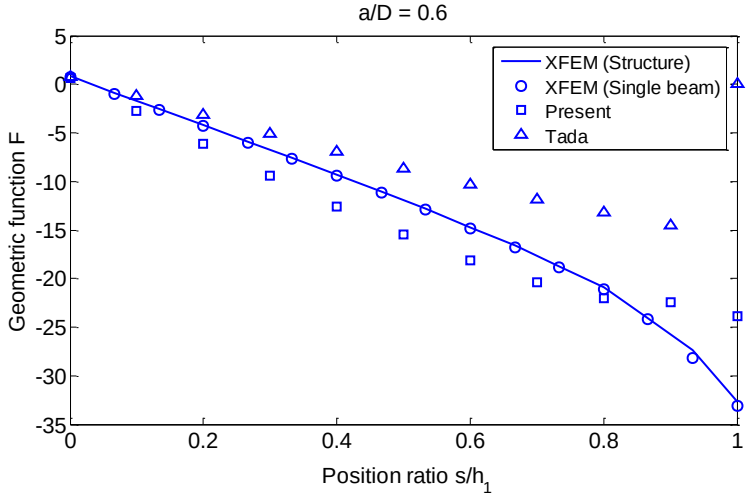

(c)

Fig. 2.20 Comparison of Mode II geometric function for different crack depth ratio (a) $\eta = 0.2$, (b) $\eta = 0.4$, (c) $\eta = 0.6$

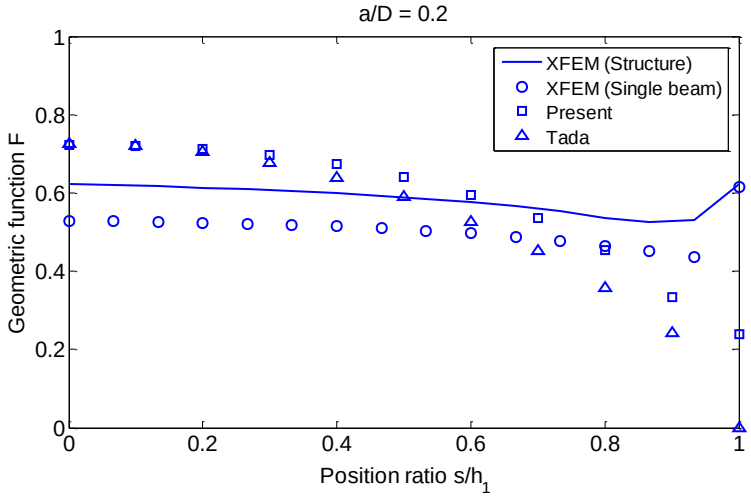

(a)

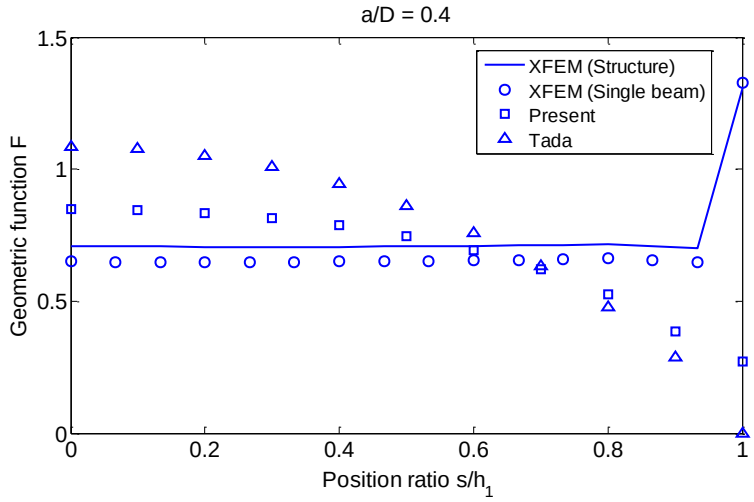

(b)

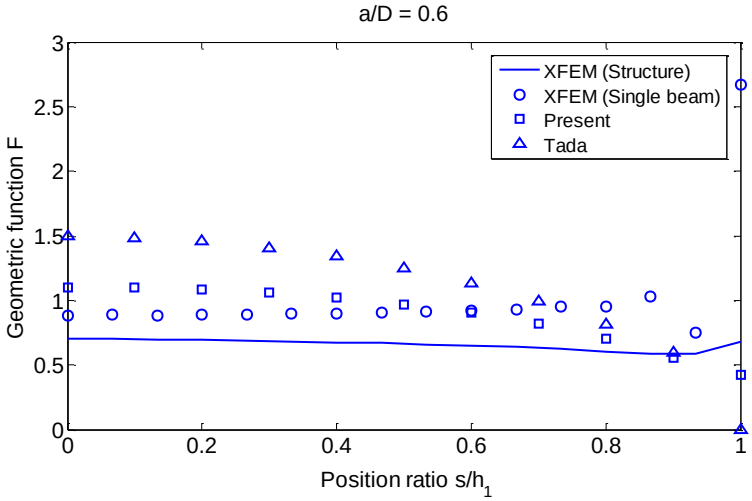

(c)

Fig. 2.21 Comparison of Mode III geometric function for different crack depth ratio (a) $\eta = 0.2$, (b) $\eta = 0.4$, (c) $\eta = 0.6$

References

[1] Valiente A. Criterios de fractura para alambres. PhD thesis, Polytechnic University of Madrid, Spain; 1980. <http://oa.upm.es/745/01/04198001.pdf>.

[2] Levan A, Royer J. Part-circular surface cracks in round bars under tension, bending and twisting. Int J Fract 1993; 61:71-99.

[3] Couroneau N, Royer J. Simplified model for the fatigue growth analysis of surface cracks in round bars under mode I. Int J Fract 1998; 20:711–718

[4] Daoud OEK, Cartwright DJ, Carney M. Strain-energy release rate for a single-edge-cracked circular bar in tension. J Strain Anal Eng Des1978; 13(2):83-9.

[5] Daoud OEK, Cartwright DJ. Strain energy release rate for a straight-fronted edge crack in a circular bar subject to bending. Eng Fract Mech 1984; 19:701-707.

[6] Ng C.K, Fenner D.N. Stress intensity factors for an edge cracked bar in tension and bending. Int J Fract 1988; 36:291-303

[7] Shin CS, Cai CQ. Experimental and finite element analyses on stress intensity factors of elliptical surface crack in a circular shaft under tension and bending. Int J Fract 2004; 129:239-264.

[8] Carpinteri A. Stress intensity factors for straight-fronted edge cracks in round bars. Eng Fract Mech 1992; 42(6):1035-40.

[9] Si E.J. Stress intensity factors for edge cracks in round bars. Eng Fract Mech 1990; 37:805-812

[10]Naik S.S, Maiti S.K. Triply coupled bending-torsion vibration of Timoshenko end Euler-Bernoulli shaft beams with arbitrarily oriented open crack. J Sound Vib 2009; 324:1067-1085

[11]Toribio J, Alvarez N, Gonzàlez B, ect. A critical review of stress intensity factor solution for surface cracks in round bars subjected to tension bending. Eng Fail Anal 2009;16:794-809

[12]James LA, Mills WJ. Review and synthesis of stress intensity factor solutions applicable to cracks in bolts. Eng Fract Mech 1988; 30:641-54.

[13]Kienzler R, Herrmann G. An elementary theory of defective beams. Acta Mech 1986; 62: 37-46.

[14]Bazant ZP. Justification and improvement of Kienzler and Herrmann's estimate of stress intensity factors of cracked beam. Eng Fract Mech 1990; 36: 523-5.

[15]Gao H, Herrmann G. On estimates of stress intensity factors for cracked beams and pipes. Eng Fract Mech 1992; 41: 695-706.

[16]Ricci P, Viola E. Stress intensity factors for cracked t-section and dynamic behaviour of T-beams. Eng Fract Mech 2006; 73(1): 91-111

[17]Parton VZ, Morozov EM. Elastic–plastic fracture mechanics. Moscow: Mir Publishers; 1978.

[18]Nobile L. Mixed mode crack initiation and direction in beams with edge crack. Theor Appl Fract Mech 2000; 33:107-10.

[19]Nobile L. Mixed mode crack growth in curved beams with radial edge crack. Theor Appl Fract Mech 2001; 36:61-13.

[20]Tada H, Paris PC, Irwin GR. The stress analysis of crack handbook. Paris Production Incorporated and Del Research Corporation; 1985.

[21]Brown W.F, Srawley, J.E, Plane strain crack toughness testing of high strength metallic materials, ASTM STP, 1966,410:63-65.

[22]Carpinteri A, Brighenti R. Part-through cracks in round bars under cyclic combined axial and bending loading. Int J Fatigure, 1996, 18:33-39.

[23]Shih, C. F., and R. J. Asaro, Elastic-Plastic Analysis of Cracks on Bimaterial Interfaces: Part I—Small Scale Yielding, Journal of Applied Mechanics, 1988, 8:537–545.

Chapter 3

Mixed mode cracking in transverse cracked shafts

3.1 Introduction

Many structural components are under developing and growing cracks during their service life. Brittle fracture is one of the major modes of failure in these cracked components and structures. Crack growth in brittle materials like ceramics, glasses, rocks, and some polymers often takes place very fast and arises serious consequences. Therefore, it is important to define an appropriate procedure for predicting the onset of brittle fracture in cracked specimens. In many practical situations, cracked components are subjected to a combination of mode I and mode II loading---mixed mode. Under mixed mode loading conditions, fracture of cracked components and structures may grow along curvilinear paths and not necessarily along the direction of original crack. Furthermore, when an estimate of crack arrest is required, the direction of fracture initiation from existing cracks must be determined particularly under mixed mode loading. Therefore, the investigation of the fracture initiation angle and the fracture propagation path under mixed mode loading is an interesting and important subject for researchers. There are a number of theoretical models and various experimental techniques to investigate mixed mode crack growth of materials. It will be reviewed in the following section.

In this work, a review about fracture criteria of single mode as well as mixed mode is proposed in the beginning. Two popular and convenient fracture criteria named maximum tangential stress (MTS) criterion and minimum strain energy density factor (SEDF) criterion are studied in detail and compared for crack initial angle and critical load domain for mixed mode. The crack initiation and direction under mixed mode conditions are studied for a shaft with transverse crack using MTS-criterion and SEDF-criterion. The crack extension direction is predicted by both of the criteria in terms of crack depth ratio and loading ratio. The crack orientation depends on the mixed of the modes. Mode I dominants in the crack grow process.

A criterion proposed by Richard for three-dimension crack propagation is introduced and applied to transverse cracked shaft. The results are compared with that obtained by MTS-criterion and SEDF-criterion as well as ABAQUS results for single mode and mixed mode.

3.2 Fracture criteria

Various fracture criteria for crack subjected to mixed mode loading have been introduced for the determination of the propagation direction and the critical stress. Griffith [1] introduced a criterion to determine the conditions to initiate the propagation of a crack. The maximum energy release rate criterion (MERR) [2, 3] followed the Griffith condition and stated that crack growth followed the orientation of maximum energy release rate. Erdogan and Sih [4] developed the maximum tangential stress criterion (MTS) which was one of the first conditions predicted critical stress and crack growth orientation. MTS criterion stated that the crack growth would occur in the direction of the maximum tangential stress and would take place when the maximum tangential stress reached a critical value, which only contained the first Mode strength toughness. Due to the simply formula and easily calculation, MTS became one of the popular criteria in the fracture mechanics. Palaniswamy and Knauss [5] introduced the G-criterion which dealt with a criterion of maximum energy release to determine both the initial crack propagation direction as well as the conditions of crack instability in terms of fracture stress σ_c, crack orientation angle θ_0, and crack length a. Sih [6] proposed the minimum elastic strain energy density criterion (S-criterion) based directly on the total strain energy density, that was, the sum of its distortional and dilatational components. Hellen and Blackburn [7] presented J-criterion in an attempt to use path-independent line integrals to study the problem of crack growth under mixed Mode loading. Theocaris and Andrianopoulos [8] proposed the named T-criterion which stated that a crack started to propagate when the dilatational strain energy T_V at a point in the vicinity of its tip reached a critical value T_{Vcr} and the curve of evaluation of T_V around crack tip the elastic-plastic boundary was used as it was obtained from the Mises yield condition. Papadopoulos [9-11] invented Det.-criterion which was based on the determinant of the stress tensor, and it was used to study crack extension angle and the critical stress of fracture under biaxial loading. The local symmetry conditions (LS) proposed by Gol'dstein and Salganik [12] in 1974 required that crack propagation occured along with the path of vanishing K_{II}.

Many modifications on those criteria have been done by a lot of researchers. Both critical load value and crack path or surface growth have been predicted by different criteria in terms of elastic singular stress states and T-stress component. Ramulu and Kobayashi [13] extended SED criterion to dynamic mixed Mode crack propagation. Chen, Adams and Silva [14] proposed a more suitable failure criterion based on a specific strain energy criterion which had been used to Model the crack initiation and propagation in a single lap joint with a brittle adhesive and a ductile adhesive. Nobile et al. [15, 16] applied the strain energy density theory to determine crack initiation and direction in orthotropic solids, cracked T-beams and circumferentially cracked pipes. Bian and Kim [17] and Bian and Taheri [18] investigated two criteria based on the relative minimum plastic zone radius

(MPZR) and maximum ratio defined for prediction of fatigue crack initiation angles which could be applied to inclined surface crack specimens and through-crack specimens under mixed Mode loading. Kidane et al. [19] evaluated the crack growth direction as a function of temperature, non-homogeneity parameter and crack-tip velocity for functionally graded materials using both maximum tangential stress and minimum strain energy density criteria. Ayatollahi et al. [20], Maccagno and Knott [21] investigated the brittle fracture behavior of composites under mixed Mode I/II loading where the experimental results were used to evaluate the minimum strain energy density (SED), maximum tangential stress (MTS) and maximum energy release rate (G) criteria, with the first criterion showing the best agreement. Fatigue crack propagation was investigated under non-proportional mixed Mode loading by Plank and Kuhn [22], and the deviation angle was well predicted via the MTS criterion. The crack propagation problems in orthotropic and piezoelectric media were studied in [23-28]. A modified maximum tensile stress criterion had been proposed by Viola and Piva [29] and Piva and Viola [30] to predict the crack paths in sheets of brittle materials under biaxial loading. The Modes of crack growth in mixed Mode conditions were reviewed for the plane and three-dimensional in reference [31]. Some other aspects relating to the present investigation can be found in [32-36].

3.2.1 Strain energy density factor criterion (SEDF)

Within the framework of brittle fracture, the well-known strain energy density theory provides a more general treatment of fracture mechanics problems by virtue of its ability in describing the multi-scale feature of material damage and in dealing with mixed Mode crack propagation problem. The strain energy density factor theory is allowed to predicting unstable crack growth in mixed Mode. The main advantages of this criterion lie in its ease and simplicity, as well as its ability to handle various combined loading situations.

From the linear theory of isotropic and homogeneous elasticity, the strain energy density faction is found to possess a singularity of the order $1/r$ near the crack front and can be expressed in terms of three stress intensity factors $K_i (i = 1,2,3)$.

$$\frac{dW}{dV} = \frac{S}{r} \tag{3.1}$$

where W is the strain energy, and V is the volume.

The core of the S-criterion is the parameter of stain energy density factor , which is a function of the stress intensity factors for linear elasticity, can be defined as

$$S(\theta, \phi) = \frac{1}{16\pi\mu \cos\phi}(a_{11}K_1^2 + 2a_{12}K_1K_2 + a_{22}K_2^2 + a_{33}K_3^2) \tag{3.2}$$

where a_{ij} are auxiliary functions depending on the elastic properties of the material, modulus of elasticity E, shear modulus of elasticity μ and Poisson's rate ν, and an polar angle measured from the crack tip θ, as following

$$a_{11} = [(3 - 4\nu - \cos\theta)(1 + \cos\theta)] \tag{3.3}$$

$$a_{12} = (2\sin\theta)[\cos\theta - (1 - 2\nu)] \tag{3.4}$$

$$a_{22} = [4(1 - \nu)(1 - \cos\theta) + (1 + \cos\theta)(3\cos\theta - 1)] \tag{3.5}$$

$$a_{33} = 4 \tag{3.6}$$

and K_i are stress intensity factors for Modes I, II and III, respectively.

Briefly the application of the S-factor to predict the crack initiation and direction is based on two hypothesizes which are given as following

(1) Crack initiation occurs when the strain energy density factor S reaches a critical factor value i.e.

$$S = S_{min} = S_c \text{ for } \theta = \theta_0, \phi = \phi_0 \tag{3.7}$$

The parameter S_c is , in fact, directly related to K_{IC} by the relation

$$S_c = \frac{(1 + \nu)(1 - 2\nu)}{2\pi E} K_{IC} \tag{3.8}$$

(2) The initial crack growth takes place in the direction of minimum strain energy density. A minimum of $S(\theta, \phi)$ is searched on a sphere centered at each point on the crack front [10]. The continuous formulation $S(\theta, \phi)$ exhibits a local minimum at (θ_0, ϕ_0)in the region $-\pi \leq \theta \leq \pi$, $-\pi/2 \leq \phi \leq \pi/2$, provided $S(\theta_0, \phi_0) \leq S(\theta, \phi)$ [11]. It should be noted that $(\theta, \phi) \propto 1/\cos\phi$, so $S(\theta, \phi)$attains a local minimum always in the normal plane to the crack front, therefore $\phi = 0$ in our case and direction of the crack growth does not depend on K_3. So, a minimum of S is searched on a circle centered at each point on the crack front i.e.

$$\frac{\partial S(\theta, \phi)}{\partial \theta} = 0 \text{ and } \frac{\partial^2 S(\theta, \phi)}{\partial \theta^2} > 0 \text{ at } \phi = 0 \tag{3.9}$$

Substituting the values of a_{ij} and K_i from Eqs. (3.2-3.6) into Eq. (3.9) and after differentiation, setting $\nu = 0.3$, the result is as following

$$\frac{\partial S}{\partial \theta} = \sin\theta\,(\cos\theta - 0.4)K_I^2 + [\cos\theta\,(\cos\theta - 0.4) - \sin^2\theta]2K_I K_{II} + \sin\theta\,(0.4 - 3\cos\theta)K_{II}^2 = 0 \tag{3.10}$$

with

$$\frac{\partial a_{11}}{\partial \theta} = \frac{1}{16\pi\mu\cos\phi} 2\sin\theta\,(\cos\theta + 2\nu - 1)$$

$$\frac{\partial a_{12}}{\partial \theta} = \frac{1}{16\pi\mu\cos\phi} [2\cos\theta\,(\cos\theta + 2\nu - 1) - 2\sin^2\theta] \tag{3.11}$$

$$\frac{\partial a_{22}}{\partial \theta} = \frac{1}{16\pi\mu\cos\phi} 2\sin\theta\,(1 - 2\nu - 3\cos\theta)$$

3.2.2 Maximum tangential stress criterion (MTS)

The maximum tangential stress criterion (MTS) formulated by Erdogan and Sih [4], is one of the first conditions predicting critical stress and crack growth orientation. It requires that the crack branching angle θ_0 at a very short distance from the crack tip satisfies the following fracture conditions

$$\frac{\partial \sigma_\theta}{\partial \theta}|_{\theta=\theta_0, r=r_0} = 0 \tag{3.12}$$

$$(\sigma_\theta)_{\theta=\theta_0, r=r_0} = \frac{K_{IC}}{\sqrt{2\pi r_0}} \tag{3.13}$$

The stress series of the mixed Mode are represented as

$$\sigma_\theta = \frac{1}{2\sqrt{2\pi r}}\cos\frac{\theta}{2}[K_I(1+\cos\theta) - 3K_{II}\sin\theta]$$

$$\sigma_r = \frac{1}{2\sqrt{2\pi r}}\left[K_I(3+\cos\theta)\cos\frac{\theta}{2} + K_{II}\,(3\cos\theta - 1)\sin\frac{\theta}{2}\right] \tag{3.14}$$

$$\tau_{r\theta} = \frac{1}{2\sqrt{2\pi r}}\cos\frac{\theta}{2}[K_I\sin\theta + K_{II}(3\cos\theta - 1)]$$

Substituting the first equation in Eq. (3.14) to the first equation in Eq. (3.12), one gets

$$K_I\sin\theta_0 + K_{II}(3\cos\theta_0 - 1) = 0 \tag{3.15}$$

Solving Eq. (3.15), the crack propagation angle is obtained as

$$\theta_0 = cos^{-1}\frac{3K_{II}^2 \pm \sqrt{K_I^4 + 8K_I^2K_{II}^2}}{K_I^2 + 9K_{II}^2} \tag{3.16}$$

where the crack propagation angle θ_0 is measured with respect to the crack plane and $\theta_0 = 0$ represents the crack propagation in the straight-ahead direction. $\theta_0 < 0$ if $K_{II} > 0$, $\theta_0 > 0$ if $K_{II} < 0$.

3.2.3 Comparison between SEDF and MTS

The crack extension angles as functions of stress intensity factors predicted by SEDF criterion (Sc-theory) and MTS criterion (Kc-theory) are shown in Fig. 3.1. For pure Mode I loading ($K_{II}/K_I = 0$), the crack propagates along its own plane $\theta_0 = 0$ as mentioned before, for both crack criteria. For pure Mode II loading ($K_I/K_{II} = 0$), the crack extension angles of Kc-theory and Sc-theory are -70.5° and -80.34°, respectively. When the value of Mode I stress intensity factor equals to the value of Mode II, the crack extension angles are -53.13° and -51.91° according to the Kc-theory and the Sc-theory, respectively. For both criteria the crack extension angle increases monotonically with the value of K_{II}/K_I increases from 0 to 1 and from 1 to ∞.

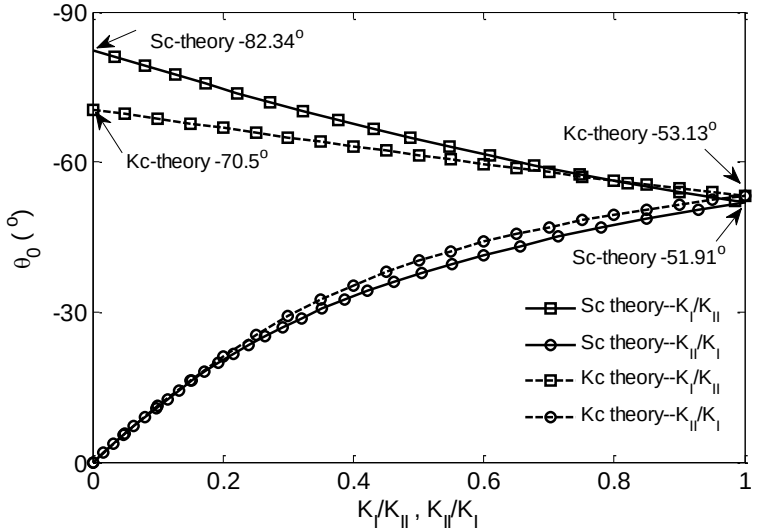

Fig. 3.1. Crack propagation angle θ_0 as a function of stress intensity factor ratio.

The critical condition only contains the first Mode toughness K_{IC}. Substituting the first equation in Eq. (3.14) to the second equation in Eq. (3.13), one gets

$$\cos\frac{\theta_0}{2}\left[K_I\cos^2\frac{\theta_0}{2}-\frac{3}{2}K_{II}\sin\theta_0\right]=K_{IC} \tag{3.17}$$

In order to apply the crisis curves to each material, the non-dimensional stress-intensity factors are introduced as follows

$$K_I^*=\frac{K_I}{K_{IC}},\qquad K_{II}^*=\frac{K_{II}}{K_{IC}} \tag{3.18}$$

In Fig. 3.2, the analysis of crack growth direction based on Eq. (3.17) and Eq. (3.18) incorporates only when K_{IC} is presented. In the surface, the same color (the plane of z-axis) constitutes a curve. It means for a fixed crack extension angle that there are different combinations of non-dimensional stress intensity factors of Mode I and Mode II.

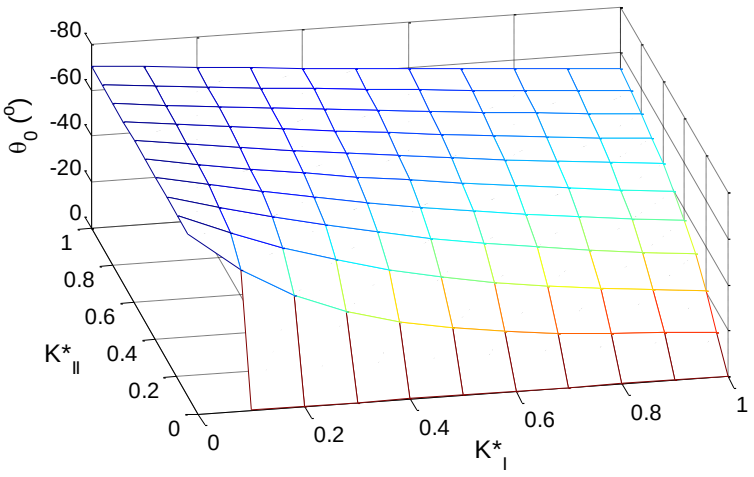

Fig. 3.2. Crack extension angle θ_0 versus non-dimensional stress intensity factors K_I^* and K_{II}^*

The curves in Fig. 3.3 represent the relationship between K_I^* and K_{II}^* in the various crack propagation direction according to SEDF criterion and MTS criterion expressed by Eq. (3.10) and Eq. (3.17). Those two curves of Kc-theory are the intersection between the crack propagation angle surface and the coordinate surface in Fig. 3.2, and the same way occurs for Sc-theory curves. They are valid for all materials and are symmetrical with respect to K_I^*. In the present figure, they are only traced in the quadrant $K_I^* \geq 0, K_{II}^* \geq 0$, for Sc-theory with $\nu = 0.3$. In other words, Fig. 3.3 indicates the possible combinations of Mode I and Mode II stress intensity factors for different crack extension.

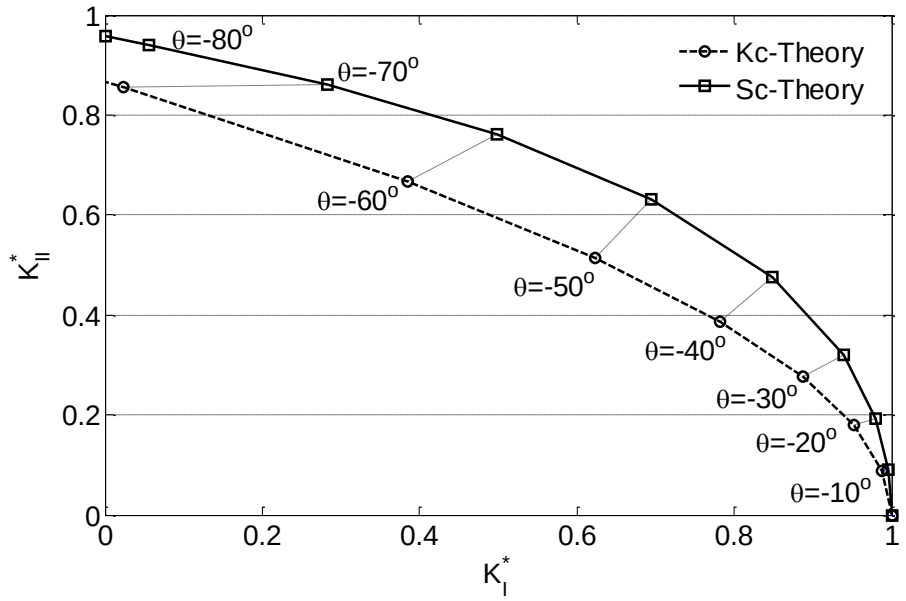

Fig. 3.3. Relation between K_I^* and K_{II}^*

For mixed mode crack, which bending moment M and shearing force Q are involved, the mixed loading ratio α is introduced as $\alpha = M/QR$. The crack propagation angle versus the crack depth ratio $\eta = a/2R$ for several mixed loading ratios according to Eq. (3.16) is presented in Fig.3.4. It

shows that the crack propagation angle decreases with the increase of crack depth ratio at different loading ratios under mixed loading, due to the difference in the increase ratio of the stress intensity factor for Mode I and Mode II. The same trend can be obtained with S-criterion, when the beam is subjected to single loading, e.g. loading ratio $\alpha = 0$ (Pure mode II) and $\alpha \to +\infty$ (Pure mode I), the crack propagation angle doesn't change with the crack depth ratio. When $\alpha \to +\infty$ and $\alpha = 0$ the crack propagates on its own plane $\theta_0 = 0$ and $\theta_0 = -70.5°$, respectively.

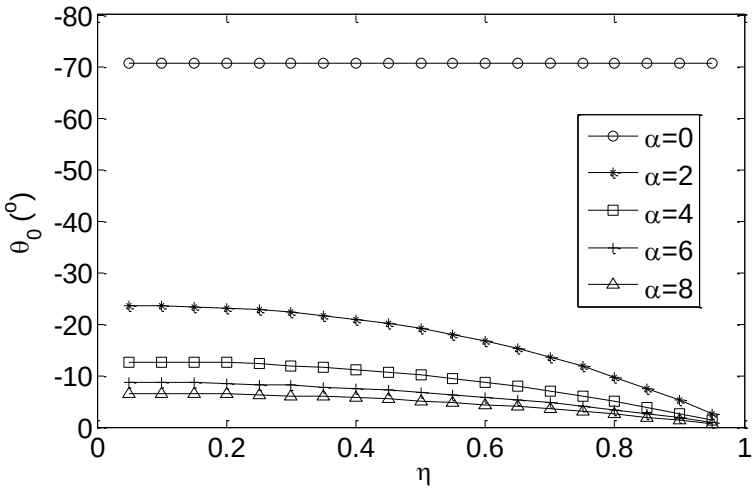

Fig. 3.4 Initial crack propagation angle θ_0 for crack depth ratio η according to MTS-criterion.

The effect of loading ratio on non-dimensional stress intensity factors are shown in Fig. 3.5 and Fig. 3.6. The Mode I non-dimensional stress intensity factor is much bigger than Mode II even if $\alpha = 1$. Particularly when crack depth ratio tends to be close to 1, Mode I is predominant in the crack propagation. For the SEDF criterion, the non-dimensional stress intensity factors have the same trend as predicted by MTS criterion that is not listed here, for the sake of brevity.

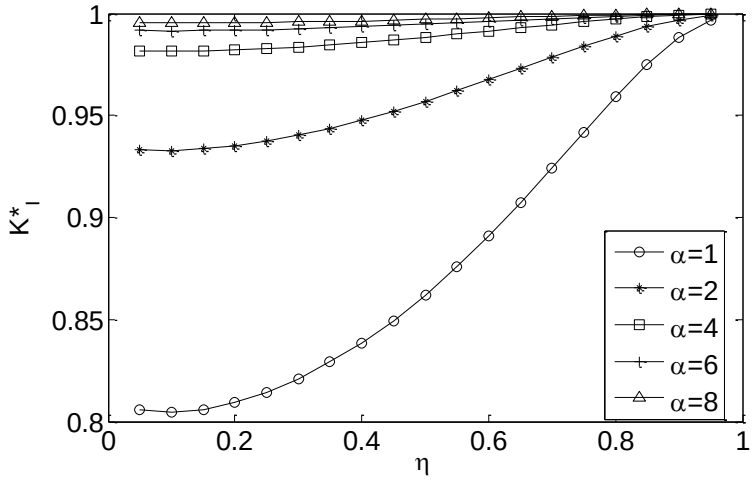

Fig. 3.5 Non-dimensional stress intensity factor K_I^* versus crack depth ratio η.

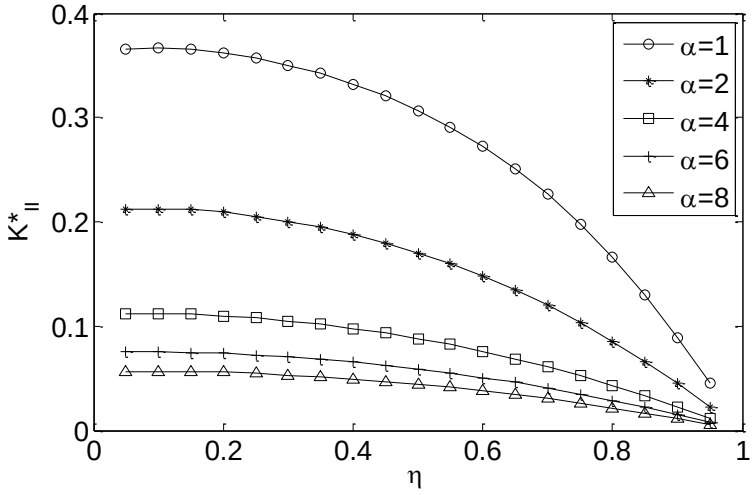

Fig. 3.6 Non-dimensional stress intensity factor K_{II}^{*} versus crack depth ratio η.

3.2.4 The criterion proposed by Richard ---- Three-dimensional crack extension

Though there are numerous fracture criteria proposed for 2D stress under Mode I, Mode II and their mixed Mode conditions, such as the maximum tangential stress criterion (MTS), the minimum strain energy density factor criterion (SEDF), the maximum energy release rate criterion (MERR) and the local symmetry criterion (LS), but only several 3D fracture criteria have been proposed, within which the related experimental work is limited. And it is well known that under Mode II loading the crack kinks with a kink angle ϕ, that under Mode III loading the crack front grows into a new plane which twisted about the angle ψ referred to the pre-crack plane, see Fig. 3.7. Both the wellknown criteria to 3D cases extended by Sih and Cha [37] and the extension of stress triaxiality condition (Mt-criterion) presented by Kong et al [38] can only predict tilt angle ϕ, not depend on twist angle ψ.

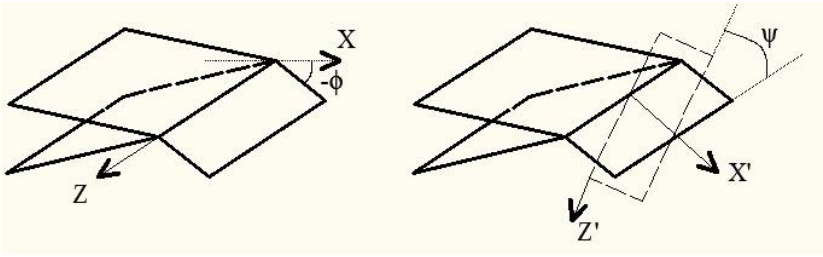

Fig. 3.7 Schematic illustration of the negative tilt ϕ and subsequent twist ψ angles

In order to investigate the initiation of crack front, a recently developed 3D fracture criterion proposed by Schollmann and Richard [39] is utilized, which can be taken into account all three basic fracture Modes I, II and III. This is so called maximum principle stress $\sigma'_1 - \text{criterion}$ (which the σ'_1 is the maximum principle stress on a virtual cylindrical surface around the crack front) reduces to the well-known MTS criterion, in case of plane mixed Mode I and Mode II loading conditions along the crack front, and thus can be taken as its 3D generalization.

According to the criterion, the kink tilt angle ϕ_0 can be determined by the following equation

$$-6K_I\Gamma - K_{II}\left(6-12\Gamma^2\right) + \frac{(4K_I - 12K_{II}\Gamma)\left[-6K_I\Gamma - K_{II}\left(6-12\Gamma^2\right)\right] - 32K_{III}^2\Gamma\left(1+\Gamma^2\right)^2}{\sqrt{(4K_I - 12K_{II}\Gamma)^2 + 64K_{III}^2\left(1+\Gamma^2\right)^2}} = 0 \tag{3.19}$$

where $\Gamma = \tan(\frac{\phi_0}{2})$, K_I, K_{II}, K_{III} are the stress intensity factors for Mode I, II and III.

And the twist angle can be calculated using

$$\psi_0 = \frac{1}{2}tan^{-1}\left(\frac{2K_{III}\Gamma}{K_I(\Gamma cos^2(\phi_0/2) - 2\upsilon\Gamma) - K_{II}(3 + 3sin^2(\phi_0/2) - 2\upsilon)}\right) \tag{3.20}$$

where υ is Poisson's ratio.

Unstable crack growth will occur if the comparative stress intensity factor K_v reaches the fracture toughness value K_{IC}. where

$$K_v = \frac{1}{2}cos\left(\frac{\phi_0}{2}\right)\left\{K_I cos^2\left(\frac{\phi_0}{2}\right) - \frac{3}{2}K_{II}\sin(\phi_0) + \sqrt{\left[K_I cos^2\left(\frac{\phi_0}{2}\right) - \frac{3}{2}K_{II}\sin(\phi_0)\right]^2 + 4K_{III}^2}\right\} \tag{3.21}$$

The comparisons of the crack initial angle along the three criteria (The maximum tangential stress criterion, Strain energy density factor criterion and Schollmann and Richard's criterion) and the results obtained by ABAQUS for different crack depth ratio are shown in Fig. 3.8. The stress intensity factors used in the three figures are the same, which obtained from ABAQUS. It should be noted that the angle from ABAQUS exported from "History output---Crack propagation direction" is the same with that obtained by the maximum tangential stress criterion, due to both of them using the same criterion. As described in the preview section, the first two criteria only consider Mode I and Mode II. In other words, those two criteria suppose that the twist angle is zero. Therefore, in order to compare the same crack propagation direction values along the three criteria, only tilt angle in the third criterion is drawn in the following figures. It's easy to see that the three criteria have very good agreement with each other. Some other comparisons about different criteria can be found in literatures [39, 40].

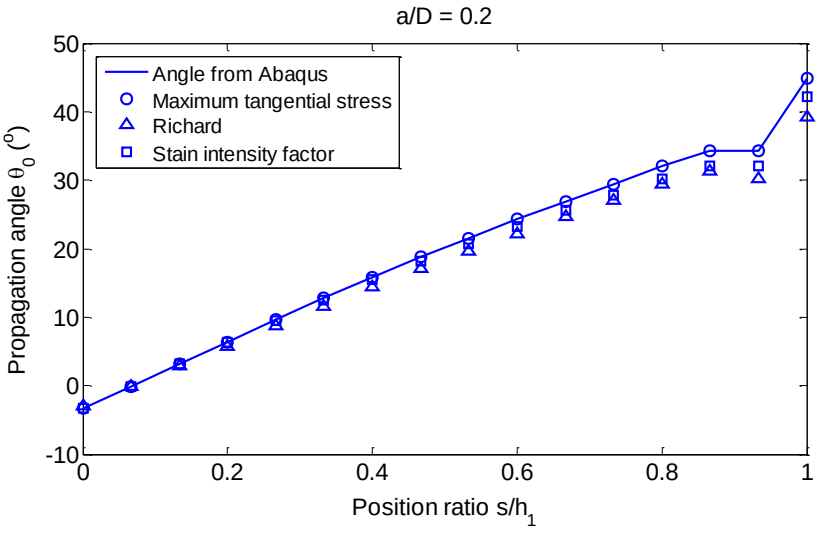

(a)

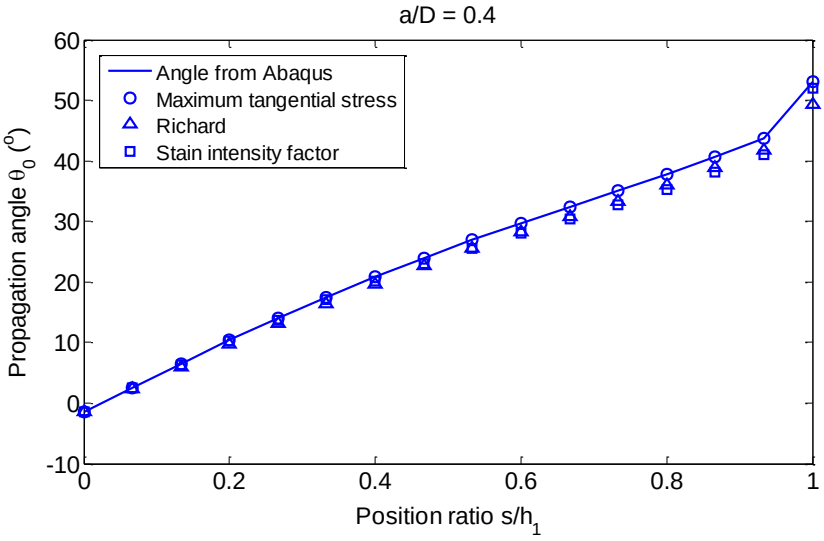

(b)

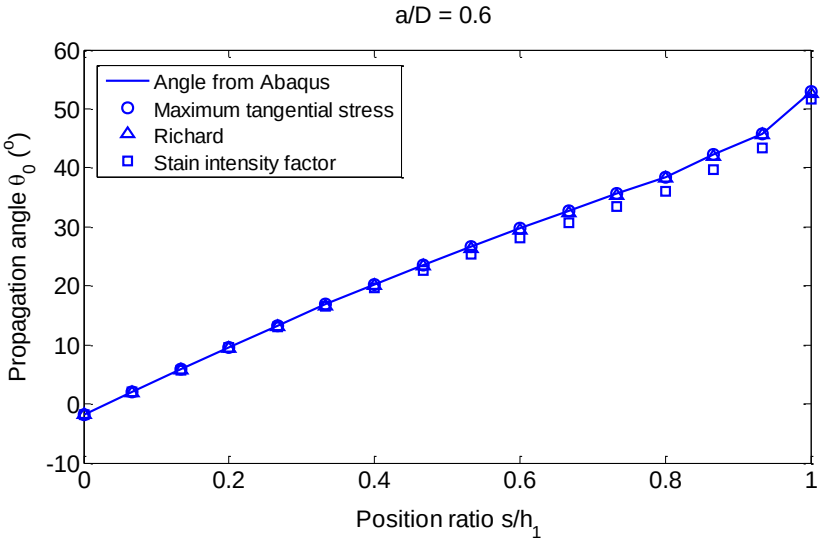

(c)

Fig. 3.8 Comparison of the crack initial angle according to those three criteria for different crack depth ratio (a) $a/D = 0.2$, (b) $a/D = 0.4$, (c) $a/D = 0.6$.

3.3 Crack initial propagation of single modes

It is obvious that the direction of the crack initiation is only determined by stress intensity factors according to the fracture criteria mentioned in section 3.2. It is well known that the knowledge of the stress intensity factors plays an important role in fracture control. In structural applications, the combination of standard loading conditions often involves K_I, K_{II} and K_{III} simultaneously. Stress intensity factors (SIFs) for many configurations are available [41-43]. In the present section, the derived simple formulae of stress intensity factors calculated by Herrmann's method are combined to SEDF criterion to predict crack growth direction and initiation for single loading modes. The details of the stress intensity factor calculation can be seen in section 2.2, Chapter 2. The results are discussed comparing with those obtained by MTS criterion.

3.3.1 Initial angle for beams under tension N

About the direction of crack initiation, it can be obtained from SEDF criterion. Setting $K_I = K_{I_N}$ and $K_{II} = K_{III} = 0$ in Eq. (3.10), considering $\partial^2 S/\partial\theta^2 > 0$, the crack propagation direction corresponds to $\theta_0 = 0$ which implies that the crack runs in its own plane. A graphic presentation of normalized strain energy density factor $S_N^* = 16\pi\mu R^3 S/N^2$ as a function of angle θ is shown in Fig 3.9.

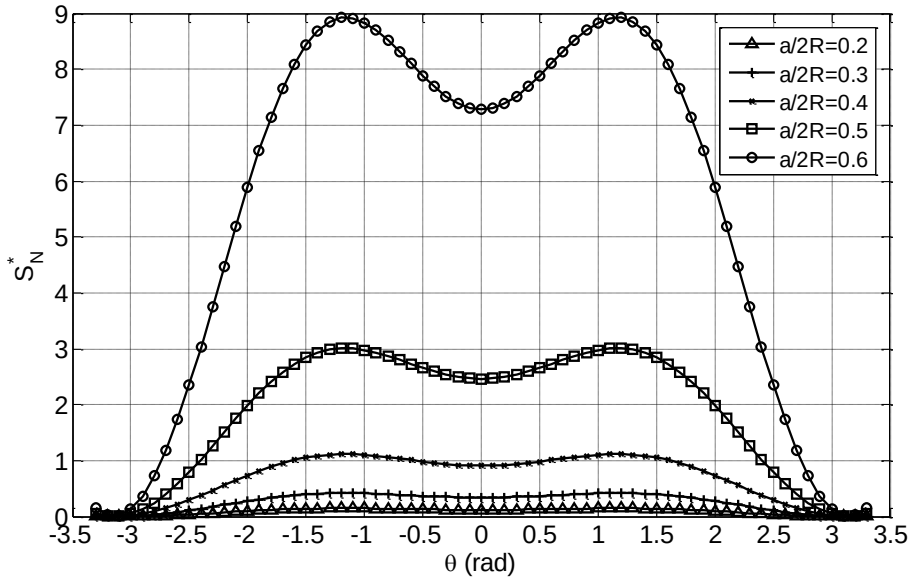

Fig. 3.9. Normalized strain energy density factor $S_N^* = 16\pi\mu R^3 S/N^2$ versus angle θ under tension.

3.3.2 Initial angle for beams under bending moment M

Information on the direction of crack initiation can be calculated by setting $K_I = K_{I_M}$ and $K_{II} = K_{III} = 0$ in Eq. (3.10), and considering the condition that $\partial^2 S/\partial\theta^2 > 0$, the propagation angle of the crack is $\theta_0 = 0$ which means the crack runs in its own plane. This corresponds to the direction

where the dilatational effect dominates. A plot of normalized strain energy density factor $S_M^* = 16\pi\mu R^5 S/M^2$ as a function of angle θ is shown in Fig.3.10.

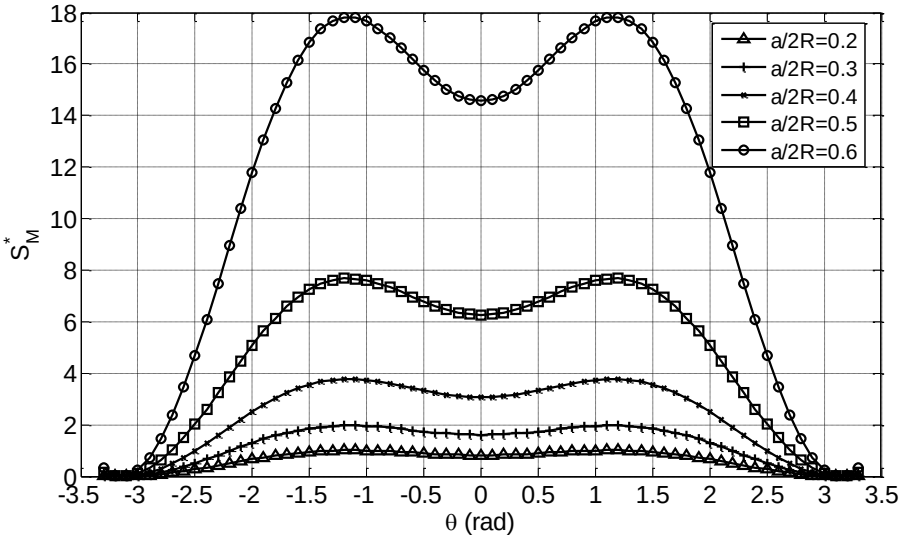

Fig.3.10 Normalized strain energy density factor $S_M^* = 16\pi\mu R^5 S/M^2$ versus angle θ under bending moment.

It is worth to note that S_{max}corresponds to location of yielding, in the present case $\theta = \pm 1.1593$. Crack instability is then assumed to take place when S_{min} equals to critical value S_C which only depends on the material. The critical load can be determined as

$$M_C = \frac{R^{5/2}}{F_M(\eta)}\sqrt{\frac{2\pi\mu S_C}{1-2\nu}} \tag{3.22}$$

3.3.3 Initial angle for beams under shear force Q

Considering that a cracked beam is subjected to shear force, setting $K_{II} = K_{II_S}$and $K_I = K_{III} = 0$ in Eq. (3.10) and paying attention to $\partial^2 S/\partial\theta^2 > 0$, the crack runs following the angle $\theta_0 = \pm 1.4371$. A plot of normalized strain energy density factor $S_Q^* = 16\pi\mu R^3 S/Q^2$ as a function of angle θ is shown in Fig.3.11.

It is worth noting that S_{max}corresponds to location of yielding, in the present case $\theta = 0$. Crack instability is then assumed to take place when S_{min} equals to critical value S_C that depends only on the material. The critical load can be determined as

$$Q_C = \frac{R^{3/2}}{F_S(\eta)}\sqrt{\frac{12\pi\mu S_C}{2-2\nu-\nu^2}} \tag{3.23}$$

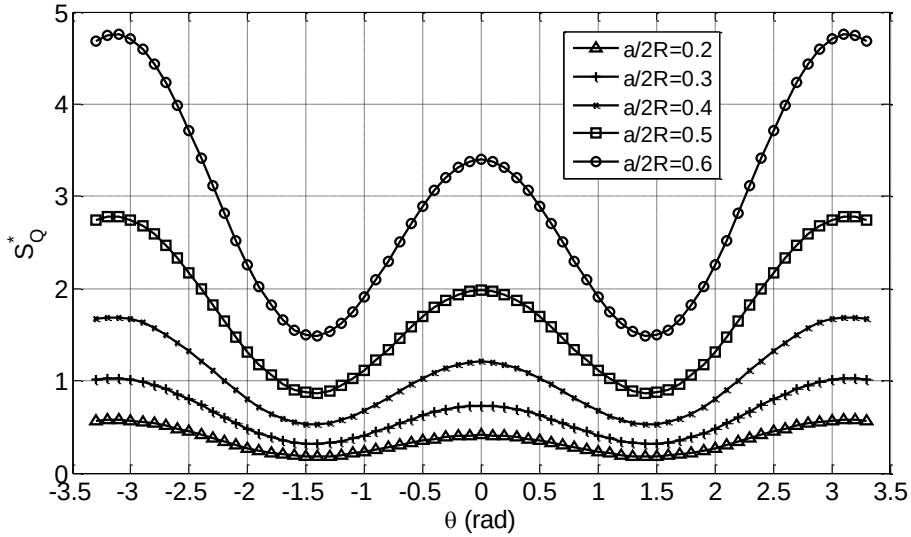

Fig.3.11. Normalized strain energy density factor $S_Q^* = 16\pi\mu R^3 S/Q^2$ versus angle θ under shear loading.

From Figs. (3.9-3.11), it can be obviously seen that the crack propagation direction of shafts subjected to single loading is independent from crack depth ratio.

3.4 Crack initial propagation of mixed modes

Considering the case of a shaft with a transverse straight front crack is subjected to a bending moment and a shear force, the cracked section is in a mixed Mode I and Mode II condition. Setting that $K_{III} = 0$ in Eq. (3.2) and substituting the stress intensity factors into Eq. (3.2), the strain energy density factor S becomes

$$S_{mix} = \frac{Q^2}{\pi R^3}\left[a_{11}\alpha^2 F_M^2(\eta) + 2a_{12}\alpha F_M(\eta)F_S(\eta) + a_{22}F_S^2(\eta)\right] \tag{3.24}$$

where $\alpha = M/QR$ is the mixed loading ratio of bending moment and shear loading.

Based on the SEDF criterion that assuming the crack could initiate on the direction of S_{min} i.e., $\partial S/\partial\theta = 0$ and $\partial^2 S/\partial\theta^2 > 0$, the expressions can be reported bellow

$$\frac{\partial S_{mix}}{\partial\theta} = \frac{Q^2}{8\pi\mu R^3}\begin{bmatrix}\alpha^2 F_M^2(\eta)\sin\theta(\cos\theta - 1 + 2\nu)\\ +2\alpha F_M(\eta)F_S(\eta)\left[\cos\theta(\cos\theta - 1 + 2\nu) - \sin^2\theta\right]\\ +F_S^2(\eta)\sin\theta(1 - 2\nu - 3\cos\theta)\end{bmatrix} = 0 \tag{3.25}$$

$$\frac{\partial^2 S_{mix}}{\partial\theta^2} = \frac{Q^2}{8\pi\mu R^3}\begin{bmatrix}\alpha^2 F_M^2(\eta)\left(-\cos\theta + 2\nu\cos\theta + \cos^2\theta - \sin^2\theta\right)\\ +2\alpha F_M(\eta)F_S(\eta)\sin\theta(1 - 2\nu - 4\cos\theta)\\ +F_S^2(\eta)\left[(1-2\nu)\cos\theta - 3\left(\cos^2\theta - \sin^2\theta\right)\right]\end{bmatrix} > 0 \tag{3.26}$$

The normalized strain energy densities S^* of mixed Mode as functions of crack depth ratio and angle for different mixed loading ratios of mixed mode are graphically presented in Figs. 3.12-3.14.

According to S-criterion, crack instability is assumed to take place when S_{min} equals to the critical value S_C that depends only on the material and crack propagation directions. For different conditions, the crack initial angle is plotted in the Figs. 3.12-3.14according to SEDF criterion. Obviously it could be seen from those graphs that the strain energy density gets bigger value when the depth of the crack increases. The same trend of strain energy density occurs to mixed loading ratio from $\alpha = 0.5$ to $\alpha = 10$.

Fig. 3.15, and Fig. 3.16 illustrate the normalized strain energy density as a function of the angle for different mixed loading ratios considering crack depth ratios $\eta = 0.2$ and $\eta = 0.6$. The normalized strain energy density factor increases when crack depth ratio and mixed loading ratio increases. However, the crack initiation angle increases when mixed loading ratio decreases. Fig. 3.17 demonstrates the initiate propagation direction angle as a function of mixed loading ratio for different crack depth ratios. As it is illustrated in Fig. 3.17, when mixed loading ratio is $\alpha = 0$, the directions of crack growth for different crack depth are the same, in fact $\alpha = 0$ means only shear loading acts on the beam. It can be seen when the mixed loading ratio $\alpha \to \infty$, the crack initiation direction gets close to zero, which means that the cracked beam is only subjected to bending moment. Those two results are the same as in the foregoing section. It can be observed that the crack propagation direction angle decreases quickly when the mixed loading ratio increases. For the same mixed loading ratio, the bigger crack depth, the smaller crack growth angle reaches.

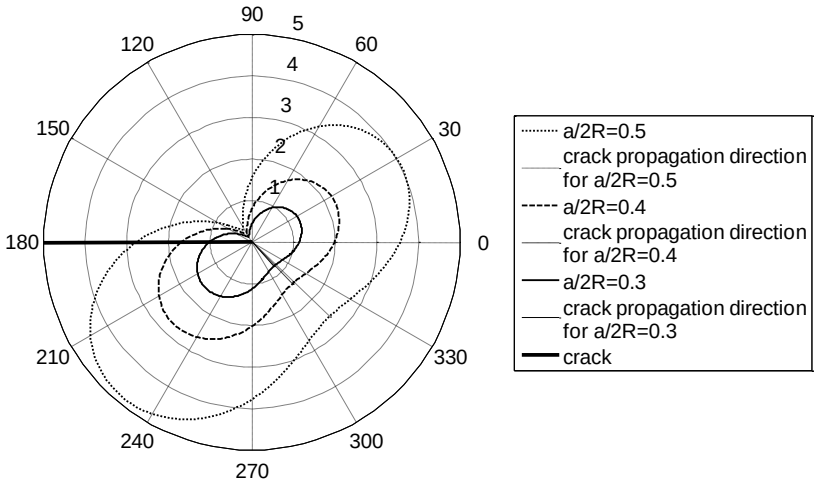

Fig.3.12 Normalized strain energy density factor $S^* = 16\pi\mu R^3 S_{\text{mix}}/Q^2$ versus angle θ for mixed Mode bending moment and shear force $\alpha = 0.5$.

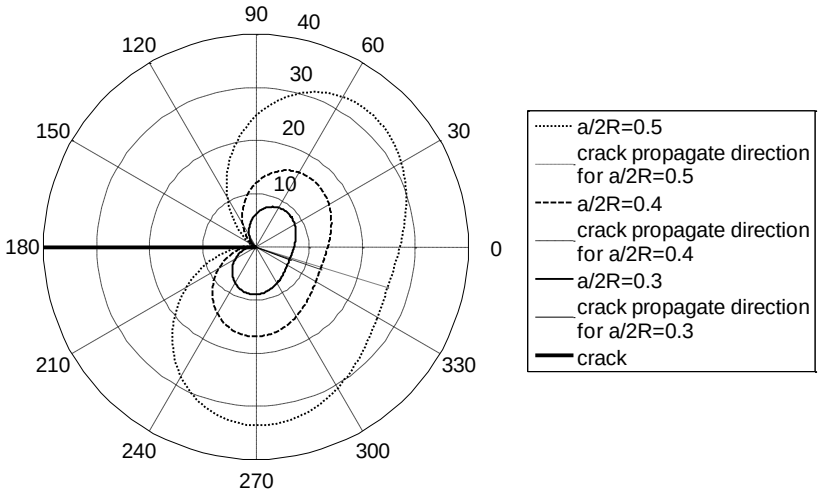

Fig.3.13 Normalized strain energy density factor $S^* = 16\pi\mu R^3 S_{\mathrm{mix}}/Q^2$ versus angle θ for mixed Mode bending moment and shear force $\alpha = 2$.

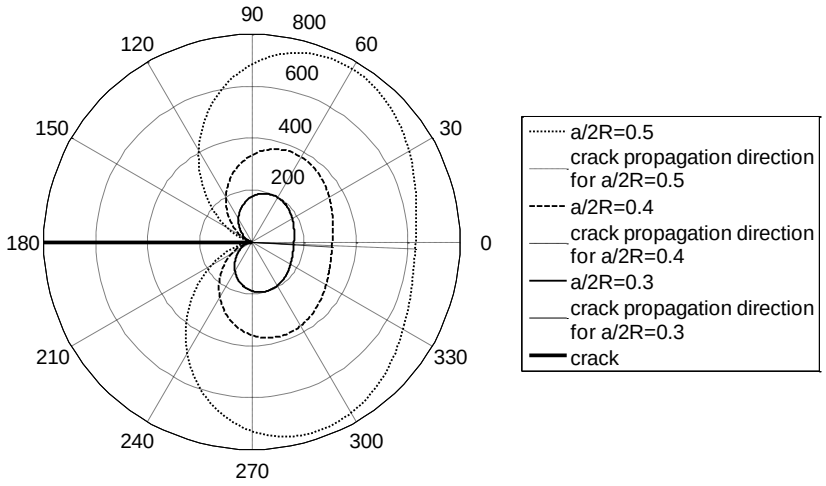

Fig.3.14 Normalized strain energy density factor $S^* = 16\pi\mu R^3 S_{\mathrm{mix}}/Q^2$ versus angle θ for mixed mode bending moment and shear force $\alpha = 10$.

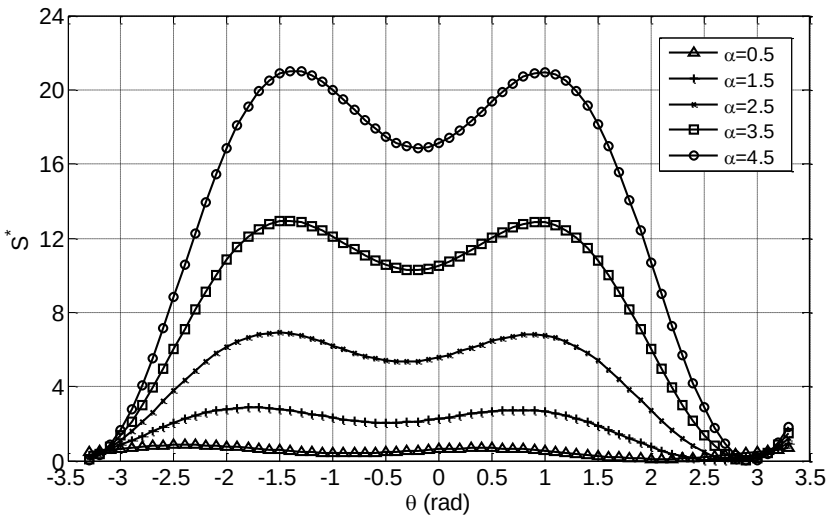

Fig.3.15 Normalized strain energy density factor $S^* = 16\pi\mu R^3 S_{\mathrm{mix}}/Q^2$ versus angle θ for mixed mode bending moment and shear force $a = 0.4R$.

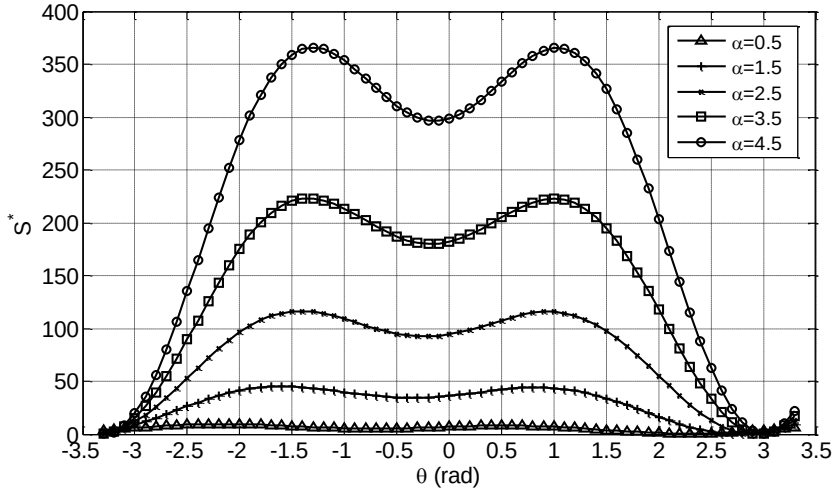

Fig.3.16 Normalized strain energy density factor $S^* = 16\pi\mu R^3 S_{\text{mix}}/Q^2$ versus angle θ for mixed Mode bending moment and shear force $a = 1.2R$.

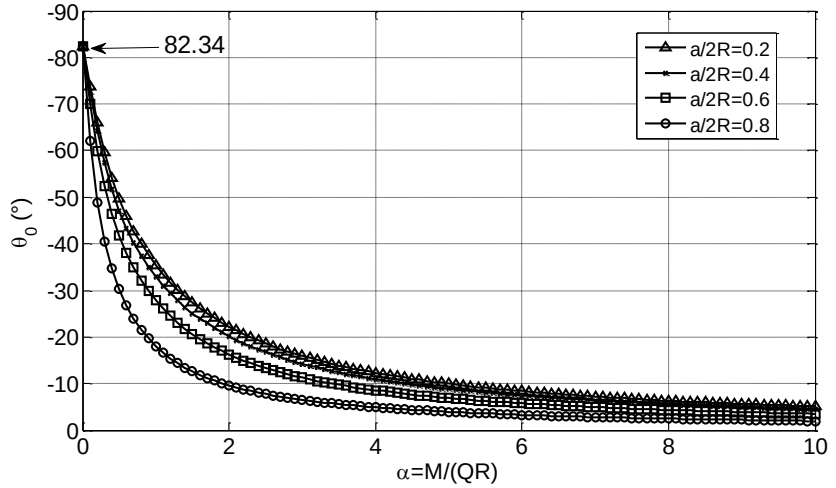

Fig.3.17 Initial crack propagation angle θ_0 versus mixed loading ratio α according to SEDF criterion.

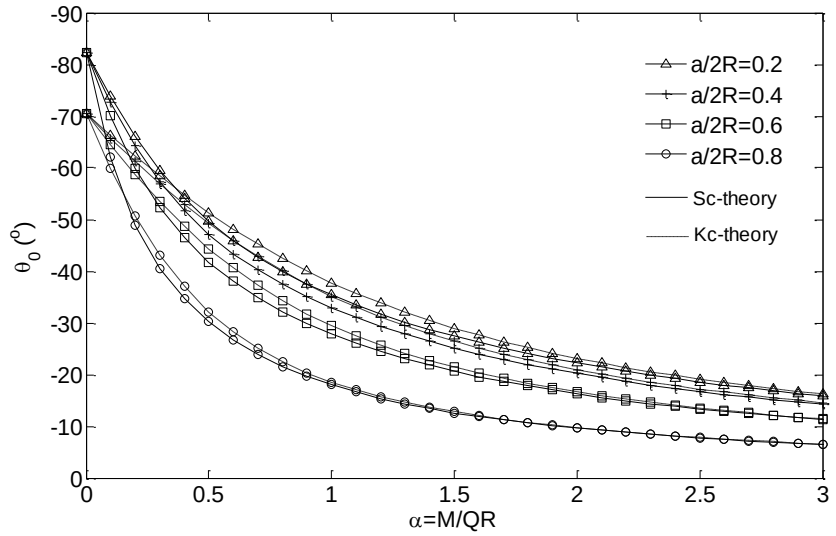

Fig. 3.18 Comparison of initial crack propagation angle θ_0 using Sc- and Kc-theories as a function of force ratio.

The comparison of initial propagation angles as functions of crack depth using SEDF criterion and MTS criterion is shown in Fig 3.18. The extension angle, derived from the two theories mentioned above, is different when the loading ratio is $\alpha < 0.5$. It means that the shearing mode is in charge of the difference between the two criteria.

As shown in section 3.3 and section 3.4, the derived simple formulas of stress intensity factors in section 2.2 Chapter 2 are used to predict the crack initiation and propagation angle in both uniaxial and mixed loading by strain energy density factor criterion. The crack runs in its own plane under the loading of tension or bending, 82.34 degrees for shear loading. The strain energy density gets bigger value when the depth of the crack and/or the loading ratio increase under mixed loading. However, the crack initiation angle decreases when the crack depth increases for a fixed loading ratio. The comparison between the strain energy density criterion and maximum tangential criterion is presented graphically.

3.5 Mixed mode crack propagation in three-dimensional

As mentioned in section 2.5 Chapter 2, the stress intensity factors of a beam with a transverse crack have to be calculated in the three-dimensional mode. The crack propagation angles calculated by SEDF criterion and Richard's criterion are investigated in the present section. The stress intensity factors involved in the two criteria come from Tada's hand book [42], the results are in section 2.5 Chapter 2, and ABAQUS, respectively. It should be noted that, the direction of crack initiation presented in ABAQUS results is calculated by the maximum tangential stress criterion.

According to Tada's results, It should be noted that, the crack propagation angles, on the surface where the place ratio equal to 1 are missing due to the stress intensity factors getting close to zero. It has been pointed out before that parameters, such as stress intensities, at the surface point are different or out of trend from that of the points inside. Therefore, the crack propagation angles of the surface in the above figures, representing in the ABAQUS element including crack line and cylindrical surface, are singularity. However, the surface point doesn't influence the good agreements of the results with each other.

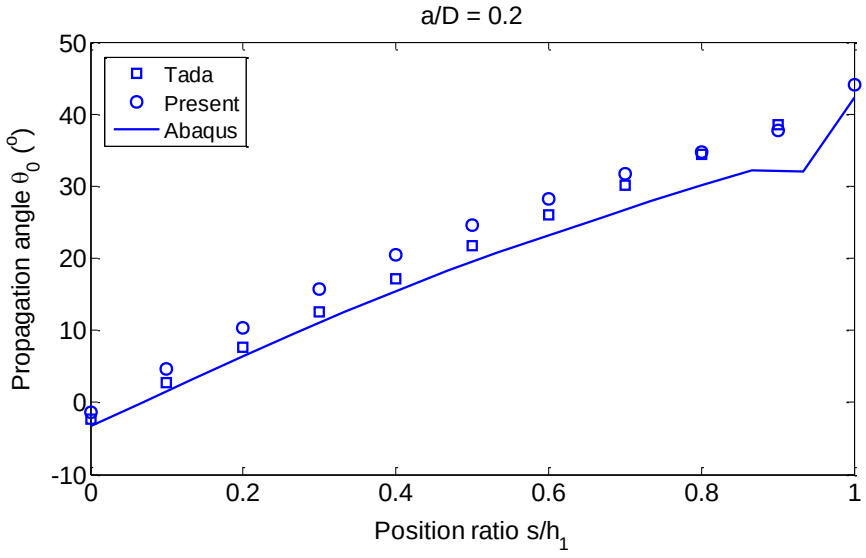

(a)

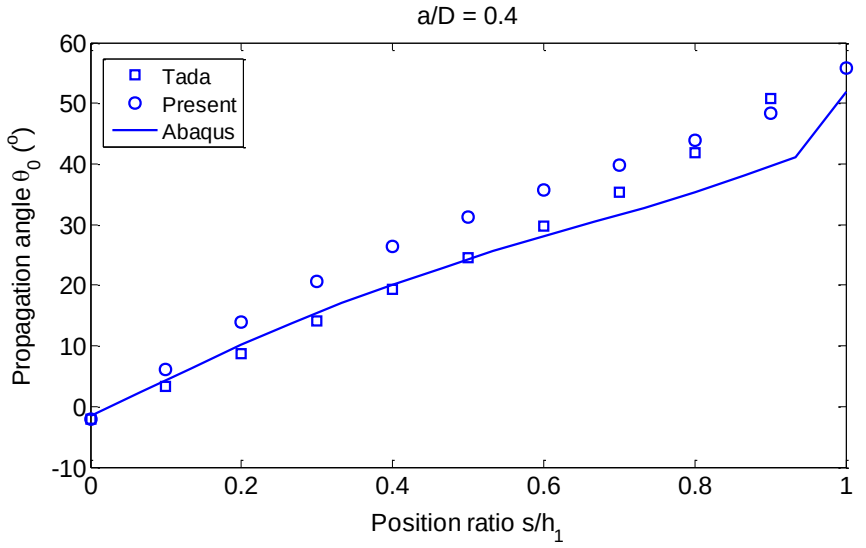

(b)

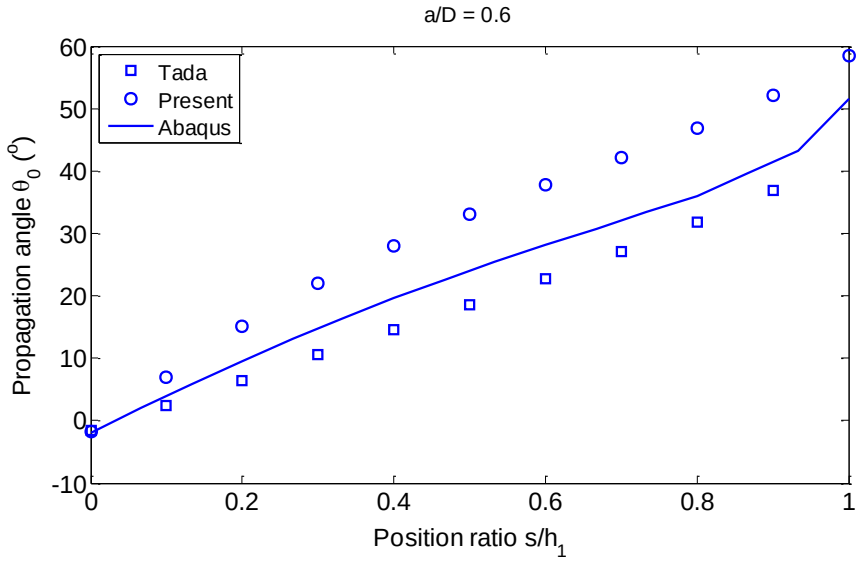

(c)

Fig. 3.19 Crack initial angle calculated by SEDF criterion for different crack depth ratio (a) $a/D = 0.2$, (b) $a/D = 0.4$, (c) $a/D = 0.6$.

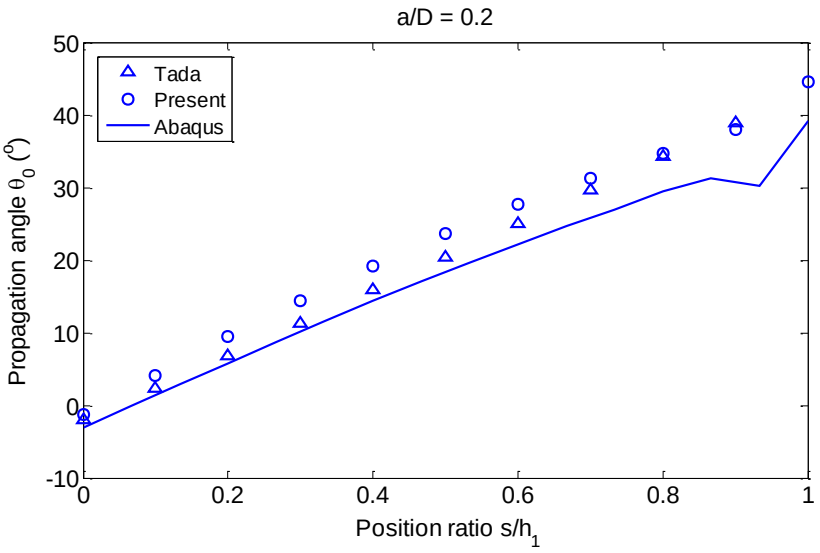

(a)

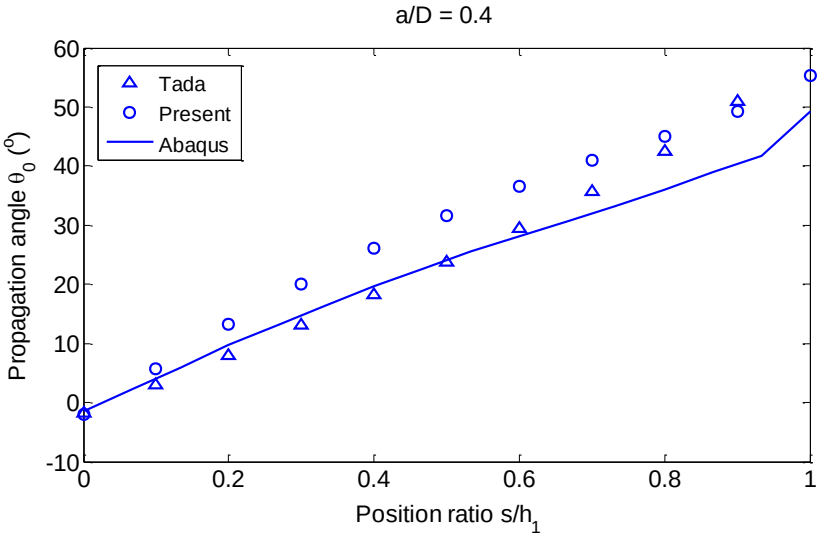

(b)

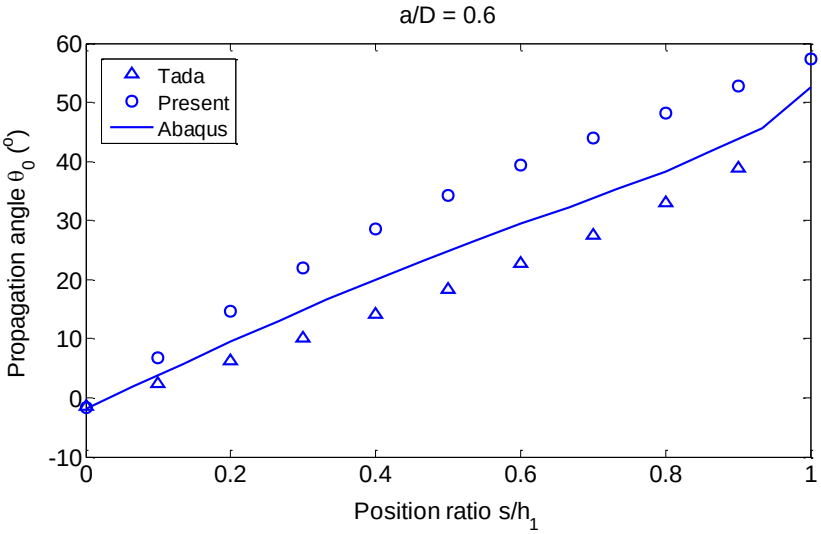

(c)

Fig. 3.20 Crack initial angle calculated by Richard's criterion for different crack depth ratio (a) $a/D = 0.2$, (b) $a/D = 0.4$, (c) $a/D = 0.6$.

Fig. 3.20 shows the crack initial angle comparison according to the fracture criterion of Richard [39] for different crack depth ratios. Same with Fig. 3.19, the stress intensity factors used in those three different criteria come from ABAQUS calculation in Tada's hand book [42], and the "Present" means calculated in Chapter 2 and the crack propagation angles at the surface points of Tada's results are missed. The good agreements of those results are shown in this figure.

References

[1] Griffith AA. The phenomena of rupture and flow in solids. Philos T Roy Soc A 1921; 221:163-36.

[2] Hussain MA, Pu SL, Underwood J. Strain energy release rate for a crack under combined mode I and mode II. Fract Anal ASTM STP 1974; 560:2–27.

[3] Wu CH. Fracture under combined loads by maximum-energy-release-rate criterion. J Appl Mech 1978; 45:553–8.

[4] Erdogan F, Sih GC. On the crack extension in plates under plane loading and transverse shear. J Bas Engng 1963; 85:519-7.

[5] Palaniswamy K, Knauss WG. Propagation of a crack under general, in-plane tension. Int J Fract 1972; 8:114-4.

[6] Sih GC. Some basic problems in fracture mechanics and new concepts. Engng Fract Mech 1973; 5:365-12.

[7] Hellen TK, Blackburn WS. The calculation of stress intensity factors for combined tensile and shear loading. Int J Fract 1975; 11:605-13.

[8] Theocaris PS, Andrianopoulos NP. The T-criterion applied to ductile fracture. Int J Fract 1982; 20:125-6.

[9] Papadopoulos GA. The stationary value of the third stress invariant as a local fracture parameter (Det.-criterion). Engng Fract Mech 1987; 27:643-12.

[10] Papadopoulos GA. The influence of geometry of edge-cracked plates on crack initiation. Engng Fract Mech. 1987; 26:945-10.

[11] Papadopoulos GA. Crack initiation under biaxial loading. Engng Fract Mech 1988; 29: 585-14.

[12] Gol'dstein RV, Salganik RL. Brittle fracture of solids with arbitrary cracks. Int J Fract 1974; 10:507–16.

[13] Ramulu M, Kobayashi AS. Strain energy density fracture criterion in elastodynamic mixed mode crack propagation. Engng Fract Mech1983; 18:1087-12.

[14] Chen Z, Adams RD, Silva L. Prediction of crack initiation and propagation of adhesive lap joints using an energy failure criterion. Engng Fract Mech 2011; 78:990-28.

[15] Carloni C, Nobile L. Crack initiation behavior of orthotropic solids as predicted by the strain energy density theory. Theor Appl Fract Mech 2002; 38:109-11.

[16] Nobile L, Carloni C, Nobile M. Strain energy density prediction of crack initiation and direction in cracked T-beams and pipes. Theor Appl Fract Mech 2004; 41:137-9.

[17] Bian LC, Kim KS. The minimum plastic zone radius criterion from crack initiation direction applied to surface cracks and through-cracks under mixed mode loading. Int J Fatigue 2004; 26:1169-10.

[18] Bian LC, Taheri F. A proposed maximum ratio criterion applied to mixed mode fatigue crack propagation. Mater Design 2011; 32:2066-7.

[19] Kidane A, Chalivendra VB, Shukla A, Chona R. Mixed-mode dynamic crack propagation in graded material under thermo-mechanical loading. Engng Fract Mech 2010; 77:2864-17.

[20] Ayatollahi MR, Shadlou S, Shokrieh MM. Mixed mode brittle fracture in epoxy/multi-walled carbon nanotube nanocomposites. Engng Fract Mech 2011; 78:2620-13.

[21] Maccagno TM, Knott JF. The fracture behavior of PMMA in mixed modes I and II. Engng Fract Mech 1989; 34:65-86.

[22] Plank R, Kuhn G. Fatigue crack propagation under non-proportional mixed mode loading. Engng Fract Mech 1999; 62: 203-27.

[23] Piva A, Viola E. Crack propagation in an orthotropic medium. Engng Fract Mech 1988; 29:535-14.

[24] Piva A, Viola E, Tornabene F. Crack propagation in an orthotropic medium with coupled elastodynamic properties. Mech Res Commun 2005; 32:153-7.

[25] Piva A, Tornabene F, Viola E. Crack propagation in a four-parameter piezoelectric medium. Eur J Mech A-Solid 2006; 25:230-20.

[26] Piva A, Viola E, Tornabene F. Elastodynamic degenerate states for a crack in an orthotropic medium. Meccanica 2006; 41:363-11.

[27] Piva A, Tornabene F, Viola E. Subsonic Griffith crack propagation in piezoelectric media. Eur J Mech A-Solid 2007; 26:442-18.

[28] Viola E, Boldrini C, Tornabene F. Non-singular term effect on the fracture quantities of a crack in a piezoelectric medium. Engng Fract Mech 2008; 75:4542-26.

[29] Viola E, Piva A. Crack paths in sheets of brittle material. Engng Fract Mech 1984; 19:1069-16.

[30] Piva A, Viola E. On paths of two equal collinear cracks. Engng Fract Mech 1984; 20:735-7.

[31] Mróz KP, Mróz Z. On crack path evolution rules. Engng Fract Mech 2010; 77:1781-27.

[32] Viola E, Piva A. Fracture behaviour by two cracks around an elliptic rigid inclusion. Engng Fract Mech 1981; 15:303-23.

[33] Viola E, Pascale G. Static analysis fatigue and fracture of cracked beams on elastic foundation. Engng Fract Mech 1985; 21:365-11.

[34] Viola E, Piva A. Second-order approximation to the crack trajectory equation. Engng Fract Mech 1986; 24:121-6.

[35] Hasan WM, Piva A, Viola E. Parameter estimation from measured displacements of crack edges in an isotropic material. Engng Fract Mech 1998; 59:697-16.

[36] Viola E, Marzani A. Crack effect on dynamic stability of beams under conservative and nonconservative forces. Engng Fract Mech 2004; 71:699-19.

[37] Sih GC, Cha CK. A fracture criterion for three-dimensional crack problems. Engng Fract Mech 1974;6:699–723.

[38] Kong XM, Schluter N, Dahl W. Effect of triaxial stress on mixed-Mode fracture. Engng Fract Mech 1995;52:379–88.

[39] Schollmann M, Richard HA, Kullmer G, Fulland M. A new criterion for the prediction of crack development in multiaxially loaded structures. Int J Fract 2002;117(2):129–141.

[40] Mróz KP, Mróz Z. On crack path evolution rules. Engng Fract Mech 2010;77:1781–1807.

[41] Sih GC, Handbook of stress-intensity factors for researchers and engineers. Institute of Fracture and Solid Mechanics, Lehigh University, Bethlehem; 1973.

[42] Tada H, Paris PC, Irwin GR. The stress analysis of cracks handbook, second ed. Paris Production; St. Louis; 1985.

[43] Murakami Y. Stress intensity factors handbook. Pergamon Press; Oxford; 1987.

Chapter 4

Dynamic behavior of cracked shafts

4.1 Introduction

Many engineering structures may have structural defects such as cracks due to long-term service, mechanical vibrations, applied cyclic loads etc. Numerous techniques, such as non-destructive monitoring tests, can be used to screen the condition of a structure. Novel techniques to inspect structural defects should be explored. Crack occurring in structural elements such as shafts, beams and plates, leads to local changes in the stiffness of these elements, and consequently their static, dynamic characteristic (changes in natural frequencies, modes of vibration, amplitudes of forced vibration, etc.) of structures has been the subjects of many investigations. In view of that, the natural frequencies and mode shapes of the structure hold information relating to the place and dimension of the damage. Vibration analysis allowing online inspection is an attractive method to detect cracks in structures. Investigation of dynamic behavior of crack structures has attracted the attention of several researchers in recent years. The vibration analysis of cracked beam with circular cross section and shafts is one of the most important branches. Dimarogonas and Papadopoulos [1], by using the theory of cracked shafts with dissimilar moments of inertia, investigated the vibration of cracked shafts in bending. Papadopoulos and Dimarogonas [2] studied the free vibration of shafts and presented the influence of the crack on the vibration behavior of the shafts. Kikidis and Papadopoulos [3] analyzed the influence of the slenderness ratio of a non-rotating cracked shaft on the dynamic characteristics of the structure. Zheng and Fan [4] studied the vibration and stability of cracked hollow-sectional beams. Dong et al. [5] presented a continuous model for vibration analysis and parameter identification of a non-rotating rotor with an open crack. They assumed that the cracked rotor was an Euler–Bernoulli beam with circular cross section. Kisa *et al* [6] presented a novel numerical technique applicable to analyze the free vibration analysis of uniform and stepped cracked beams with circular cross section in which the finite element and component mode synthesis methods were used together.

One of the goals of this chapter is to determine the vibration characteristics of circular cross section beams with a single edge crack, under axial force, bending moment, shear forces and torque, by employing Euler-Bernoulli and Timoshenko theories and by using the line-spring model. The line-spring mode has the features of having two nodes and zero length. A general method for extending

fracture mechanics through the compliance concept to the analysis of a structure containing cracked members is considered in Okamura et al [7]. The beam is detached into parts from the crack section. These substructures are joined by using line-spring model in which the flexibility matrices taking into account the interaction forces derived by virtue of fracture mechanics theory as the inverse of the compliance matrix found with the appropriate stress intensity factors and strain energy release rate expressions. The stiffness matrix is derived from an integration of stress intensity factors. As the line-spring element includes the three degrees of freedom commonly associated with nodes in beam element, the governing matrix equation of the cracked structures is derived by assembly of the conventional beam element in conjunction with line-spring model. The resulting eigenvalue problems are solved to find the natural frequencies and the associated mode shapes. The influences of the crack depth and position on the natural frequencies and corresponding mode shapes are examined for structures graphically represented. The variations of the natural frequencies with the crack depth can be used to estimate the crack size in the structures. Furthermore, the sudden changes in the higher mode shapes of vibration may be used to accurately determine the crack position in the structures. The stiffness matrix is derived starting from an integration of stress intensity factors. Since the line-spring element includes three degree of freedoms commonly associated with nodes in beam-elements, the governing matrix equation of the cracked structures is derived by assembly of the conventional beam elements in conjunction with the line-spring model. Numerical and graphical results for the conventional Euler-Bernoulli and Timoshenko plane structures are presented and compared. The equation of motion of the Timoshenko model includes translational and rotatory mass matrices.

Two examples of a transverse open crack have been carried out for various crack depths and crack locations. The first study is about a beam of uniform circular cross section with transverse crack subjected to axial force, bending moment and shearing force. The coupling effect of tension and bending is considered. The crack is represented by a line-spring element. The Castigliano's theorem is used here to compute the coupling compliances of the cracked beam section. A cantilever cracked beam subjected to bending moment M, shearing force S and torque T is the second example. The line-spring model is featured with two nodes and zero length, therefore the shearing force S does not interact with the bending moment. The compliance matrix for the line-spring model can be derived according to Okamura *et al* [7] and Carpinteri *et al* [8] theory which is based on the relationship between load and deflection. As with simple beams, the bending and torsional motions are uncoupled. The natural bending mode, tension mode and rotation mode shaping as a function of crack depth ratio and crack locations are studied.

To reveal the accuracy and effectiveness of the offered method, a number of numerical examples are given for free vibration analysis of beams with transverse non-propagating open cracks. Numerical results showing good agreement with the results of other available studies, has addressed the effects of the location and depth of the cracks on the natural frequencies and mode shapes of the cracked beams.

4.2 Differential equations of motion for the cracked system

The net ligament effect of a cracked beam can be replaced by an elastic hinge connecting both the cross-sections of the beam separated by an ideal plane containing the crack. About the elastic line-hinge assume that the crack is a through-crack and the crack represents the net ligament effect by certain axial force, bending moment, shear force and torque acting directly on the faces of this through-crack. The spring has the features of having two nodes and zero length. The expressions of the stress intensity factors evaluated above can be used for determining the stiffness matrix of a line-spring with which the cracked section of a beam can be modeled. Consider that two undamped components A and B join together by means of springs capable of carrying axial, bending, shearing and torsional effects are shown in Fig. 4.1.

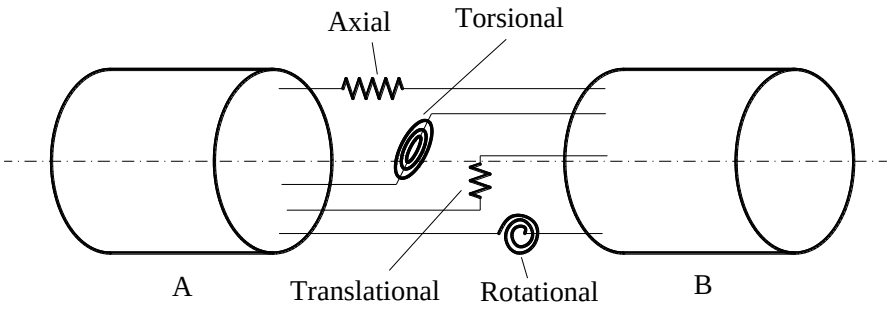

Fig.4.1. Model of the components connected by spring

By applying the standard finite element method to this system, the differential equation of motion for free vibration is given as

$$M\ddot{x} + (K + K_f)x = 0 \tag{4.1}$$

where $M = \sum_n M^e$ and $K = \sum_n K^e$ are global consistent mass matrix and the stiffness matrix for the entire structure without crack, respectively, with M^e and K^e are the extend forms of mass matrix m^e and stiffness matrix k^e for the finite beam element without crack, n is the number of the finite element. K_f is the stiffness matrix for the line spring model expressed in the extended form in order to incorporate the line-spring stiffness matrix K_f into the assembly procedure of the global stiffness

matrix for the entire structure. $x=[r_1,h_1,\theta_1,\varphi_1,\cdots,r_i,h_i,\theta_i,\varphi_i,\cdots,r_n,h_n,\theta_n,\varphi_n,]^T$ is the generalized displacement vector.

After imposing the appropriate end conditions, if the global nodal displacement vector x is assumed to be harmonic in time with circular frequency $x = A^* exp(i\omega t)$, the equation will become an eigenvalue problem of the standard form

$$(K'-\omega^2 M)A^*=0 \tag{4.2}$$

where A^* is a vector of displacement amplitudes of vibration.

The solution of the above eigenvalue problem yields the natural frequencies and the corresponding mode shapes of the cracked structure which depends on the crack position, crack size, geometric dimensions of the structure, the boundary conditions and mechanical parameters of the material.

4.3 Cracked cantilever beams subjected to tension, bending moment and shear force

As an application example of the stress intensity factors obtained by section method, a beam of uniform circular cross section with transverse crack of depth a subjected to axial force, bending moment and shearing force, see Fig.4.2, is investigated. The coupling effect of tension and bending is considered. The Castigliano's theorem is used here to compute the coupling compliances of the cracked beam section.

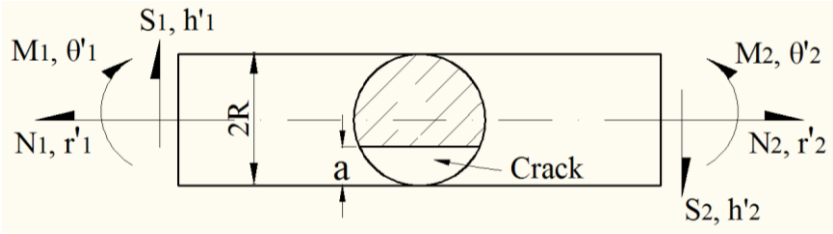

Fig. 4.2. Cracked beam under tension, bending and shearing force

4.3.1 Stiffness matrix of the cracked section

According to Castigliano's second theorem, if the strain energy of a linearly elastic structure could be expressed as a function of force Q_i, then the partial derivative of the strain energy with respect to force gives the displacement u_i in the direction of Q_i. As could be seen from above this can also be expressed as

$$u_i = \frac{\partial U}{\partial Q_i} \tag{4.3}$$

Combining the strain energy release rate $\mathcal{G}$ proposed by Irwin [9], represents the elastic energy in relation to a unit increase in length ahead of the crack front,

$$\mathcal{G} = \frac{1}{E'}(K_I^2 + K_{II}^2) + \frac{1+\nu}{E}K_{III}^2 \tag{4.4}$$

where $E' = E/(1-\nu^2)$ is for plane strain, $E' = E$ is for plane stress, E is Young's modulus, ν is Poisson's coefficient. K_I, K_{II} and K_{III} are stress intensity factors for Mode I, Mode II and Mode III, respectively, calculated by section method in the present application. The details of the stress intensity factors can be found in section 2.3, Chapter 2.

Eq. (4.3) gives the expression between displacement and strain energy release rate as

$$u_i = \frac{\partial}{\partial Q_i}\int_A \left[\frac{1}{E'}\left(K_I^2 + K_{II}^2\right) + \frac{1+\nu}{E}K_{III}^2\right]dA \tag{4.5}$$

In the present application, the flexibility coefficients as the function of the crack shape and the stress intensity factors for involved Mode I and Mode II can be introduced as following

$$c_{ij} = \frac{\partial u_i}{\partial Q_j} = \frac{\partial^2}{\partial Q_i \partial Q_j}\int_A \frac{1}{E'}\left[\left(K_{I_N} + K_{I_M}\right)^2 + K_{II_S}^2\right]dA \tag{4.6}$$

The flexibility coefficients c_{ij} are obtained from the fracture mechanics method proposed by Dimarogonas and Paipetis [10].

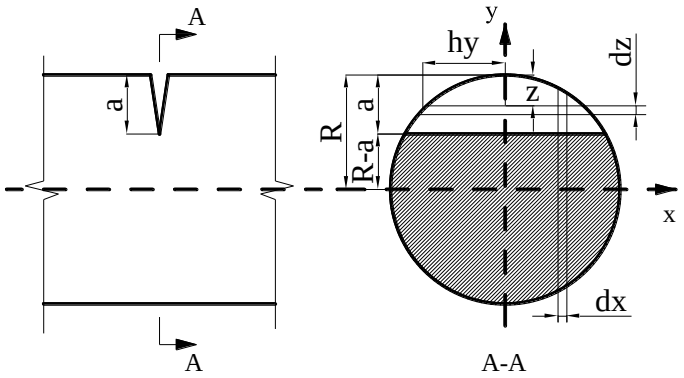

Fig. 4.3. The geometry of the cracked circular cross section

For the crack of maximum depth a, the crack is bounded in the x direction by $-h_y$ and h_y, and in the y direction by 0 and a. The boundary width of the crack at each y, can be calculated using Pythagorean Theorem from Fig. 4.3.

$$h_y = \sqrt{R^2 - y^2} = \sqrt{R^2 - (R-z)^2} \tag{4.7}$$

Substituting the forces and stress intensity factors into Eq. (4.6), the flexibility coefficients are obtained as following and plotted in Fig.4.4.

$$c_{11}=\frac{\partial^2}{\partial N^2}\int_A\frac{1}{E'}\left(K_{I_N}^2\right)dA=\frac{4\pi}{E'}\int_0^a\int_{-h_y}^{h_y}b\left[\frac{1}{A^c}+\frac{e}{I^c}(R+e-z-b)\right]^2dxdz$$

$$c_{13}=\frac{\partial^2}{\partial M\partial N}\int_A\frac{1}{E'}\left(2K_{I_N}K_{I_M}\right)dA=\frac{4\pi}{E'}\int_0^a\int_{-h_y}^{h_y}\sqrt{b_mb_n}\,\frac{1}{I^c}(R+e-z-b_m)\left(\frac{1}{A^c}+\frac{e}{I^c}(R+e-z-b_n)\right)dxdz$$

$$c_{22}=\frac{\partial^2}{\partial S^2}\int_A\frac{1}{E'}\left(K_{II_S}^2\right)dA=\frac{\pi}{E'}\int_0^a\int_{-h_y}^{h_y}b\,\frac{Q_x^{*2}}{I^{c2}\left[R^2-(R-z-b)^2\right]}dxdz \tag{4.8}$$

$$c_{33}=\frac{\partial^2}{\partial M^2}\int_A\frac{1}{E'}\left(K_{I_M}^2\right)dA=\frac{4\pi}{E'}\int_0^a\int_{-h_y}^{h_y}b\left(\frac{R+e-z-b}{I^c}\right)^2dxdz$$

$$c_{12}=c_{21}=c_{23}=c_{32}=0\,,\ c_{31}=c_{13}$$

where A^c, I^c, e and Q_x^* are functions of coordinate variable z, b_m and b_n are the values under bending and tension, respectively. All the constants can be found in section 2.3 in Chapter 2.

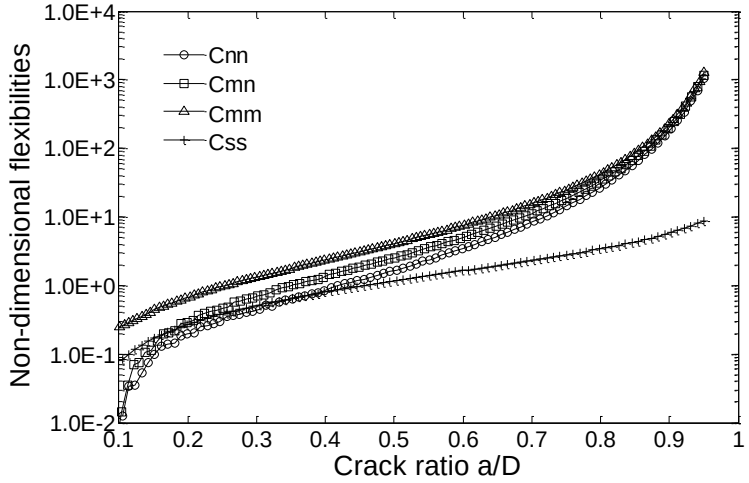

Fig. 4.4. Non-dimensional flexibilities coefficients (Cmsn, Section method)

Since the shearing force does not contribute to the opening mode of the crack, the compliance matrix, in relation to displacement vector, can be written as

$$c=\begin{bmatrix}c_{11} & 0 & c_{13}\\ 0 & c_{22} & 0\\ c_{31} & 0 & c_{33}\end{bmatrix} \tag{4.9}$$

The inverse of the compliance matrix c^{-1} as the stiffness matrix of the nodal point can be used to further analysis and given as

$$k_f = c^{-1} \tag{4.10}$$

4.3.2 Stiffness matrix for a beam finite element

For general loading, a local stiffness matrix relates forces to displacements. According to Okamura et al [7], cracked element can be separated at the cracked section and both portions may be connected by a spring with spring constants D_M, D_S, D_N, corresponding to bending moment M, shear force S and axial force N, respectively. As an extension version of stiffness matrices of Nobile and Viola [11], for a beam finite element subjected to general plane loading, including bending moment M, shearing force S and axial force N, the strain energy of a beam element without crack is

$$E_s = \frac{1}{2EI}\left(M^2 l - MSl^2 + \frac{S^2 l^3}{3}\right) + \frac{1}{2}\frac{N^2 l}{EA} + \frac{1}{2}\frac{S^2 l}{\mu\Lambda} \tag{4.11}$$

where E is the Young's modulus, μ is the shear modulus, l is the length of the beam element, A is the area of the cross section and $\Lambda = A/\kappa$, a coefficient depends on the shear coefficient κ which $\kappa = 9/10$ is for circular section. [12]

The flexibility matrices of uncracked element with constrains Fig.4.1 may be calculated by means of Castigliano's theorem

$$c_{ij} = \partial^2 E_s / \partial P_i \partial P_j \qquad i, j = 1,2,3,4,5,6 \tag{4.12}$$

$$c^e = \begin{bmatrix} c_{11} & 0 & 0 & c_{14} & 0 & 0 \\ 0 & c_{22} & c_{23} & 0 & c_{25} & c_{26} \\ 0 & c_{32} & c_{33} & 0 & c_{35} & c_{36} \\ c_{41} & 0 & 0 & c_{44} & 0 & 0 \\ 0 & c_{52} & c_{53} & 0 & c_{55} & c_{56} \\ 0 & c_{62} & c_{63} & 0 & c_{65} & c_{66} \end{bmatrix} \tag{4.13}$$

The stiffness matrix for the uncracked element can be derived as

$$k^e = c^{e-1} \tag{4.14}$$

According to Eq. (4.14) and simple algebraic calculation, we obtain the uncracked element stiffness matrix expressed as

$$k^e = \begin{bmatrix} \frac{AE}{l} & 0 & 0 & \frac{-AE}{l} & 0 & 0 \\ 0 & \frac{12EI}{(1+\Gamma)l^3} & \frac{-6EI}{(1+\Gamma)l^2} & 0 & \frac{-12EI}{(1+\Gamma)l^3} & \frac{-6EI}{(1+\Gamma)l^2} \\ 0 & \frac{-6EI}{(1+\Gamma)l^2} & \frac{(4+\Gamma)EI}{(1+\Gamma)l} & 0 & \frac{6EI}{(1+\Gamma)l^2} & \frac{(2-\Gamma)EI}{(1+\Gamma)l} \\ \frac{-AE}{l} & 0 & 0 & \frac{AE}{l} & 0 & 0 \\ 0 & \frac{-12EI}{(1+\Gamma)l^3} & \frac{6EI}{(1+\Gamma)l^2} & 0 & \frac{12EI}{(1+\Gamma)l^3} & \frac{6EI}{(1+\Gamma)l^2} \\ 0 & \frac{-6EI}{(1+\Gamma)l^2} & \frac{(2-\Gamma)EI}{(1+\Gamma)l} & 0 & \frac{6EI}{(1+\Gamma)l^2} & \frac{(4+\Gamma)EI}{(1+\Gamma)l} \end{bmatrix} \tag{4.15}$$

where $\Gamma = \frac{12\kappa EI}{\mu A l^2}$ is for Timoshenko beams. If setting $\Gamma = 0$ is the stiffness matrix reduced to elements of the classical Euler-Bernoulli beam model.

4.3.3 Mass matrix for a beam finite element

The mass matrices can be derived by using the Kinetic energy of the beam element of length l

$$E_k = \frac{1}{2}\int_0^l \rho A\left(\frac{\partial r}{\partial t}\right)^2 dx + \frac{1}{2}\int_0^l \rho A\left(\frac{\partial h}{\partial t}\right)^2 dx + \frac{1}{2}\int_0^l \rho I\left(\frac{\partial \theta}{\partial t}\right)^2 dx \tag{4.16}$$

where ρ is the mass density of the material, A is the area of cross section, I is the area moment of inertia and r, h and θ are the translational displacement of axial and shearing force and rotation of bending, respectively. The total mass matrix of the finite element is

$$\mathrm{m^e} = \mathrm{m_r} + \mathrm{m_h} + \mathrm{m_\theta} \tag{4.17}$$

The consistent translational $\mathrm{m_r}$ and $\mathrm{m_h}$ and rotational $\mathrm{m_\theta}$ mass matrices are assumed the same both for cracked and uncracked elements. Letting

$$\mathrm{m_t} = \mathrm{m_r} + \mathrm{m_h} \tag{4.18}$$

where $\mathrm{m_t}$ is the total translational mass matrix, Eq. (4.17) yields

$$\mathrm{m^e} = \mathrm{m_t} + \mathrm{m_\theta} \tag{4.19}$$

The following mass matrices will be derived

$$m_t = \frac{\rho A l}{(1+\Gamma)^2}\begin{bmatrix} \frac{(1+\Gamma)^2}{3} & 0 & 0 & \frac{(1+\Gamma)^2}{6} & 0 & 0 \\ & \frac{13}{35}+\frac{7\Gamma}{10}+\frac{\Gamma^2}{3} & \left(\frac{11}{210}+\frac{11\Gamma}{120}+\frac{\Gamma^2}{24}\right)l & 0 & \frac{9}{70}+\frac{3\Gamma}{10}+\frac{\Gamma^2}{6} & -\left(\frac{13}{420}+\frac{3\Gamma}{40}+\frac{\Gamma^2}{24}\right)l \\ & & \left(\frac{1}{105}+\frac{\Gamma}{60}+\frac{\Gamma^2}{120}\right)l^2 & 0 & \left(\frac{13}{420}+\frac{3\Gamma}{40}+\frac{\Gamma^2}{24}\right)l & -\left(\frac{1}{140}+\frac{\Gamma}{60}+\frac{\Gamma^2}{120}\right)l^2 \\ & & & \frac{(1+\Gamma)^2}{3} & 0 & 0 \\ & symm & & & \frac{13}{35}+\frac{7\Gamma}{10}+\frac{\Gamma^2}{3} & -\left(\frac{11}{210}+\frac{11\Gamma}{120}+\frac{\Gamma^2}{24}\right)l \\ & & & & & \left(\frac{1}{105}+\frac{\Gamma}{60}+\frac{\Gamma^2}{120}\right)l^2 \end{bmatrix} \tag{4.20}$$

$$m_\theta = \frac{\rho I}{l(1+\Gamma)^2}\begin{bmatrix} 0 & 0 & 0 & 0 & 0 & 0 \\ & \frac{6}{5} & \left(\frac{1}{10}-\frac{\Gamma}{2}\right)l & 0 & -\frac{6}{5} & \left(\frac{1}{10}-\frac{\Gamma}{2}\right)l \\ & & \left(\frac{2}{15}+\frac{\Gamma}{6}+\frac{\Gamma^2}{3}\right)l^2 & 0 & -\left(\frac{1}{10}-\frac{\Gamma}{2}\right)l & -\left(\frac{1}{30}+\frac{\Gamma}{6}-\frac{\Gamma^2}{6}\right)l^2 \\ & & & 0 & 0 & 0 \\ & symm & & & \frac{6}{5} & -\left(\frac{1}{10}-\frac{\Gamma}{2}\right)l \\ & & & & & \left(\frac{2}{15}+\frac{\Gamma}{6}+\frac{\Gamma^2}{3}\right)l^2 \end{bmatrix} \tag{4.21}$$

The above mass matrices depend upon Γ and both these matrices reduce to the Euler-Bernoulli model by setting $\Gamma = 0$.

4.3.4 Numerical studies

Considering a Timoshenko cantilever beam with circular cross section, the geometrical properties of the beam are length $L = 1m$, slenderness ratio $R/L = 0.1$, Young's modulus $E = 210 \times 10^9 N/m^2$, Poisson's ratio $\nu = 0.33$ and mass density $\rho = 7.9 \times 10^3 kg/m^3$, shear coefficient $\chi = 10/9$. The cantilever beam discretized into 40 finite elements and the numerical results are expressed in terms of the following dimensionless parameters: $A_n^n = A_n^*/A_{n0}^*$ is the displacement amplitude ratio, where A_n^* is the n^{th} computed displacement amplitude of the cracked structure, and A_{n0}^* is the n^{th} exact displacement amplitude of the corresponding uncracked structure, $d = L1/L = 0.2, 0.4, 0.6$ is the dimensionless crack position parameter and $\eta = a/D = 0.2, 0.4, 0.6$ is the crack depth ratio.

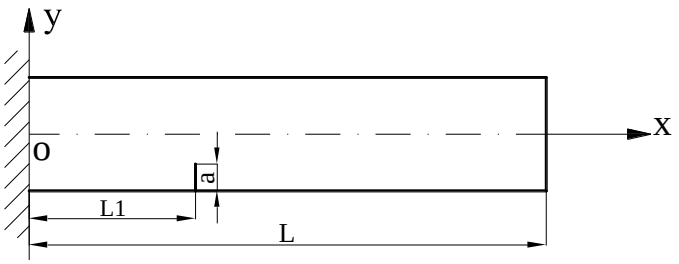

Fig.4.5. Cantilever beam with a transverse crack

The results obtained by the present work for slenderness ratio 0.1, crack depth ratio 0.4 and crack position 0.4 are compared with uncracked beam, and those of Kisa and Gurel [6], and as is noticed from Fig.4.6, an excellent concurrence has been found to belong the results.

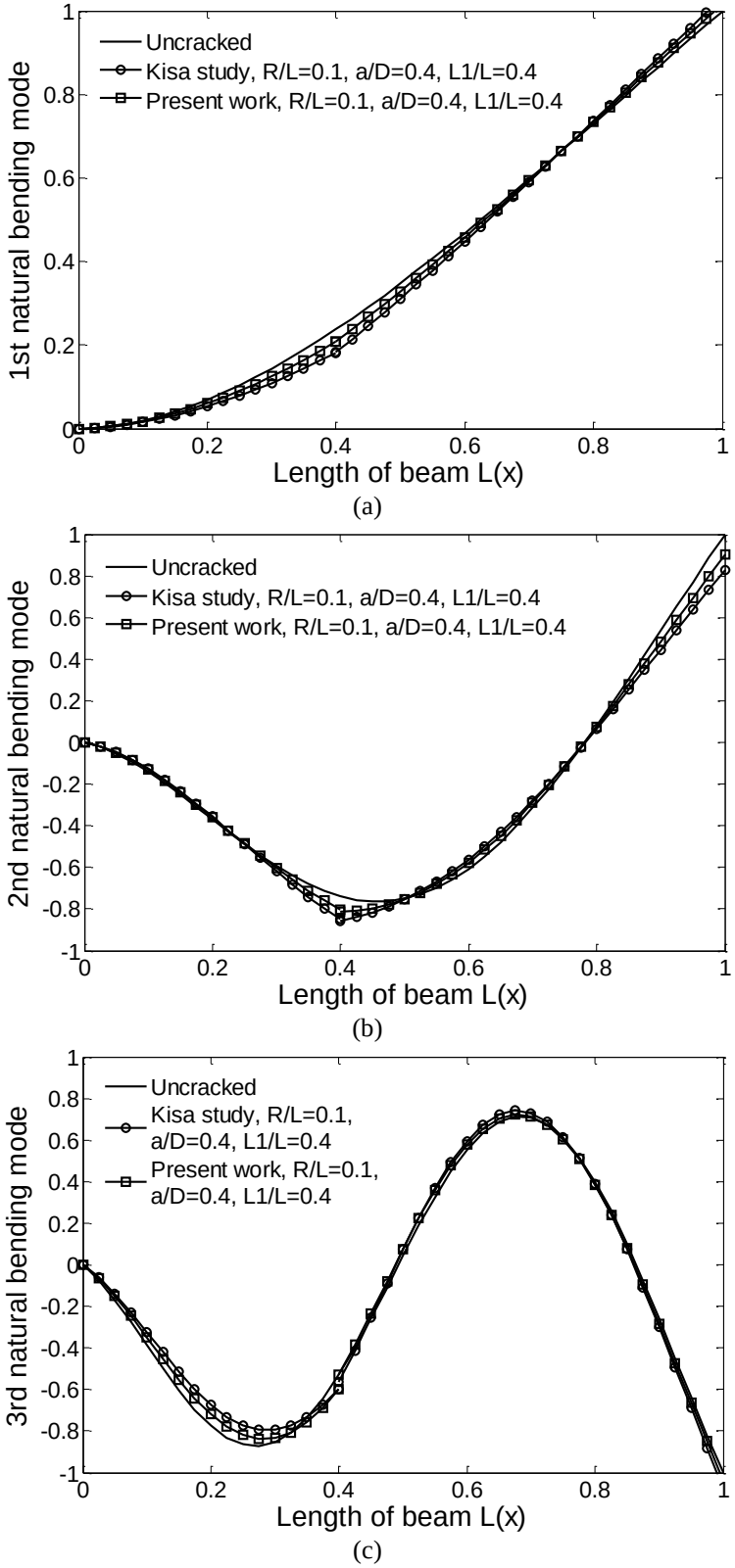

Fig. 4.6. Comparisons of non-dimensional natural bending modes for crack depth ratio $a/D = 0.4$, crack slenderness ratio $R/L = 0.1$, crack location $L1/L = 0.4$, (a) the first mode, (b) the second mode, (c) the third mode

Figs.4.7-4.11 illustrating the first fifth natural bending mode shapes as a function of crack depth ratio for crack locations $L1/L = 0.2,0.4, 0.6$ and slenderness ratio $R/L = 0.1$. The deeper the crack and higher the mode number, the clearer the position of crack, as is expected.

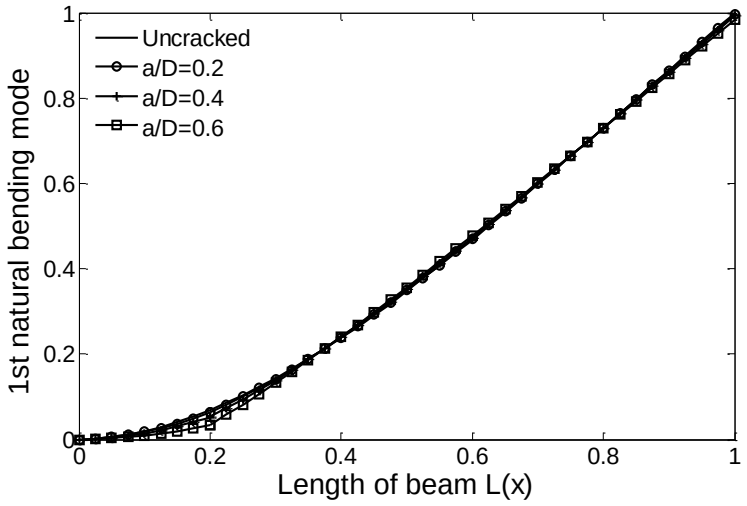

(a)

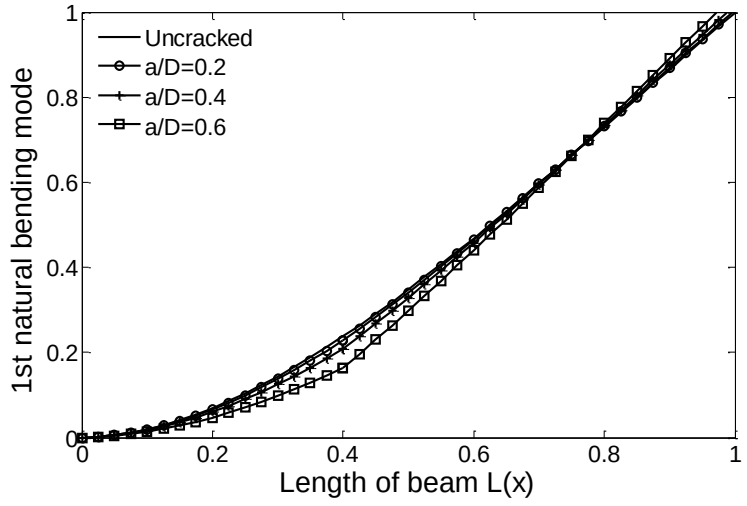

(b)

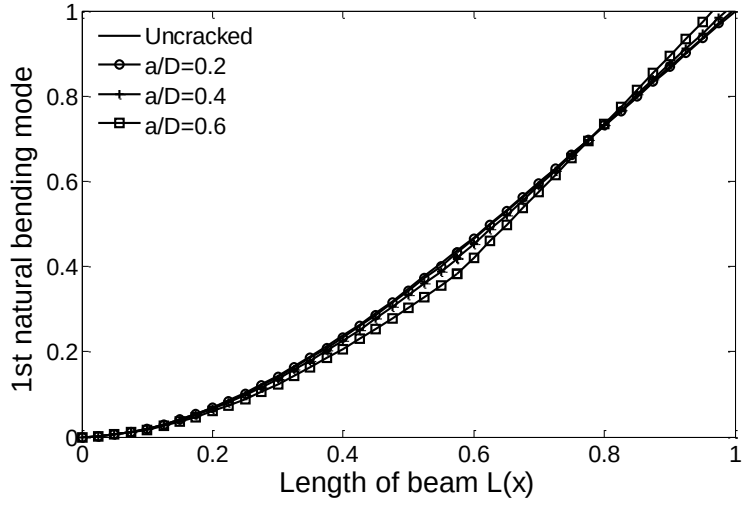

(c)

Fig. 4.7 First natural bending mode as a function of depth, for slenderness ratio $R/L = 0.1$, and different crack position (a) $L1/L = 0.2$, (b) $L1/L = 0.4$, (c) $L1/L = 0.6$.

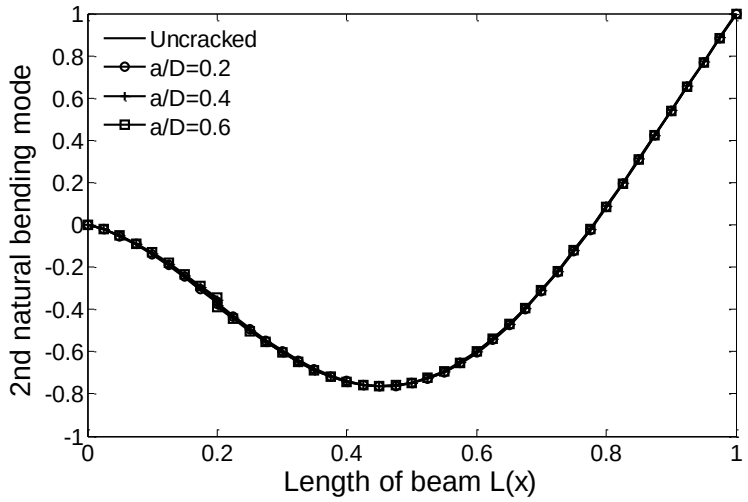

(a)

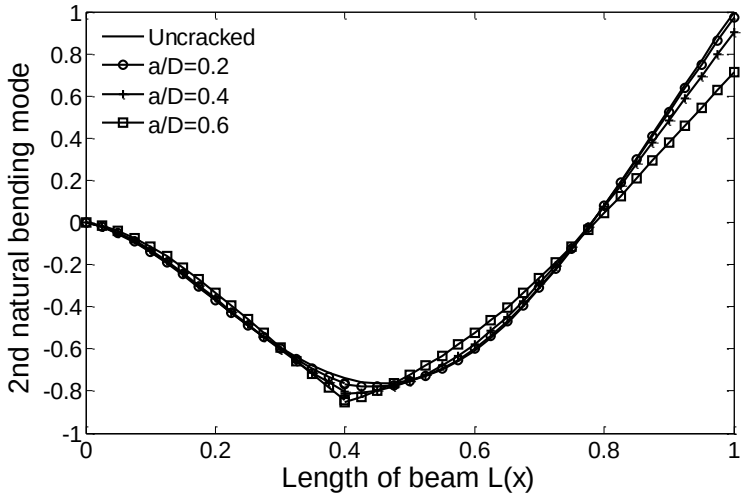

(b)

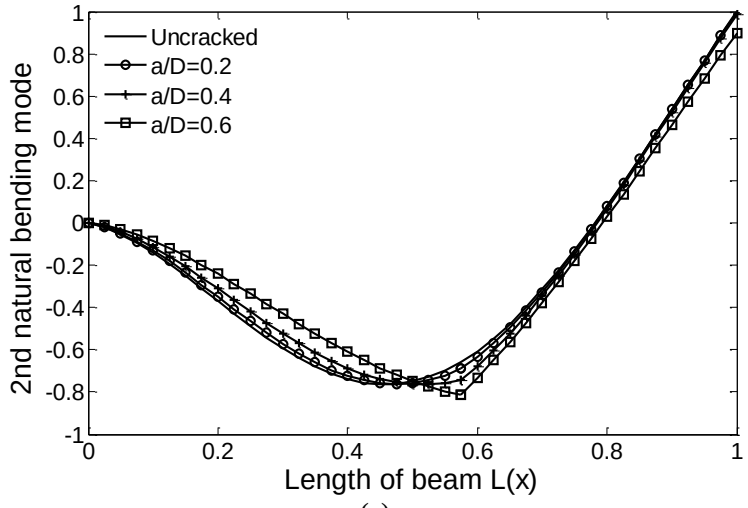

(c)

Fig. 4.8 The second natural bending mode as a function of depth, for slenderness ratio $R/L = 0.1$, and different crack position (a) $L1/L = 0.2$, (b) $L1/L = 0.4$, (c) $L1/L = 0.6$.

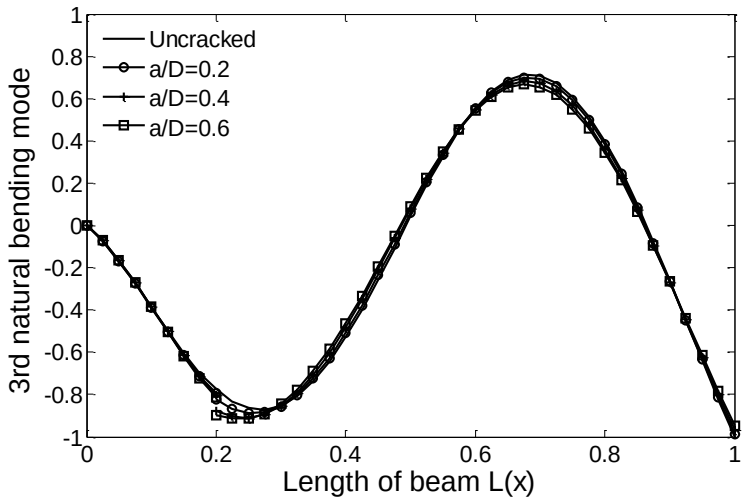

(a)

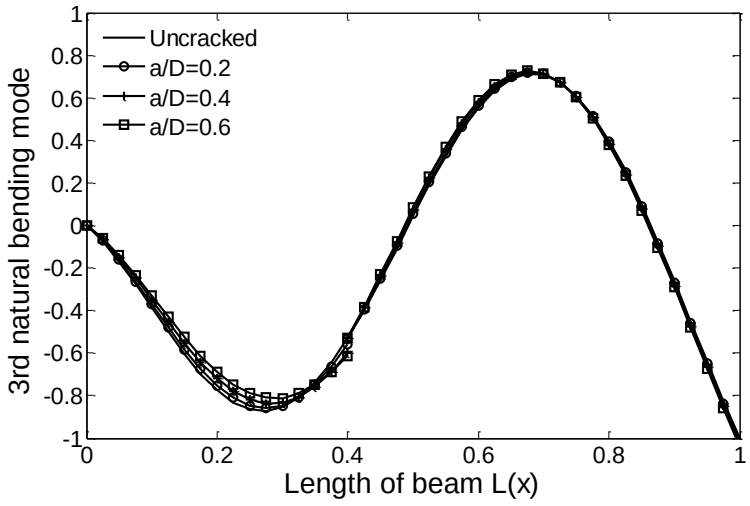

(b)

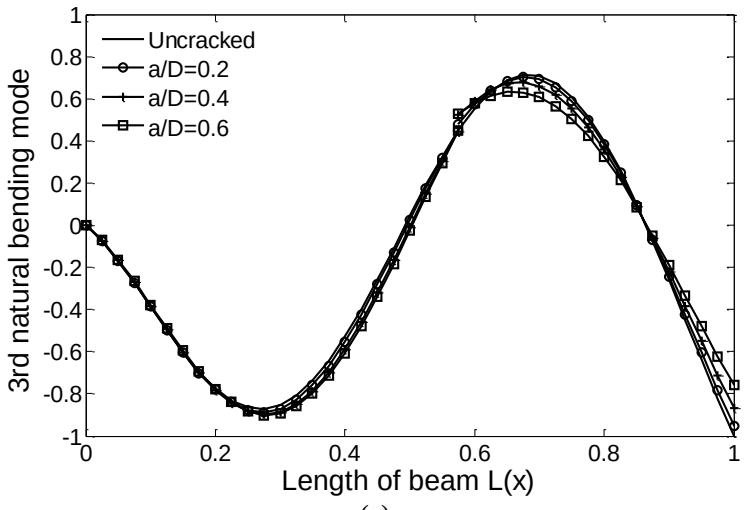

(c)

Fig. 4.9 Third natural bending mode as a function of depth, for slenderness ratio $R/D = 0.1$, and different crack position (a) $L1/L = 0.2$, (b) $L1/L = 0.4$, (c) $L1/L = 0.6$.

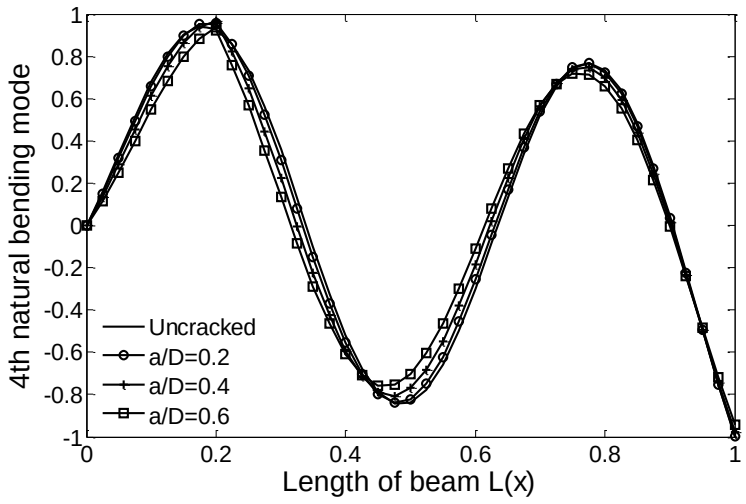

(a)

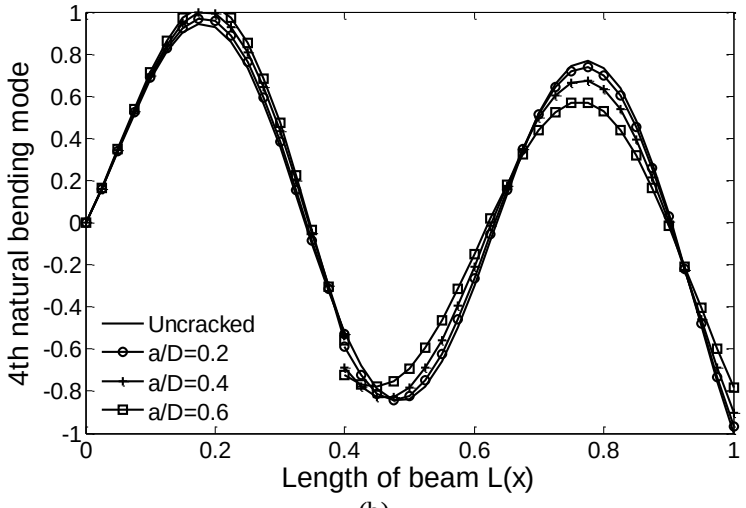

(b)

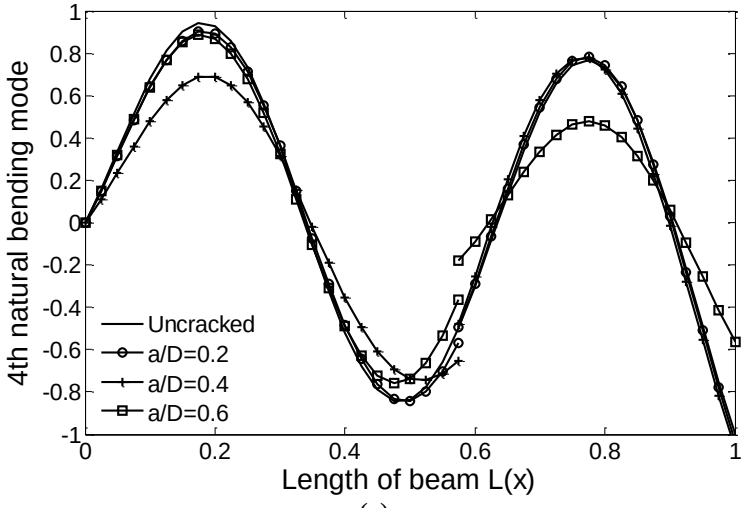

(c)

Fig. 4.10 Fourth natural bending mode as a function of depth, for slenderness ratio $R/D = 0.1$, and different crack position (a) $L1/L = 0.2$, (b) $L1/L = 0.4$, (c) $L1/L = 0.6$.

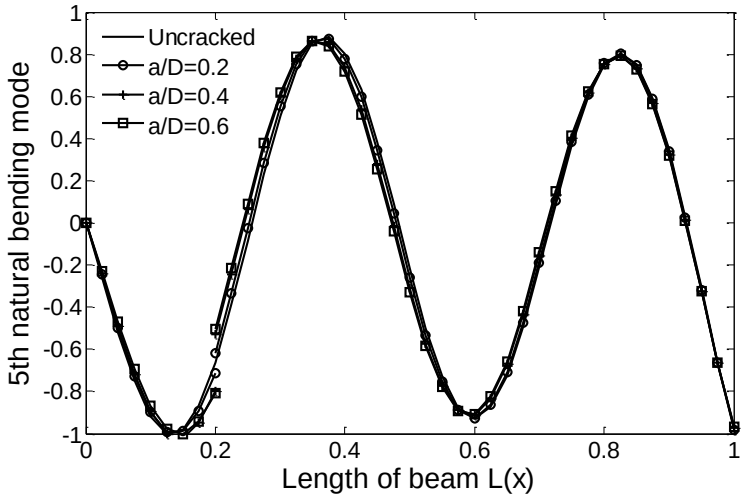

(a)

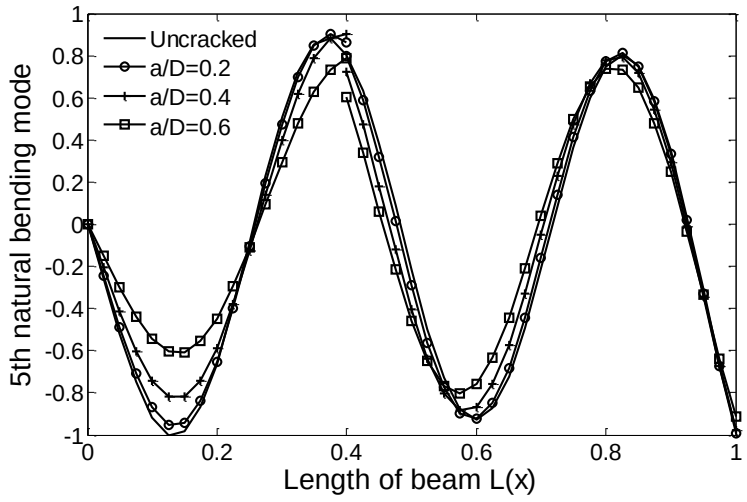

(b)

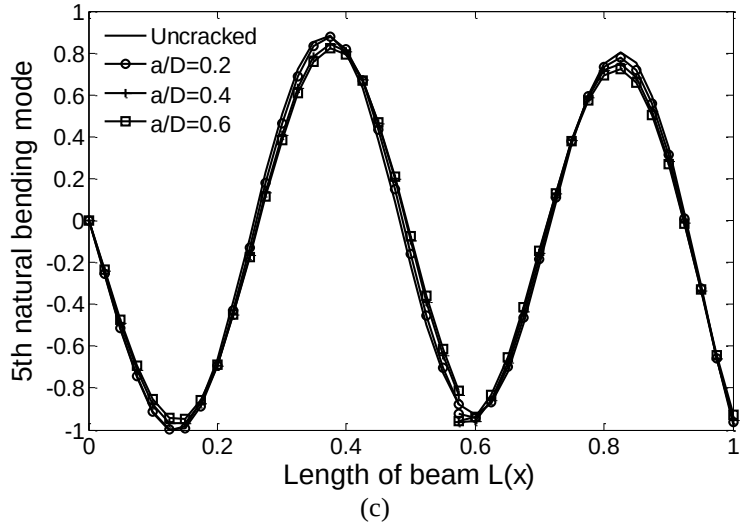

(c)

Fig. 4.11 Fifth natural bending mode as a function of depth, for slenderness ratio $R/D = 0.1$, and different crack position (a) $L1/L = 0.2$, (b) $L1/L = 0.4$, (c) $L1/L = 0.6$.

Figs.4.12-4.14 illustrate the modes of the first, second and third flexural vibration, respectively. As expected the modes for cracked shaft show discontinuities at the crack location. It is apparent that the change in mode shape can become an efficient sign for crack identification. It can be clearly ob-

served that as the crack progresses, the discontinuities show progressively large difference which can be used to identify the depth of the crack.

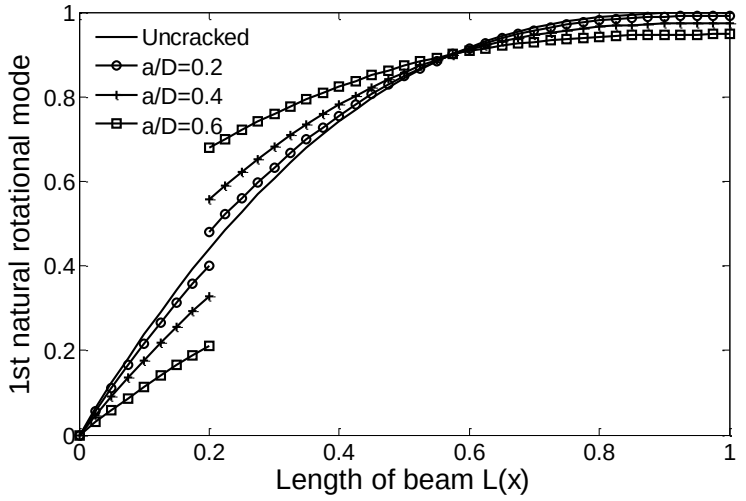

(a)

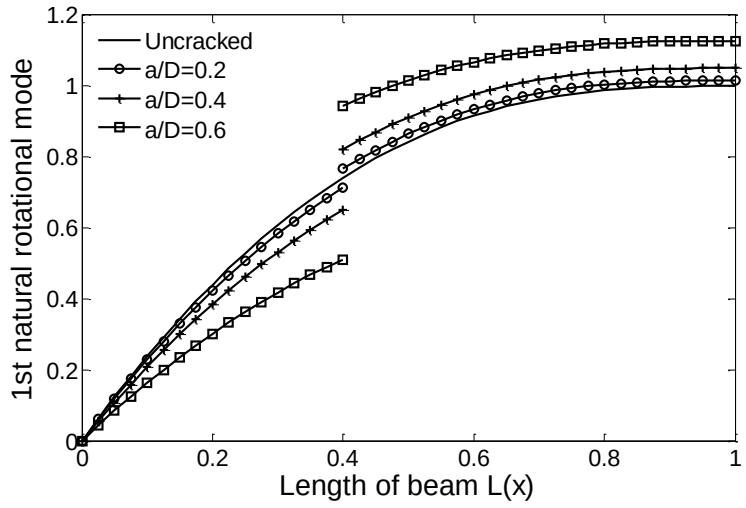

(b)

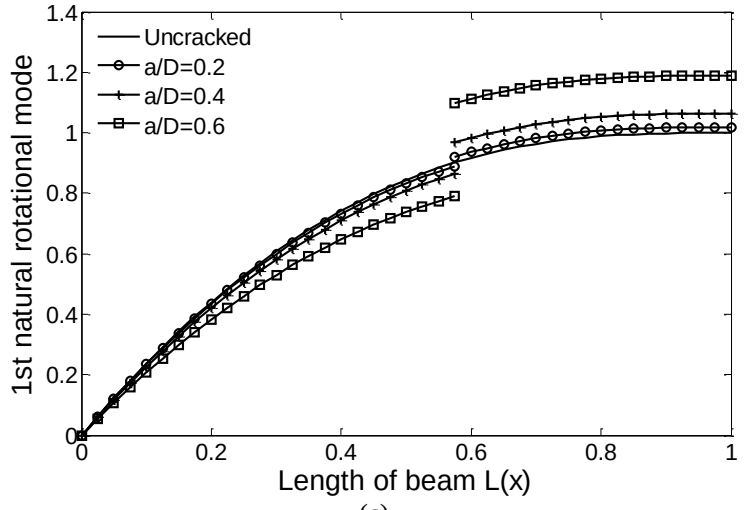

(c)

Fig. 4.12. First natural rotational mode as a function of depth, for slenderness ratio $R/D = 0.1$, and different crack position (a) $L1/L = 0.2$, (b) $L1/L = 0.4$, (c) $L1/L = 0.6$.

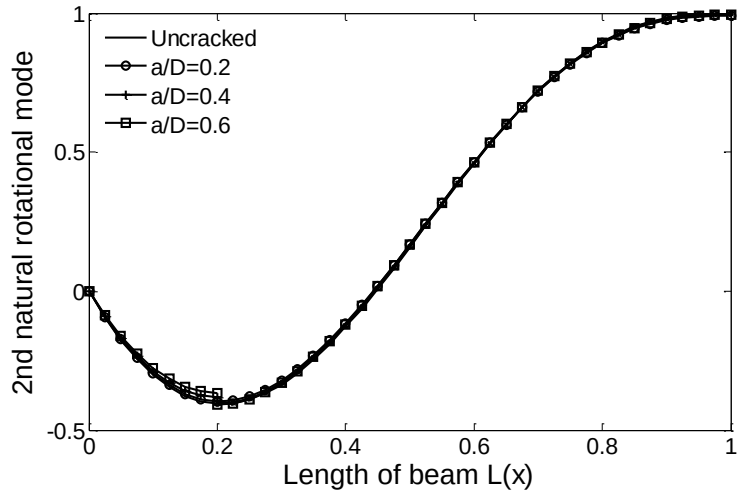

(a)

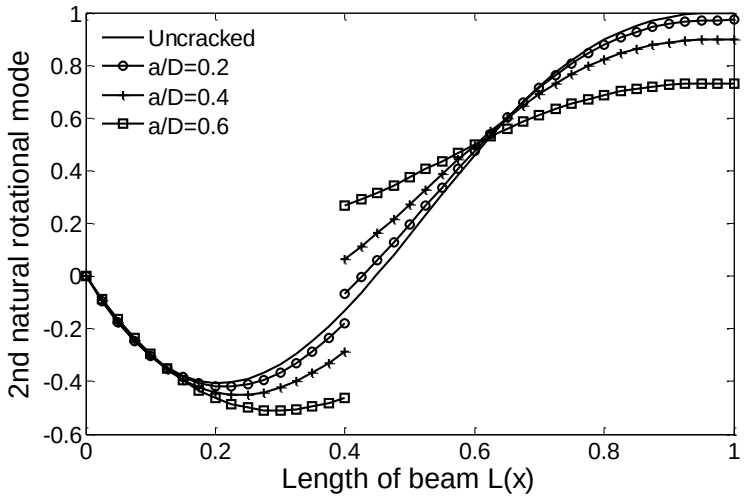

(b)

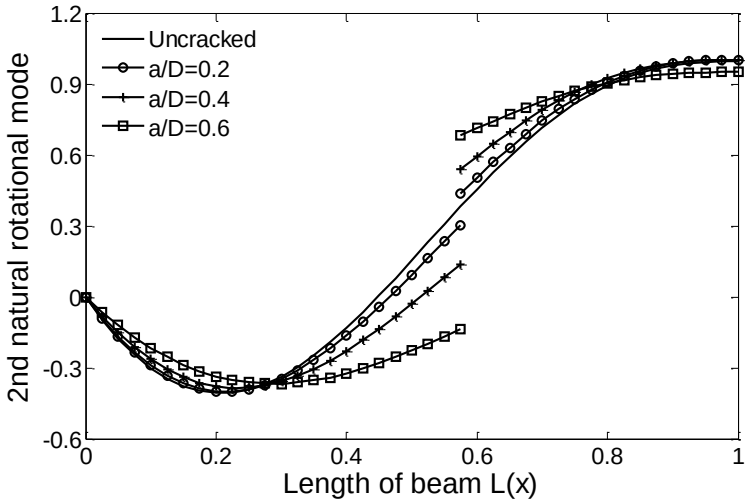

(c)

Fig.4.13. Second natural rotational mode as a function of depth, for slenderness ratio $R/D = 0.1$, and different crack position (a) $L1/L = 0.2$, (b) $L1/L = 0.4$, (c) $L1/L = 0.6$.

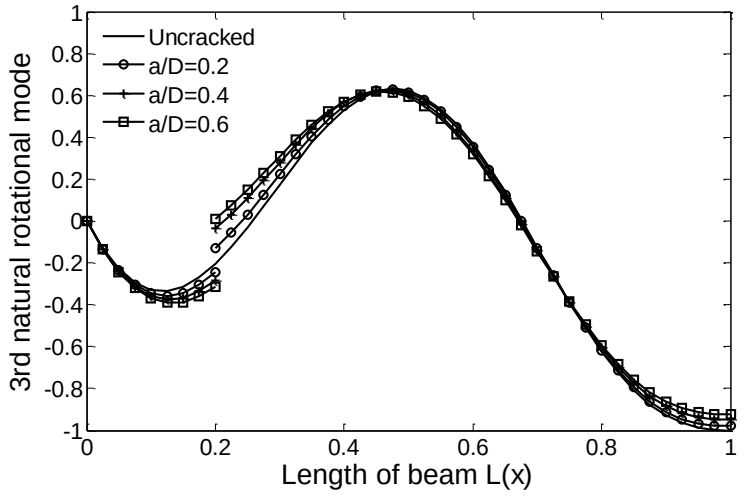

(a)

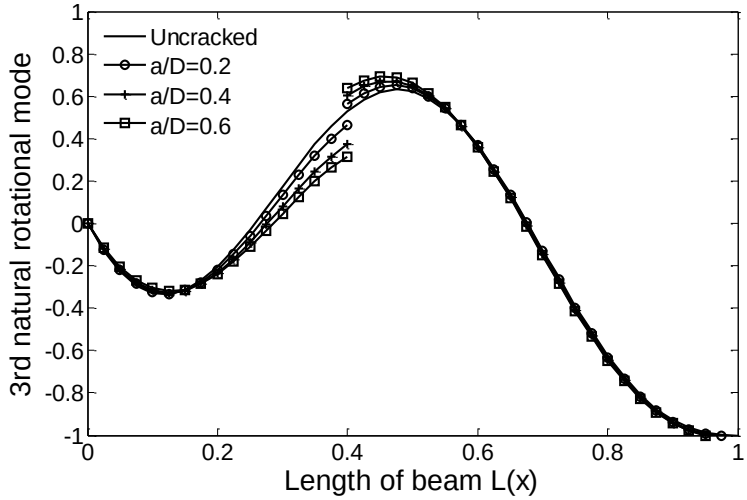

(b)

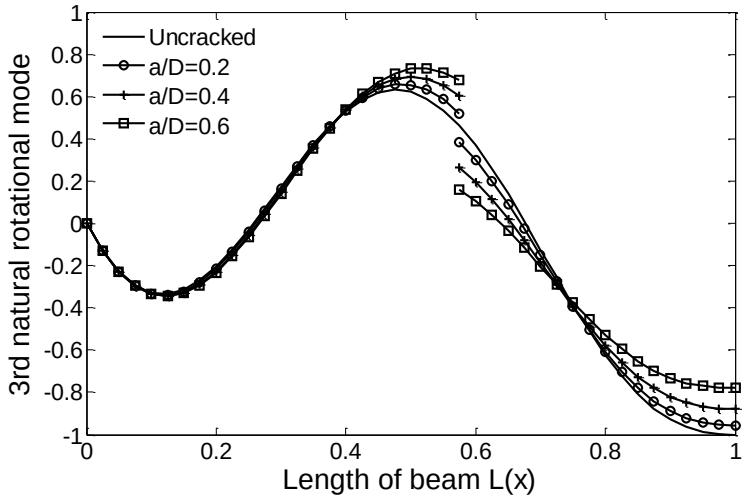

(c)

Fig. 4.14. Third natural rotational mode as a function of depth, for slenderness ratio $R/D = 0.1$, and different crack position (a) $L1/L = 0.2$, (b) $L1/L = 0.4$, (c) $L1/L = 0.6$.

The same situation is observed for the longitudinal vibration, as is show in Figs.4.15-4.17 for the previous first three modes, although, one of the three modes as the crack location L1/L=0.2 just on the dip of the amplitude, is excepted.

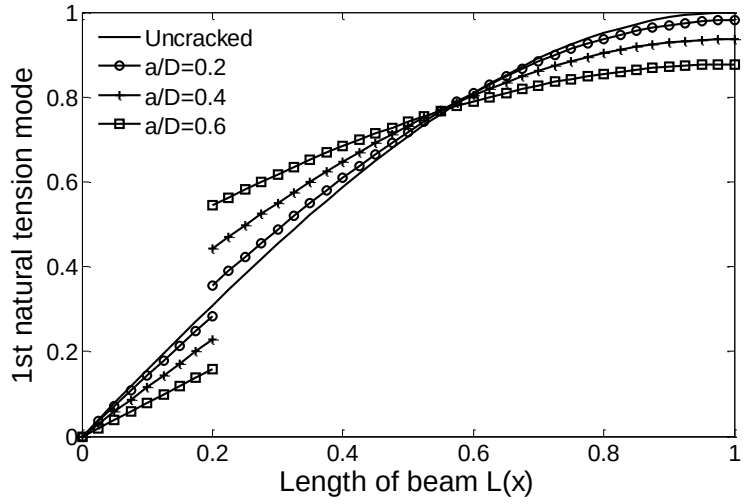

(a)

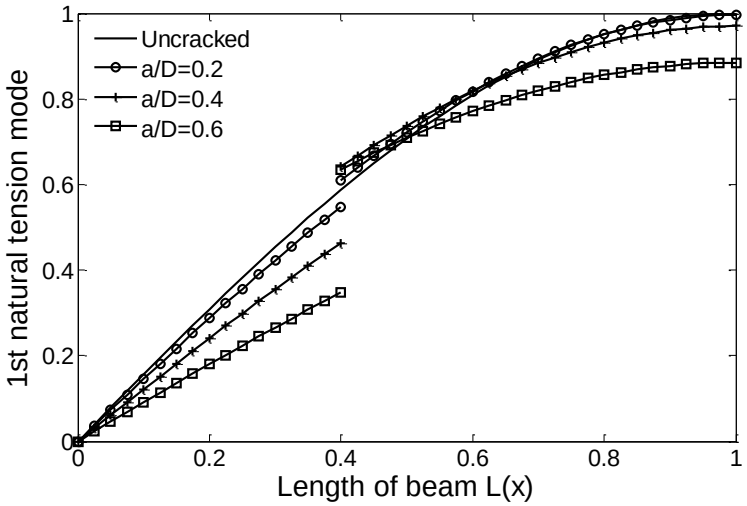

(b)

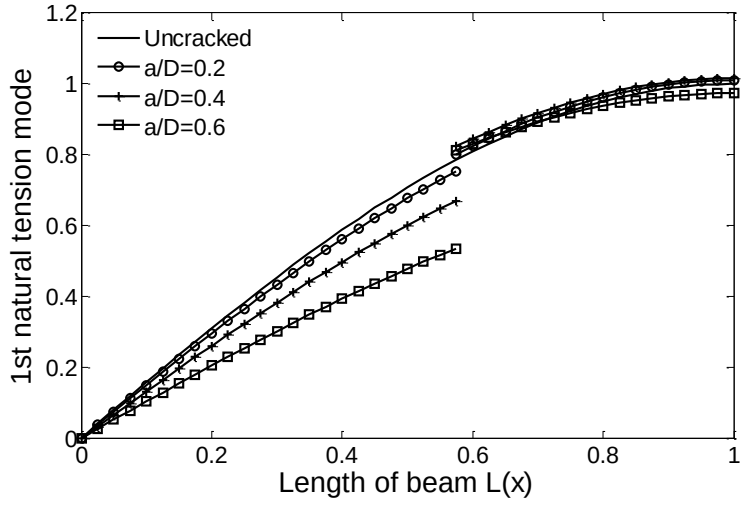

(c)

Fig. 4.15. First natural tension mode as a function of depth, for slenderness ratio $R/D = 0.1$, and different crack position (a) $L1/L = 0.2$, (b) $L1/L = 0.4$, (c) $L1/L = 0.6$.

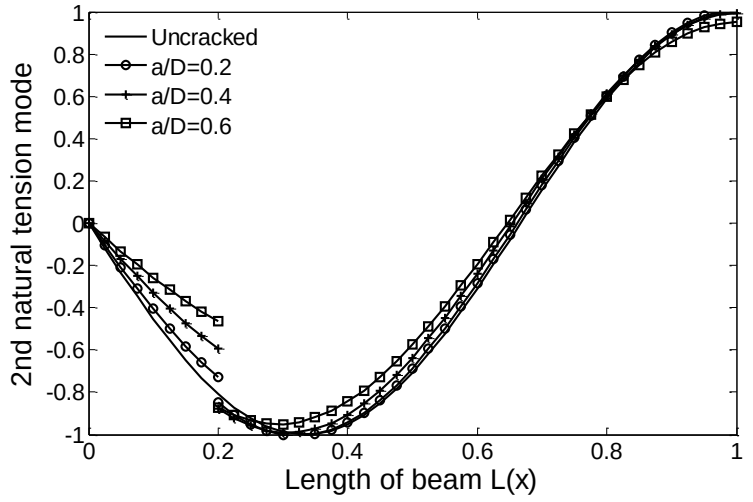

(a)

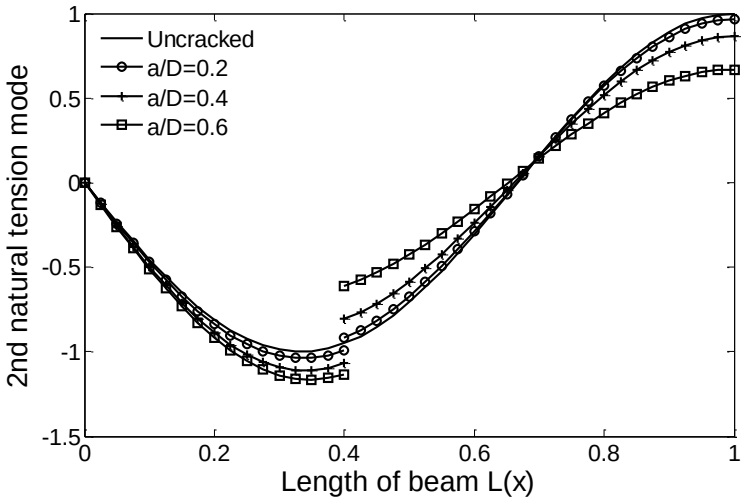

(b)

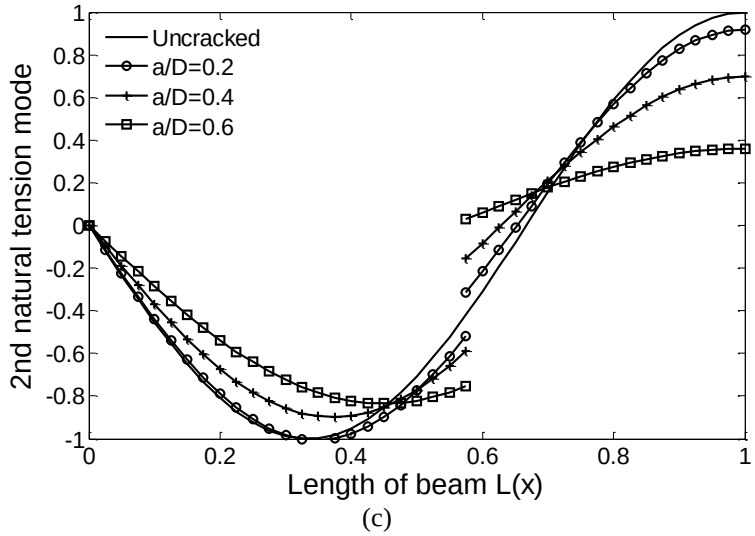

(c)

Fig. 4.16. Second natural tension mode as a function of depth, for slenderness ratio $R/D = 0.1$, and different crack position (a) $L1/L = 0.2$, (b) $L1/L = 0.4$, (c) $L1/L = 0.6$.

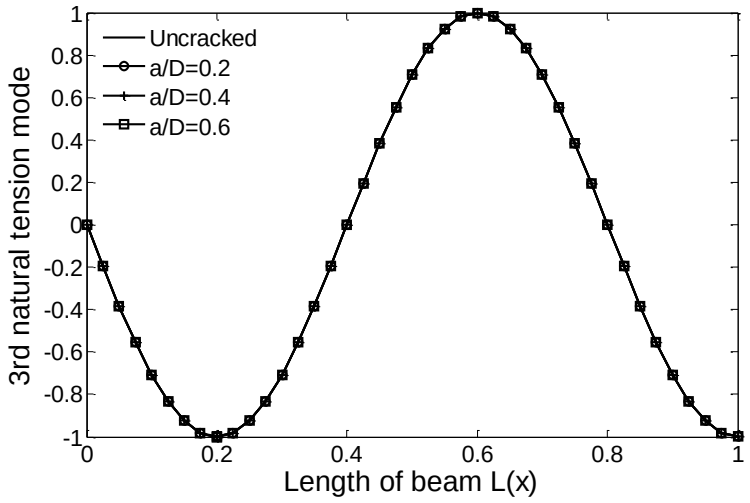

(a)

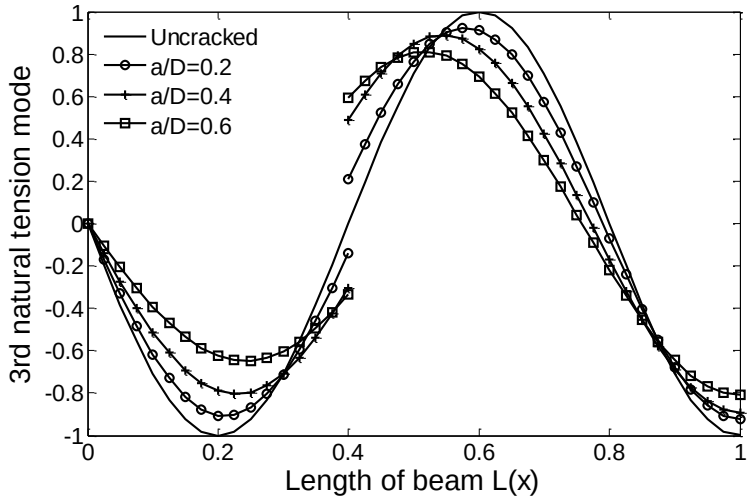

(b)

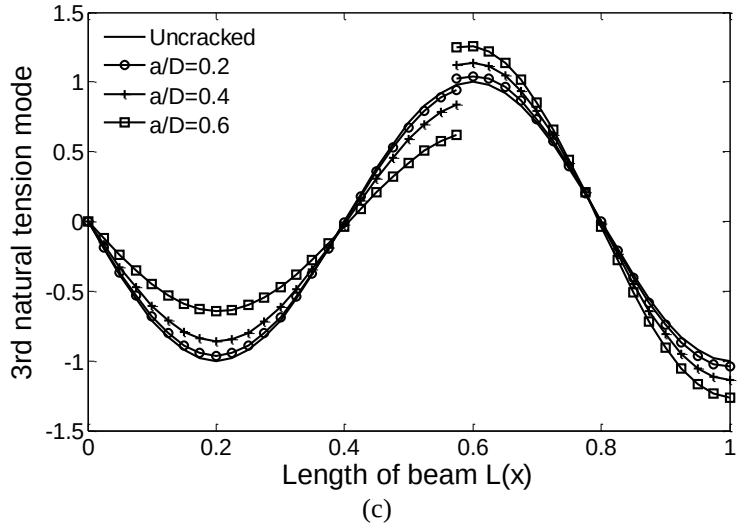

(c)

Fig. 4.17. Third natural tension mode as a function of depth, for slenderness ratio $R/D = 0.1$, and different crack position (a) $L1/L = 0.2$, (b) $L1/L = 0.4$, (c) $L1/L = 0.6$.

4.4 Cantilever cracked beam subjected to bending moment, shear force, and torque

4.4.1 Stiffness matrix of the line-spring

As mentioned in section 4.2, a schematic illustration of the line-spring model for edge-cracked beam is given in Fig. 4.1. The line-spring model features with two nodes and zero length, therefore the shearing force S does not interact with the bending moment. The compliance matrix for the line-spring model can be derived according to the theory presented by Okamura et al [7] and Carpinteri et al [8] which based on the relationship between load and deflection. The static equilibrium of a cantilever cracked beam subjected to bending moment M, shearing force S and torque T requires that

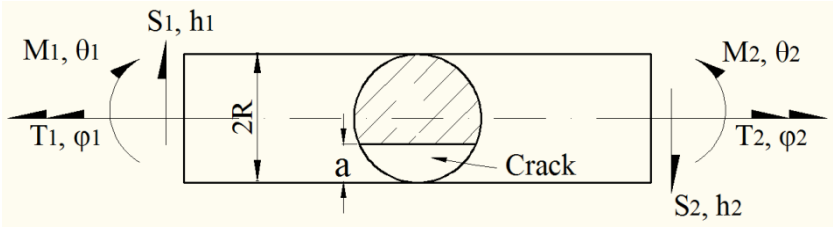

Fig.4.18. End conditions for forces and displacement of the beam element.

$$\theta = \lambda_{mm} M \ , \ h = \lambda_{ss} S \ , \ \varphi = \lambda_{tt} T \tag{4.22}$$

in which the rotations θ and φ and the deflection h across the line-spring are expressed in terms of the nodal displacements $\theta = \theta_1 - \theta_2$, $\varphi = \varphi_1 - \varphi_2$ and $h = h_1 - h_2$ (see Fig.4.18). λ_{mm}, λ_{ss} and λ_{tt} are compliances for bending moment, shear force and torque, respectively.

Moreover, compliances are related to the connection between energy release rates $\mathcal{G}$ and stress intensity factors given by Irwin and Kies [13]. Compliances for the cracked beam element are derived by the following equations

$$G_m = \frac{1-\nu^2}{E} K_{I_M}^2 = \frac{M^2}{2} \frac{d\lambda_{mm}}{dA} \tag{4.23}$$

$$G_s = \frac{1-\nu^2}{E} K_{II_S}^2 = \frac{S^2}{2} \frac{d\lambda_{ss}}{dA} \tag{4.24}$$

$$G_T = \frac{1+\nu}{E} K_{III_T}^2 = \frac{T^2}{2} \frac{d\lambda_{tt}}{dA} \tag{4.25}$$

After integrating, the compliance components of line-spring are obtained by the following relations

$$\lambda_{mm} = \frac{2(1-\nu^2)}{E} \int_0^A \left(\frac{K_{I_M}}{M} \right)^2 dA \tag{4.26}$$

$$\lambda_{ss} = \frac{2(1-\nu^2)}{E}\int_0^A \left(\frac{K_{II_S}}{S}\right)^2 dA \tag{4.27}$$

$$\lambda_{tt} = \frac{2(1+\nu)}{E}\int_0^A \left(\frac{K_{III_T}}{T}\right)^2 dA \tag{4.28}$$

where E is Young's modulus, ν equals Poisson's ratio for plane-strain and zero for plane-stress, dA is an infinitesimal incremental of crack area, K_{I_M} is the Mode I stress intensity factor caused by bending moment M, K_{II_S} is the Mode II stress intensity factor caused by shear force S, and K_{III_T} is Mode III stress intensity factor caused by the torque T. The details of the stress intensity factors can be found in section 2.2, Chapter 2.

Substituting the stress intensity factors into Eqs (4.26) to (4.28), the local flexibility due to the crack can be obtained as the same geometrical boundary limit in the foregoing section, and can be written as

$$\lambda_{mm} = \frac{2(1-\nu^2)}{ER^5}\int_0^a \int_{-h_y}^{h_y} F_M^2(z/D)dxdz \tag{4.29}$$

$$\lambda_{ss} = \frac{2(1-\nu^2)}{ER^3}\int_0^a \int_{-h_y}^{h_y} F_S^2(z/D)dxdz \tag{4.30}$$

$$\lambda_{tt} = \frac{2(1+\nu)}{ER^5}\int_0^a \int_{-h_y}^{h_y} F_T^2(z/D)dxdz \tag{4.31}$$

The numerical integration methods are adopted here. Dimensionless flexibility coefficients are calculated numerically along with the subsequent expressions and drawn in Fig.4.19.

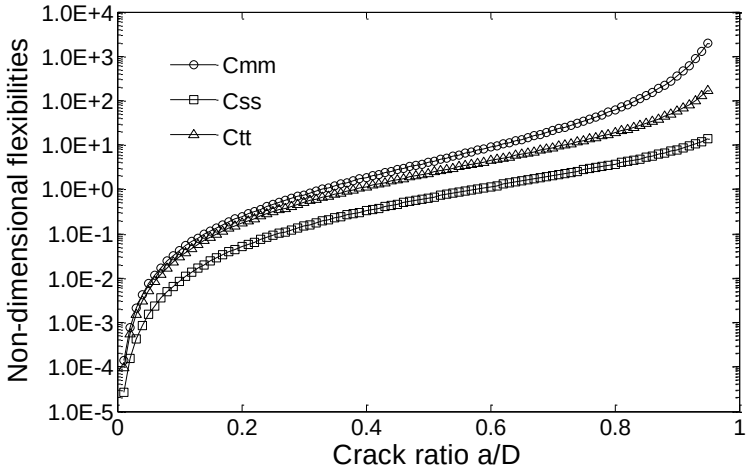

Fig. 4.19. Non-dimensional compliance coefficients as a function of the crack depth ratio a/D.

$$\lambda_{mm}^* = E' R^3 \lambda_{mm} \tag{4.32}$$

$$\lambda_{ss}^{*} = E' R \lambda_{ss} \tag{4.33}$$

$$\lambda_{tt}^{*} = E' R^{3} \lambda_{tt} \tag{4.34}$$

The matrix of rigidity of the cracked element puts the vector of the nodal displacements $q_c = [h_1, \theta_1, \varphi_1, h_2, \theta_2, \varphi_2]$ in relation with the vector of the nodal forces $F_c = [S_1, M_1, T_1, S_2, M_2, T_2]$. The stiffness matrix of a line-spring k_f is given as follows

$$k_f = \begin{bmatrix} 1/\lambda_{ss} & 0 & 0 & -1/\lambda_{ss} & 0 & 0 \\ 0 & 1/\lambda_{mm} & 0 & 0 & -1/\lambda_{mm} & 0 \\ 0 & 0 & 1/\lambda_{tt} & 0 & 0 & -1/\lambda_{tt} \\ -1/\lambda_{ss} & 0 & 0 & 1/\lambda_{ss} & 0 & 0 \\ 0 & -1/\lambda_{mm} & 0 & 0 & 1/\lambda_{mm} & 0 \\ 0 & 0 & -1/\lambda_{tt} & 0 & 0 & 1/\lambda_{tt} \end{bmatrix} \tag{4.35}$$

4.4.2 Mass matrix and stiffness matrix of an uncracked beam element

The beam element will be assumed to be straight bar of uniform cross section capable of bending moment and shearing force in the plane of its cross section, and twisting moments about its centroidal axis. The stiffness matrix of such a beam element is of order 6×6 if all the forces are considered independently of each other. The stiffness properties for a uniform beam element will be derived directly from the differential equations for beam displacements used in the general engineering theory of beams subjected to loads. The derivation details of the stiffness can be found in the literature [14].

$$k^{e} = \begin{bmatrix} \frac{12EI}{(1+\Gamma)l^3} & \frac{6EI}{(1+\Gamma)l^2} & 0 & \frac{-12EI}{(1+\Gamma)l^3} & \frac{6EI}{(1+\Gamma)l^2} & 0 \\ \frac{6EI}{(1+\Gamma)l^2} & \frac{(4+\Gamma)EI}{(1+\Gamma)l} & 0 & \frac{-6EI}{(1+\Gamma)l^2} & \frac{(2-\Gamma)EI}{(1+\Gamma)l} & 0 \\ 0 & 0 & \frac{\mu J}{l} & 0 & 0 & \frac{-\mu J}{l} \\ \frac{-12EI}{(1+\Gamma)l^3} & \frac{-6EI}{(1+\Gamma)l^2} & 0 & \frac{12EI}{(1+\Gamma)l^3} & \frac{-6EI}{(1+\Gamma)l^2} & 0 \\ \frac{6EI}{(1+\Gamma)l^2} & \frac{(2-\Gamma)EI}{(1+\Gamma)l} & 0 & \frac{-6EI}{(1+\Gamma)l^2} & \frac{(4+\Gamma)EI}{(1+\Gamma)l} & 0 \\ 0 & 0 & \frac{-\mu J}{l} & 0 & 0 & \frac{\mu J}{l} \end{bmatrix} \tag{4.36}$$

where l is the length of the beam element, E is the Young's modulus, I is the moment of inertia of the cross section, J is the polar moment of inertia of the cross section, Γ represents shear deformation parameter. $\Gamma = 12\kappa EI/\mu A l^2$ is for Timoshenko beams. Γ can be taken as zero for the classical Euler-Bernoulli beam which leads to a force-displacement relationship in which the effects of shear deformations are neglected. μ represents shear modulus.

For the uncracked elements, the mass matrices can be derived by using the Kinetic energy of the beam element of length l

$$E_k = \frac{1}{2}\int_0^l \rho A\left(\frac{\partial h}{\partial t}\right)^2 dx + \frac{1}{2}\int_0^l \rho I\left(\frac{\partial \theta}{\partial t}\right)^2 dx + \frac{1}{2}\int_0^l \rho J\left(\frac{\partial \varphi}{\partial t}\right)^2 dx \tag{4.37}$$

where ρ is the mass density of the material, A is the area of cross section, I is the area moment of inertia, J is the polar moment of inertia, and h, θ and φ are the translational displacement of shearing force, rotation of bending and torque, respectively.

Let $m^e = m_t + m_\theta$ denotes the total mass matrix of the finite element with m_t the total mass matrix of translational mass inertia and torsional mass inertia, m_θ represents the rotatory inertia of the beam. They are firstly derived independently by Archer and by McCalley.

$$m_t = \frac{\rho A l}{(1+\Gamma)^2}\begin{bmatrix} \frac{13}{35}+\frac{7\Gamma}{10}+\frac{\Gamma^2}{3} & \left(\frac{11}{210}+\frac{11\Gamma}{120}+\frac{\Gamma^2}{24}\right)l & 0 & \frac{9}{70}+\frac{3\Gamma}{10}+\frac{\Gamma^2}{6} & -\left(\frac{13}{420}+\frac{3\Gamma}{40}+\frac{\Gamma^2}{24}\right)l & 0 \\ & \left(\frac{1}{105}+\frac{\Gamma}{60}+\frac{\Gamma^2}{120}\right)l^2 & 0 & \left(\frac{13}{420}+\frac{3\Gamma}{40}+\frac{\Gamma^2}{24}\right)l & -\left(\frac{1}{140}+\frac{\Gamma}{60}+\frac{\Gamma^2}{120}\right)l^2 & 0 \\ & & \frac{(1+\Gamma)^2 J}{3A} & 0 & 0 & \frac{(1+\Gamma)^2 J}{6A} \\ & & & \frac{13}{35}+\frac{7\Gamma}{10}+\frac{\Gamma^2}{3} & -\left(\frac{11}{210}+\frac{11\Gamma}{120}+\frac{\Gamma^2}{24}\right)l & 0 \\ & symm & & & \left(\frac{1}{105}+\frac{\Gamma}{60}+\frac{\Gamma^2}{120}\right)l^2 & 0 \\ & & & & & \frac{(1+\Gamma)^2 J}{3A} \end{bmatrix} \tag{4.38}$$

$$m_\theta = \frac{\rho I}{l(1+\Gamma)^2}\begin{bmatrix} \frac{6}{5} & \left(\frac{1}{10}-\frac{\Gamma}{2}\right)l & 0 & -\frac{6}{5} & \left(\frac{1}{10}-\frac{\Gamma}{2}\right)l & 0 \\ & \left(\frac{2}{15}+\frac{\Gamma}{6}+\frac{\Gamma^2}{3}\right)l^2 & 0 & -\left(\frac{1}{10}-\frac{\Gamma}{2}\right)l & -\left(\frac{1}{30}+\frac{\Gamma}{6}-\frac{\Gamma^2}{6}\right)l^2 & 0 \\ & & 0 & 0 & 0 & 0 \\ & & & \frac{6}{5} & -\left(\frac{1}{10}-\frac{\Gamma}{2}\right)l & 0 \\ & symm & & & \left(\frac{2}{15}+\frac{\Gamma}{6}+\frac{\Gamma^2}{3}\right)l^2 & 0 \\ & & & & & 0 \end{bmatrix} \tag{4.39}$$

4.4.3 Numerical studies

The example geometrical and material parameters are the same with those in section 4.3. Figs.4.20-4.24 showing the first five natural bending mode as a function of crack depth ratio for slenderness ratio R/D=0.1 and crack position L1/L=0.2, 0.4 and 0.6.

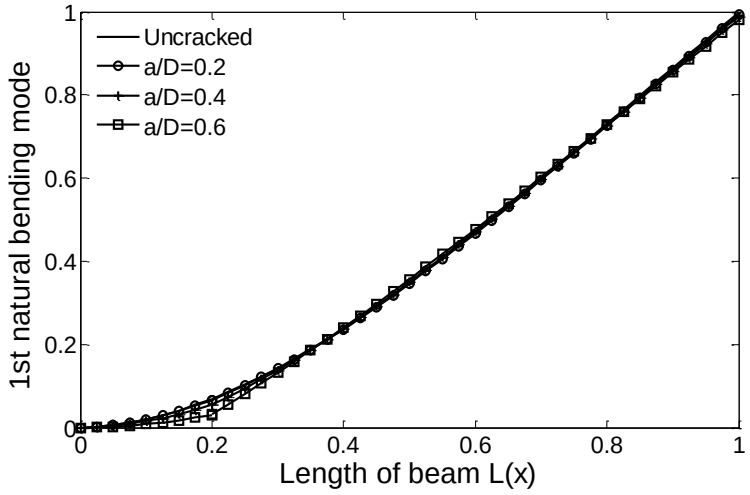

(a)

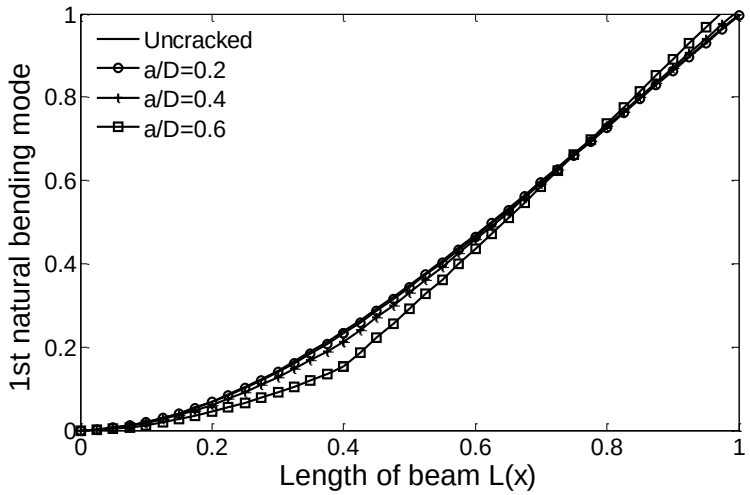

(b)

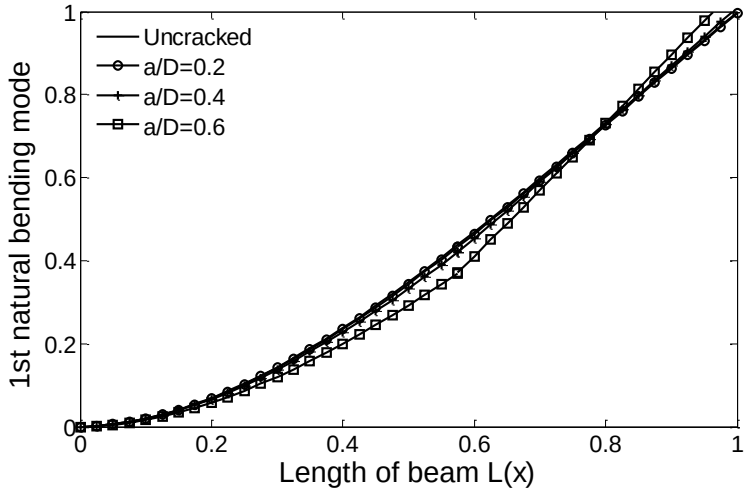

(c)

Fig. 4.20. First natural bending mode as a function of depth, for slenderness ratio $R/D = 0.1$, and different crack position (a) $L1/L = 0.2$, (b) $L1/L = 0.4$, (c) $L1/L = 0.6$.

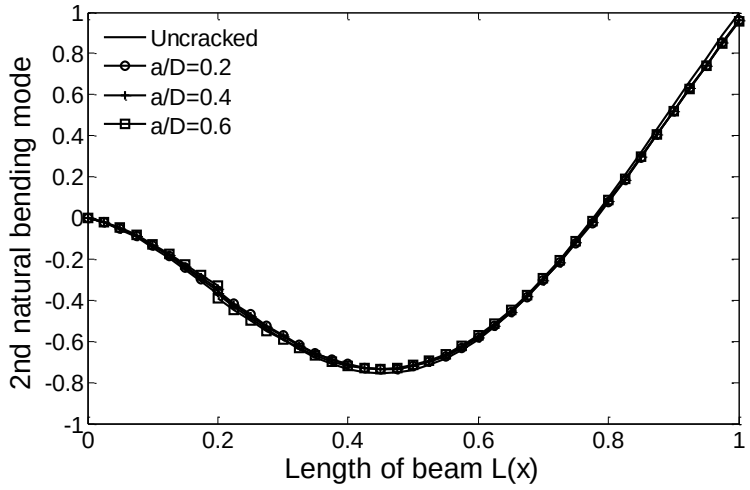

(a)

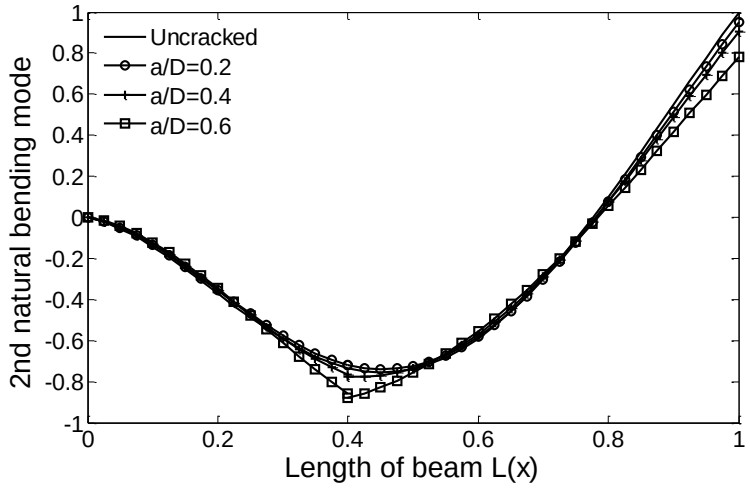

(b)

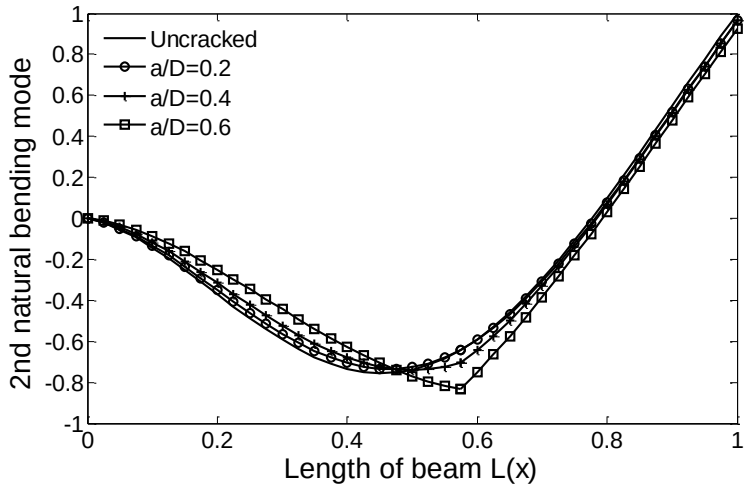

(c)

Fig. 4.21. Second natural bending mode as a function of depth, for slenderness ratio $R/D = 0.1$, and different crack position (a) $L1/L = 0.2$, (b) $L1/L = 0.4$, (c) $L1/L = 0.6$.

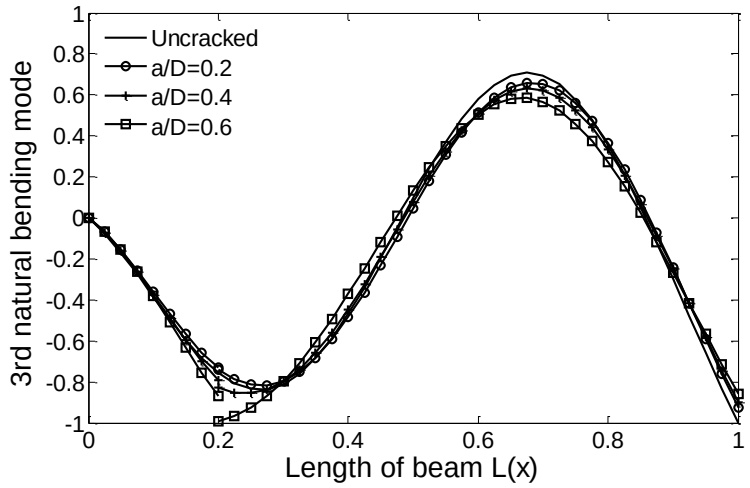

(a)

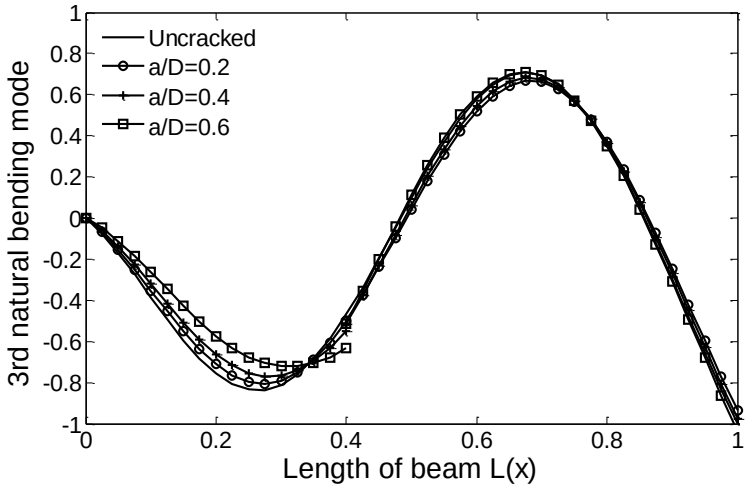

(b)

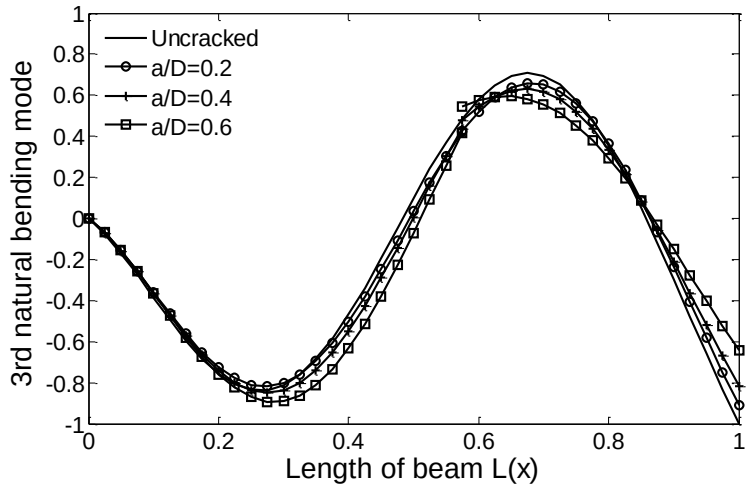

(c)

Fig. 4.22. Third natural bending mode as a function of depth, for slenderness ratio $R/D = 0.1$, and different crack position (a) $L1/L = 0.2$, (b) $L1/L = 0.4$, (c) $L1/L = 0.6$.

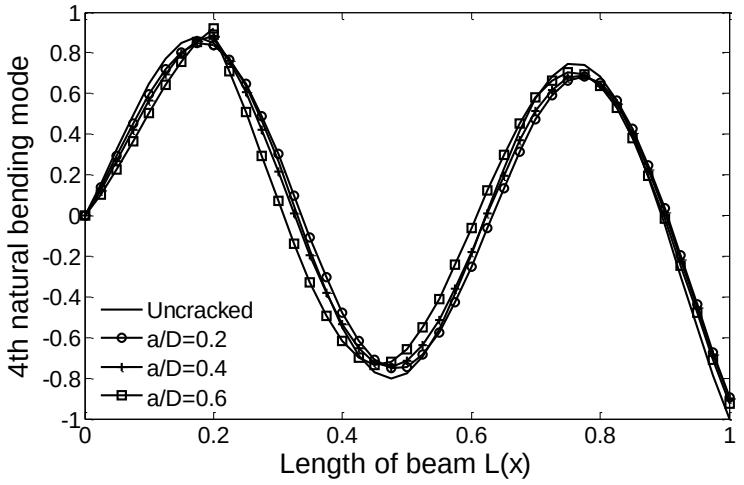

(a)

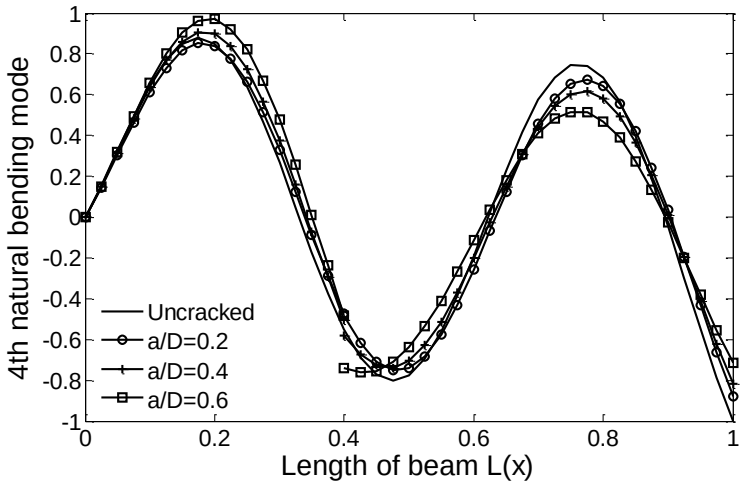

(b)

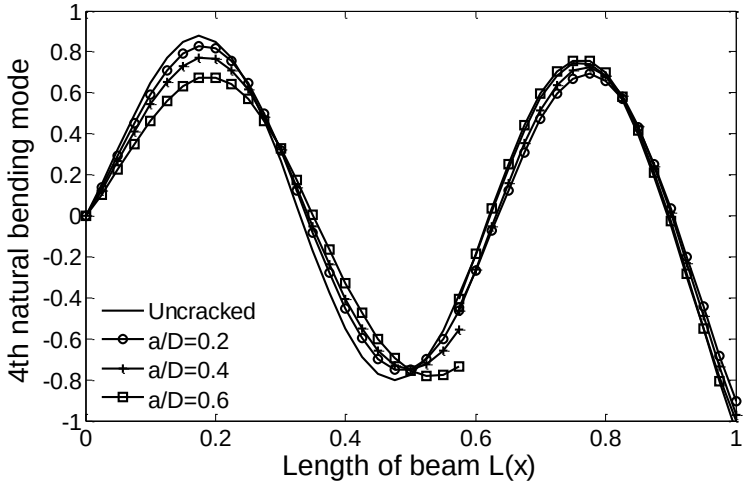

(c)

Fig. 4.23. Fourth natural bending mode as a function of depth, for slenderness ratio $R/D = 0.1$, and different crack position (a) $L1/L = 0.2$, (b) $L1/L = 0.4$, (c) $L1/L = 0.6$.

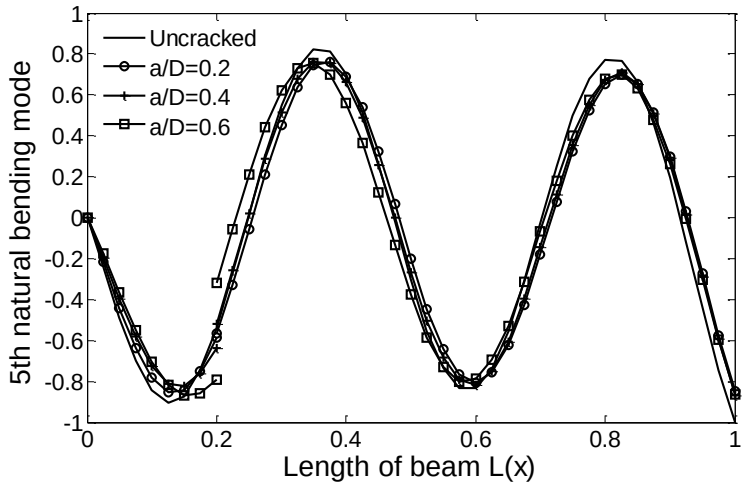

(a)

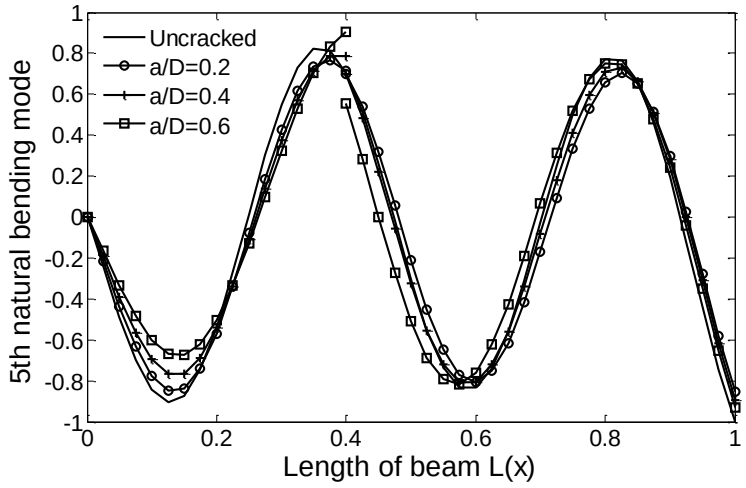

(b)

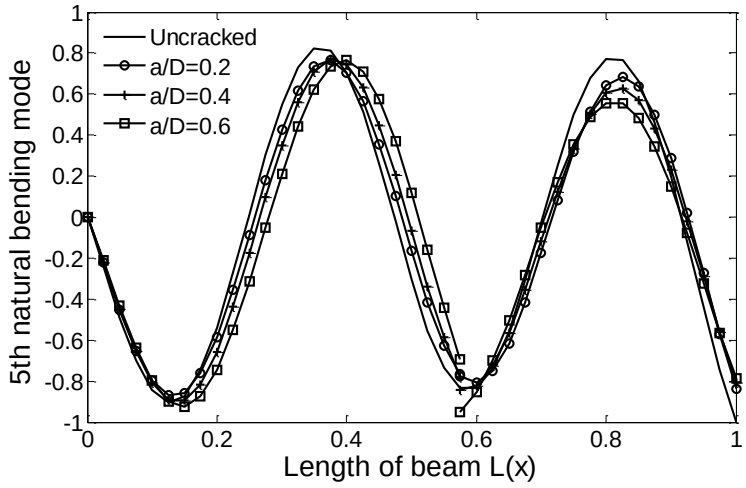

(c)

Fig. 4.24. Fifth natural bending mode as a function of depth, for slenderness ratio $R/D = 0.1$, and different crack position (a) $L1/L = 0.2$, (b) $L1/L = 0.4$, (c) $L1/L = 0.6$.

The first three flexural vibration modes are shown in Figs. 4.25-4.27, respectively. Those plots show the same discontinuities characteristics as described in the section 4.3.

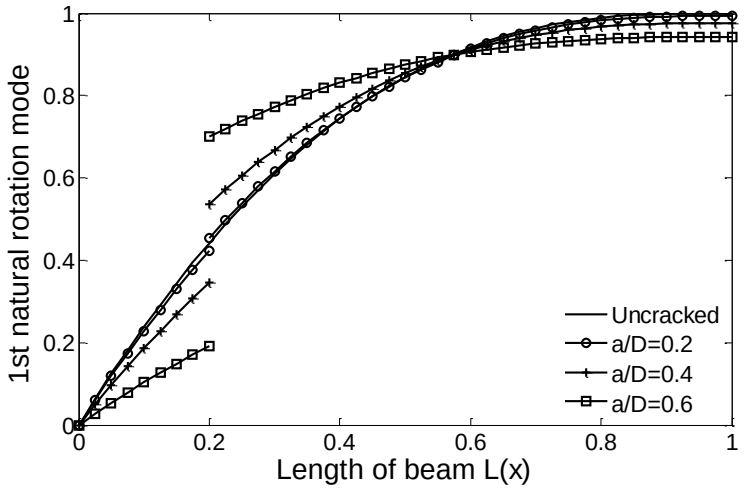

(a)

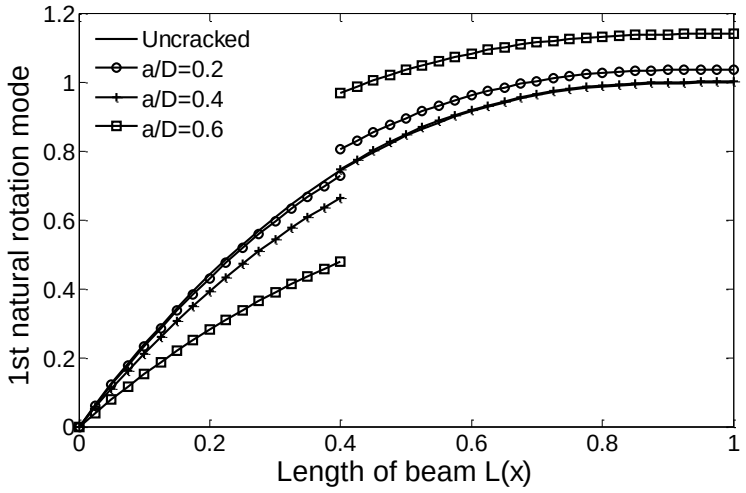

(b)

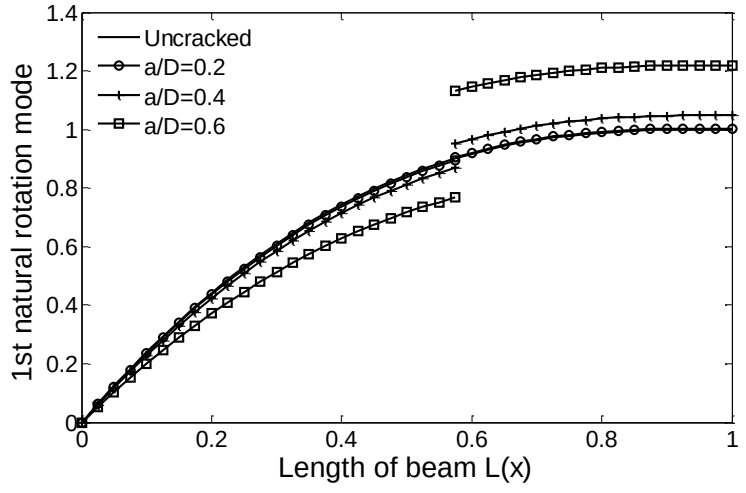

(c)

Fig. 4.25. First natural rotational mode as a function of depth, for slenderness ratio $R/D = 0.1$, and different crack position (a) $L1/L = 0.2$, (b) $L1/L = 0.4$, (c) $L1/L = 0.6$.

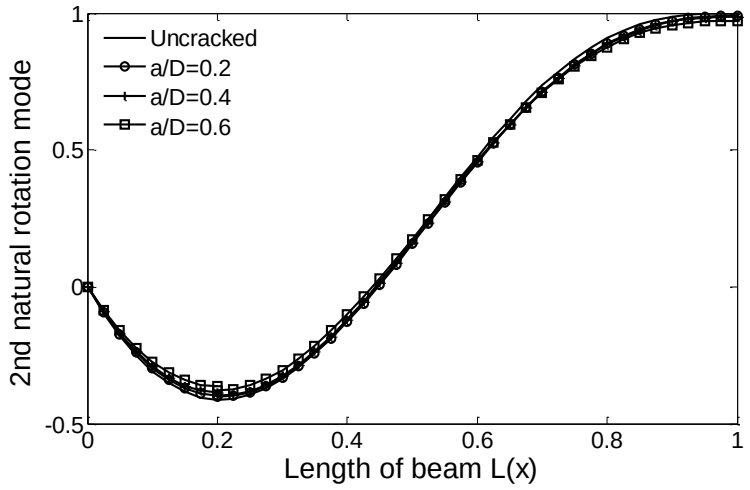

(a)

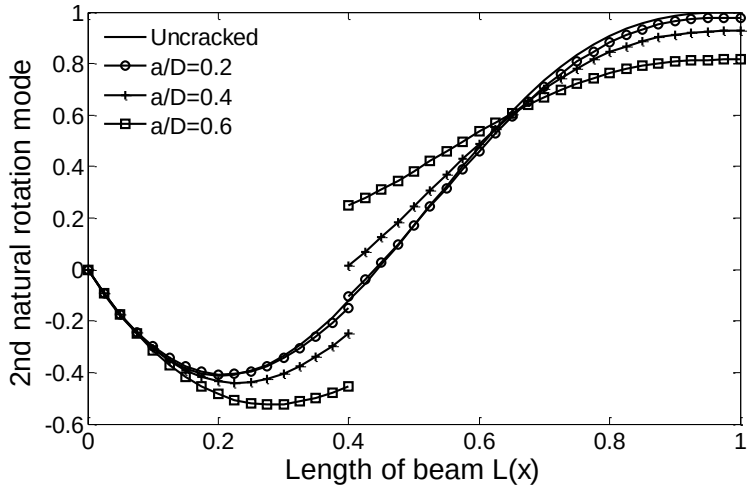

(b)

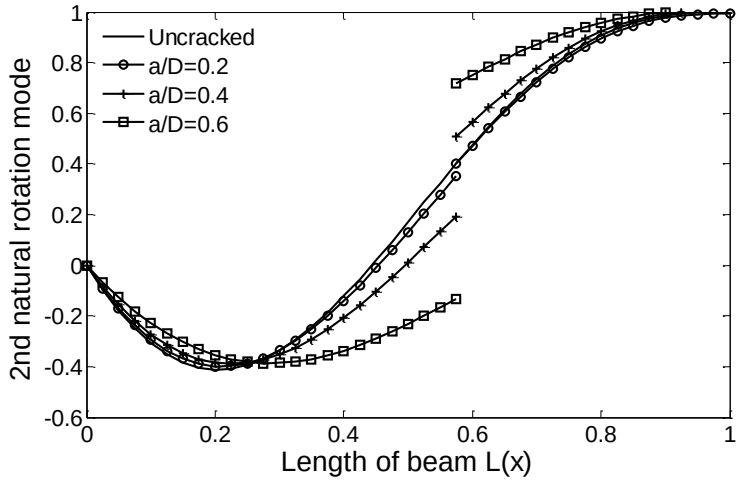

(c)

Fig. 4.26. Second dimensionless natural rotational mode as a function of depth, for slenderness ratio $R/D = 0.1$, and different crack position (a) $L1/L = 0.2$, (b) $L1/L = 0.4$, (c) $L1/L = 0.6$.

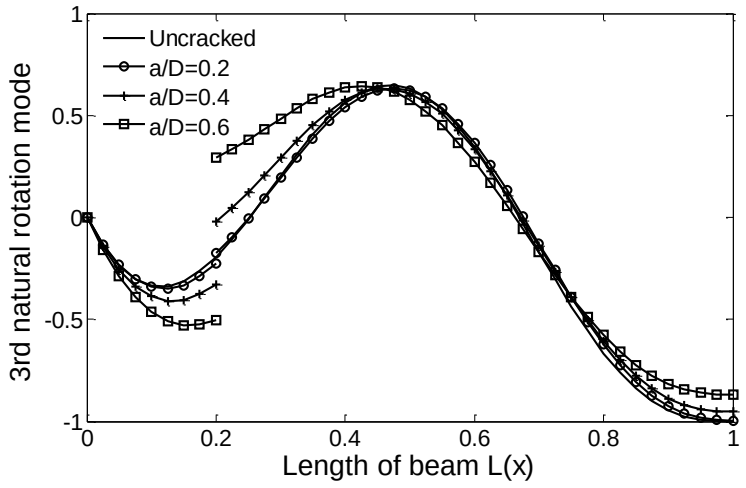

(a)

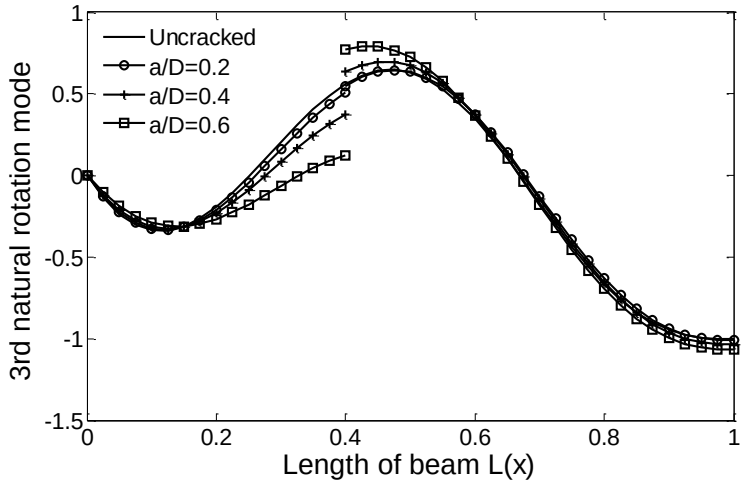

(b)

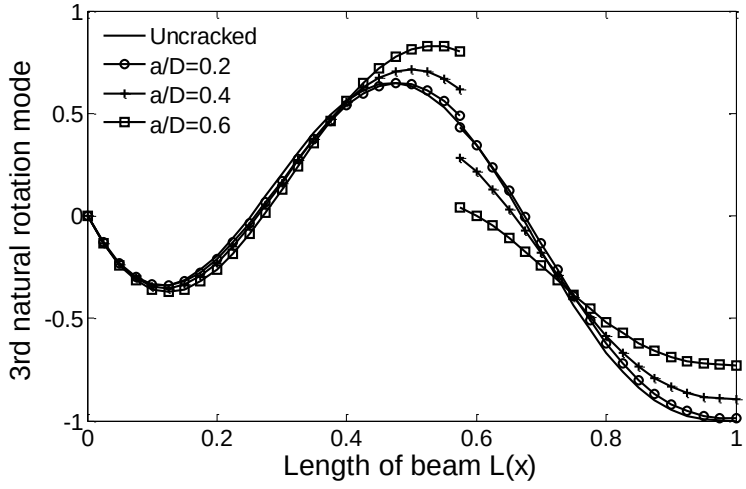

(c)

Fig. 4.27. Third dimensionless natural rotational mode as a function of depth, for slenderness ratio $R/D = 0.1$, and different crack position (a) $L1/L = 0.2$, (b) $L1/L = 0.4$, (c) $L1/L = 0.6$.

References

[1] A.D. Dimarogonas, C.A. Papadopoulos, Vibrations of cracked shafts in bending, J. Sound Vib. 91 (1983) 583–593.

[2] C.A. Papadopoulos, A.D. Dimarogonas, Coupled longitudinal and bending vibrations of a rotating shaft with an open crack, J. Sound Vib. 117 (1987) 81–93.

[3] M.L. Kikidis, C.A. Papadopoulos, Slenderness ratio effect on cracked beam, J. Sound Vib. 155 (1992) 1–11.

[4] D.Y. Zheng, S.C. Fan, Vibration and stability of cracked hollow-sectional beams, J. Sound Vib. 267 (2003) 933–954.

[5] G.M. Dong, J. Chen, J. Zou, Parameter identification of a rotor with an open crack, Eur. J. Mech. A: Solids 23 (2004) 325–333.

[6] Kisa M., M. Arif Gurel, Free vibration analysis of uniform and stepped cracked beams with circular cross sections, Int. J. Eng. Sci, 2007, 45:364-380.

[7] Okamura H, Watanabe K, Takano T, Deformation and strength of cracked member under bending moment and axial force, Engng Fract Mech, 1975,7:531-539.

[8] Carpinteri A, Di Tommaso A, Viola E, Fatigue evolution of multi-cracked frame structures, Proceeding International Conference Analysis Experimental Fracture Mechanics, 417-430, Edited by GC Sih, Rome, 1980.

[9] Irwin GR, Fracture mode transition of a crack traversing a plate, J Basic Engng, 1960,82:417-425.

[10]Dimarogonas AD, Paipetis SA, Analytical methods in Rotor Dynamics, Applied Science Pubisher.1983.

[11]Nobile L, Viola E. Cracked beam element formulation for structural analysis. Transactions, SMiRT 16, Washington DC, August 2001.

[12]Hutchinson J. R., Shear Coefficients for Timoshenko Beam Theory, Journal of Applied Mechanics 2001;68:87-92

[13]Irwin GR, Kies JA. Welding J. Res. Suppl. 1954; 23:193-8.

[14]Przemieniecki J.S., Theory of Matrix Structural Analysis, Dover Pub., 1985

Chapter 5

Numerical analysis and comparison for an interfacial crack under biaxial loading

5.1 Introduction

As it is well known, the fracture property of composite materials can be strongly affected by the toughness of the interface between constituents. Therefore, the problem of a crack lying along the interface of two dissimilar materials has become very important in describing the fracture mechanics behavior. Such a problem was first studied by Williams [1], who discovered for the first time the stress and displacement oscillatory character in proximity to the crack tip. England [2] showed that the upper and lower crack faces would wrinkle and overlap near the crack tips. Erdogan [3] and Rice and Sih [4] derived the expressions of the stress field near the crack tip and introduced the complex stress intensity factor. The framework of fracture mechanics analysis for interface cracks was outlined by Willis [5].

In order to avoid the oscillatory singularity of stress and strain near the crack tip, various attempts have been made over the past decades. Comninou [6] introduced the contact zone model that allowed the crack faces to come into contact near the crack. Piva and Viola [7], and Viola and Piva [8] reported the analytical elastic solution of the in-plane biaxial loading of two dissimilar materials with a crack along their common interface. The complex variable technique coupled with the principle of superposition of effects was applied to compressible as well as incompressible materials. Rice [9] re-examined the elastic fracture mechanics concepts for the isotropic interface crack including stress field near tip, complex stress intensity factor, contact zone, plastic zone as well as some possible definitions of stress intensity factor of classical type. Leguillon [10] numerically investigated the interface crack tip singularity under the assumption that there would be a contact zone along the crack front; the friction contact case and Coulomb's friction law were examined. Comninou [11] presented an overview of the interface crack problem and described some preliminary experimental results in the fatigue and fracture of interface crack. Mykhailova et al. [12] devoted to the application of boundary integral equations for solving the problem of a linear crack located on the dissimilar interface under time-harmonic loading. Cornetti et al. [13] provided a method to determine the load causing delamination along an interface in a composite structure. Hills and Barber [14] discussed the properties of elastic solutions to interface crack problems in both open

and unilateral formulations. They showed that if the contact zone was sufficiently small compared with the other dimensions in the problem, the unilateral solution can be approximated by embedding a universal contact field within the surrounding asymptotic field of the open solution. In this case, the open solution containing all the information could be relevant in determining fracture using a Linear Elastic Fracture Mechanics (LEFM) criterion. Shi et al. [15] used the eigenvalue problem to determine asymptotic stress and displacement fields near the interface corner. A path independent conservative line integral was used to obtain the stress intensities.

Another important problem in fracture mechanics is the prediction of crack growth path under imposed loading and of its rate of growth. The most popular and simplest criteria are the maximum tangential stress criterion (MTS) [16], the strain energy density factor criterion (SEDF) [17] and the maximum energy release rate criterion (MERR) [18, 19]. There are also other criteria proposed in the course of years by different authors. The T-criterion proposed by Theocaris and Andrianopouls [20]. Papadopoulos [21] introduced the Det.-criterion which was based on the determinant of the stress tensor. Goldstein and Salganik [22] established a condition requiring that crack propagation occured along the path of vanishing the Mode II stress intensity factor. Yang and Qin [23] proposed a numerical method capable of modeling interfacial cracking of bi-materials and damage in composites with either weak or strong interfaces. Corneti et al [24] introduced a failure criterion in the framework of finite fracture mechanics. The models of crack growth in mixed mode conditions were reviewed for the plane and three-dimensional states of stress in reference [25].

As regards the fracture criteria for a crack at interface between dissimilar materials, Piva and Viola [7] proposed a fracture criterion based on the MTS criterion, that could be used to assess whether an interface crack would extend along the interface or into one of the two adjacent materials in the plane perpendicular to the direction of maximum circumferential stress evaluated at a small distance from the crack tip. He, along with Hutchinson [26] suggested a criterion based on the energy release rate for predicting the kinking angle. They showed that the competition between crack advance within the interface and kinking depended on relative toughness of the interface to that of the joining material. Moreover, the kinking occured in the direction where the energy release rate was maximum. Yuuki and Xu [27] and Yuuki et al. [28] carried out fracture tests of aluminum epoxy dissimilar materials with an interface crack under comprehensive mixed mode conditions. Using the brazil-nut-sandwich compression tests, they showed that the fracture angles were well predicted by the criterion proposed by the authors themselves. Ayatollahi and Mirsayar [29] developed a fracture criterion, referred to as the modified maximum tangential stress criterion, which took into account the effect of T-stress in addition to the stress intensity factors for predicting the kinking angle in the interface cracks. Rudraraju et al. [30] presented a variational multiscale approach to predict mixed

mode in-plane cohesive crack propagation. A comparative study of numerical results with the corresponding experimental observations of crack propagation in laminate fiber reinforced composite panel was also presented.

Furthermore, there are some experimental and special researches that deserve to be mentioned. Theocaris and Andrianopoulos [31] introduced the Mises elastic-plastic boundary to define the core region. They used the minimum value of the radium of the elastic-plastic boundary for defining the direction of crack propagation. Spyropoulos [32] constructed the zone of yield initiation for the interface crack problem using the Mieses yield criterion according to the two-term stress solution reported in [7]. In [33] the strain energy density criterion was applied to determine the direction of crack initiation for various biaxial load factors and material combinations. Buyukozturk and Hearing [34] investigated fracture of two-phase composites in terms of parameters that influence the cracking scenarios in the interfacial regions and affect the fracture behavior of the concrete. Numerical and physical model tests were performed to study the influence of constituent fracture properties on the behavior of concrete composites. A series of interfacial crack experiments were conducted by Choi and Chai [35] using biaxial loading device for various mixed modes. Lee et al. [36] revisited the criterion to prevent kink of a crack out of a bi-material interface under the presence of in-plane residual stresses. They predicted that in-plane residual stresses control the energetic conditions to prevent crack kinking out of the interface. The change in the stress state near the crack tip due to its own contribution to the singular stress field like globally applied loadings was required. In other words, the problem at issue cannot be handled in purely local terms, but a global approach should be adopted. Kayupov and Dzenis [37] modeled the crack propagating under quasi-static loading and in fatigue life by nonlinear finite element analysis. Goyal et al. [38] proposed a new strength-fracture model for decohesion elements including the geometric nonlinearity of the adherent and adhesive. The initiation and progression of interfacial cracks and/or cohesive cracks was simulated by positioning decohesion elements at the adherent-adhesive interface and between bulk adhesive element. At an earlier date, the authors had postulated an irreversible cohesive-decohesive constitutive law for modeling the delamination process using interfacial surface discontinuities [39]. Yang et al. [40] calculated the critical stresses, taking into account the influence of the adjacent ply angle and the crack size, for the initiation of crack propagation in the transverse direction and in the tunneling direction of a crack embedded in the central layer of a composite laminate. They showed that transverse cracking was a more possible fracture mode in composite laminates with initial crack-like defects. Kaminski [41] pointed a mathematical model and its numerical realization of the composite materials with stochastic interface defects. The composite was discretized using the Boundary Element Method.

Although great progress has been made in solving elasticity problems involving lines of discontinuities, the mathematical formulation of the problem of interfacial cracks remains inadequately treated. Recently, several authors [42, 43] have attempted to solve the interface problem by using the dislocation method, which can remove the oscillation singularity. For engineering estimations of the strength of cracked composite, the use of numerical method involving a simpler calculation procedure can be suitable, even if a little bit lower accuracy is involved. The geometries of the investigation cracked models are different. In the present paper, the comparison between numerical results and analytical solutions of an interfacial crack is presented. The influences of size effect, biaxial loading factor and radius distance on the stresses components distribution, damages zone and the crack extension angle are studied. The conclusion shows an excellent agreement between the numerical results and the analytical calculations.

This paper focuses on the fracture process connected with a finite central crack along the plane interface between two bonded dissimilar materials, subjected to biaxial loading at infinity. The local fracture criterion, for the damaged composite elastic system, involves a suitable defined radial distance from the crack tip, a biaxial loading condition, as well as singular and non-singular stress terms. The analytical solution, based upon the complex potential, stems from the boundary value problem formulated for the two bonded media model subjected to biaxial loading at infinity. Using the proposed Finite Element Method, numerical solutions to the interfacial crack problems are worked out with reference to external loading conditions applied at finite distances from the interfacial crack. Models of different materials properties, interface crack lengths, biaxial loading conditions and interfacial fracture strengths have been investigated. The analytical and numerical results of this study are also examined to see their similarity and differences. As far as the crack initiation angle is concerned, the present results are compared with the ones reported in literature. The effects of the model dimension, the radial distance from the crack tip and the biaxial factor on the stress distribution are studied. Particular attention is paid to the size of oscillatory area, as well as the plastic zone. Then the crack propagation angle obtained from the global fracture criterion and the numerical method is represented graphically. The conclusion shows an excellent agreement between the numerical results and the analytical calculations.

The main novelty of this study consists of finding the ratio of finite distances of loading and crack lengths for which the above analytical and numerical solutions, involving models of damaged composite bi-material systems, which are comparable. The finite critical distance from the crack tip should be specified to provide stress and stain states, as well as to apply criteria of crack extension at the interface, or its extension into one of the two dissimilar media.

5.2 Theoretical background

A central line crack of length 2a lies on the interface between two bonded dissimilar isotropic homogeneous materials showing in Fig. 5.1. E_i, ν_i and μ_i (i = 1, 2) are the Young's modulus, the Poisson's ratios and the shear modulus of material 1 and material 2, respectively. Without loss of any generality, the length of the crack is assumed to be unity or, in other words, all the length parameters are normalized by the crack length 2a.

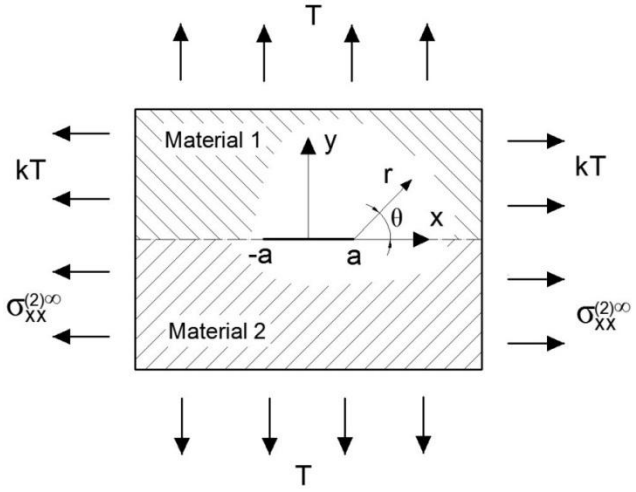

Fig. 5.1. Geometric model and loading contribution for analysis.

The solution of the plane elastic problem is reduced to the calculation of the potential functions $\Phi_j(z)$ and $\Psi_j(z), j = 1,2$ of the complex variable $z = x + iy$ is related to stresses and displacements by the well-known equation of Kolosov-Muskhelishvili [44]:

$$\sigma_{xx}^{(j)} + \sigma_{yy}^{(j)} = 2\left[\Phi_j(z) + \overline{\Phi}_j(\bar{z})\right] \tag{5.1}$$

$$\sigma_{yy}^{(j)} - \sigma_{xx}^{(j)} + 2i\sigma_{xy}^{j} = 2\left[\bar{z}\Phi'_j(z) + \Psi_j(z)\right] \tag{5.2}$$

$$2\mu_j D^{(j)} = \chi_j \varphi_j(z) - z\overline{\Phi}_j(\bar{z}) - \overline{\Psi}_j(\bar{z}) \tag{5.3}$$

$$\varphi_j(z) = \int \Phi_j(z)dz\,, \qquad \psi_j(z) = \int \Psi_j(z)dz \tag{5.4}$$

In eqs. (5.1-5.4), $\sigma_{xx}^{(j)}$, $\sigma_{yy}^{(j)}$ and $\sigma_{xy}^{(j)}$ are the stress tensor components with respect to a Cartesian coordinate system centered in the crack, $\chi_j = 3 - 4\nu_j$ for plane strain and $\chi_j = (3 - \nu_j)/(1 + \nu_j)$ for plane stress, $D^{(j)} = u_j + iv_j$ is the complex displacement, $j = 1,2$ refer to the material 1 and 2, respectively. The four potential functions Φ_j and Ψ_j can be determined by the boundary conditions

and the conditions at infinity [7]. The crack surfaces are free of traction and the two bounded materials are subjected to biaxial load at infinity. It's worthy to note that the horizontal stress component, which is discontinuous across the bond line can be expressed as

$$\sigma_{xx}^{(2)\infty} = (k\mu + \gamma)T \tag{5.5}$$

where

$$\mu = \frac{\mu_2(1+\chi_1)}{\mu_1(1+\chi_2)}, \qquad \gamma = \frac{\alpha(3+\mu)-(1+3\mu)}{1+\alpha}, \qquad \alpha = \frac{\mu_1+\mu_2\chi_1}{\mu_2+\mu_1\chi_2} \tag{5.6}$$

α is relate to one of Dundurs parameters β [45].

$$\alpha = \frac{1-\beta}{1+\beta} \text{ with } \beta = \frac{\mu_1(\chi_2-1)-\mu_2(\chi_1-1)}{\mu_1(\chi_2+1)+\mu_2(\chi_1+1)} \tag{5.7}$$

The solution of the elastic problem is obtained by the application of the principle of superposition as is already presented in a preview paper [7].

$$u_1 + iv_1 = \begin{cases} \left[\frac{k+1}{4} - \frac{1}{1+\alpha}\right]\frac{T(\chi_1+1)}{2\mu_1}x + \frac{T(\chi_1+1)}{2\mu_1(1+\alpha)}i\sqrt{\alpha(a^2-x^2)}exp\left[i\epsilon log\left|\frac{x+a}{x-a}\right|\right], |x| \le a \\ \left[\frac{k+1}{4} - \frac{1}{1+\alpha}\right]\frac{T(\chi_1+1)}{2\mu_1}x \pm \frac{T(\chi_1-\alpha)}{2\mu_1(1+\alpha)}\sqrt{x^2-a^2}exp\left[i\epsilon log\left|\frac{x+a}{x-a}\right|\right], \ |x| \ge a \end{cases} \tag{5.8}$$

$$u_2 + iv_2 = \begin{cases} \mu\left[\frac{k+1}{4} - \frac{1}{1+\alpha}\right]\frac{T(\chi_2+1)}{2\mu_2}x - \frac{T(\chi_2+1)}{2\mu_2(1+\alpha)}i\sqrt{\alpha(a^2-x^2)}exp\left[i\epsilon log\left|\frac{x+a}{x-a}\right|\right], |x| \le a \\ \mu\left[\frac{k+1}{4} - \frac{1}{1+\alpha}\right]\frac{T(\chi_2+1)}{2\mu_2}x \pm \frac{T(\alpha\chi_2-1)}{2\mu_2(1+\alpha)}\sqrt{x^2-a^2}exp\left[i\epsilon log\left|\frac{x+a}{x-a}\right|\right], \ |x| \ge a \end{cases} \tag{5.9}$$

where $\epsilon = \frac{\log\alpha}{2\pi}$ is the well-known bi-elastic constant.

It appears that the displacement field verifies the continuity condition on the bond line and over the crack surface gives rise to the dislocation

$$\Delta u + i\Delta v = \frac{iT\sqrt{\alpha}(\mu+1)(\chi_2+1)}{2\mu_2(1+\alpha)}\sqrt{a^2-x^2}exp\left[i\epsilon log\left|\frac{x+a}{x-a}\right|\right] \tag{5.10}$$

From the expressions of displacement eqs. (5.8-5.10), it notes that the biaxial load parameter has the same effect on the displacements in the two media, but does not affect the dislocation over the crack surface. As pointed out in [2-4], the relative displacement described above oscillates rapidly near the tips of the crack and is thus physically unreasonable because the interpenetration of the material on either side of the crack is predicted at such points. The extent of contact zone proposed by Comninous [6] is unknown, but can be obtained from the oscillatory solution computing the largest

distance r_c from the crack tip at which the crack opening displacement becomes zero [9]. In the present investigation, it is expressed as

$$\mathrm{Im}(\Delta u + i\Delta v) = 0 \tag{5.11}$$

Then, the contact zone size r_c is estimated by the transcendental equation $\cos\left(\epsilon \log\left|\frac{x+a}{x-a}\right|\right) = 0$, or normalized with the crack length 2a as

$$\frac{r_c}{2a} = \frac{1}{1 + e^{\pi/2\epsilon}} \tag{5.12}$$

For example, when $E_1 = 1,\ E_2 = 10^6, \nu_1 = 0, \nu_2 = 0.5, T = 1, a = 0.5, k = 0$. From Abaqus model, the interpenetration is shown in Fig.5.2. The dislocation of the two crack faces on the crack tip is infinite according to eq. (5.10), but it also can be considered on the bonded interface line. So the value is set to zero here, see Fig 5.2, at $r = 0.5$. The dashed line means material 1 interpenetrates into material 2, the crack face of more compliant material interpenetrates into the crack face of stiff material. The ratio of interpenetration distance r_c to crack length 2a is $r_c/2a = 1.2542 \times 10^{-4}$, the same with the value obtained from eq.(5.12). These results have good agreement with England's estimation [2]. For the interface crack in tension the contact zone model provides a contact zone of the order of 10^{-4} of the crack length for $\beta = 0.5$, diminishing to zero as β approaches to zero.

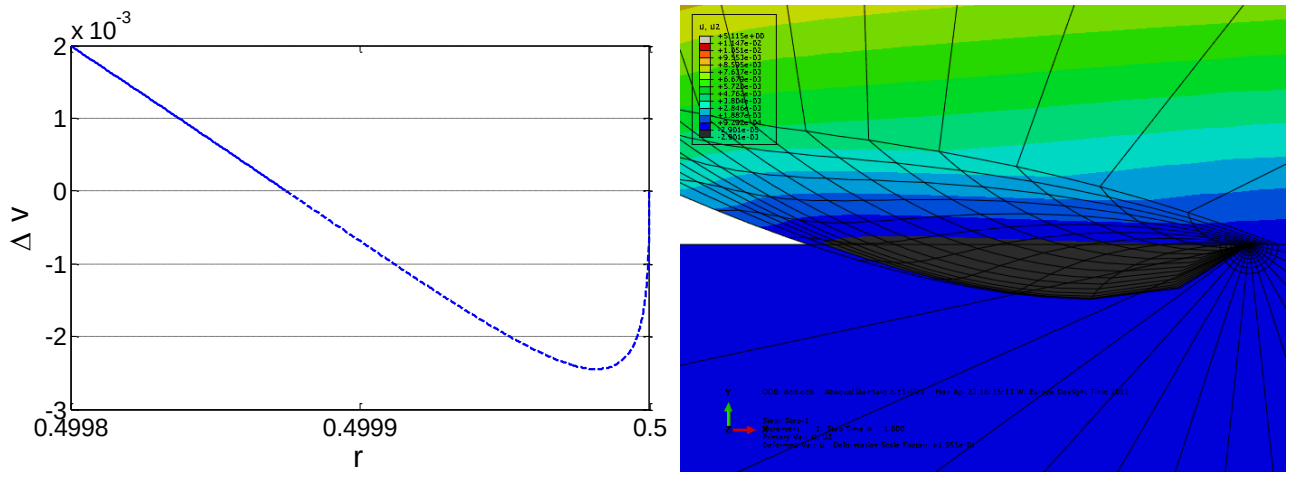

Fig. 5.2. The interpenetration displacement.

Confining our attention to the right tip region, by considering the transformation:

$$z - a = \zeta = re^{i\theta}, \qquad 0 < r/a \ll 1 \tag{5.13}$$

and expressing the eqs. (5.1-5.4) as power series expansions, one can obtain the following approximate expressions for the complex stress distributions

$$\begin{cases} \sigma_{xx}^{(1)} + \sigma_{yy}^{(1)} \cong (k+1)T - \dfrac{4T}{1+\alpha} + \dfrac{\lambda H(\zeta)}{\sqrt{2\pi\zeta}} + \dfrac{\bar{\lambda}\bar{H}(\bar{\zeta})}{\sqrt{2\pi\bar{\zeta}}} \\ \sigma_{yy}^{(1)} - \sigma_{xx}^{(1)} + 2i\sigma_{xy}^{(1)} \cong -(k+1)T + \dfrac{4T}{1+\alpha} + \dfrac{\alpha\bar{\lambda}\bar{H}(\zeta)}{\sqrt{2\pi\zeta}} - \dfrac{\lambda H(\zeta)}{2\sqrt{2\pi\zeta}}\left(c_1 + \bar{c_1}\dfrac{\bar{\zeta}}{\zeta}\right) \end{cases} \tag{5.14}$$

$$\begin{cases} \sigma_{xx}^{(2)} + \sigma_{yy}^{(2)} \cong \mu(k+1)T - \dfrac{4\mu T}{1+\alpha} + \dfrac{\alpha\lambda H(\zeta)}{\sqrt{2\pi\zeta}} + \dfrac{\alpha\bar{\lambda}\bar{H}(\bar{\zeta})}{\sqrt{2\pi\bar{\zeta}}} \\ \sigma_{yy}^{(2)} - \sigma_{xx}^{(2)} + 2i\sigma_{xy}^{(2)} \cong -\mu(k+1)T + \dfrac{4\mu T}{1+\alpha} + \dfrac{\bar{\lambda}\bar{H}(\zeta)}{\sqrt{2\pi\zeta}} - \dfrac{\alpha\lambda H(\zeta)}{2\sqrt{2\pi\zeta}}\left(c_1 + \bar{c_1}\dfrac{\bar{\zeta}}{\zeta}\right) \end{cases} \tag{5.15}$$

where $H(\zeta) = exp(-i\epsilon \log\zeta)$, $\lambda = \frac{2c_1 T\sqrt{a\pi}}{1+\alpha} exp(i\epsilon \log l)$, $l = 2a$, $c_1 = 1 - 2i\epsilon$.

The explicit expressions of the Cartesian stress components in terms of the polar variables (r, θ) can be obtained. Moreover, the distribution of the local circumferential stress $\sigma_{\theta\theta}$ can be evaluated as following

$$\sigma_{\theta\theta}^{(j)} = \frac{\sigma_{xx}^{(j)} + \sigma_{yy}^{(j)}}{2} + \frac{1}{2} Re\left[\frac{\zeta}{\bar{\zeta}}\left(\sigma_{yy}^{(j)} - \sigma_{xx}^{(j)} + 2i\sigma_{xy}^{(j)}\right)\right] \tag{5.16}$$

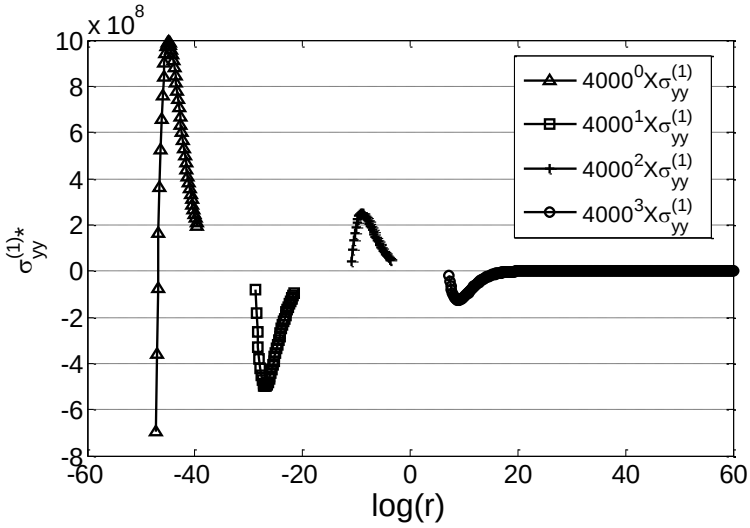

Fig. 5.3. $\sigma_{yy}^{(1)}$ Oscillatory front of the crack tip.

Those stress components as the analytical solutions will be compared with finite element computations presented in the next section. Fig. 5.3 graphically presents the oscillatory of the vertical stress front of the crack tip. However, Hutchinson et al. [46] tabulated strain values on α and β for six representative material combinations and found that β was quite small for most of the combinations. Therefore, the oscillation zone ignored here is reasonable.

5.3 The non-linear stress-strain response

It is possible by a simple procedure, to obtain the component ε of the strain corresponding to the component T of the applied load for some cracks configuration. In fact, from the Castigliano's theorem we have

$$\varepsilon = \frac{\partial W}{\partial T}|_{T=T(a)} \tag{5.17}$$

where $T(a)$ is a typical limit point stress for crack length a, W is the average strain energy per unit volume corresponding to the model of Fig.5.1 with fixed bond cracks of length a loaded to the level $T(a)$. We can write

$$W = W_0 + W_c = W_0^{(1)} + W_0^{(2)} + W_c \tag{5.18}$$

where $W_0^{(i)}(i = 1, 2)$ are the average strain energies of material i without crack and W_c is the average strain energy contribution due to crack.

The stain energy density in model without crack can be evaluated by the usual method using results from the theoretical analysis in section 5.2.

$$Average\ Strain\ Energy = \frac{1}{V}\int_V \frac{1}{2E}\left(\sigma_{xx}^2 + \sigma_{yy}^2 - 2\nu\sigma_{xx}\sigma_{yy} + 2(1+\nu)\sigma_{xy}^2\right)dV \tag{5.19}$$

in which V is the volume of the model.

For the bimaterial system without crack on the interface, the stress components in the above equation can be obtained by substituted the solutions $\Phi_0^{(j)}$, $\Psi_0^{(j)}$ to the eq. (5.1) and eq. (5.2).

where

$$\Phi_0^{(1)} = \frac{k+1}{4}T \tag{5.20}$$

$$\Psi_0^{(1)} = \frac{1-k}{2}T \tag{5.21}$$

$$\Phi_0^{(2)} = \frac{k\mu+\gamma+1}{4}T \tag{5.22}$$

$$\Psi_0^{(2)} = -\frac{k\mu+\gamma-1}{2}T \tag{5.23}$$

The stresses can be calculated as

$$\sigma_{xx}^{(1)} = kT;\ \sigma_{yy}^{(1)} = T;\ \sigma_{xy}^{(1)} = 0 \tag{5.24}$$

$$\sigma_{xx}^{(2)} = (k\mu+\gamma)T;\ \sigma_{yy}^{(2)} = T;\ \sigma_{xy}^{(2)} = 0 \tag{5.25}$$

therefore

$$W_0^{(1)} = \frac{T^2}{2E_1}[k^2 + 1 - 2\nu_1 k] \tag{5.26}$$

$$W_0^{(2)} = \frac{T^2}{2E_2}[(k\mu + \gamma)^2 + 1 - 2\nu_2(k\mu + \gamma)] \tag{5.27}$$

The strain energy due to the presence of crack W_c is evaluated using the stress intensity factors (energy release rate). The leading terms of stress components σ_{yy}, σ_{xy} along interface $\theta = 0$ in the vicinity of the crack can be expressed as [3, 9]

$$\sigma_{yy} + i\sigma_{xy}|_{\theta=0} = \frac{K_1 + iK_2}{\sqrt{2\pi r}}\left(\frac{r}{l}\right)^{i\epsilon} \tag{5.28}$$

where i denotes the imaginary unit, K_1, K_2 are the stress intensity factors, r is the radial distance from the crack tip, l is a reference length, and ϵ is the bielastic constant.

$$K_1 = \sqrt{2\pi r}\left(\sigma_{yy}\, cosQ + \sigma_{xy}\, sinQ\right) \tag{5.29}$$

$$K_2 = \frac{\sqrt{2\pi r}\left(\sigma_{xy}\, cosQ - \sigma_{yy}\, sinQ\right)}{cos2Q} \tag{5.30}$$

where $Q = \epsilon ln\left(\frac{r}{l}\right)$.

The strain energy release rate for the actual field, which is the loading condition for the crack problem under consideration, can be related to the stress intensity factors as follows

$$G = \frac{1}{H}K\overline{K} = \frac{1}{H}(K_1^2 + K_2^2) \tag{5.31}$$

where $\overline{K}$ is the complex conjugate of K, and

$$\frac{1}{H} = \frac{1}{16\cosh^2(\pi\epsilon)}\left[\frac{\chi_1 + 1}{\mu_1} + \frac{\chi_2 + 1}{\mu_2}\right] \tag{5.32}$$

The stain energy due to presence of crack is

$$W_c = \frac{2}{V}\int_0^a G da = \frac{T^2 a^2 \pi(1 + 4\epsilon^2)\alpha}{4(1+\alpha)^2 L^2}\left[\frac{\chi_1 + 1}{\mu_1} + \frac{\chi_2 + 1}{\mu_2}\right] \tag{5.33}$$

Hereby, the dimensionless average strain energy for crack presence is defined as

$$W_c^* = \frac{W_c E^*}{T^2} \tag{5.34}$$

where

$$\frac{1}{E^*} = \frac{1}{E_1} + \frac{1}{E_2} \tag{5.35}$$

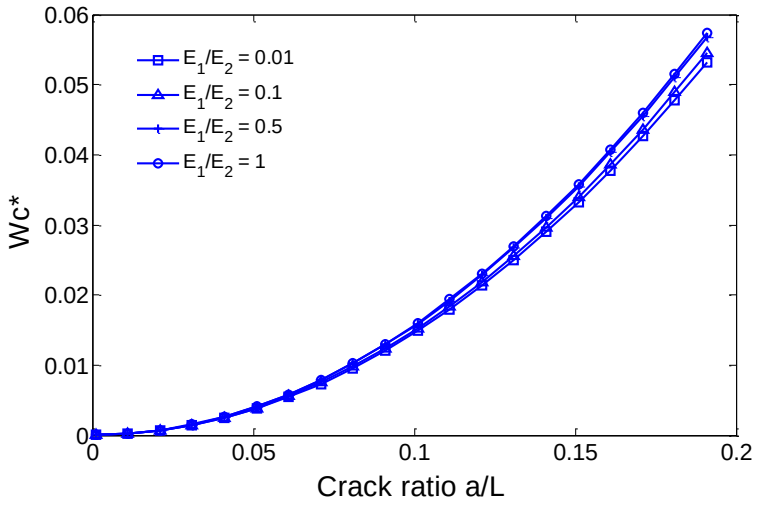

Fig. 5.4 Dimensionless crack average strain energy against crack length ratio.

Fig. 5.4 shows the dimensionless crack average strain energy which independent on biaxial factor k against crack length ratio for various values of the Young's moduli ratio. It's worthy to note that this relationship is the same for switching the Young's moduli of the two materials. Moreover, those curves are the same when $\frac{E_1}{E_2} = \frac{E_2}{E_1}$.

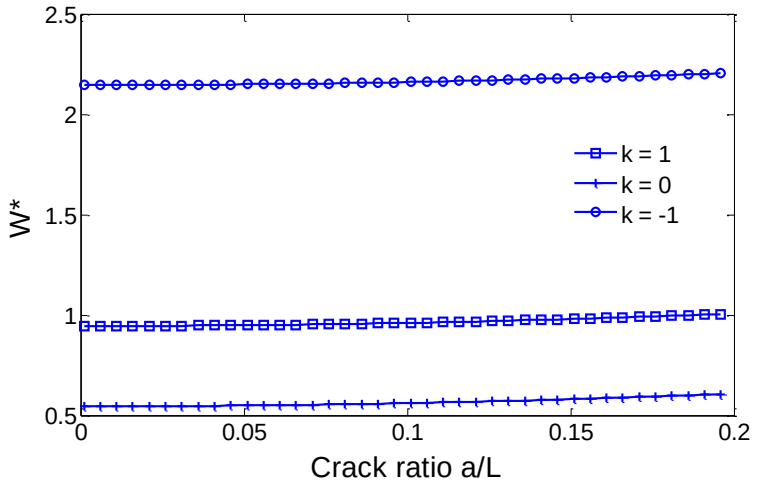

Fig. 5.5 Dimensionless strain energy for various biaxial loading factors.

Fig. 5.5 shows the dimensionless stain energy of the biomaterial system $W^* = WE^*/T^2$ against crack length ratio for different biaxial loading factor and the same material combination $E_1/E_2 = 0.5$. It's worth noting that the impact of biaxial loading factor on the strain energy is much greater than crack length.

By calculating eqs. (5.26), (5.27) and (5.33), it could be obtained from eq. (5.17) a stress-strain law in the following form

$$\varepsilon = \frac{T}{E_1}[k^2 + 1 - 2\nu_1 k] + \frac{T}{E_2}[(k\mu + \gamma)^2 + 1 - 2\nu_2(k\mu + \gamma)] + \frac{Ta^2\pi(1 + 4\epsilon^2)\alpha}{2(1+\alpha)^2 L^2}\left[\frac{\chi_1 + 1}{\mu_1} + \frac{\chi_2 + 1}{\mu_2}\right] \tag{5.36}$$

The stress-strain law is linear, for fixed value of the crack length, it must be terminate at the critical value T_c of T which causes the crack extension.

It follows that a non-linear response, due to progressive bond separation, can be obtained by considering the sequence of critical points (T_c, ε_c) on the linear response curves corresponding to successively larger values a_c of a.

From the debonding criterion described in [7], the dimensionless critical loading T^* and strain ε^* can be expressed in the following forms

$$T^* = \frac{T_c\sqrt{\pi r_0}}{K_b} \tag{5.37}$$

$$\varepsilon^* = \frac{\varepsilon\sqrt{\pi r_0}E^*}{K_b} \tag{5.38}$$

For a bimaterial system with dimension $L = 10$, $r_0 = 0.05$ and unit thickness, $E_1/E_2 = 0.5$, $\nu_1 = \nu_2 = 0.3$, the stress-strain responses for varies biaxial loading factor are showed in Fig. 5.6. Fig. 5.7 shows the effects of material combination on the stress-strain response for $k = 0$ and $k = 1$. The characteristic of non-linear stress-strain response of biaxial loading factor $k = 0$ is more obvious than that of $k = 1$ for the same material combination.

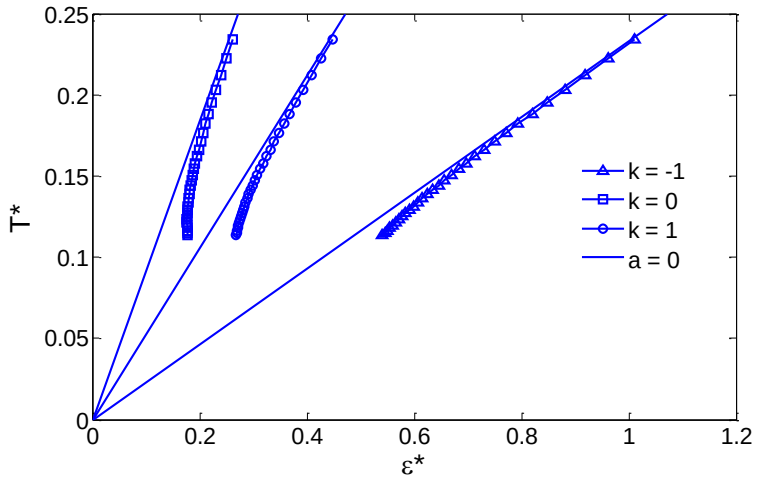

Fig. 5.6 Influence of the biaxial loading factor on the stress-strain response.

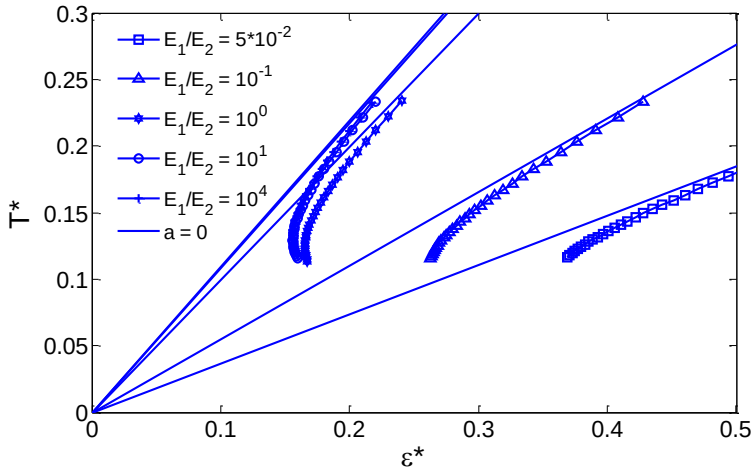

(a)

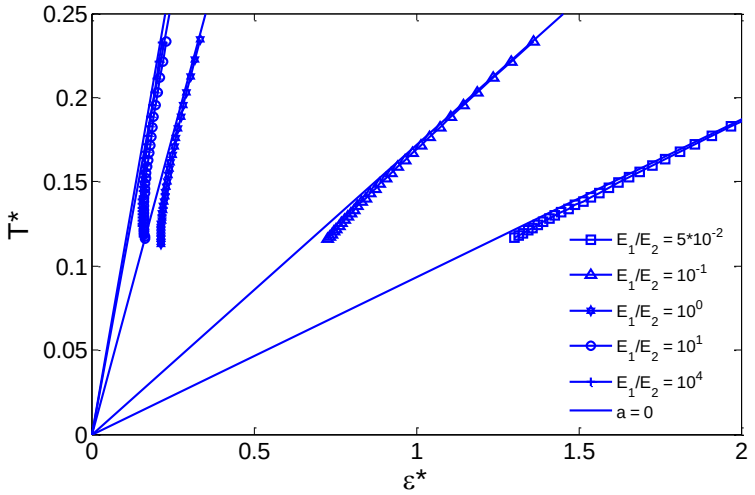

(b)

Fig. 5.7 Material combination effect on the stress-strain response for (a) $k = 0$, (b) $k = 1$.

5.4 Numerical model

The two-dimensional interfacial crack system shown in Fig. 5.8 is used for the mechanical analysis. Dissimilar linear elastic material combination, with Young's modulus $\mathrm{E}_1 = 50\mathrm{N/mm}^2$ for material 1, $\mathrm{E}_2 = 100\mathrm{N/mm}^2$ for material 2 and Poisson's ratios $\nu_1 = \nu_2 = 0.3$, constitutes the domain of the model. An interfacial crack with sharp crack tip is embedded at the center of bond line.

In order to investigate the effect of the model dimension on the mechanical parameters, different scale models are involved. Keeping the crack length $2\mathrm{a} = 1$, but changing the model dimension $\mathrm{L} = 2.5, 5, 10$ and 20 respectively, the following ratios between model dimension and half crack length $\mathrm{L/a} = 5, 10, 20$ and 40 can be considered. The analysis is carried out using finite element code Abaqus [47]. The whole cracked system is modeled as is shown in Fig. 5.9 where the finite element mesh is also illustrated. 8-nodes isoparametric quadrilateral generalized plane stress elements

are used for this analysis. The ring zone completely surrounding the crack tip, from one crack face to the opposite crack face, for creating collapsed 8-node isoparametric elements and calculating the J integral will be illustrated in details in the following.

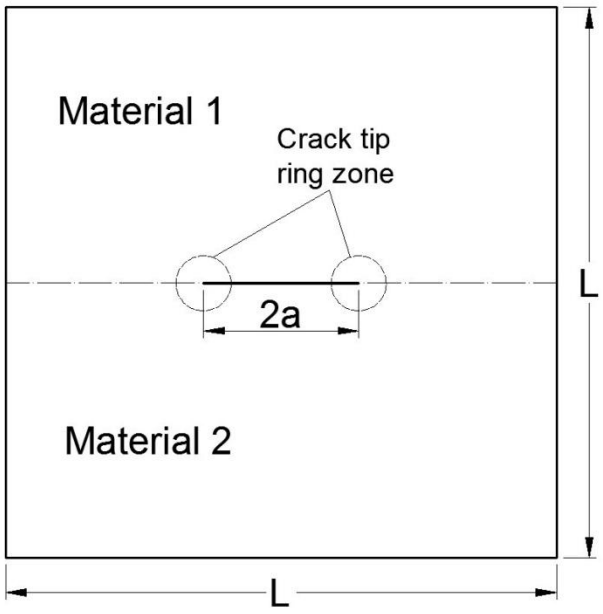

Fig.5.8. Two-dimensional model of interfacial crack in dissimilar media.

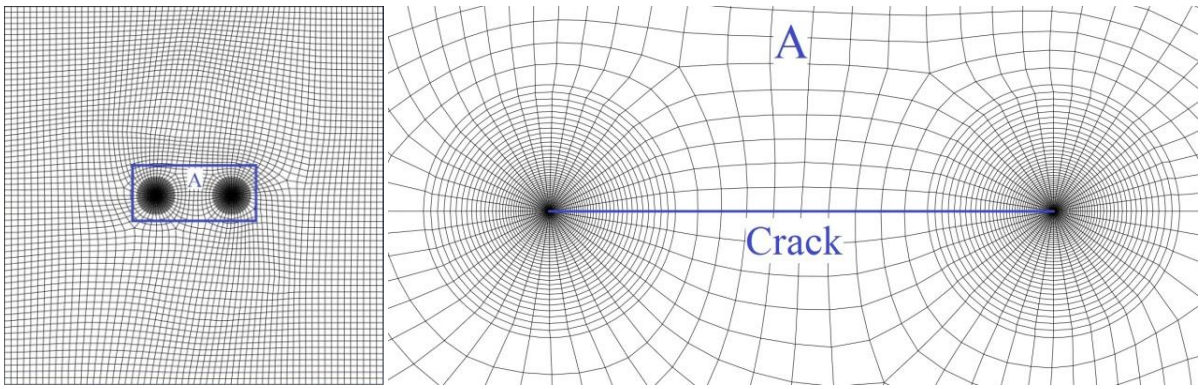

(a) (b)

Fig. 5.9. Finite element mesh of the cracked system when L=5 (a) Model for the whole system, (b) Mesh near the interface crack.

Sharp cracks are usually modeled using small-strain assumptions when geometric nonlinearities are ignored. It is noted that for a sharp crack the strain field becomes singular at the crack tip. However the large-strain zone is very localized. The accuracy of the J-integral and the stress intensity factors can be improved when the singularity is included in the stress and strain calculations. If r is the distance from the crack tip, the strain singularity in small-strain analysis for linear elasticity is $\propto r^{-\lambda}, (\lambda = 1/2)$. For interface crack, the singularity of the crack tip is $\lambda = 1/2 \pm i\epsilon$. As introduced in [48], for the present particular case $\epsilon = 0.037$, the singularity of $\lambda = 1/2 \pm i\epsilon$ can be well approximated by the singularity of $\lambda = 1/2$. The crack tip is modeled with a ring of collapsed

quadrilateral elements, as shows in Fig.5.10, generally second-order elements are used and the elements are collapsed as follows

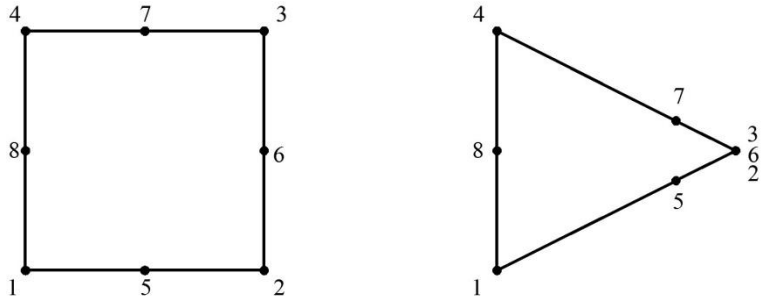

Fig. 5.10. Collapsed two-dimensional element.

Collapse one side of an 8-node isoparametric element (CPE8R, for example) so that all three nodes---3, 6 and 2---have the same geometric location (on the crack tip). Move the mid-side nodes on the sides connected to the crack tip to the $1/4$-point nearest the crack tip. One can create "quarter point" spacing with second-order isoparametric elements when you generate nodes for a region of a mesh. This procedure is able to create the stain singularity

$$\varepsilon \to \frac{A}{r} + \frac{B}{r^{1/2}} \text{ as } r \to 0 \tag{5.39}$$

Abaqus/Standard offers the evaluation of several parameters for fracture mechanics studies based on either the conventional finite element method or the extended finite element method, such as the stress intensity factors, the contour integral, the direction of cracking initiation and so on.

The stress intensity factors of two dimensions K_I and K_{II} in homogeneous material are related to the energy release rate (J-integral, calculated directly in Abaqus/Standard) through

$$J = \frac{1}{\overline{E}}(K_I^2 + K_{II}^2) \tag{5.40}$$

where $\overline{E} = E$ is for plane stress and $\overline{E} = E/(1-\nu^2)$ is for plane stain.

5.5 Results comparison

5.5.1 Circumferential stress

In order to simplify the comparison, the loading $T = 1$ is used in both analytical and numerical calculation. Therefore, the circumferential stress and Mises stress can be considered as dimensionless. In the numerical calculations of the present paper, $E_1 = 50$, $E_2 = 100, \nu_1 = \nu_2 = 0.3$ and $k = -1, 0, 1, 2, 3$ are assumed. According to eq. (5.12), $r_c/2a = 3.6732 \times 10^{-23}$, the oscillatory zone is so small that can be omitted.

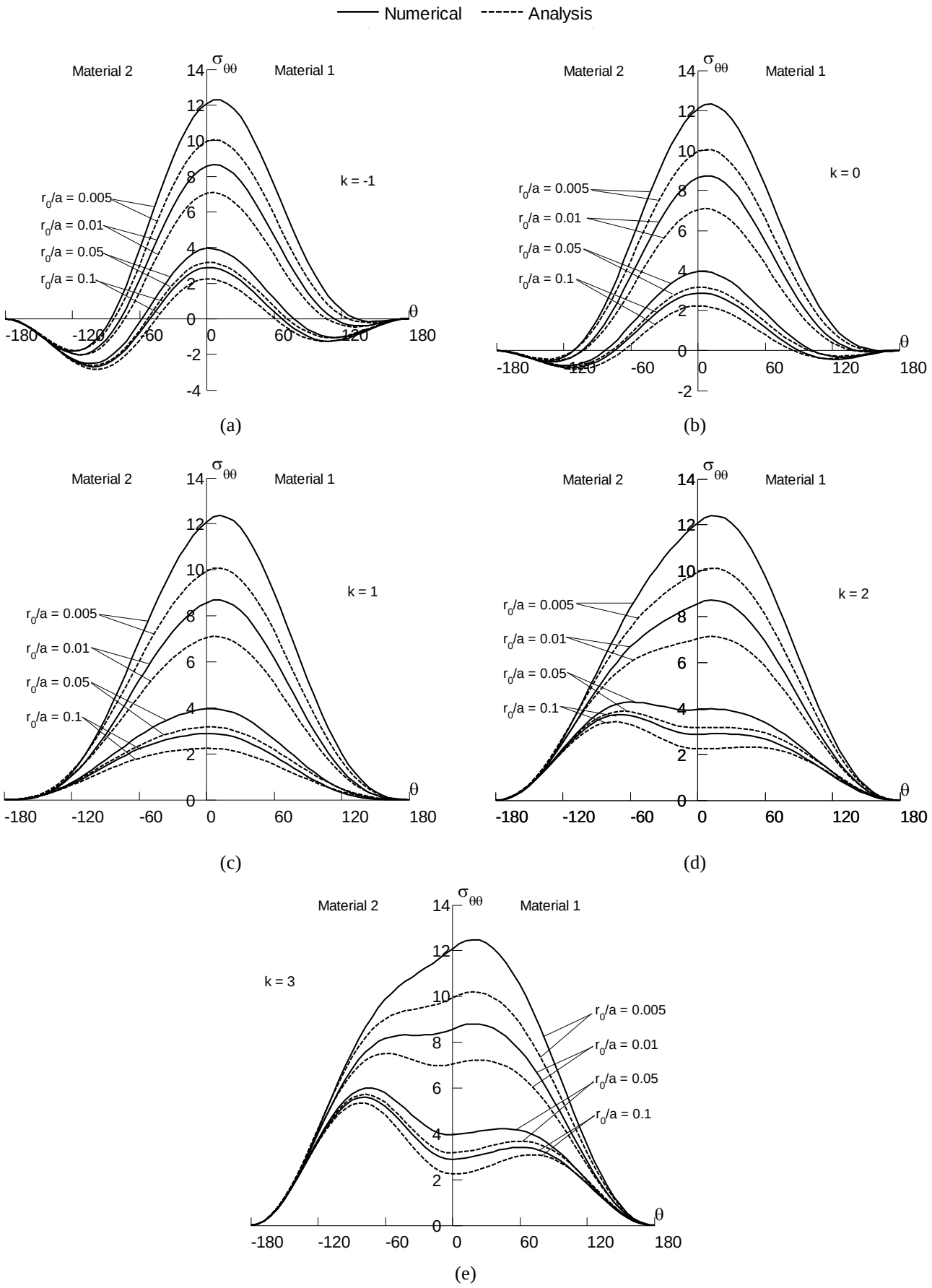

Fig. 5.11. Comparisons of circumferential stresses $\sigma_{\theta\theta}$ for various biaxial factors k and the ratios r_0/a when $L/a = 5$

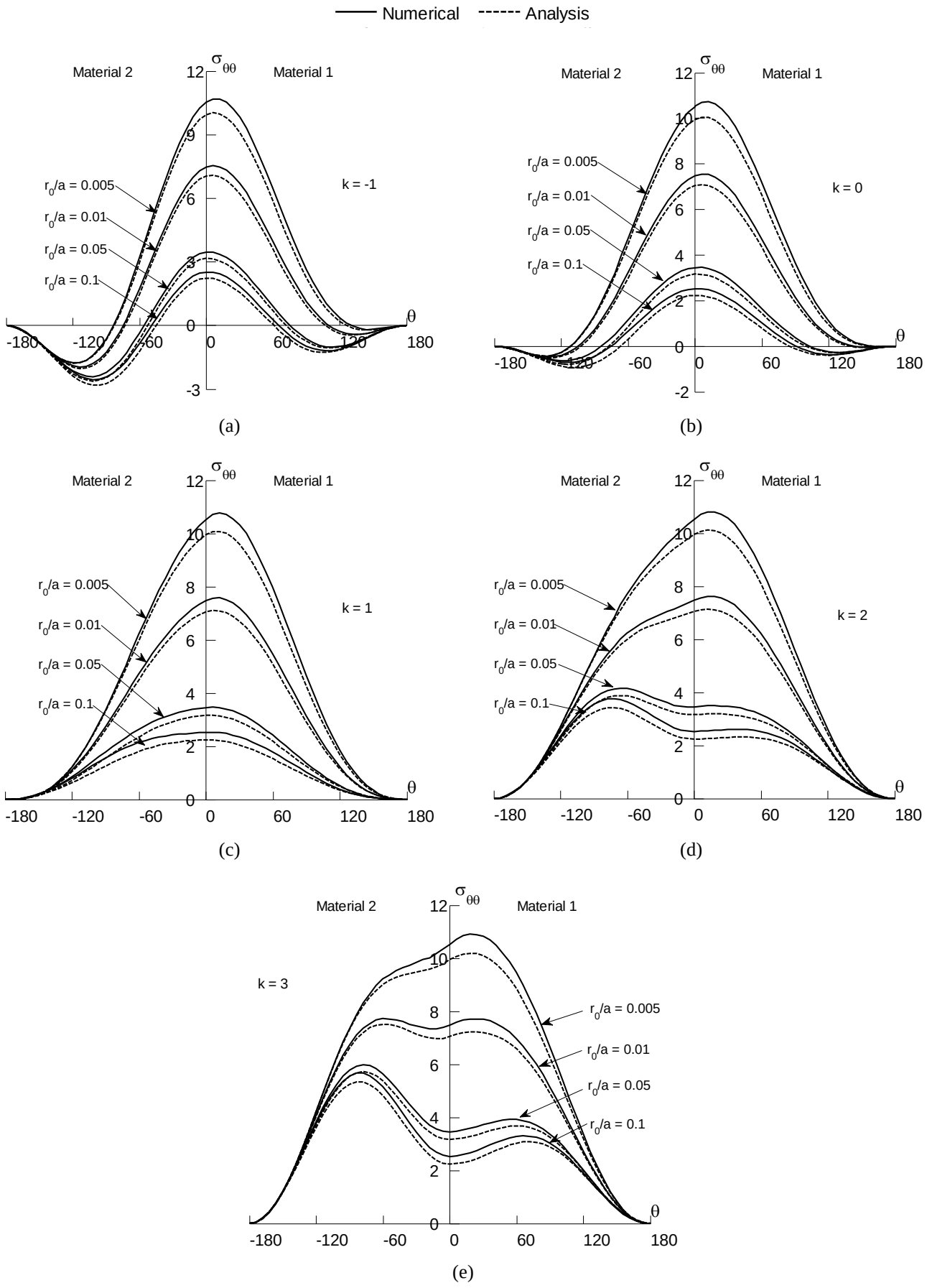

Fig. 5.12. Comparisons of circumferential stresses $\sigma_{\theta\theta}$ for various biaxial factors k and the ratios r_0/a when $L/a = 10$

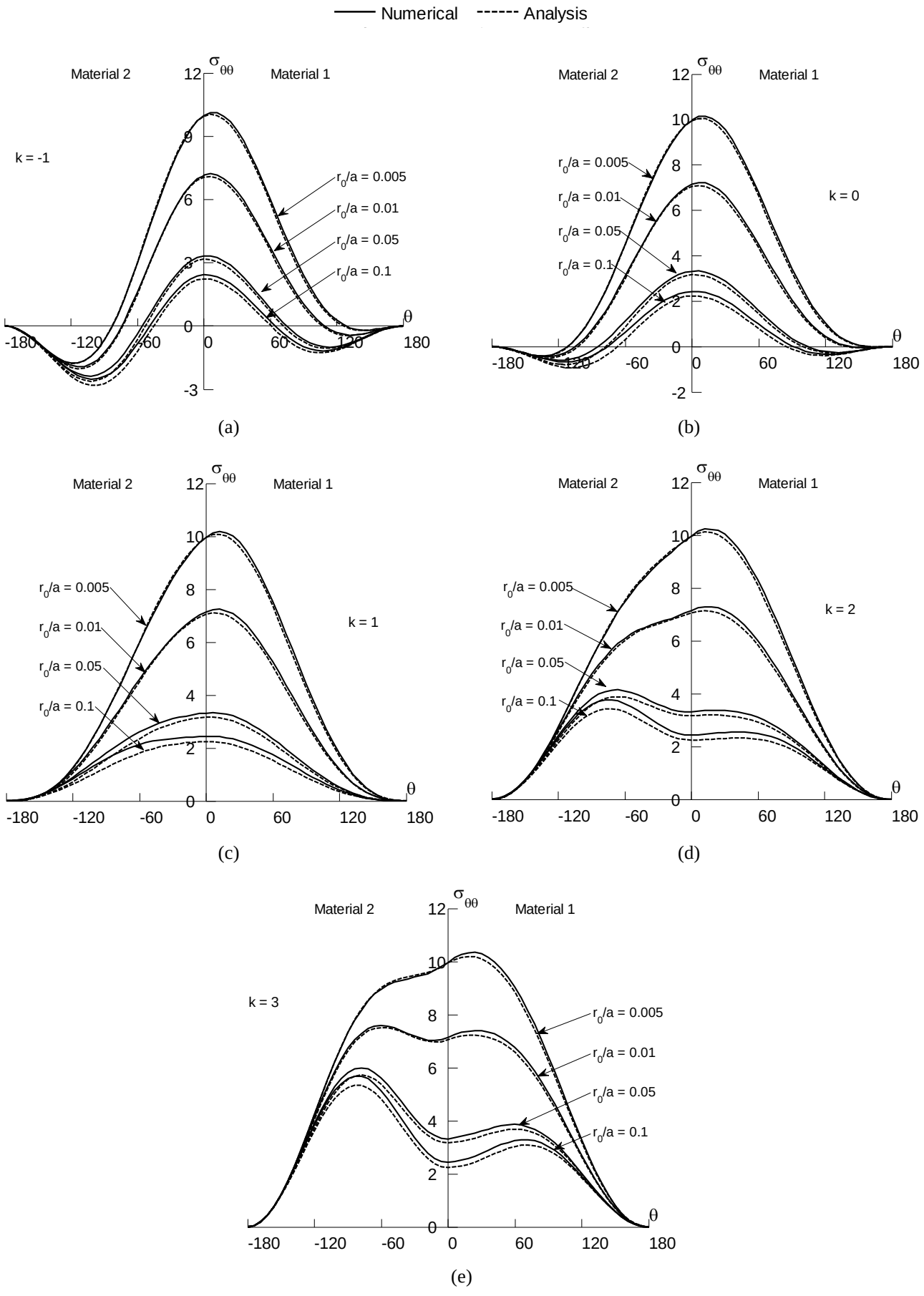

Fig. 5.13. Comparisons of circumferential stresses $\sigma_{\theta\theta}$ for various biaxial factors k and the ratios r_0/a when $L/a = 20$

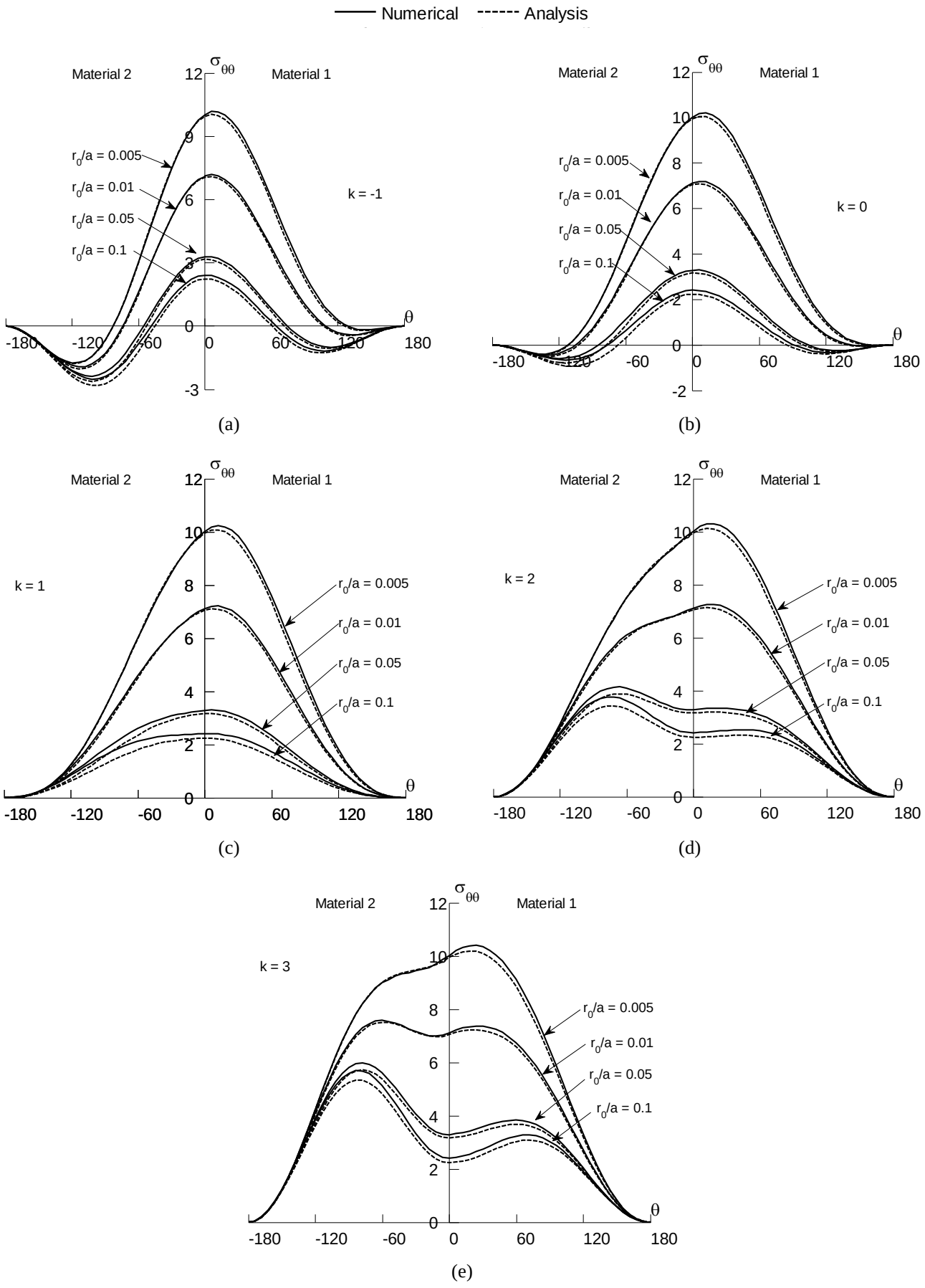

Fig. 5.14. Comparisons of circumferential stresses $\sigma_{\theta\theta}$ for various biaxial factors k and the ratios r_0/a when $L/a = 40$

Comparisons of circumferential stress $\sigma_{\theta\theta}$ at the front of the crack tip under varies biaxial factors in terms of polar angle θ are shown in Figs. 5.11-5.14 for different dimension sizes. It's easy to see that the circumferential stresses on the crack surface ($\theta = -\pi$ and π) are zero as assumed in the boundary condition, and the circumferential stress continue across the bonded line, $\theta = 0$, $\sigma_{\theta\theta} = \sigma_{yy}$. The analytical results are always smaller than the numerical results. Obviously, the dimension of the model effects on the accuracy of the numerical results. The bigger the dimension factor is, the closer the numerical results to the analytical results, no matter how close to the crack tip and the bi-axial factor. However, when the dimension ratio exceeds one threshold value, the numerical results tend to become the same of the analytical ones. For the sake of saving the computation expense, the dimension ratio approximately equals to 20 according to the presented results. The closer to the crack tip, the greater of the circumferential stress, due to the stress concentration of the linear elastic theory.

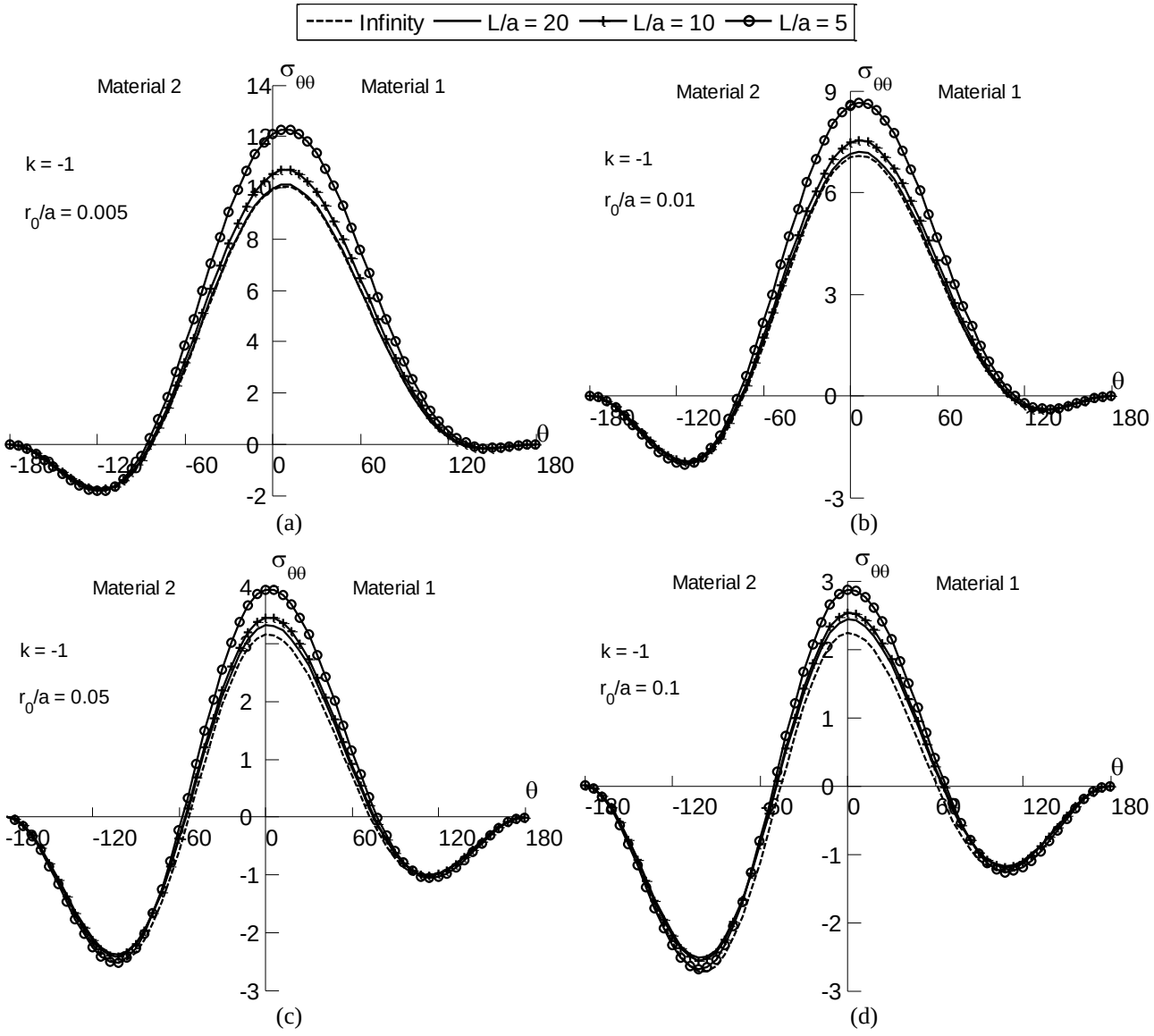

Fig. 5.15. Comparisons of circumferential stresses $\sigma_{\theta\theta}$ for various dimensions L/a and the ratios r_0/a when $k = -1$.

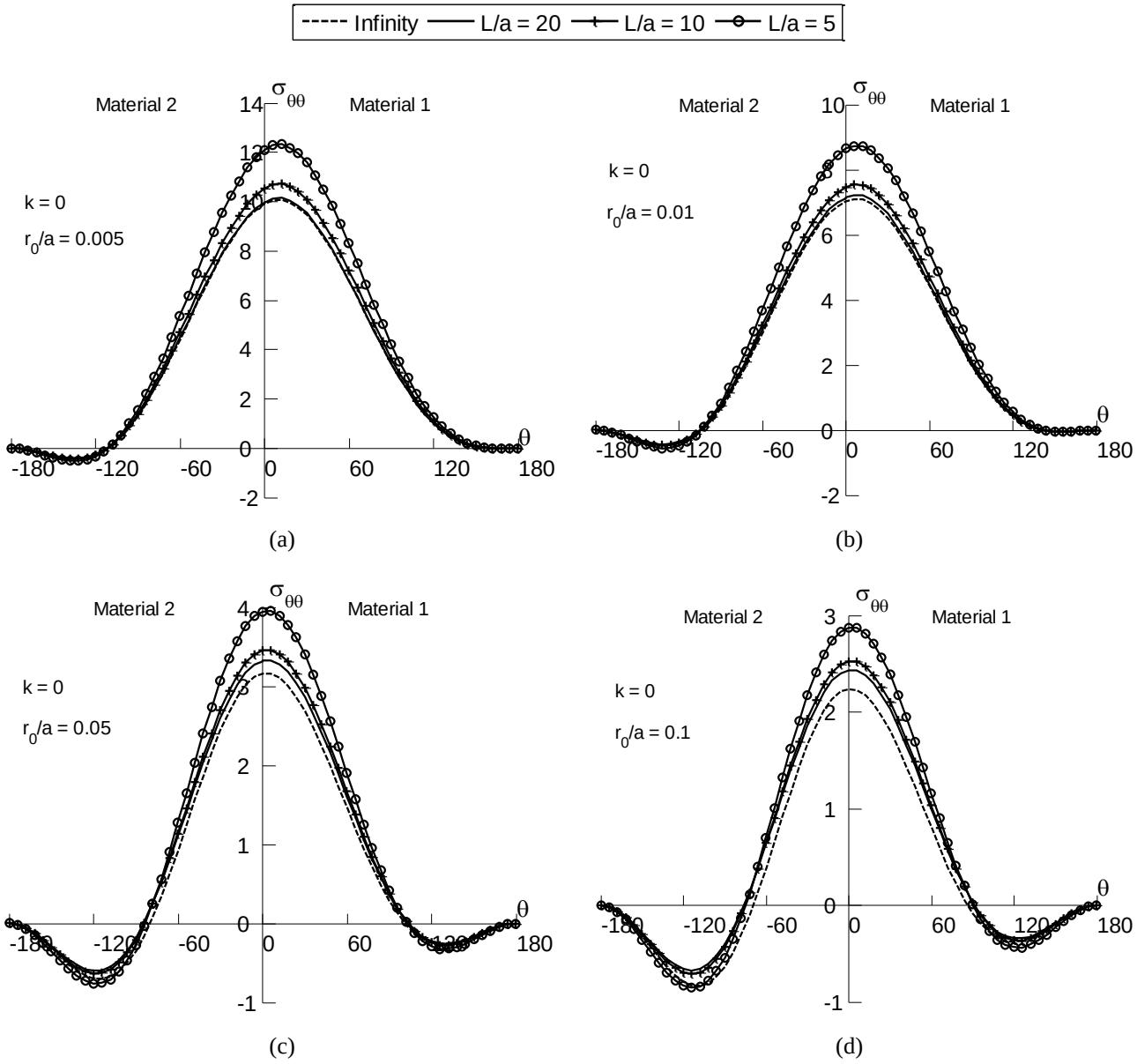

Fig. 5.16. Comparisons of circumferential stresses $\sigma_{\theta\theta}$ for various dimensions L/a and the ratios r_0/a when $k = 0$.

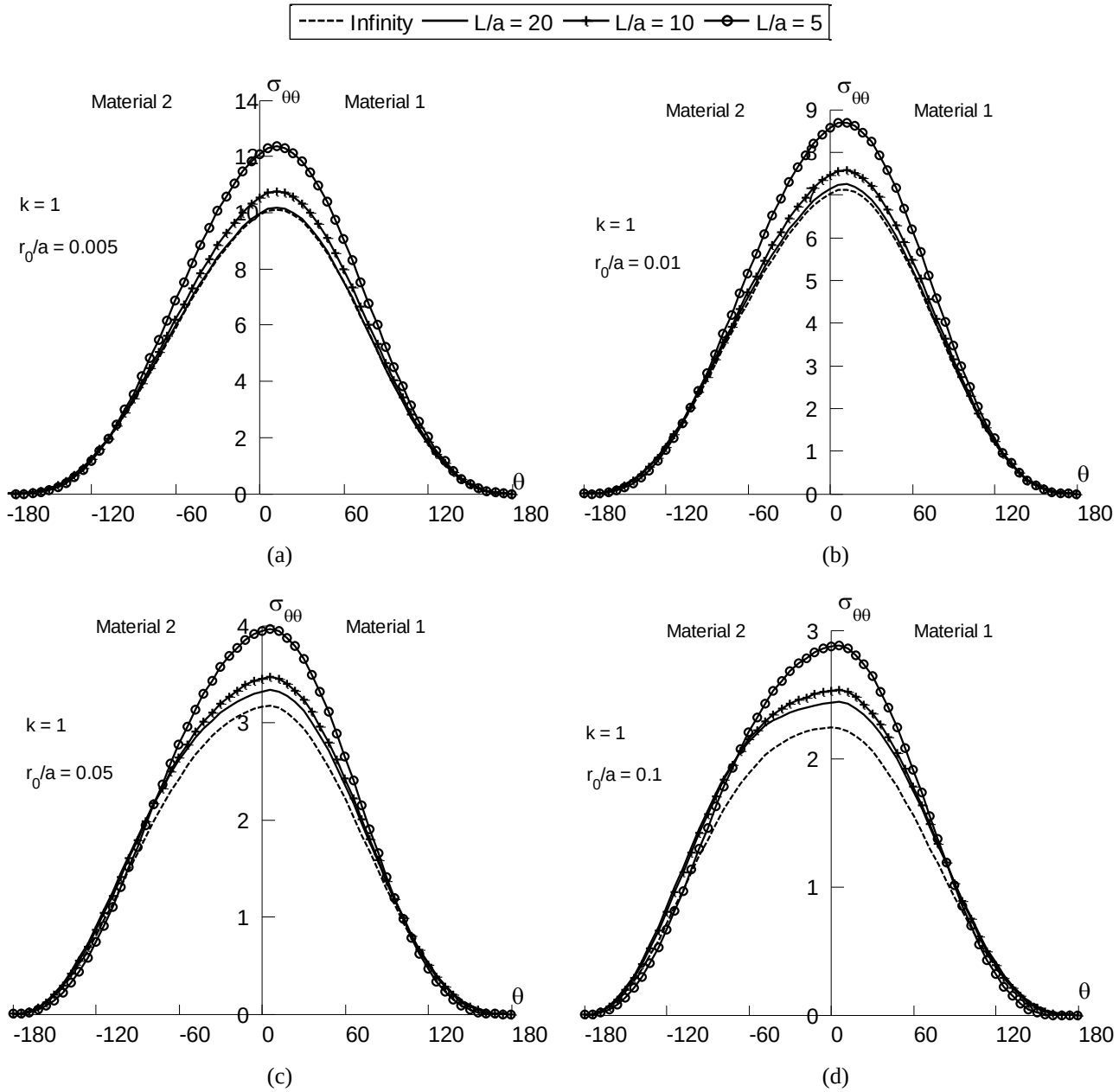

Fig. 5.17. Comparisons of circumferential stresses $\sigma_{\theta\theta}$ for various dimensions L/a and the ratios r_0/a when $k = 1$.

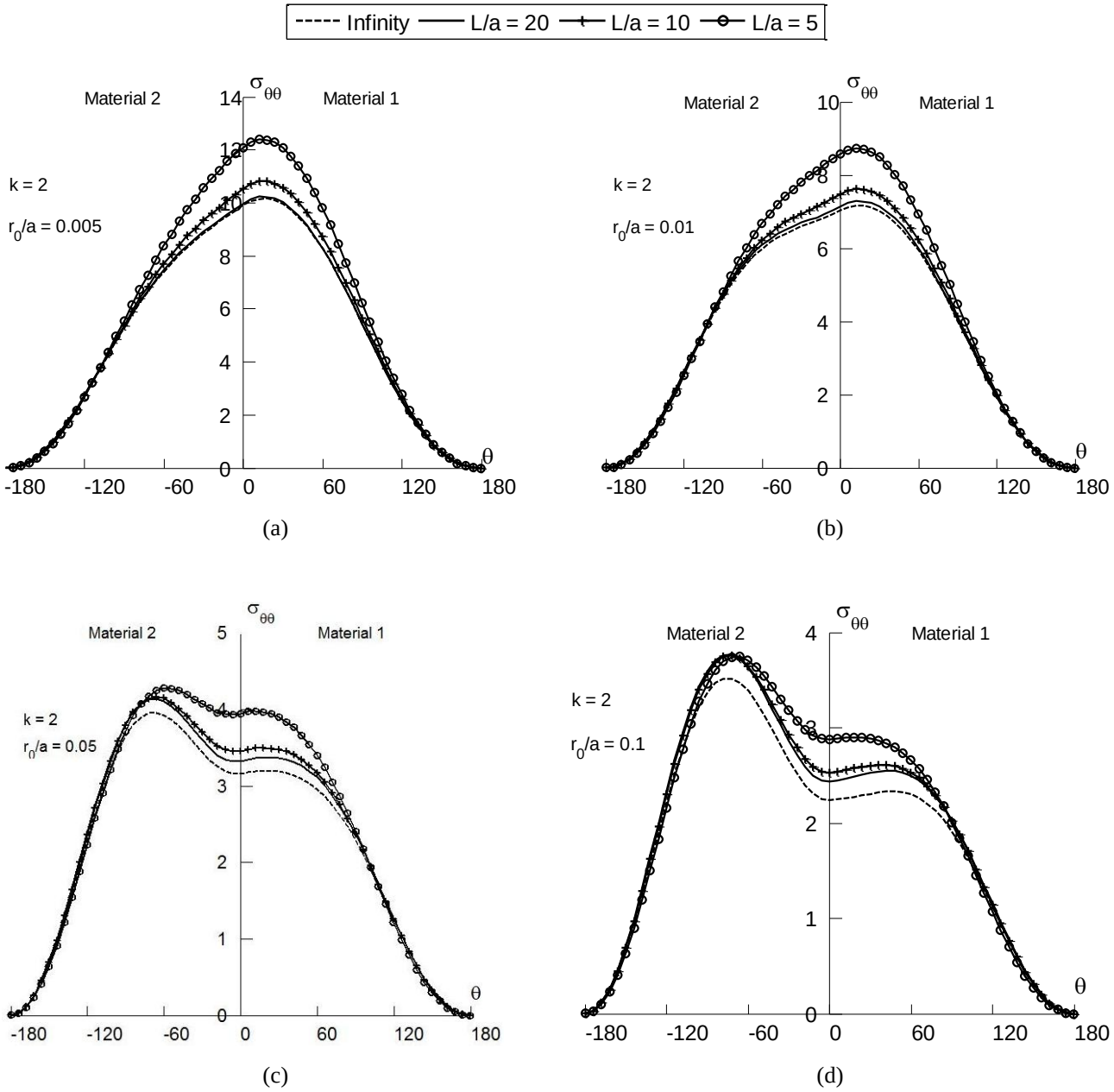

Fig. 5.18. Comparisons of circumferential stresses $\sigma_{\theta\theta}$ for various dimensions L/a and the ratios r_0/a when $k = 2$.

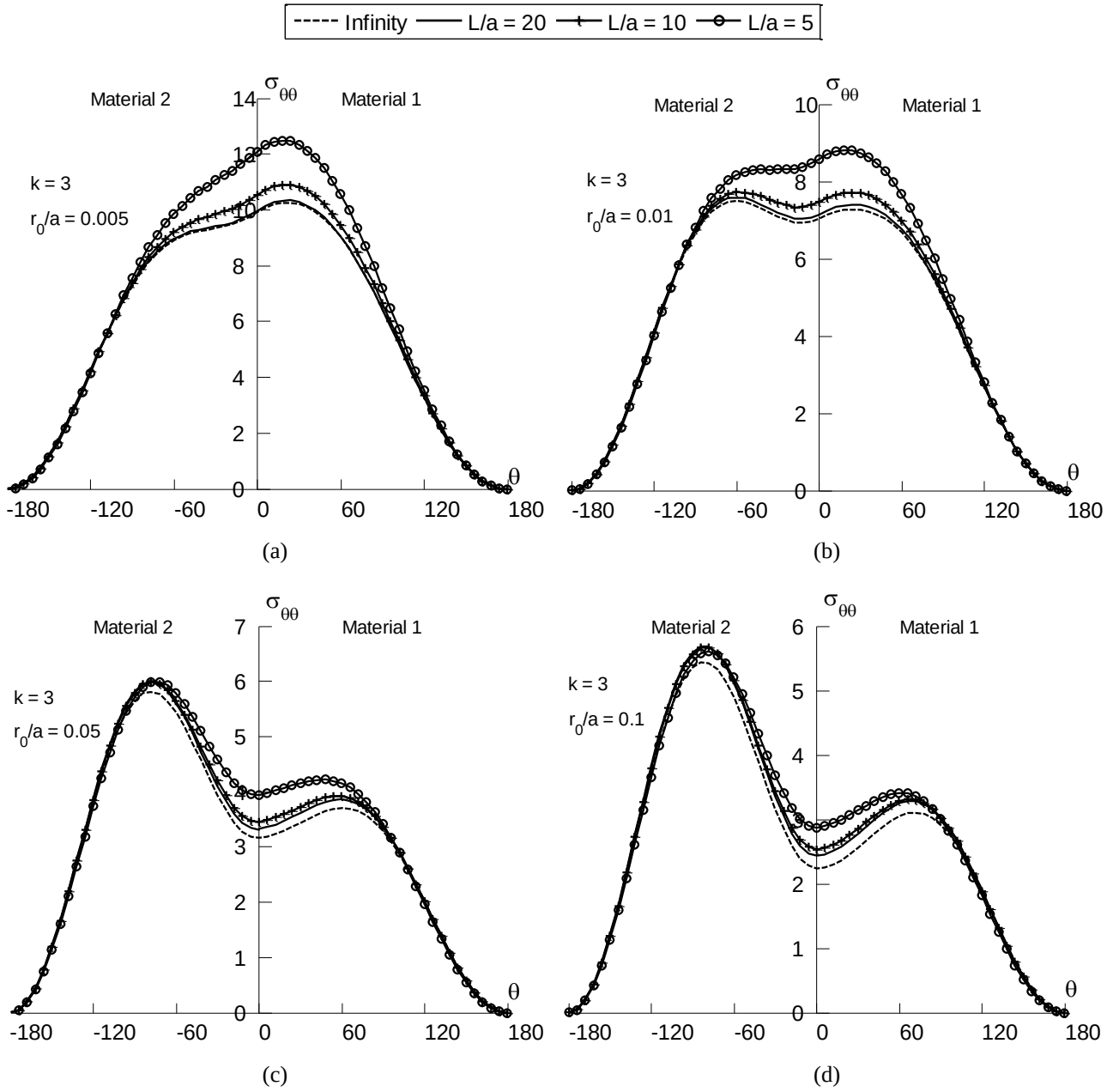

Fig. 5.19. Comparisons of circumferential stresses $\sigma_{\theta\theta}$ for various dimensions L/a and the ratios r_0/a when $k = 3$.

The effects of biaxial factors and distances before the crack tip to the circumferential stresses are studied. From Figs. 15-19, the circumferential stress law against the polar angle seriously depends on the biaxial factor k. However, according to the expressions of the stress components, the influence of the biaxial load is only on the normal stress σ_{xx} as reported in [7]. For a crack embedded in a homogeneous, isotropic and linearly elastic material, when the effect of the normal stress collinear to the plane of the crack is discarded, any failure condition is evaluated at a very small, but unknown, radial distance r_0 from the crack tip [16]. The importance of the distance r_0 has been extensively discussed in the literatures [7], and for the uniaxial loading conditions it is found that all the experimental results considered except one are in the area between two curves corresponding to

$$\frac{r_0}{a} = 10^{-2} \text{ and } \frac{r_0}{a} = 10^{-1} \tag{5.41}$$

For a better comparison of the influence of the dimension size, biaxial factor and the distance from the crack tip on the difference between analytical and numerical results, the relative errors of circumferential stress between those two results are calculated from the following formula for various dimension ratios, biaxial factors and distances from crack tip and are shown in Fig. 5.20.

$$\eta_\theta = \frac{\sigma^{(j)}_{\theta\theta\_ans} - \sigma^{(j)}_{\theta\theta\_num}}{\sigma^{(j)}_{\theta\theta\_ans}}, \qquad (j = 1, 2) \tag{5.42}$$

where the superscript j is the index of materials, the subscripts ans and num are analytical and numerical results, respectively.

Fig. 5.20 (a) and (b) correspond to Fig. 5.19 (b) and Fig. 5.13 (e), respectively. Fig. 5.20 (c) is a comprehensive graph of Fig. 5.13 (a-e). It clearly shows from Fig. 5.20 (a) that the relative errors expressed as the different between the analytical and numerical solutions are getting smaller as the dimension size ratio L/a increase. For $L/a = 5$ the error is up to the maximum 20%. When $L/a > 20$, the errors are very close to each other and less than 2 except the positions where circumferential get close to zero due to the character of the relative error definition. This character should be considered also in all the following analysis. For $k = -1$ and 0, the circumferential stress curves have two intersections with horizontal axis, respectively, there are four singular points due to the reasons mentioned before. Ignoring the singular points in Fig. 5.20 (c), the relative errors tend to be close to zero for different biaxial factors. It means the numerical calculation can be used for various biaxial factors. The difference of analytical and numerical solutions among the various distances from crack tip is compared in Fig. 5.20 (b). All the errors are less than 10, especially for $\frac{r_0}{a} = 0.005$ and 0.01, the numerical and analytical results are very close to each other.

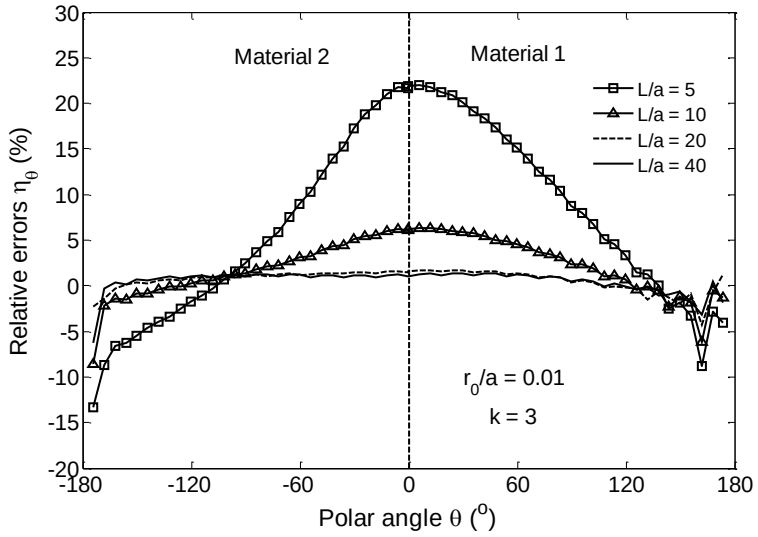

(a)

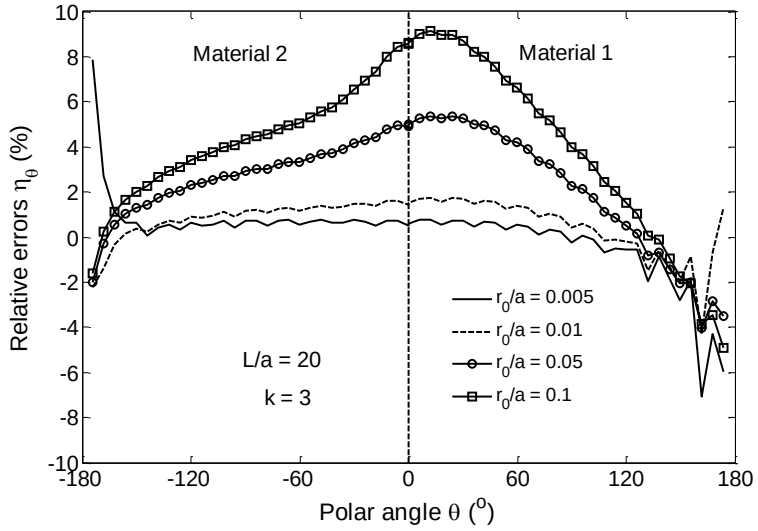

(b)

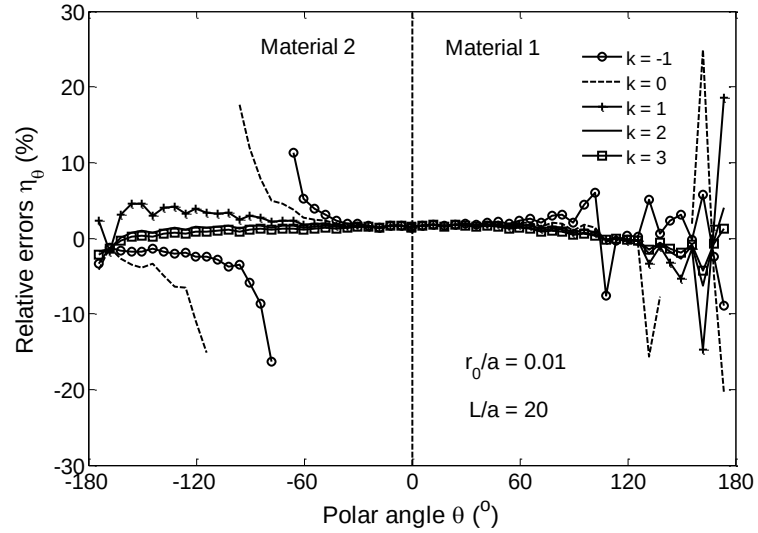

(c)

Fig. 5.20 Angular variation of the relative errors between analytical and numerical solutions for circumferential stress (a) various dimensions, (b) various biaxial factors, (c) various distances from crack tip.

5.5.2 Mises stress

For plane stress condition, the Mises equivalent stress can be written in the following form

$$\sigma_e^j = \left[\sigma_{xx}^{(j)2} + \sigma_{yy}^{(j)2} - \sigma_{xx}^{(j)}\sigma_{yy}^{(j)} + 3\sigma_{xy}^{(j)2}\right]^{1/2} \tag{5.43}$$

where $\sigma_{xx}^{(j)}$, $\sigma_{yy}^{(j)}$ and $\sigma_{xy}^{(j)}$ are the normal and shear stresses at points close to the tip of the crack, and j is the usual material index.

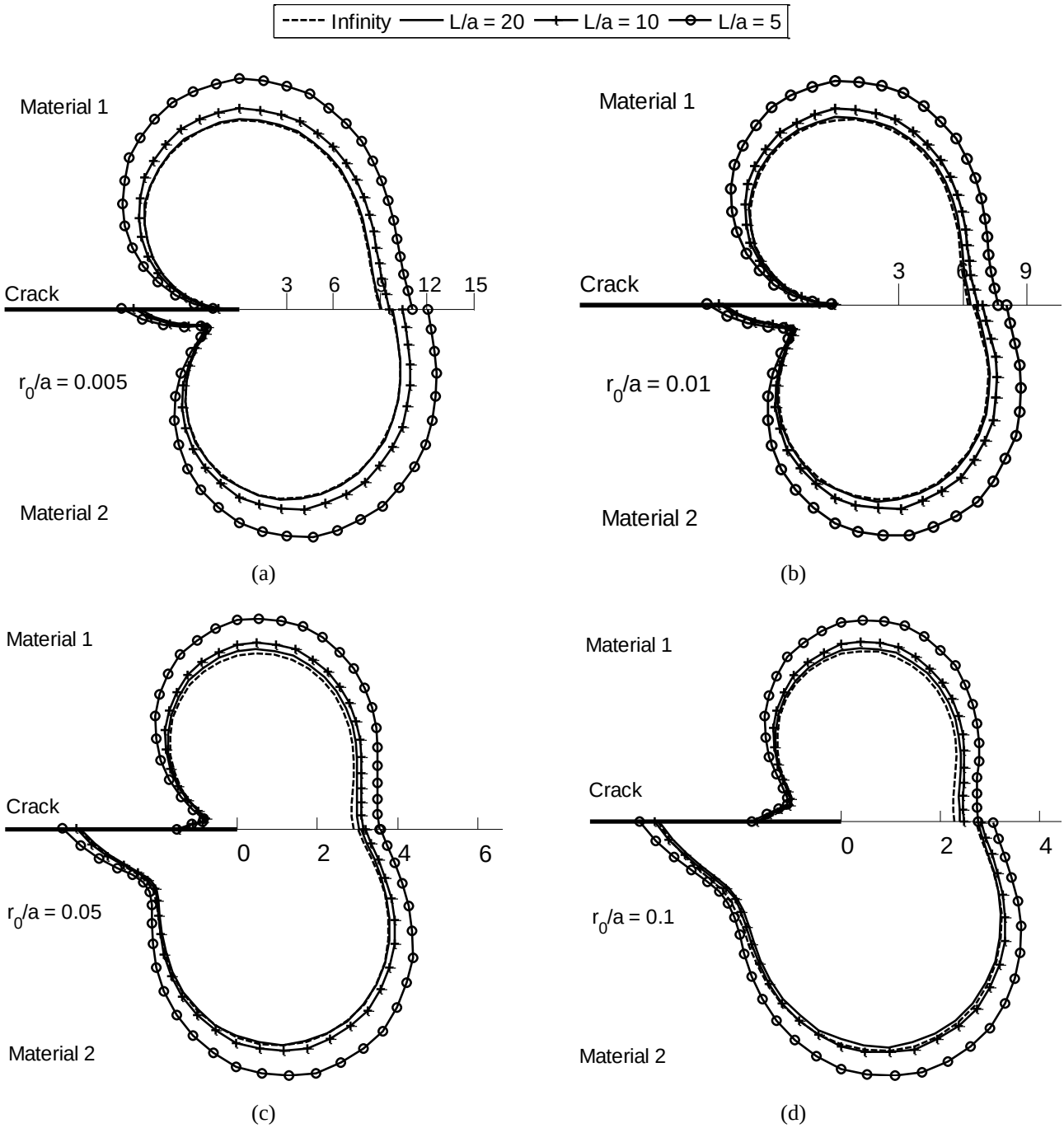

Fig. 5.21. Angular variation of the equivalent Mises stress for various values of the ratio r_0/a and dimensions L/a when $k = -1$.

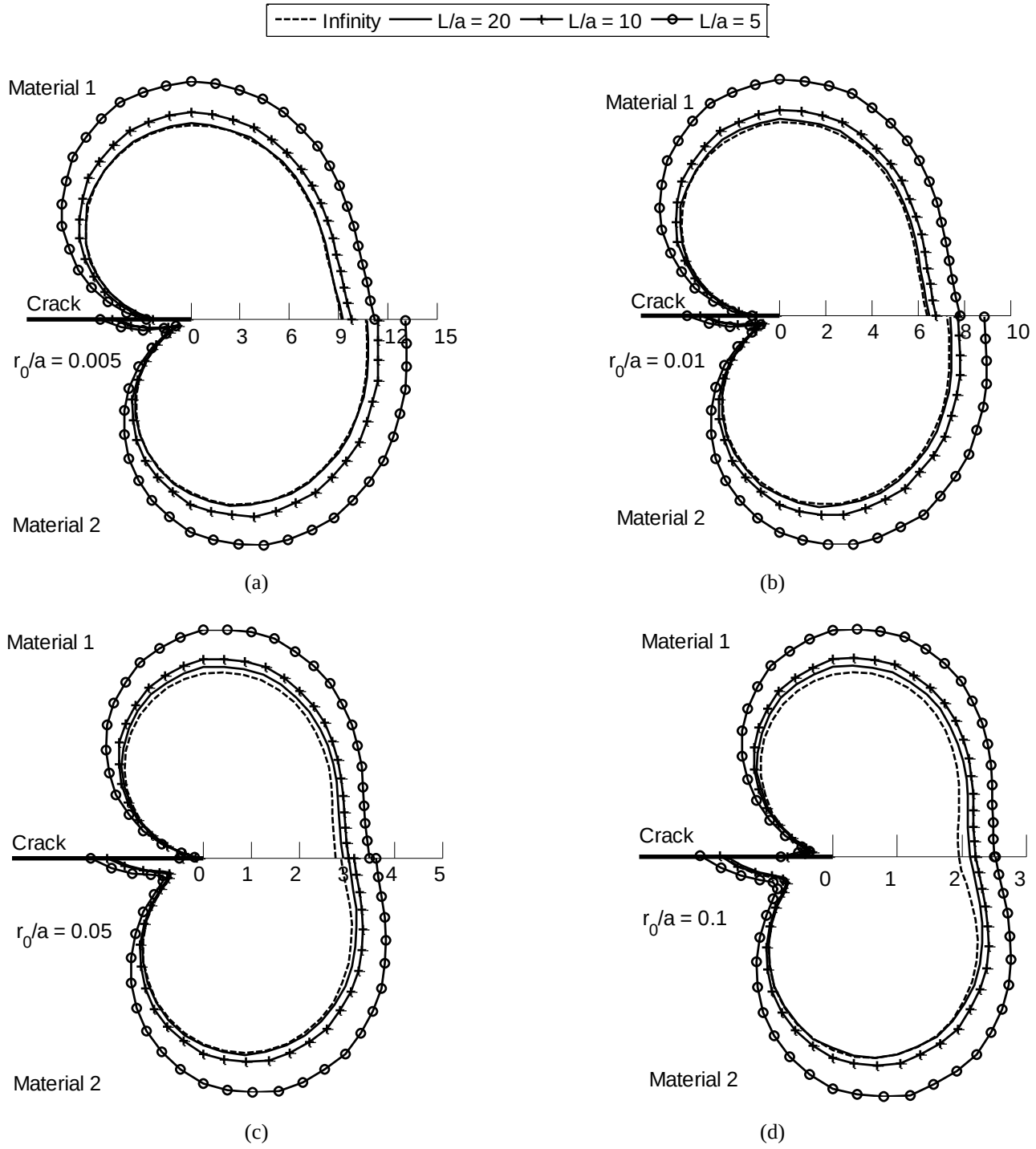

Fig. 5.22. Angular variation of the equivalent Mises stress for various values of the ratio r_0/a and dimensions L/a when $k = 0$.

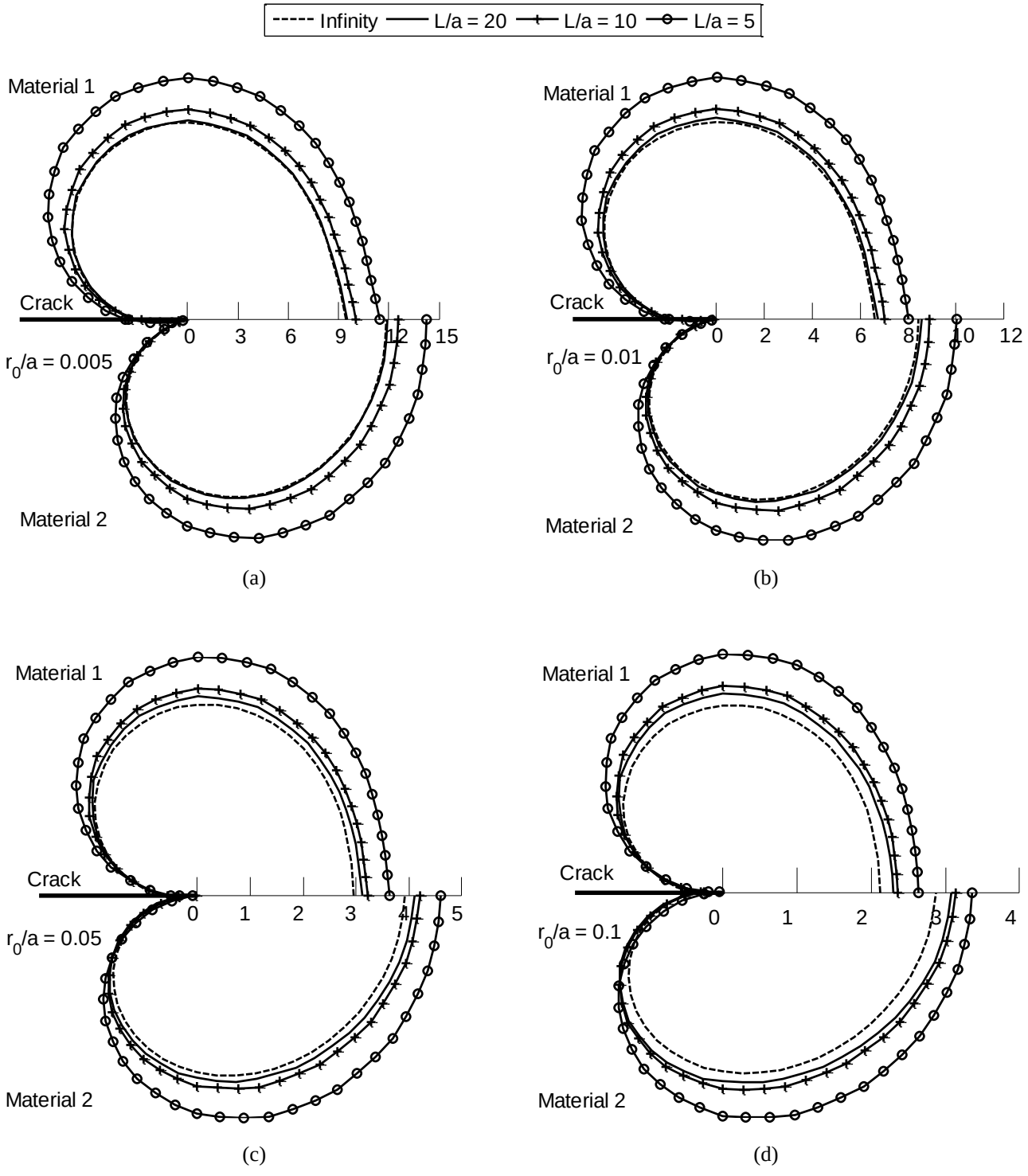

Fig. 5.23. Angular variation of the equivalent Mises stress for various values of the ratio r_0/a and dimensions L/a when $k = 1$.

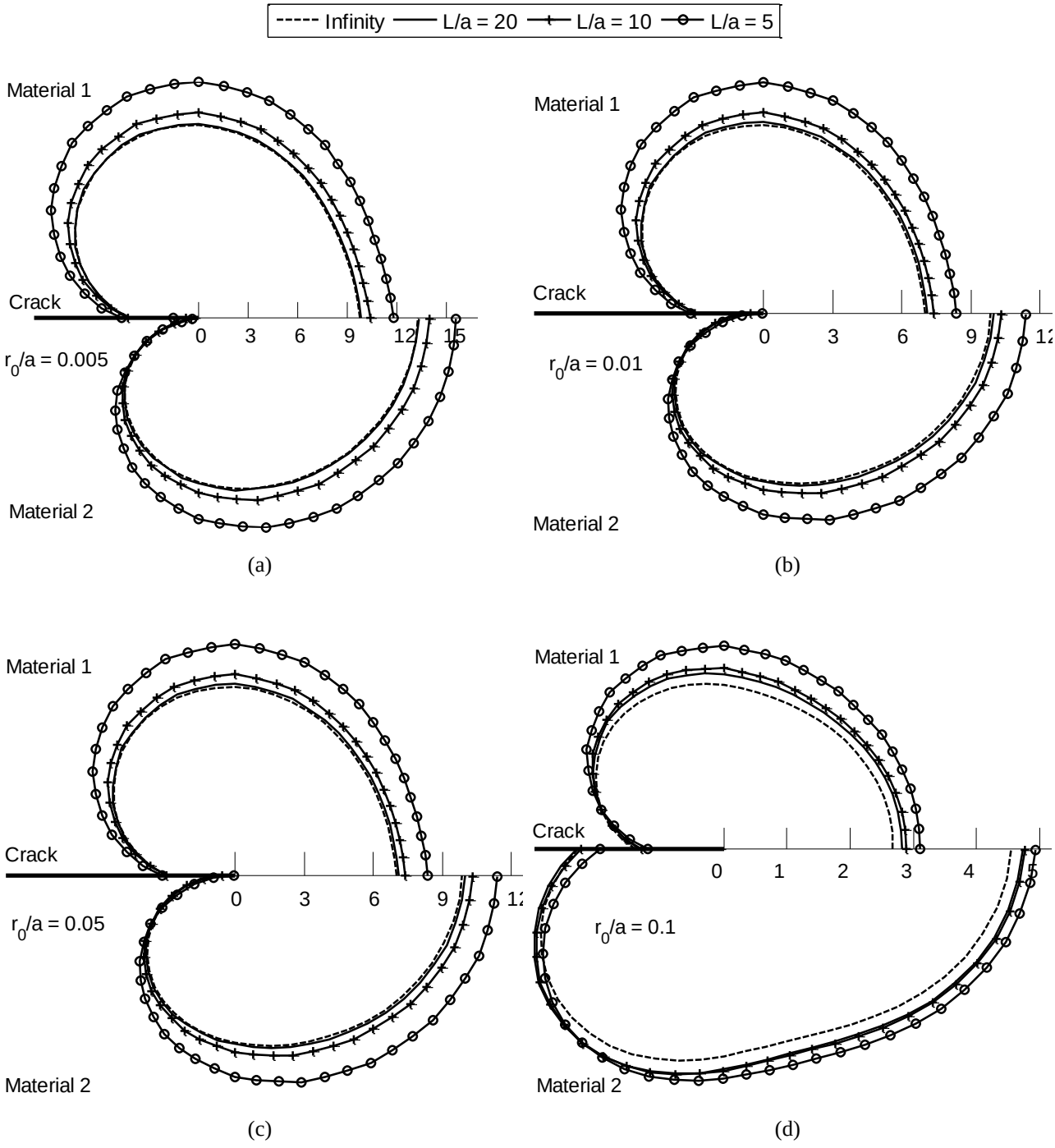

Fig. 5.24. Angular variation of the equivalent Mises stress for various values of the ratio r_0/a and dimensions L/a when $k = 2$.

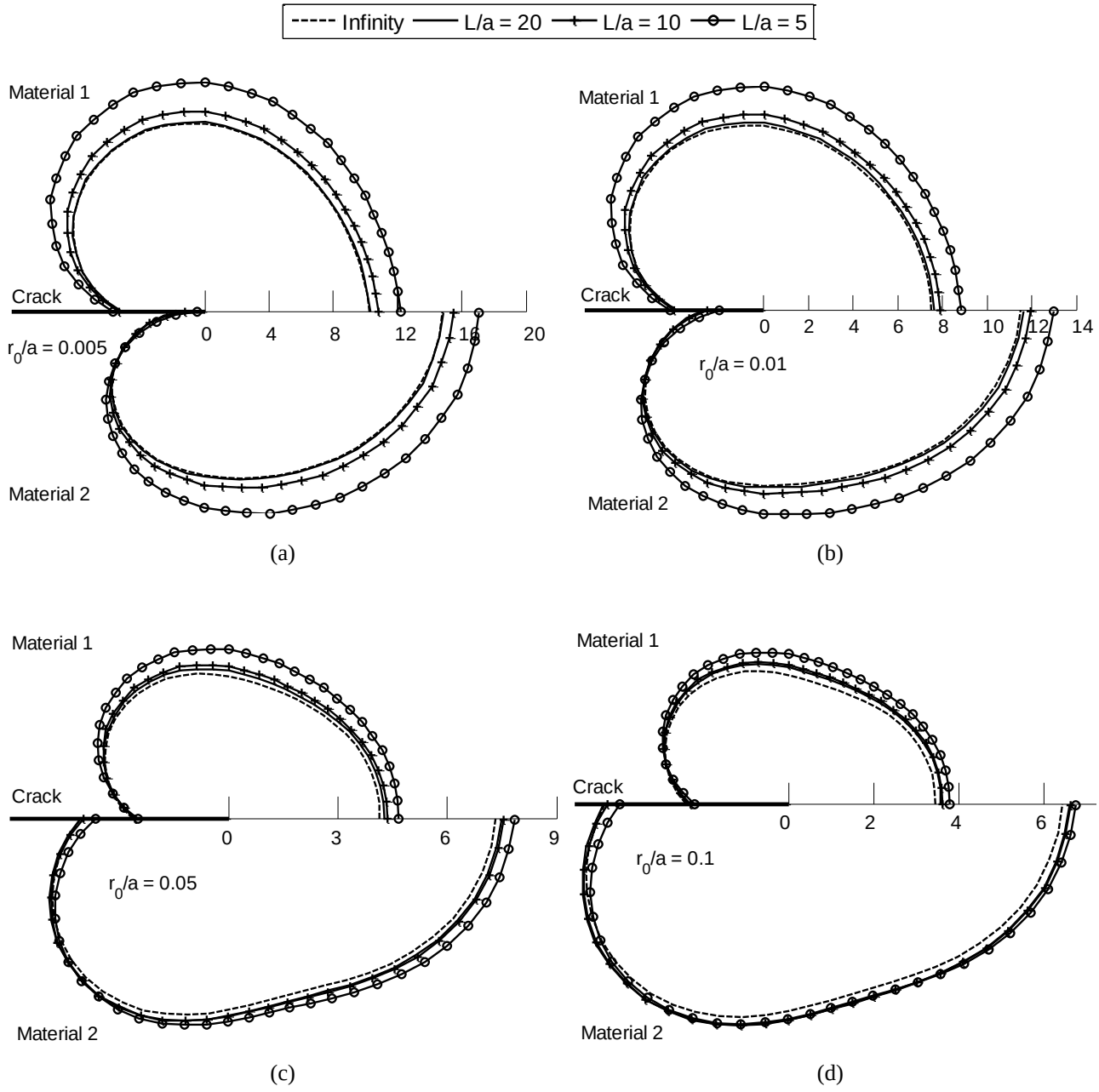

Fig. 5.25. Angular variation of the equivalent Mises stress for various values of the ratio r_0/a and dimensions L/a when $k = 3$.

The Mises stresses around the crack tip for different dimension models against to polar angle for bi-axial factor $k = -1, 0, 1, 2, 3$, respectively, are shown in Figs. 21-25. The dashed curves refer the infinity dimension models which come from the analytical results. The Mises stresses are obtained from eq. (5.43). From every single picture, the numerical results for dimension parameter $L/a = 20$ are the most approximate to the analytical results for all the values of distance r_0 and biaxial factor k. It's worthy noting that, different from circumferential stresses, the Mises stresses are not continue at both crack interface and bonded line. It can be noted that, the Mises stresses have the same shape (the curves haven't intersect) in both of the media when biaxial loading parameter exceeds zero and the bigger the biaxial loading parameter, the bigger the Mises stresses.

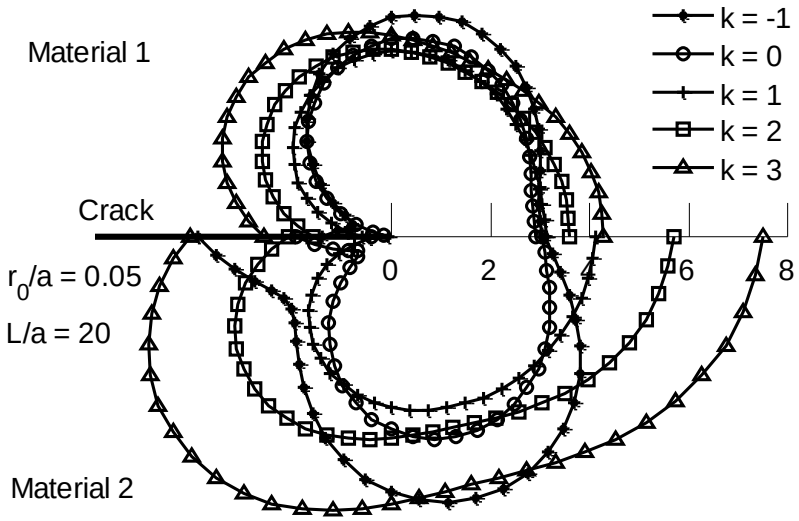

Fig. 5.26. Effect of biaxial factor k on the Mises equivalent stresses for $L/a = 10$ and $r_0/a = 0.05$.

The influence of biaxial factor k on the Mises stress distribution for $L/a = 10$ and $r_0/a = 0.05$ is shown in Fig. 5.26. It shows that the biaxial factor effects on Mises stresses for stronger material more than weaker one.

Similar to analysis of circumferential stress, the relative error of Mises stress is defined as

$$\eta_e = \frac{\sigma_{e\_ans}^{(j)} - \sigma_{e\_num}^{(j)}}{\sigma_{e\_ans}^{(j)}}, \qquad (j = 1, 2) \tag{5.44}$$

where the superscript j is the index of materials, the subscripts ans and num are analytical and numerical results, respectively.

The Mises stress differences between numerical and analytical solutions are plotted in Fig. 5.27, they also indicate use of the numerical solution which will be in the desired accuracy as testified in circumference stress.

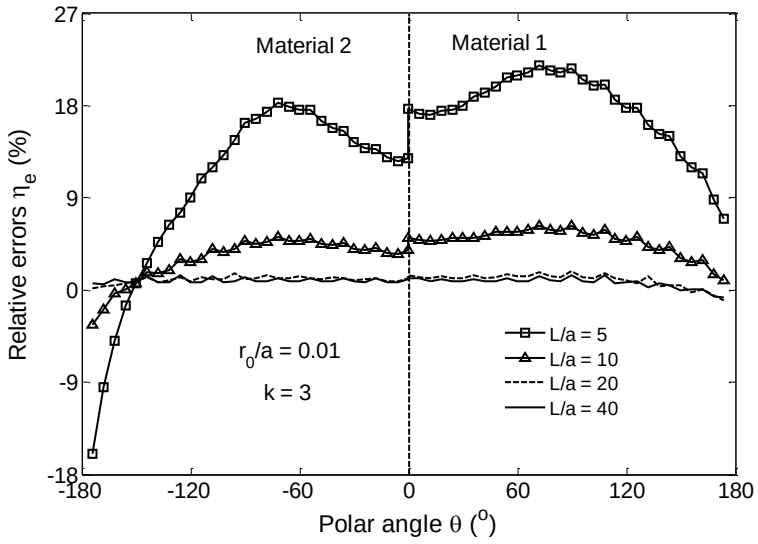

(a)

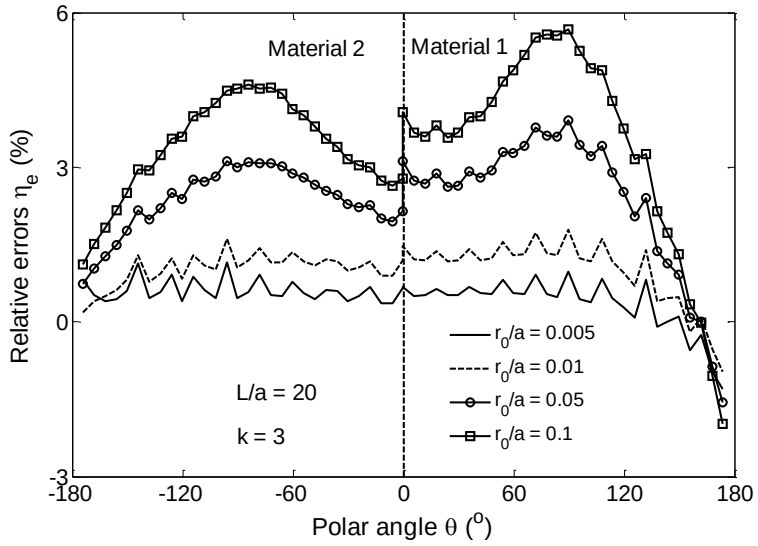

(b)

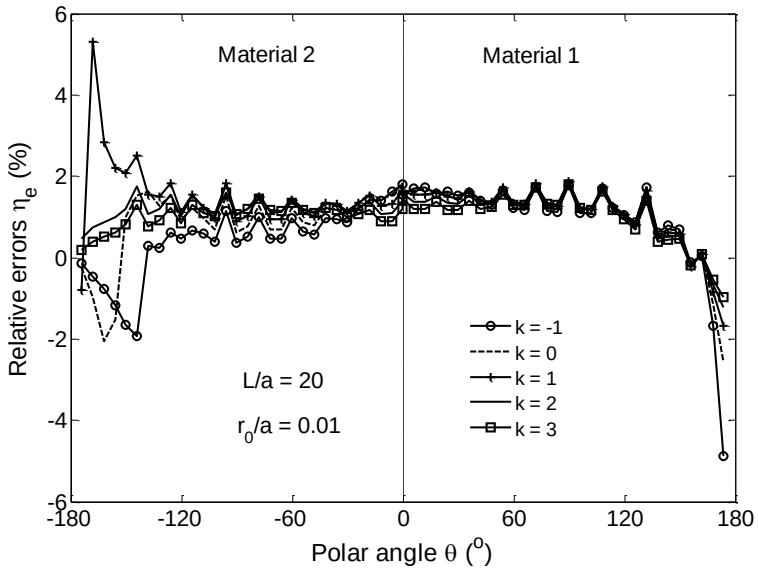

(c)

Fig. 5.27 Angular variation of the relative errors between analytical and numerical solutions for Mises stress (a) various dimension, (b) various biaxial factor, (c) various distance from crack tip.

5.5.3 Small plastic zone

The tendency of real materials, especially metals, which exhibiting a yield stress should be taken into account. In fact, there is always a region, although very small, around the crack tip, where plastic deformation occurs and stress singularities are not allowed. The crack tip distance r_0 of which the stress has to be evolution should exceed the fracture core zone for insuring the linear elastic theories are suitable. Therefore, the crisis distance of the external border of the elastic-plastic zone is very important. The characteristic dimension of the plastic zone, when one or both of the joined solids deforms plastically, depending on the material properties, including the yield strength σ_0 of the weaker of the two materials, the ratios of yield strengths, and dimensionless properties describe strain hardening and ratios of elastic constants. To investigate the effect of the biaxial load and dimension size on the size of plastic zone near the tip of a crack at the interface, Mises yield conditions can be applied

$$\sigma_e^{(j)} = \sigma_0^{(j)}, \ \ j = 1, 2 \tag{5.45}$$

where $\sigma_e^{(j)}$ are the Mises equivalent stresses and $\sigma_0^{(j)}$ are the uniaxial yielding stresses.

According to Mises criterion, the solid semicircles in Fig. 5.28 refer to the values of load levels $\sigma_0^{(1)}/T = 6$ in material 1 and $\sigma_0^{(2)}/T = 8$ in material 2, respectively. It may be observed that, for the fixed loading conditions, up to some distances r_0 from the crack tip and in almost the whole angular range, the equivalent stress $\sigma_e^{(j)}$ will exceeds the yield stress $\sigma_0^{(j)}$, i.e. plastic deformation occurs. But the above elastic analysis allows only a rough estimate of the plastic behavior of the two dissimilar media in a small neighborhood of the interface crack tip due to the Mises stress obtained from linear elastic theory. It's a simplified version of method introduced by Theocaris and Andrianopoulos [20].

From Fig. 5.28 (a)-(c), it verifies again that when dimension ratio $L/a = 20$, the numerical studies can be taken the place of analytical investigate, in other words, for some research objects that analytical results are impossible or difficult to be obtained, especially the practical objects, researchers can use numerical approaches to create and calculate the model.

The Mises stresses on the interface front of the crack tip calculated in dissimilar media against to the ratio of the distance from crack tip to crack length are graphically shown in Fig 5.29. It is worthwhile saying that for varies biaxial factors the plastic lengths on the bonded line in both media are different. In the present case, the bigger the biaxial factor is, the larger the plastic region is.

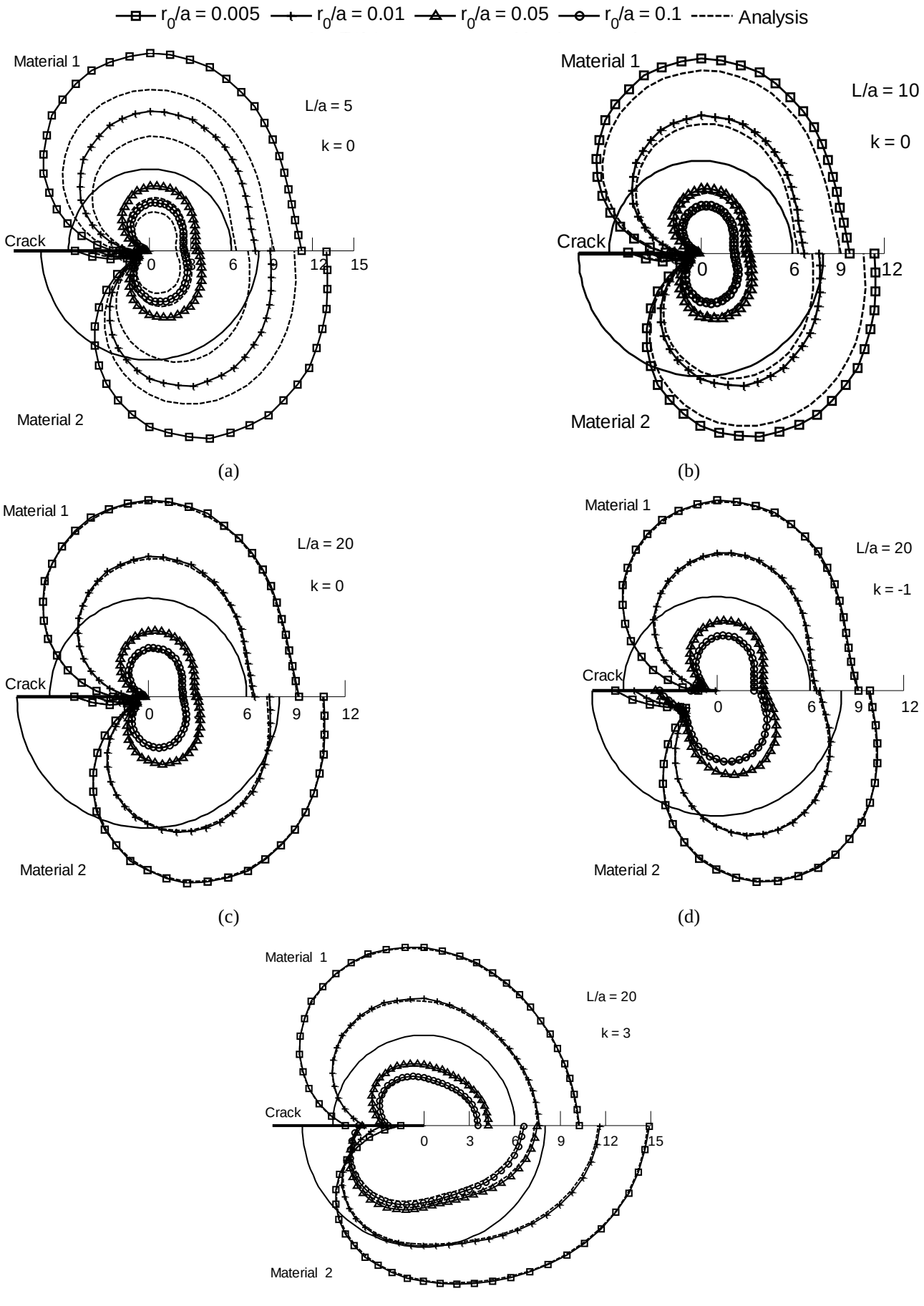

Fig. 5.28. Plastic zone according to Mises criterion for varies distance r_0 and different biaxial factors k.

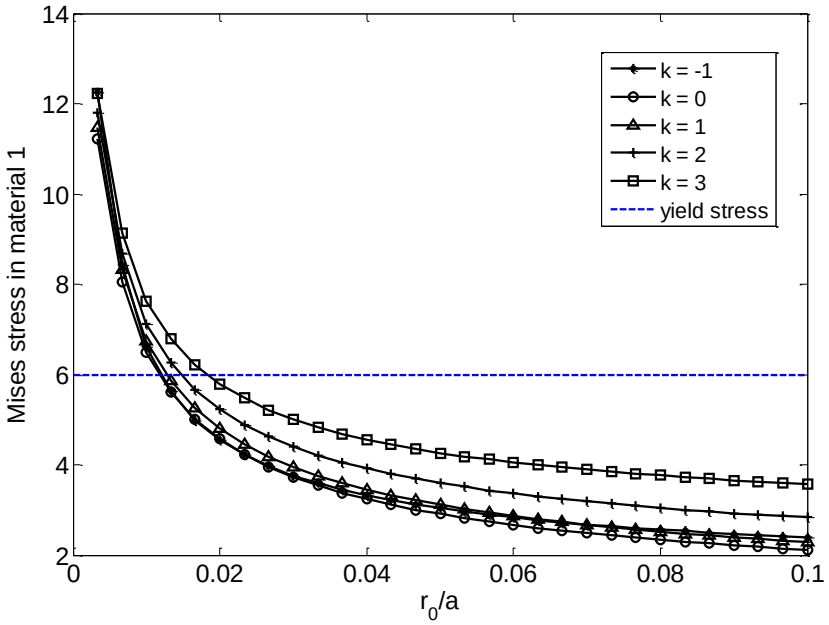

(a)

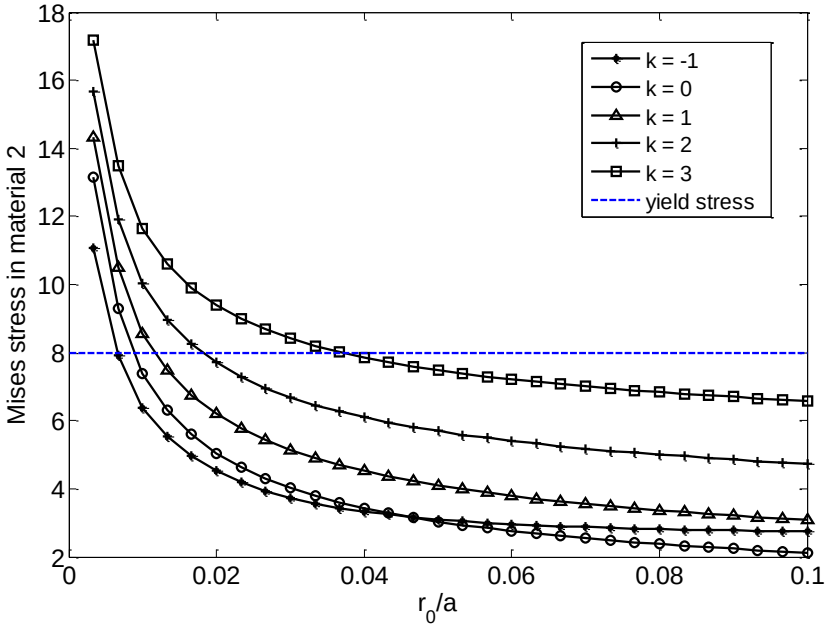

(b)

Fig. 5.29. Mises stresses on the interface front of crack tip (a) Material 1, (b) Material 2. Dashed lines refer to the values of load levels $\sigma_0^{(1)}/T = 6$, $\sigma_0^{(2)}/T = 8$, respectively. $L/a = 20$

It must be emphasized that although $\sigma_0^{(j)}$ means uniaxial yielding stresses, the material constant which shown in Fig. 5.28 the two semicircles in both media, the Mises stress is not a circular distribution around the crack tip. Therefore, according to Mises criterion, the plastic zone is not a circular region around the crack tip, but depends on the polar angle, as shown in Fig. 5.30 for load levels $\sigma_0^{(1)}/\mathrm{T} = 6$ and $\sigma_0^{(2)}/\mathrm{T} = 8$ and Fig. 5.31 are for different load levels. Note that for $\mathrm{k} = -1$ the compressive loading parallelling to the crack axis gives increased maximum distances to the zones

created as indicated in [32]. It also illustrated that the plastic zone in the weaker material is bigger than that in the stronger one. Fig. 5.31 (a) and (b) demonstrate the influence of the various yield stress levels on the zones of plastic for biaxial load factor $k = 2$ and $k = -1$, respectively. It can be seen that the smaller the yield stress level is, the bigger the plastic zone is. For $k > 0$, the plastic zones wider but lower than $k < 0$. On the bonded line, the Mises yielding initiation boundaries are much smaller in weaker material for listed yield load levels for $k = 2$, but inversely for $k = -1$.

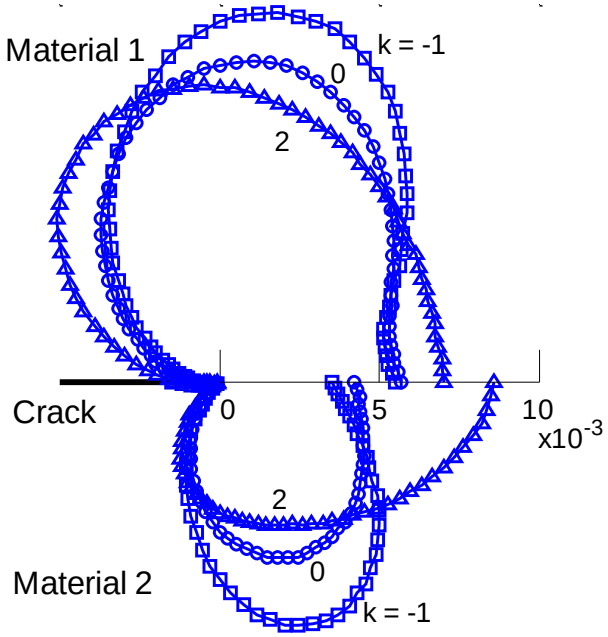

Fig. 5.30 Mises yield initiation boundary for different values of biaxial factor for load levels $\sigma_0^{(1)}/T = 6$, $\sigma_0^{(2)}/T = 8$.

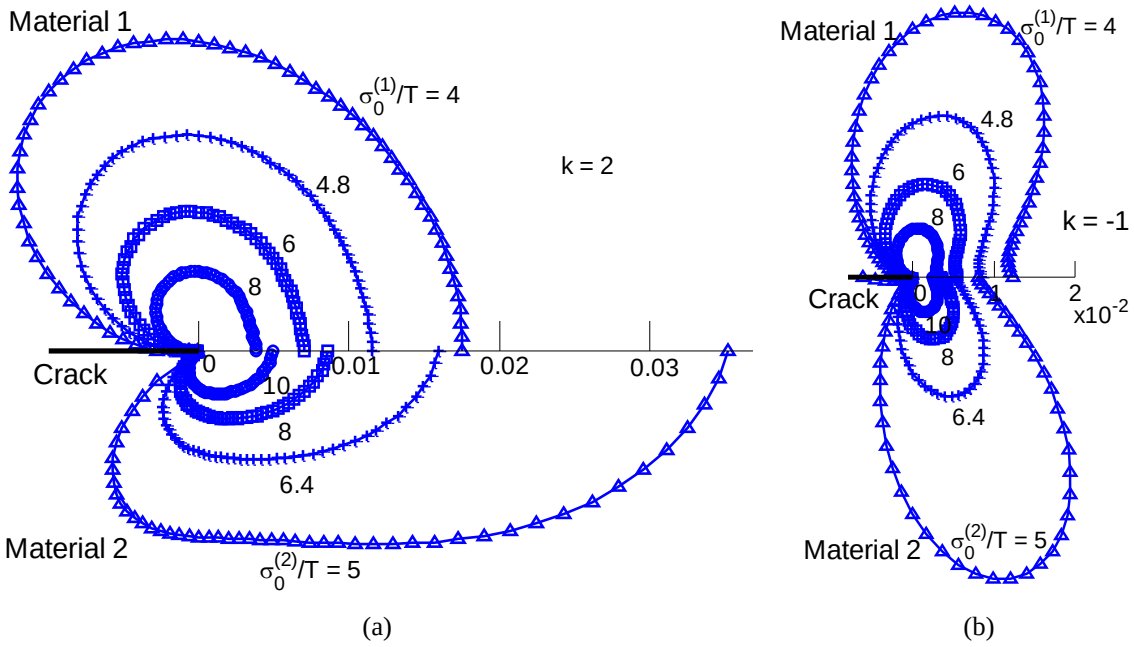

Fig. 5.31 Mises yield initiation boundary for different values load levels (a) $k = 2$ and (b)$k = -1$.

5.6 Remarks and conclusions

In this paper, analytical and numerical solutions concerning the fracture process of an interfacial crack between dissimilar materials under biaxial loading are compared and discussed. The effect of several parameters on the model response is investigated. The examined parameters are: the dimensions of the finite geometrical model, material combinations, the biaxial loading factor, strength at interface and the characteristic distance at which critical conditions must be evaluated. The model response includes the circumferential stress, the Mises equivalent stress, shape and extension of the plastic zone, the crack extension angle of the damaged system. The study of the stress field around the singular points is of particular interest, since the stress state affects the behavior of the cracked composite system. It appears that the fracture propagation takes place into one of the two bonded media or along the bond line, depending on the fracture properties of the two materials, the kind of bond and the biaxial loading factor. One of the aims of this study consists in finding the dimension of the finite interfacial crack system for which the analytical and numerical solutions are comparable. In this way, the analytical solution can be used for assessing displacements, stresses and strains of damaged systems of finite dimensions.

In order to point out some aspects connected with the proposed approach, in the following a number of general observations are reported.

a) As far as a crack embedded in a homogeneous, isotropic and linearly elastic material is concerned, any failure condition is evaluated at a very small, but unknown, radial distance r_0 from the crack tip, when the effect of the normal stress collinear to the plane of the crack is discarded. However, the analysis involving only singular terms in the stress and displacement expressions may not be adequate [52-56]. The omission of the second term of the series representation for the stresses is arbitrary and equivalent to ignore the biaxiality of the applied load. When the nonsingular term in hand is considered, the critical conditions of related stress quantities must be evaluated at a small and specified radial distance from the crack tip. Such a distance, which generally include the core region affected by damage and nonlinear deformation, is known as characteristic distance and represents an unknown parameter to be specified experimentally or analytically [7, 25, 54, 55]. The characteristic distance under discussion can be considered as a material property. In conclusion, to make possible the application of criteria of crack extension at the interface, or its deviation into one of the two dissimilar bonded media, a small distance from the crack tip has to be specified.

b) Regarding the application of fracture mechanics to investigate the static behavior of composite structures, in this study the mathematical model of the interfacial crack between two dissimilar materials is reviewed. The use of such a model in the analysis of adhesive joints has been the subject of debate for at least five decades, since Malyshev and Salganik [51] proposed the energy release rate

G as the fracture parameter for a crack propagating on the interface. However, the G parameter cannot represent the inflection of the mixed mode ratio, therefore the use of stress intensity factors K_I, K_{II} as the fracture parameters have been introduced [7-9, 46, 48-50]. In analyzing interface crack problems in composite structures, the crack advancing process and the failure mechanisms affecting the interface and the bonded dissimilar materials need to be determined. The knowledge of the toughness parameter, which is a function of the radial direction starting from the crack tip, allows the calculation of the applied critical load for the cracking process in heterogeneous media [2, 7-8, 53].

c) Damaged regions at the interface between two dissimilar media can be modeled as line cracks which tend to enhance the initiation of failure by fracture [57-62]. The stress and displacement fields near the crack tip have to account for the influence of the load parallel to the crack direction. The finite critical distance from the crack tip should be specified to provide stress and strain states, as well as to apply criteria of crack extension at the interface, or its extension into one of the two dissimilar materials. In fact, the interfacial crack model has three possible paths when the loading is increased. The most possible path is along the interface when the bonding strength of the interface is weaker than the strength of the adherent materials. However, the interface crack kinks into one of the bonded media when the fracture parameter at a certain distance from the crack tip assumes its maximum value along a radial direction different from the interface itself. In bonded composite structures, the prediction of the growth of an interface crack between two dissimilar materials, or its deviation into one of the two adherent media, constitutes the most important problem involving the fracture process of composite structures. Such a problem is generally solved on the assumption of Linear Elastic Fracture Mechanics (LEFM). However, the experimental evidence for the problem under discussion suggests that the effects of nonlinear deformation and damage accumulation at crack tip should also be included. As a matter of fact, the fracture process should be based upon physical models accounting for damage processes in front of the crack tip. However, the exact descriptions of these processes need further investigations.

d) The interfacial crack model in a composite structure can also be described by assuming that the adherents are joined along the common part of their boundary by a continuous distribution of linear springs of proper stiffness, which simulate the presence of the adhesive. Such an interface model is able to represent the behavior of a thin, soft, elastic layer. It is usually referred to as “elastic interface”, “week interface” or “imperfect interface”. When the layer thickness approaches to zero, the stiffness of the springs vanishes. Moreover, if the two adherents of the interface model are made of the same material, the strong interface case corresponds to a crack in a homogeneous material.

In this paper two kinds of interface have been considered. For strong interfaces, cracks sometimes kink out of the interface itself and then extended into one of two adjacent materials. In addition, a fracture criterion is used for predicting the kinking angle of interface crack between two dissimilar isotropic elastic media. As said above, for the prediction of the initial crack extension the fracture criterion takes the effect of the non-singular stress terms into account. It is worth noting that the prediction of crack propagation, coupled with the evaluation of the corresponding critical external loading, is a valuable resource for ensuring structural integrity and damage tolerance of structures of relevant interest.

e) When a fracture criteria is applied, at a constant distance r_0 from the crack tip, to predict crack propagation the circle with radius r_0 centered at the crack tip is referred to as the "core region". It is important to emphasize that, from the physical point of view, crack propagation is a process involving the configuration change of a body, since new surfaces are created. In order to reflect the evolving domain boundaries, the grid of the numerical discretization have to be changed. An incremental grid refinement and remeshing is required. As a matter of fact, cracks can also be represented as displacement discontinuities in the continuum domain. The magnitude of the displacement discontinuity is physically represented by the magnitude of the crack opening.

The concept of discontinuous displacement fields have to be mathematically treated to develop a numerical framework for the problem of strong discontinuities due to strain localization [30]. The formation of new surfaces is controlled by surfaces laws, which are different from the constitutive laws of continuum.

f) The general interface fracture problem is of paramount importance for many micromechanics models and numerical problems of fracture mechanics. It has been shown that there is the oscillatory singularity near the interface crack tip, which is physically unreasonable since it leads to overlapping near the ends of the crack. In order to correct such unsatisfactory feature, a number of proposals of interfacial crack models have been put forward over the past decades. Initial studies on crack problems with interfaces revealed that the stress singularities exhibited an inverse square-root and the size of contact zone was very small in comparison with the crack length in a tensile field [1-4, 7, 9]. In order to calculate the critical interfacial fracture mechanics parameters, such as stress intensity factors and energy release rates for particular materials groups, the insertion of a thin, isotropic, homogeneous layer at the interface and the location of the crack within the interlayer have also been performed. This technique converts the interface crack problem into a homogeneous crack problem. Even if the interlayer is not physically present, it was artificially introduced for calculating the interfacial fracture parameters.

The interface fracture problem addressed by the present paper arises in numerous engineering applications and is anything but closed. Recently, a study upon the problem at issue presents a modified interface dislocation model to remove the oscillation singularity for interface fracture [43]. The critical interfacial fracture mechanics parameters, such as the stress intensity factor, the mode mixity and the energy release rates can be calculated. It is noticed that the Dirac delta function can be approached by a locally-distributed continuous function.

When fracture mechanics problems are analyzed, fracture processes are often assumed to occur within the boundary of the local singular stress field of the crack of concern. The assumption under discussion, referred to as K-dominant field, enables the use of infinite geometry, which eliminates the necessity of the consideration of geometrical shape. In this approach, only local properties and information around the primary crack tip are taken into account [36].

g) In this study, nonlinear phenomena connected with crack initiation and propagation, damage or large deformations are not considered. Within the framework of LEFM, the fracture itself and others non-linear phenomena that precede it are assumed to take place only within local regions which are small compared to the dimensions of cracks. As a matter of fact, composite materials, because of their intrinsic heterogeneities, are often affected by several nonlinear phenomena causing micro-structural evolution, such as void growth, micro-cracking and interfacial debonding. These damage mechanisms, in conjunction with eventual contact interaction between crack faces, strongly affect the behavior of composites. As a result, it is essential to analyze the effects of micro-structural phenomena on the macroscopic failure behavior of composite materials and structures. The analysis of the mechanical behavior of composite taking into account nonlinear phenomena, such as crack initiation and propagation, requires a computational effort. In [37], a nonlinear finite element model for a cracked single-lap adhesive joint with laminate adherents was developed. It was also shown that stresses, energy release rates, and stress intensity factors vary nonlinearly with the crack length. It should be emphasized that crack initiation analysis can be developed by using a coupled stress-energy approach, in order to study fracture onset in proximity of singularity and stress concentration.

References

[1] Williams ML. The stresses around a fault or crack in dissimilar media. Bull. Seismol. Soc. Amer. 1959; 49(2):199-204.

[2] England AH. A crack between dissimilar media. J. Appl. Mech. 1965; 32(2):400-402.

[3] Erdogan F. Stress distribution in bonded dissimilar materials with cracks. J. Appl. Mech. 1965; 32(2):403-410.

[4] Rice JR, Sih GC. Plane problems of cracks in dissimilar media. J. Appl. Mech. 1965; 32(2):418-423.

[5] Willis JR. Fracture mechanics of interfacial cracks. J. Mech. Phys. Solids 1971; 19(6): 353-368.

[6] Comninou M. The interface crack. J. Appl. Mech. 1977; 44(4):631-636.

[7] Piva A, Viola E. Biaxial load effects on a crack between dissimilar media. Engng. Fract. Mech. 1980; 13(1):143-174.

[8] Viola E, Piva A. Plane strain interfacial fracture analysis of a bimaterial incompressible body. Engng. Fract. Mech. 1981; 15(1-2):131-142.

[9] Rice JR. Elastic fracture mechanics concepts for interfacial cracks. J. Appl. Mech. 1988; 55 (1): 98-103.

[10] Leguillon D. Interface crack tip singularity with contact and friction. C.R.Acad.Sci. Paris 1999;327(5) :437-442.

[11] Comninou M. An overview of interface cracks. Engng Fract Mech 1990; 37(1):197-208.

[12] Mykhailova II, Menshykou OV, Menshykova MV, Guz IA. Boundary integral equations for an interface linear crack under harmonic loading. J. Comput. Appl Math. 2010; 234(7):2279-2286.

[13] Cornetti P, Mantic V, Carpinteri A. Finite fracture mechanics at elastic interfaces. Int. J. Solids Struct. 2012; 49(7-8): 1022-1032

[14] Hills DA, Barber JR. Interface cracks. Int. J. Mech. Sci. 1993; 35(1): 27-37.

[15] Shin KC, Liu H, Lee JJ, Choi ST. Interfacial crack tip field in anisotropic/isotropic biomaterials. Compos Struct 2004; 66(1-4):673-676.

[16] Erdogan F, Sih GC. On the crack extension in plates under plane loading and transverse shear. J Basic Engng 1963; 85:519-525.

[17] Sih GC. Some basic problems in fracture mechanics and new concepts. Engng Fract Mech 1973; 5(2): 365-77.

[18] Hussain MA, Pu SL, Underwood J. Strain energy release rate for a crack under combined mode I and mode II. Fract Anal ASTM STP 1974;560:2-28.

[19] Wu CH. Fracture under combined loads by maximum-energy-release-rate-criterion. J. Appl. Mech. 1978; 45(3):553-558.

[20] Theocaris PS, Andrianopoulos NP. The T-criterion applied to ductile fracture. Int. J. Fract 1982; 20(4):125-130.

[21] Papadopoulos GA. The stationary value of the third stress invariant as a local fracture parameter. (Det.-criterion). Engng Fract Mech 1987; 27(6): 643-652.

[22] Gol'dstein RV, Salganik RL. Brittle fracture of solids with arbitrary cracks. Int J Fract 1974;10(4):507-523.

[23] Yang QS, Qin QH. Numerical simulation of cracking processes in dissimilar media. Compos Struct 2001; 53(4): 403-407.

[24] Corneti P, Pugno N, Carpinteri A, Taylor D. Finite fracture mechanics: A coupled stress and energy failure criterion. Engng Fract Mech 2006;73(14): 2021-2033.

[25] Mróz KP, Mróz Z. On crack path evolution rules. Engng Fract Mech 2010; 77(11):1781-1807.

[26] He MY, Hutchinson JW. Kinking of a crack out of an interface. J. Appl. Mech. 1989; 56(2):270-278.

[27] Yuuki R, Xu JQ. Stress based criterion for an interface crack kinking out of the interface in dissimilar materials. Engng Fract Mech 1992; 41(5): 635-644.

[28] Yuuki R, Liu JQ, Xu JQ, Ohira T, Ono T. Mixed mode fracture criteria for an interface crack. Engng Fract Mech 1994; 47(3): 367-377.

[29] Ayatollahi MR, Mirsayar MM. Kinking angles for interface cracks. Procedia Engng 2011; 10:325-329.

[30] Rudraraju S, Salvi A, Garikipati K, Waas AM. Predictions of crack propagation using a variational multiscale approach and its application to fracture in laminated fiber reinforced composites. Compos Struct 2012; 94(11): 3336-3346.

[31] Theocaris PS, Andrianopoulos NP. The Mises elastic-plastic boundary as the core region in fracture criteria. Engng Fract Mech 1982; 16(3):425-432.

[32] Spyropoulos CP. An improved determination of the zones of yield initiation for the interface crack problem. Engng Frac Mech 1990; 36(2): 287-295.

[33] Spyropoulos CP. Crack initiation direction from interface of bonded dissimilar media. Theor Appl Fract Mech 2003; 39(1): 99-105.

[34] Buyukozturk O, Hearing B. Crack propagation in concrete composites influenced by interface fracture parameters. Int J Solids Struct 1998; 35(31-32):4055-4066.

[35] Choi BS, Chai YS. Interfacial crack propagation under various mode-mixes, KSME Int. J. 2002; 16(1):39-45.

[36] Lee W, Shin H, Yoo YH. Revisited criterion to present kinking of a crack out of a bi-material interface under the presence of in-plane residual stresses -- a global approach. Int. J. Engng Sci 2004; 42(3): 257-270.

[37] Kayupov M, Dzenis YA. Stress concentrations caused by bond cracks in single-lap adhesive composite joints. Compos Struct 2001;54(2-3):215-220.

[38] Goyal VK, Johnson ER., Goyal VK. Predictive strength fracture model for composite bonded joints. Compos Struct 2008;82(3):434-446.

[39] Goyal VK, Johnson ER, Davila CG. Irreversible constitutive law for modeling the delamination process using interfacial surface discontinuities. Compos Struct 2004;65(3-4):289-305.

[40] Yang TL, Liu YB, Wang J. A study of the propagation of an embedded crack in a composite laminate of finite thickness. Compos Struct 2003;59(4):473-479.

[41] Kaminski M. Stochastic boundary element method analysis of the interface defects in composite materials. Compos Struct 2012;94(2):394-402.

[42] O'Day MP, Curtin WA. Bimaterial interface fracture: A discrete dislocation model. J Mech Phys Solids 2005; 53(2):359-382.

[43] Zhang AB, Wang BL. An opportunistic analysis of the interface crack based on the modified interface dislocation method. Int. J. Solids Struct 2012 In press.

[44] Muskhelishvili NI. Some basic problems of the mathematical theory of elasticity. 3rd Ed. Noordhoff. Groningen, 1953.

[45] Dundurs J. Edge-bonded dissimilar orthogonal elastic wedges. J. Appl. Mech. 1969;36(3):650-652.

[46] Hutchinson JW, Mear M, Rice JR. Crack paralleling an interface between dissimilar materials. ASME J. Appl. Mech. 1987;54(4):828-832.

[47] ABAQUS/CAE 6.11 user's manual.

[48] Huynh DBP, Belytschko T. The extended finite element method for fracture in composite materials. Int. J. Numer. Meth. Eng. 2009;77:214-239.

[49] Ayatollahi MR, Sedighiani K. A T-stress controlled specimen for mixed mode fracture experiments on brittle materials. Eur J Mech A-Solid 2012; 36:83-93.

[50] Wang TT, Kwei TK, Zupko HM. Tensile strength of butt-joined epoxy-aluminum plates. Int. J. Fract. Mech. 1970; 6(2):127-137.

[51] Malyshev BM, Salganik RL. The strength of adhesive joints using the theory of fracture. Int. J. Fract. Mech. 1965, I: 114-128.

Appendix

The Cartesian components of the stress tensor near the right tip of the interface crack are readily obtained from [7]. We have in the medium 1, for $0 < r/a \ll 1$ and $0 \le \theta \le \pi$, the following expressions

$$\sigma_{xx}^{(1)} \cong (k+1)T - \frac{4T}{1+\alpha} + \frac{T\sqrt{a\alpha\pi}}{(1+\alpha)\sqrt{2\pi r}}\left\{3e^{\epsilon(\theta-\pi)}\left[cos\left(\epsilon log\frac{r}{l}+\frac{\theta}{2}\right)-2\epsilon sin\left(\epsilon log\frac{r}{l}+\frac{\theta}{2}\right)\right] - e^{-\epsilon(\theta-\pi)}\left[cos\left(\epsilon log\frac{r}{l}-\frac{\theta}{2}\right)-2\epsilon sin\left(\epsilon log\frac{r}{l}-\frac{\theta}{2}\right)\right]\right\} - \frac{T\sqrt{a\alpha\pi}e^{\epsilon(\theta-\pi)}}{(1+\alpha)\sqrt{2\pi r}}(1+4\epsilon^2)sin\theta sin\left(\epsilon log\frac{r}{l}+\frac{3\theta}{2}\right) \quad (A.1)$$

$$\sigma_{yy}^{(1)} \cong \frac{T\sqrt{a\alpha\pi}}{(1+\alpha)\sqrt{2\pi r}}\left\{e^{\epsilon(\theta-\pi)}\left[cos\left(\epsilon log\frac{r}{l}+\frac{\theta}{2}\right)-2\epsilon sin\left(\epsilon log\frac{r}{l}+\frac{\theta}{2}\right)\right] + e^{-\epsilon(\theta-\pi)}\left[cos\left(\epsilon log\frac{r}{l}-\frac{\theta}{2}\right)-2\epsilon sin\left(\epsilon log\frac{r}{l}-\frac{\theta}{2}\right)\right]\right\} + \frac{T\sqrt{a\alpha\pi}e^{\epsilon(\theta-\pi)}}{(1+\alpha)\sqrt{2\pi r}}(1+4\epsilon^2)sin\theta sin\left(\epsilon log\frac{r}{l}+\frac{3\theta}{2}\right) \quad (A.2)$$

$$\sigma_{xy}^{(1)} \cong \frac{T\sqrt{a\alpha\pi}}{(1+\alpha)\sqrt{2\pi r}}\left\{e^{\epsilon(\theta-\pi)}\left[sin\left(\epsilon log\frac{r}{l}+\frac{\theta}{2}\right)+2\epsilon cos\left(\epsilon log\frac{r}{l}+\frac{\theta}{2}\right)\right] + e^{-\epsilon(\theta-\pi)}\left[sin\left(\epsilon log\frac{r}{l}-\frac{\theta}{2}\right)+2\epsilon cos\left(\epsilon log\frac{r}{l}-\frac{\theta}{2}\right)\right]\right\} + \frac{T\sqrt{a\alpha\pi}e^{\epsilon(\theta-\pi)}}{(1+\alpha)\sqrt{2\pi r}}(1+4\epsilon^2)sin\theta cos\left(\epsilon log\frac{r}{l}+\frac{3\theta}{2}\right) \quad (A.3)$$

and in the medium 2 for $0 < r/a \ll 1$ and $-\pi \le \theta \le 0$,

$$\sigma_{xx}^{(2)} \cong \mu\left((k+1)T - \frac{4T}{1+\alpha}\right) + \frac{T\sqrt{a\alpha\pi}}{(1+\alpha)\sqrt{2\pi r}}\left\{3e^{\epsilon(\theta+\pi)}\left[cos\left(\epsilon log\frac{r}{l}+\frac{\theta}{2}\right)-2\epsilon sin\left(\epsilon log\frac{r}{l}+\frac{\theta}{2}\right)\right] - e^{-\epsilon(\theta+\pi)}\left[cos\left(\epsilon log\frac{r}{l}-\frac{\theta}{2}\right)-2\epsilon sin\left(\epsilon log\frac{r}{l}-\frac{\theta}{2}\right)\right]\right\} - \frac{T\sqrt{a\alpha\pi}e^{\epsilon(\theta+\pi)}}{(1+\alpha)\sqrt{2\pi r}}(1+4\epsilon^2)sin\theta sin\left(\epsilon log\frac{r}{l}+\frac{3\theta}{2}\right) \quad (A.4)$$

$$\sigma_{yy}^{(2)} \cong \frac{T\sqrt{a\alpha\pi}}{(1+\alpha)\sqrt{2\pi r}}\left\{e^{\epsilon(\theta+\pi)}\left[cos\left(\epsilon log\frac{r}{l}+\frac{\theta}{2}\right)-2\epsilon sin\left(\epsilon log\frac{r}{l}+\frac{\theta}{2}\right)\right]\right.$$
$$\left.+\,e^{-\epsilon(\theta+\pi)}\left[cos\left(\epsilon log\frac{r}{l}-\frac{\theta}{2}\right)-2\epsilon sin\left(\epsilon log\frac{r}{l}-\frac{\theta}{2}\right)\right]\right\}$$
$$+\frac{T\sqrt{a\alpha\pi}e^{\epsilon(\theta+\pi)}}{(1+\alpha)\sqrt{2\pi r}}(1+4\epsilon^2)sin\theta sin\left(\epsilon log\frac{r}{l}+\frac{3\theta}{2}\right) \quad (A.5)$$

$$\sigma_{xy}^{(2)} \cong \frac{T\sqrt{a\alpha\pi}}{(1+\alpha)\sqrt{2\pi r}}\left\{e^{\epsilon(\theta+\pi)}\left[sin\left(\epsilon log\frac{r}{l}+\frac{\theta}{2}\right)+2\epsilon cos\left(\epsilon log\frac{r}{l}+\frac{\theta}{2}\right)\right]\right.$$
$$\left.+\,e^{-\epsilon(\theta+\pi)}\left[sin\left(\epsilon log\frac{r}{l}-\frac{\theta}{2}\right)+2\epsilon cos\left(\epsilon log\frac{r}{l}-\frac{\theta}{2}\right)\right]\right\}$$
$$+\frac{T\sqrt{a\alpha\pi}e^{\epsilon(\theta+\pi)}}{(1+\alpha)\sqrt{2\pi r}}(1+4\epsilon^2)sin\theta cos\left(\epsilon log\frac{r}{l}+\frac{3\theta}{2}\right) \quad (A.6)$$

The biaxial parameter k affects the stress σ_{xx} alone through a term which independent of the radial distance from crack tip, as in the homogeneous.

As far as the stress region is concerned, we shall assume that the quantity controlling the fracture initiation is the circumferential stress evaluated at a small radial distance r_0 from the crack tip.

We have in the medium 1, for $0 < r/a \ll 1$ and $\theta = 0$, the following expressions

$$\sigma_{xx}^{(1)} \cong (k+1)T - \frac{4T}{1+\alpha} + \frac{T\sqrt{a\alpha\pi}}{(1+\alpha)\sqrt{2\pi r}}\left\{(3e^{-\pi\epsilon}-e^{\epsilon\pi})\left[\cos\left(\epsilon log\frac{r}{l}\right)-2\epsilon\,\sin\left(\epsilon log\frac{r}{l}\right)\right]\right\} \quad (A.7)$$

$$\sigma_{yy}^{(1)} \cong \frac{T\sqrt{a\pi}}{\sqrt{2\pi r}}\left\{\left[cos\left(\epsilon log\frac{r}{l}\right)-2\epsilon sin\left(\epsilon log\frac{r}{l}\right)\right]\right\} \quad (A.8)$$

$$\sigma_{xy}^{(1)} \cong \frac{T\sqrt{a\pi}}{\sqrt{2\pi r}}\left\{\left[sin\left(\epsilon log\frac{r}{l}\right)+2\epsilon cos\left(\epsilon log\frac{r}{l}\right)\right]\right\} \quad (A.9)$$

and in the medium 2 for $0 < r/a \ll 1$ and $\theta = 0$,

$$\sigma_{xx}^{(2)} \cong \mu\left((k+1)T - \frac{4T}{1+\alpha}\right)$$
$$+\frac{T\sqrt{a\alpha\pi}}{(1+\alpha)\sqrt{2\pi r}}\left\{(3e^{\pi\epsilon}-e^{-\pi\epsilon})\left[cos\left(\epsilon log\frac{r}{l}\right)-2\epsilon sin\left(\epsilon log\frac{r}{l}\right)\right]\right\} \quad (A.10)$$

$$\sigma_{xy}^{(1)}(\theta=0) = \sigma_{xy}^{(2)}(\theta=0) \quad (A.11)$$

$$\sigma_{yy}^{(1)}(\theta=0) = \sigma_{yy}^{(2)}(\theta=0) \quad (A.12)$$

Chapter 6

Explicit solution for an interfacial crack under general loading

6.1 Introduction

Many structures are composed of different materials formed in layers for both man-made and natural origin. The layers are bonded together along interfaces. Since the last two decades, the importance of composite materials has increased very rapidly in engineering applications because of their high strength and light weight. However, there are flaws at the interfaces of composite bodies because improper adhesion may lead to serious danger, thus a better understanding of interface fracture mechanics is needed.

The asymptotic elastic field of a semi-infinite crack lying along an interface between dissimilar isotropic materials subjected to static loading was first considered by Williams [1] for plane strain condition. A number of solutions for the stress and the displacement field near the crack tip were obtained by England [2], Erdogan [3] and Rice and Sih [4]. Extensions to anisotropic elasticity for the near tip field have been made by Gotoh [5], Bogy [6], and Kuo and Bogy [7], as well as Ting [8, 9]. The elasticity solutions for a variety of such crack problems involve oscillatory singularities have been worked out. Some progress have been reported from this point of view by Atkinson [10] who has resolved the anomalies of the elastic fields near the tip of an interfacial crack by introducing a realistic model of the interface, and subsequently by Comninou [11-13] who has shown that the stress singularities lose the oscillatory behavior near the tip of an interfacial crack, by assuming that the crack is not completely open and that its surfaces are in contact near the crack tip. The exact full field solutions of interface cracks in anisotropic dissimilar media are obtained by Ma and Luo [14].

The boundary value problem of an interfacial crack under biaxial loading is solved on the basis of the well-known complex variable technique and the superposition principle by Piva and Viola [15]. The stress and displacement fields near the crack tip are completely determined, and the effects of the biaxial load parameter are pointed out. In a later article [16], the method mentioned above is applied to incompressible materials. For the model with a crack lies on the interface between two isotropic materials subjected to tension and shear, Salganik [17] presented the exact solution of the stress distribution on the x-axis in the vicinity of the crack tip.

In this work, we describe the process of fracture induced by a central line crack initially in equilibrium at the interface of two dissimilar media, which is subjected at infinity to a system of general loading. Each medium is assumed to be homogeneous, isotropic and linear elastic. The explicit solutions of stresses around the crack tip are obtained by complex variable technique of Muskhelishvili and the superposition principle.

6.2 Theoretical analyses

Fig. 6.1 shows the general configuration near the crack tip on the interface bonded by two dissimilar isotropic homogeneous materials. Material 1 with the subscript 1 is above the interface, while material 2 with the subscript 2 is below. E_i, υ_i and μ_i (i = 1, 2) are the Young's modulus, the Poisson's ratios and the shear modulus of the respective materials are shown below.

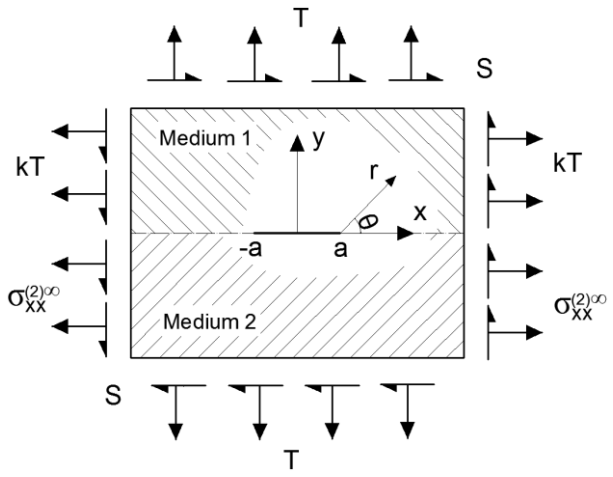

Fig. 6.1. Crack between dissimilar media under general loading

The solution of plane elastic problem is reached through the well-known complex equilibrium equations of Kolosov-Muskhelishvili

$$\sigma_{xx}^{(j)} + \sigma_{yy}^{(j)} = 4Re\left[\Phi_j(z)\right] \tag{6.1a}$$

$$\sigma_{yy}^{(j)} - \sigma_{xx}^{(j)} + 2i\sigma_{xy}^{(j)} = 2\left[\bar{z}\Phi'_j(z) + \Psi_j(z)\right] \tag{6.1b}$$

$$2\mu_j D^{(j)} = \chi_j \varphi_j(z) - z\overline{\Phi}_j(\bar{z}) - \overline{\psi}_j(\bar{z}) \tag{6.1c}$$

$$\varphi_j(z) = \int \Phi_j(z)dz\,, \qquad \psi_j(z) = \int \Psi_j(z)dz \tag{6.1d}$$

where $\sigma_{xx}^{(j)}$, $\sigma_{yy}^{(j)}$ and $\sigma_{xy}^{(j)}$ are the stress tensor components with respect to a Cartesian coordinate system centered in the crack, elastic parameter $\chi_j = 3 - 4\upsilon_j$ is for plane strain and $\chi_j = \left(3 - \upsilon_j\right)/\left(1 + \upsilon_j\right)$ is for plane stress, $D^{(j)} = u_j + i\upsilon_j$ is the complex displacement, $j = 1{,}2$ refers to

the medium 1 and 2, respectively. The four potential functions Φ_j and Ψ_j will be determined by the boundary conditions and the conditions at infinity.

By assuming the following conditions at infinity for medium 1 M_1

$$\sigma_{xx}^{(1)\infty} = kT, \qquad \sigma_{yy}^{(1)\infty} = T, \qquad \sigma_{xy}^{(1)\infty} = S, \qquad \omega^{(1)\infty} = 0 \tag{6.2}$$

where k is the biaxial load parameter and ω denotes the rotation, the conditions at medium 2 M_2 infinity for will be expressed in the following form

$$\sigma_{xx}^{(2)\infty} = (k\mu + \gamma)T, \qquad \sigma_{yy}^{(2)\infty} = T, \qquad \sigma_{xy}^{(2)\infty} = S, \qquad \omega^{(2)\infty} = S(\mu_2 - \mu_1)/2\mu_1\mu_2 \tag{6.3}$$

where

$$\mu = \frac{\mu_2(1+\chi_1)}{\mu_1(1+\chi_2)}, \gamma = \frac{\alpha(3+\mu) - (1+3\mu)}{1+\alpha}, \alpha = \frac{\mu_1 + \mu_2\chi_1}{\mu_2 + \mu_1\chi_2} \tag{6.4}$$

If the traction free conditions on the crack surfaces and the traction and displacement continuity conditions along the bond line are assumed, the potential functions corresponding to the conditions eqs. (6.2) and (6.3) can be written as

$$\Phi_1(z) = \frac{T - iS}{1+\alpha} h(z)X(z) + \left[\frac{k+1}{4}T - \frac{T - iS}{1+\alpha}\right] \tag{6.5a}$$

$$\Psi_1(z) = \frac{\alpha(T+iS)}{1+\alpha}\bar{h}(z)\bar{X}(z) + \frac{T - iS}{1+\alpha}\left[\frac{a^2 + 2i\epsilon az}{z^2 - a^2}h(z) - z\right]X(z) - 2\left[\frac{k+1}{4}T - \frac{T}{1+\alpha}\right] \tag{6.5b}$$

$$\Phi_2(z) = \frac{\alpha(T - iS)}{1+\alpha} h(z)X(z) + \mu\left[\frac{k+1}{4}T - \frac{T - iS}{1+\alpha}\right] \tag{6.5c}$$

$$\Psi_2(z) = \frac{(T+iS)}{1+\alpha}\bar{h}(z)\bar{X}(z) + \frac{\alpha(T - iS)}{1+\alpha}\left[\frac{a^2 + 2i\epsilon az}{z^2 - a^2}h(z) - z\right]X(z) - 2\mu\left[\frac{k+1}{4}T - \frac{T}{1+\alpha}\right] \tag{6.5d}$$

where $h(z) = z - 2i\epsilon a$, $X(z) = \frac{1}{\sqrt{z^2 - a^2}}\left(\frac{z+a}{z-a}\right)^{i\epsilon}$, $\epsilon = \frac{log\alpha}{2\pi}$

These solutions can be obtained by a slightly different method developed by Sih and Rice [4, 18] which involves combining the method of eigenfunction expansions with complex function theory. From eq. (6.1) and eq. (6.5) the stresses and displacements at any point of the two media can be computed.

Viola and Piva [16] have reported the behavior of a crack between two dissimilar media under plane strain conditions and biaxial and shear loading at infinity. They assumed that the two bonded media are incompressible, therefore, the oscillatory behavior of the elastic fields disappears and the simplified stress expressions are obtained.

It is well known that, the stresses ahead of an interface crack remains proportional to $1/\sqrt{r}$ as in the case of a homogeneous material, but they possess an oscillatory character of stress and displacement fields near the tips of the interfacial crack.

In particular, confining our attention to the crack tip region, taking

$$z - a = \zeta = re^{i\theta}, \quad 0 < r/a \ll 1 \tag{6.6}$$

and expressing $X(z)$ as power series expansions, we obtain the following approximate expressions for the complex stress distributions

$$\sigma_{xx}^{(1)} + \sigma_{yy}^{(1)} \cong (k+1)T - \frac{4T}{1+\alpha} + \frac{\lambda H(\zeta)}{\sqrt{2\pi\zeta}} + \frac{\bar{\lambda}\bar{H}(\bar{\zeta})}{\sqrt{2\pi\bar{\zeta}}} \tag{6.7a}$$

$$\sigma_{yy}^{(1)} - \sigma_{xx}^{(1)} + 2i\sigma_{xy}^{(1)} \cong -(k+1)T + \frac{4T}{1+\alpha} + \frac{\alpha\bar{\lambda}\bar{H}(\zeta)}{\sqrt{2\pi\zeta}} - \frac{\lambda H(\zeta)}{2\sqrt{2\pi\zeta}}\left(c_1 + \bar{c_1}\frac{\bar{\zeta}}{\zeta}\right) \tag{6.7b}$$

$$\sigma_{xx}^{(2)} + \sigma_{yy}^{(2)} \cong \mu(k+1)T - \frac{4\mu T}{1+\alpha} + \frac{\alpha\lambda H(\zeta)}{\sqrt{2\pi\zeta}} + \frac{\alpha\bar{\lambda}\bar{H}(\bar{\zeta})}{\sqrt{2\pi\bar{\zeta}}} \tag{6.7c}$$

$$\sigma_{yy}^{(2)} - \sigma_{xx}^{(2)} + 2i\sigma_{xy}^{(2)} \cong -\mu(k+1)T + \frac{4\mu T}{1+\alpha} + \frac{\bar{\lambda}\bar{H}(\zeta)}{\sqrt{2\pi\zeta}} - \frac{\alpha\lambda H(\zeta)}{2\sqrt{2\pi\zeta}}\left(c_1 + \bar{c_1}\frac{\bar{\zeta}}{\zeta}\right) \tag{6.7d}$$

where

$$H(\zeta) = \exp(-i\epsilon log\zeta) \tag{6.8a}$$

$$\lambda = \frac{2c_1(T - iS)\sqrt{\pi a}}{1+\alpha}\exp(i\epsilon logl) \tag{6.8b}$$

$$c_1 = 1 - 2i\epsilon \tag{6.8c}$$

$$l = 2a \tag{6.8d}$$

Rewriting $H(\zeta)$ and obtaining the expresses of $\bar{H}(\bar{\zeta})$, $\bar{H}(\zeta)$, $\bar{\lambda}$, $\sqrt{\zeta}$ and $\sqrt{\bar{\zeta}}$ as following

$$H(\zeta) = \exp(-i\epsilon logr)\exp(\epsilon\theta) \tag{6.9a}$$

$$\bar{H}(\bar{\zeta}) = \exp(i\epsilon logr)\exp(-\epsilon\theta) \tag{6.9b}$$

$$\bar{H}(\zeta) = \exp(i\epsilon logr)\exp(\epsilon\theta) \tag{6.9c}$$

$$\bar{\lambda} = \frac{2\bar{c_1}(T + iS)\sqrt{\pi a}}{1+\alpha}\exp(-i\epsilon logl) \tag{6.9d}$$

$$\sqrt{\zeta} = \sqrt{r}e^{i\theta/2} \tag{6.9e}$$

$$\sqrt{\bar{\zeta}} = \sqrt{r}e^{-i\theta/2} \tag{6.9f}$$

Substituting eqs. (6.8) and (6.9) to eq. (6.7), the Cartesian coordinate stress components in medium 1 and medium 2 can be obtained as showing in Appendix I.

For the polar stress components which are of relevance for the following, these complex relations can be written as

$$\sigma_{\theta\theta}^{(j)} = \frac{1}{2} Re\left[\sigma_{xx}^{(j)} + \sigma_{yy}^{(j)} + \frac{\zeta}{\bar{\zeta}}\left(\sigma_{yy}^{(j)} - \sigma_{xx}^{(j)} + 2i\sigma_{xy}^{(j)}\right)\right] \tag{6.10a}$$

$$\sigma_{r\theta}^{(j)} = \frac{1}{2} Im\left[\frac{\zeta}{\bar{\zeta}}\left(\sigma_{yy}^{(j)} - \sigma_{xx}^{(j)} + 2i\sigma_{xy}^{(j)}\right)\right] \tag{6.10b}$$

Therefore, the corresponding approximate polar stress expressions are obtained by substituting Cartesian coordinate stress components to eq. (6.10) as showing in Appendix I.

For the same model in Fig. 1, Salganik [17] presented an exact solution of the stress distribution on the x-axis in the vicinity of the crack tip as

$$\sigma_{yy} + i\sigma_{xy} = \frac{\sqrt{a\pi}(1 + 2i\epsilon)(T + iS)}{\sqrt{2\pi r}}\left(\frac{r}{2a}\right)^{i\epsilon} \tag{6.11}$$

The solutions in eq. (6.11) are the same with the solutions in the present eqs. (AI.2) and (AI.3), which can be simply written as

$$\sigma_{yy}^{(1)} = \sigma_{yy} = \sqrt{\frac{a}{2r}}\left[(T - 2\epsilon S)\cos Q - (2\epsilon T + S)\sin Q\right] \tag{6.12a}$$

$$\sigma_{xy}^{(1)} = \sigma_{xy} = \sqrt{\frac{a}{2r}}\left[(T - 2\epsilon S)\sin Q + (2\epsilon T + S)\cos Q\right] \tag{6.12b}$$

where $Q = \epsilon \ln\left(\frac{r}{2a}\right)$.

It can be easily seen that, the same with the solution of bi-material system under biaxial loading, the circumferential stress coincides with the stress σ_{yy} along the interface bonded line ($\theta = 0$), i.e. it is continuous across the interface, and because of this property it shows a suitable quantity in view of the interfacial fracture analysis.

$$\sigma_{\theta\theta}^{(1)}|_{\theta=0} = \sigma_{\theta\theta}^{(2)}|_{\theta=0} = \sqrt{\frac{a}{2r}}\left[(T - 2\epsilon S)cos\left(\epsilon log\frac{r}{l}\right) - (2\epsilon T + S)sin\left(\epsilon log\frac{r}{l}\right)\right] \tag{6.13a}$$

$$\sigma_{r\theta}^{(1)}|_{\theta=0} = \sigma_{r\theta}^{(2)}|_{\theta=0} = \sqrt{\frac{a}{2r}}\left[(T - 2\epsilon S)sin\left(\epsilon log\frac{r}{l}\right) + (2\epsilon T + S)cos\left(\epsilon log\frac{r}{l}\right)\right] \tag{6.13b}$$

The load parallelling to the crack affects the circumferential stresses though the non-singular terms. In the next section it will be shown that the role-played by these terms in the correct description of stress related quantities and fracture interpretation.

The biaxial parameter k only affects the stress σ_{xx} along through a term which is independent of the radial distance from the tip, as in the homogeneous case and in the bi-material system under the bi-axial loading. As pointed out by Piva and Viola [15], the arbitrary omission of this term leads to significant errors in the calculation of the quantities related to σ_{xx} such as the tensile stress, the maximum shear stress, etc. and limits severely the prevision of the angle of incipient crack extension. The shear loading S only produces the singular stresses among σ_{xx}, σ_{yy} and σ_{xy}. The influence of the loading ratio between tensile T and shear S on the circumferential stress, maximum shear stress and strain energy density will be investigated in the next section.

The SIFs of an interface crack according to the originally definition proposed by Erdogan [3] are related with the stresses along the x-axis near the right crack tip as

$$\left(\sigma_{yy} + i\sigma_{xy}\right)_{\theta=0} = \frac{K_I + iK_{II}}{\sqrt{2\pi r}}\left(\frac{r}{l_k}\right)^{i\epsilon} \tag{6.14}$$

where K_I and K_{II} are the mode I and mode II SIFs of an interface crack respectively.

$$K_I + iK_{II} = \sqrt{a\pi}(1 - 2i\epsilon)(T \pm iS)\ for\ l_k = 2a \tag{6.15}$$

where the " $+$ " and the " $-$ " correspond to the right and left crack tips, respectively. The Young's moduli and Poisson's ratios are set to be $E_1 = 1 \times 10^5 MPa$, $E_2 = 1 \times 10^6 MPa$ and $\nu_1 = \nu_2 = 0.3$, respectively. The corresponding biomaterial constant is $\epsilon = -0.07582$.

Using the definition by Erdogan [3], the relationship between the energy release rate $\mathcal{G}$ and the SIFs is expressed as the following equations by Malyshev and Salganik [19]

$$\mathcal{G} = \beta(K_I^2 + K_{II}^2) \tag{6.16}$$

where

$$\beta = \frac{1}{16cosh^2(\epsilon\pi)}\left[\frac{\kappa_1 + 1}{\mu_1} + \frac{\kappa_2 + 1}{\mu_2}\right] \tag{6.17}$$

6.3 Numerical results

In the previous analysis the local fields of elastic stresses in the immediate neighborhood of the interfacial crack tip is obtained. This knowledge is essential in the application of fracture theories to

cracked materials. The aim of this section is to point out the effect of the biaxial load factor and loading ratio on the circumferential stress, the maximum shear stress and the strain energy density.

6.3.1 Circumferential stress

The dimensionless circumferential stresses $\frac{\sigma_{\theta\theta}^{(i)}}{T}, i = 1,2$ evaluated at $\frac{r_0}{a} = 0.05$ are represented in Fig. 2 for differently value of the biaxial load parameter k for the same material combinations, i.e. $\frac{E_1}{E_2} = 0.5$, $\nu_1 = \nu_2 = 0.3$. Each curve corresponds to a fixed value of the ratio between shear loading and tensile loading. It appears that, according to expressions (circumferential stresses), $\sigma_{\theta\theta}^{(1)} = \sigma_{\theta\theta}^{(2)}$ at $\theta = 0$, the circumferential stresses are continuous across the bonding interface and are depending on the both ratios of shear loading and tensile loading, the radial distance from the crack tip and crack length either on the loading effect parameter k. Moreover, the circumferential stress is absent at the crack surfaces of both the materials.

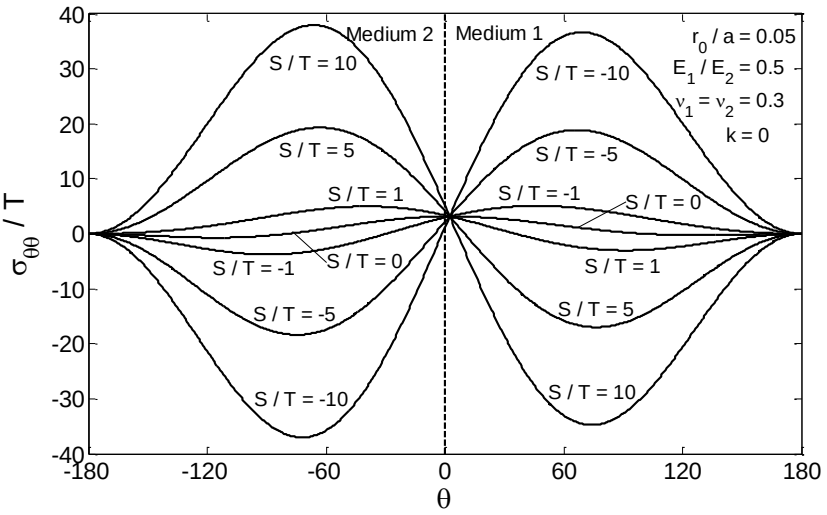

(a)

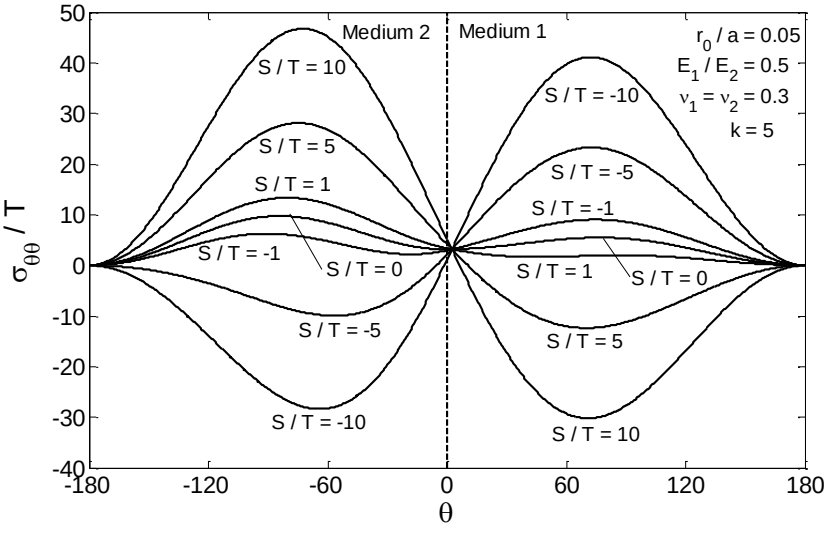

(b)

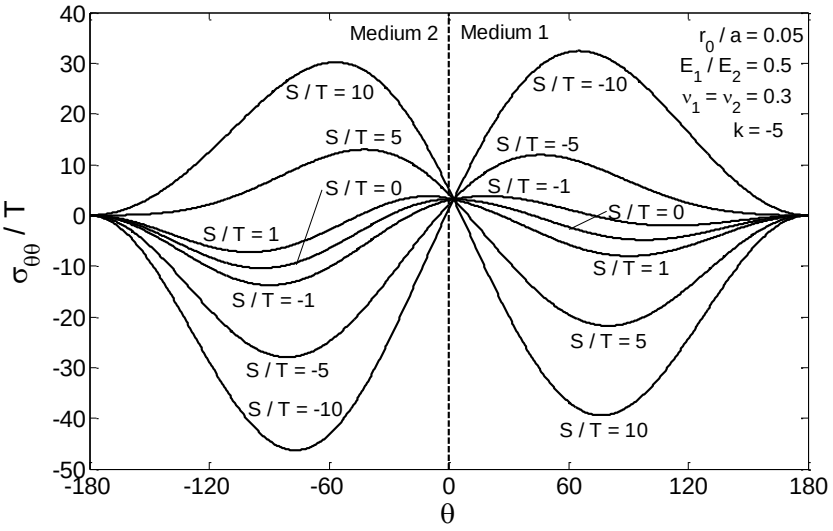

(c)

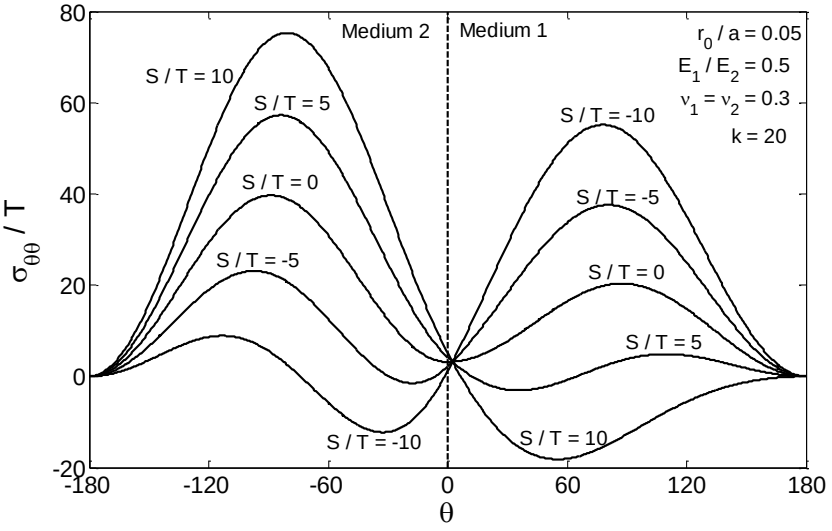

(d)

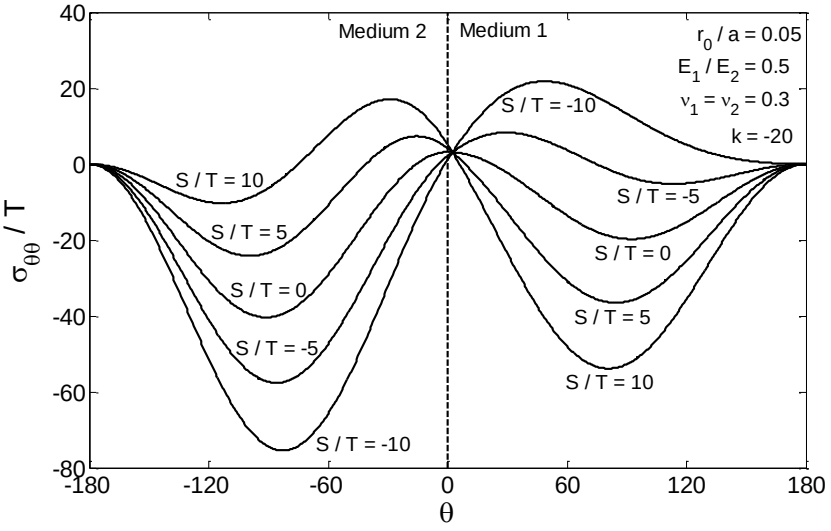

(e)

Fig. 6.2. Dimensionless circumferential stresses for different loading ratio of (a) $k = 0$; (b) $k = 5$; (c) $k = -5$; (d) $k = 20$; (e) $k = -20$.

In special case when the two bonded media are assumed to be incompressible and plane strain, i.e. $\nu_i = 0.5, \chi_i = 3 - 4\nu_i, i = 1,2$, the expressions of stresses and the foregoing results reduce to those reported in the literature [16]. When $E_1 = E_1$ and $\nu_1 = \nu_2$ the crack is embedded into a homogenous medium and the foregoing results reduce to those presented in the literature [20, 21].

The following figures in Fig. 6.3 show the effect of biaxial loading parameter k on dimensionless circumferential stress for different loading ratio of shearing load and tensile load S/T, i.e. 0, 0.1, 1, 3 and 10, respectively, and the same material combinations, i.e. $E_1/E_2 = 0.5$, $\nu_1 = \nu_2 = 0.3$ at the same location before crack tip $r_0/a = 0.1$. It is noted that, the maximum value of $\sigma_{\theta\theta}/T$ is, generally, a function of biaxial loading parameter k in both materials. In the next section, this dependence of $\sigma_{\theta\theta}/T$ on the load biaxiality will enter into use for the purpose of formulating a fracture criterion and the influence of the loading ratio on the prevision angle of initial crack extension will be discussed. Further, the effect of location before crack tip which calculate the stress components on the circumferential stress is comparing in Fig. 6.4 and Fig. 6.3(c).

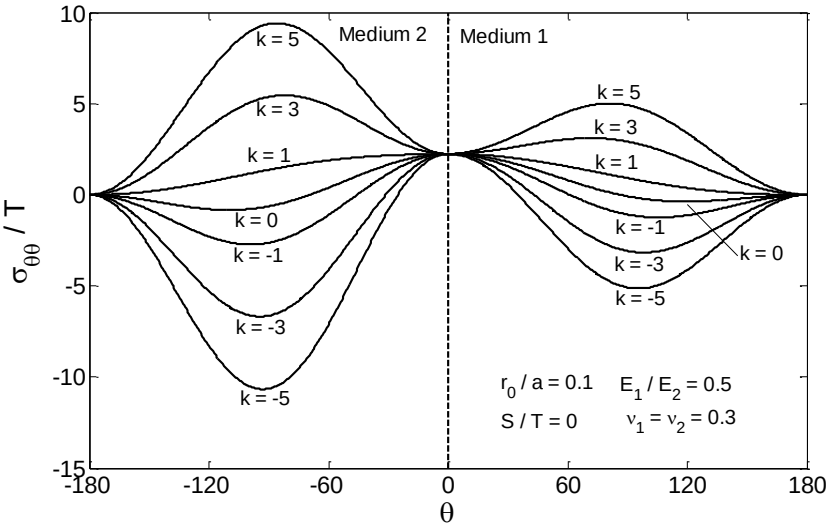

(a)

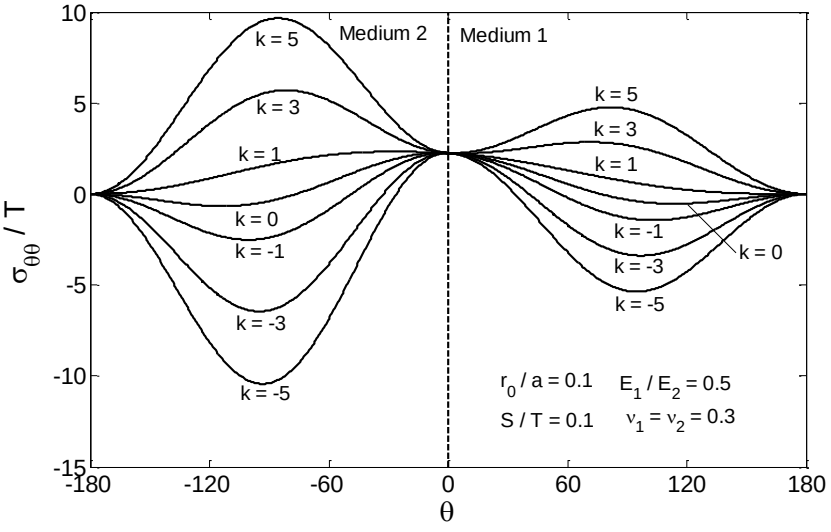

(b)

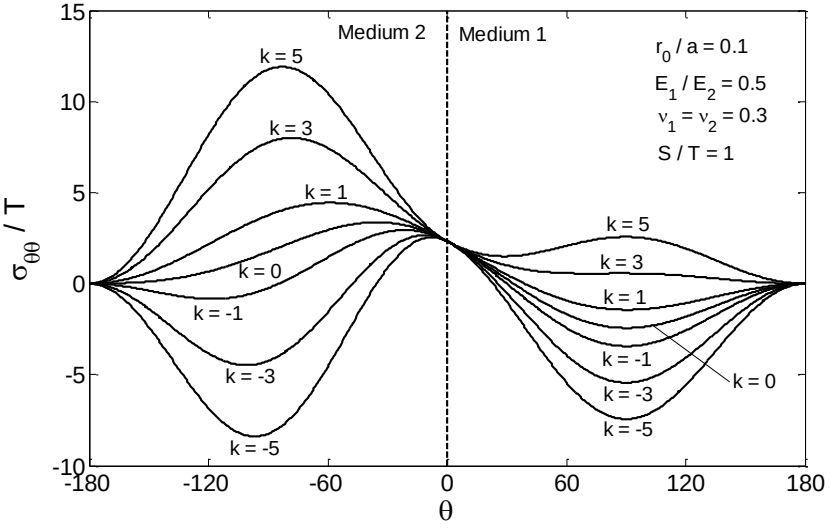

(c)

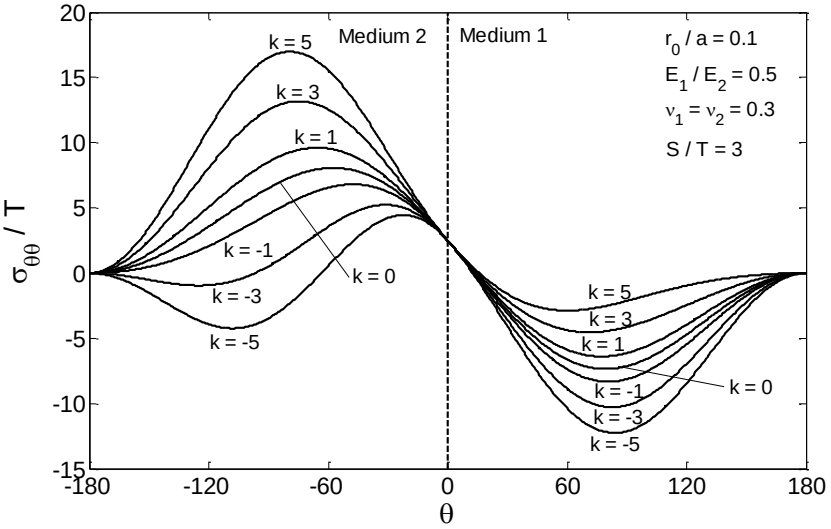

(d)

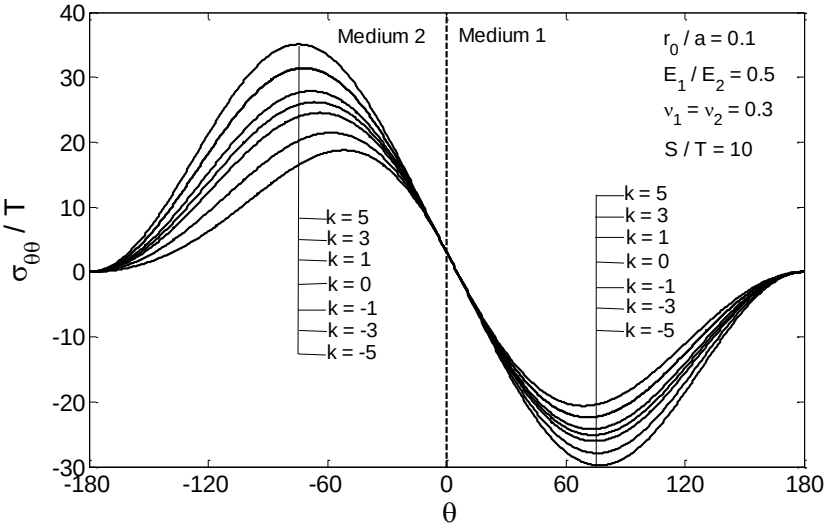

(e)

Fig. 6.3. Dimensionless circumferential stresses for different biaxial load parameter and loading ratio (a) $S/T = 0$; (b) $S/T = 0.1$; (c) $S/T = 1$; (d) $S/T = 3$; (e) $S/T = 10$.

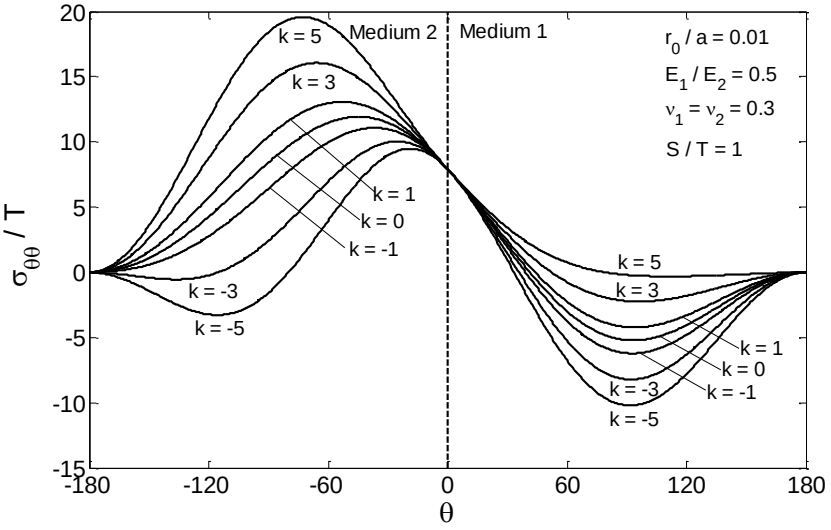

Fig. 6.4. Dimensionless circumferential stresses for different biaxial load parameter and $\frac{r_0}{a} = 0.01$ and $S/T = 1$.

6.3.2 Maximum shear stress

The maximum shear stress τ_m at points close to the tip of the crack can be expressed as follows

$$\tau_m^{(j)} = \frac{1}{2}\left[\left(\sigma_{xx}^{(j)} - \sigma_{yy}^{(j)}\right)^2 + 4{\sigma_{xy}^{(j)}}^2\right]^{1/2} \tag{6.18}$$

where $\sigma_{xx}^{(j)}$, $\sigma_{yy}^{(j)}$ and $\sigma_{xy}^{(j)}$ are the Cartesian components of stress.

In Fig. 6.5, the angular variation of the dimensionless maximum shear stress evaluated at $\frac{r_0}{a} = 0.1$ is illustrated for media combination $\frac{E_1}{E_2} = 0.5$ and $\nu_1 = \nu_2 = 0.3$ under various loading conditions $\frac{S}{T} = 0.1, \frac{1}{3}, 1, 3, 10$ and loading ratio $k = -5, -3, -1, 0, 1, 3, 5$, respectively.

It can be noted from those figures that the maximum shear stresses are not continuous across the bonding line owing to the discontinuity of σ_{xx}. The maximum shear stress can be used to determine the plastic zone according to Tresca criterion. The contents about plastic zone will be discussed in the future.

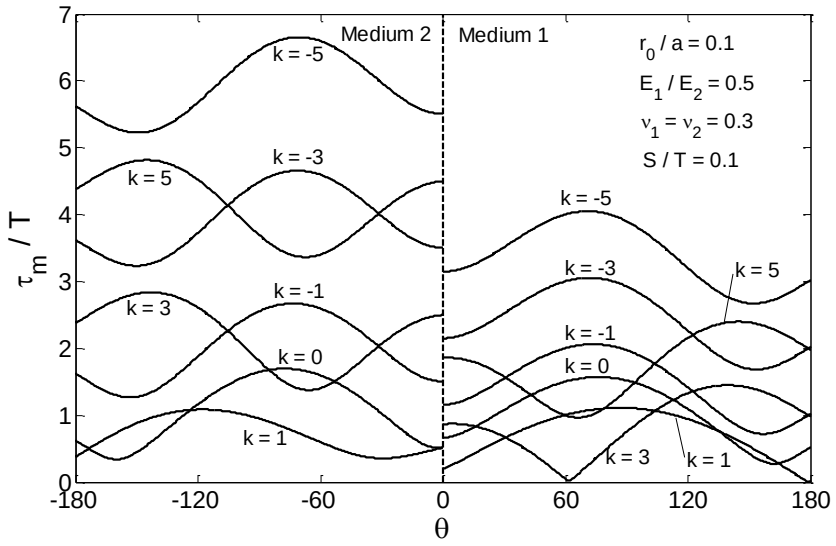
Medium 2
Medium 1
$r_0 / a = 0.1$
$E_1 / E_2 = 0.5$
$\nu_1 = \nu_2 = 0.3$
S / T = 0.1
k = -5
k = -3
k = 5
k = 3
k = -1
k = 0
k = 1
τ_m / T
θ

(a)

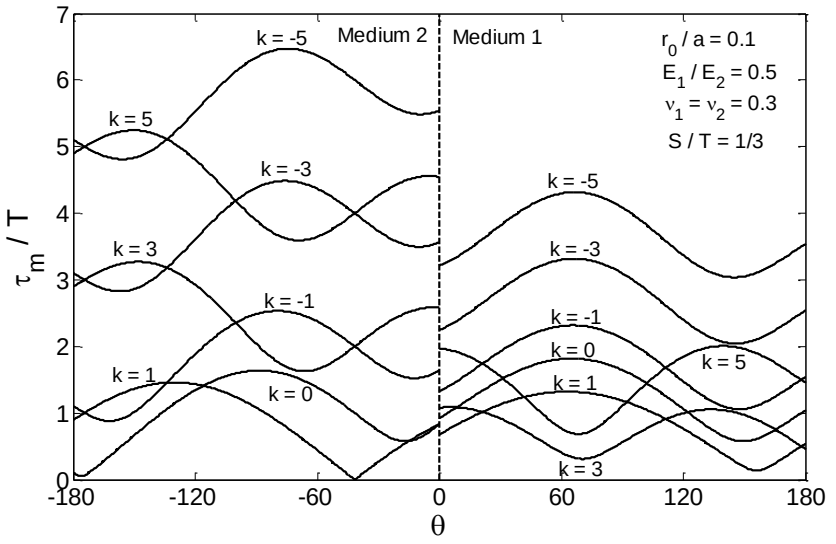
Medium 2
Medium 1
$r_0 / a = 0.1$
$E_1 / E_2 = 0.5$
$\nu_1 = \nu_2 = 0.3$
S / T = 1/3
k = -5
k = 5
k = -3
k = 3
k = -1
k = 1
k = 0
τ_m / T
θ

(b)

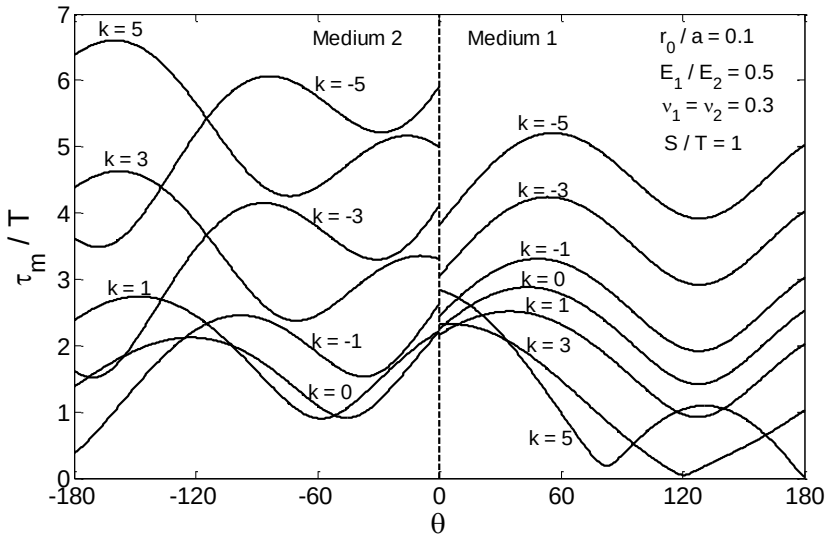
Medium 2
Medium 1
$r_0 / a = 0.1$
$E_1 / E_2 = 0.5$
$\nu_1 = \nu_2 = 0.3$
S / T = 1
k = 5
k = -5
k = 3
k = -3
k = 1
k = -1
k = 0
τ_m / T
θ

(c)

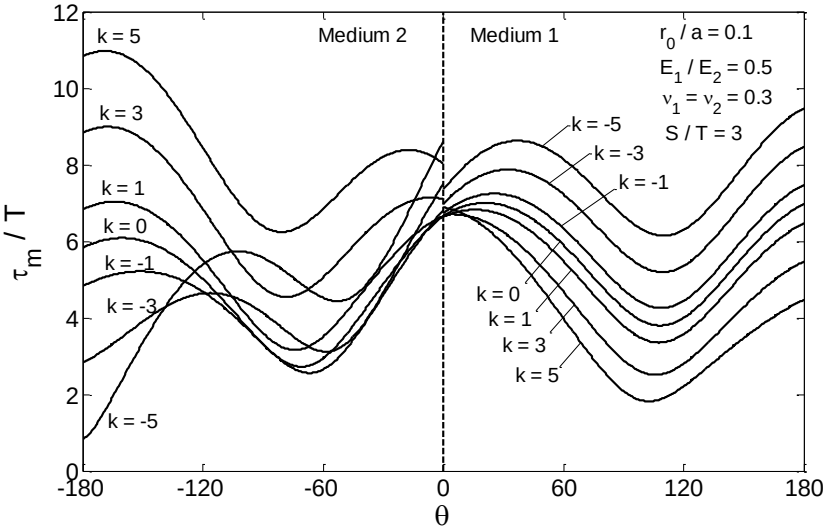

(d)

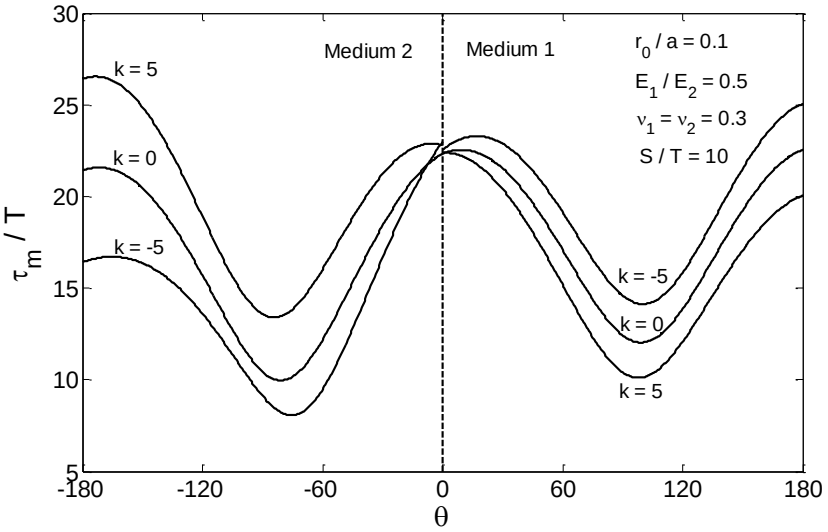

(e)

Fig. 6.5. The angular variation of the dimensionless maximum shear stress for different biaxial parameter and loading ratio (a) $S/T = 0.1$; (b) $S/T = 1/3$; (c) $S/T = 1$; (d) $S/T = 3$; (e) $S/T = 10$.

6.3.3 Stain energy density factor

The energy density field $\frac{dW}{dV}$ in the vicinity of the crack border may be expressed in the well-known form

$$\frac{dW}{dV} = \frac{S}{r} + nonsingular\ terms \tag{6.19}$$

The coefficient of $\frac{1}{r}$ in the above equation is referred to as the strain energy density factor. Since the strain energy density $\frac{dW}{dV}$ approaches infinity as r tends to zero, a finite $\frac{dW}{dV}$ is evaluated at a criti-

cal distance r_c. The region inside r_c where the material is expected to be nonlinear elastic and plastic is called the core region.

The intensity of the strain energy density for the state of plane stress at a critical distance r_c can be written as

$$S' = r_c \left(\frac{dW}{dV}\right)^* \tag{6.20}$$

or

$$S' = r_c \frac{1}{2E}\left[\sigma_{xx}^2 + \sigma_{yy}^2 - 2\nu\sigma_{xx}\sigma_{yy} + 2(1+\nu)\sigma_{xy}^2\right] \tag{6.21}$$

where the non-singular terms and higher order terms in r_c have been dropped. S is a $1/r_c$ energy singularity function near the crack tip. It also can be rewritten as a dimensionless formula as follows

$$\mathrm{S_c^*} = \frac{\mathrm{S'E^*}}{\mathrm{aT^2}} \tag{6.22}$$

where $\frac{1}{E^*} = \frac{1}{E_1} + \frac{1}{E_2}$.

By substituting the stress components eqs AI.(1-6) of interfacial crack to the relation eq. (6.21), we can obtain a generalized form of the strain energy density factor for bi-material body in general loading, which contrary to the strain energy density factor of homogenous isotropic fractural material, depending on the radial distance from the crack tip.

The following figures in Figs 6.6-6.11 show the dimensionless strain energy density factor S_c^* against polar angle θ around the crack tip with $r_0/a = 0.1$ for different biaxial factor k and traction ratio S/T in homogeneous material and dissimilar material combination.

Neither as the maximum circumferential stress continues across bonded interface in both homogenous material and dissimilar material, nor as the maximum shear stress discontinues across bonded interface in both homogenous material and dissimilar material, the strain energy density factor continues across bonded interface in homogenous material but discontinues in dissimilar materials combination. It is well known that, the crack propagation angle in homogenous material can be determined according to strain energy density factor criterion [22]. Unlike the circumferential stress, continuing across the interface, which can be used as a fracture criterion according to maximum tangential criterion, the strain energy density discontinues across the interfacial bonded line. The strain energy density factor fracture criterion only can be used in material 1 and material 2 separately. In order to apply the SEDF-criterion to all the range of the model including the interface be-

tween dissimilar media, an extension of SEDF-criterion or the criterion of crack extents along the interface based on SEDF-criterion should be created.

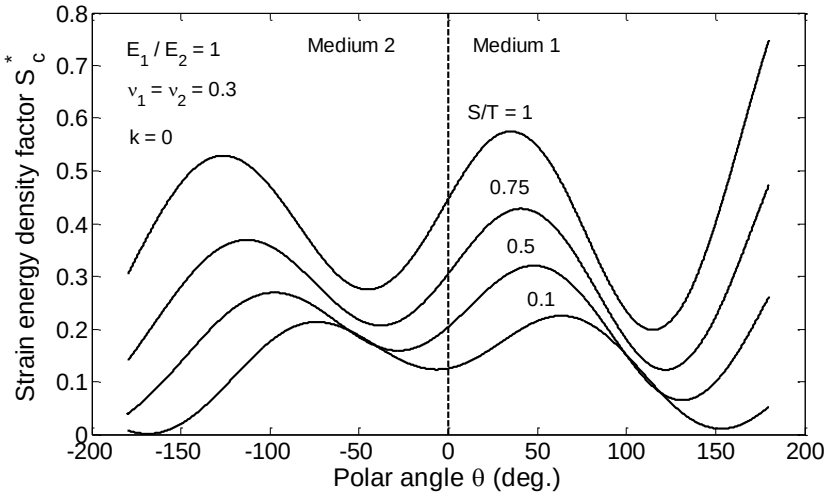

(a)

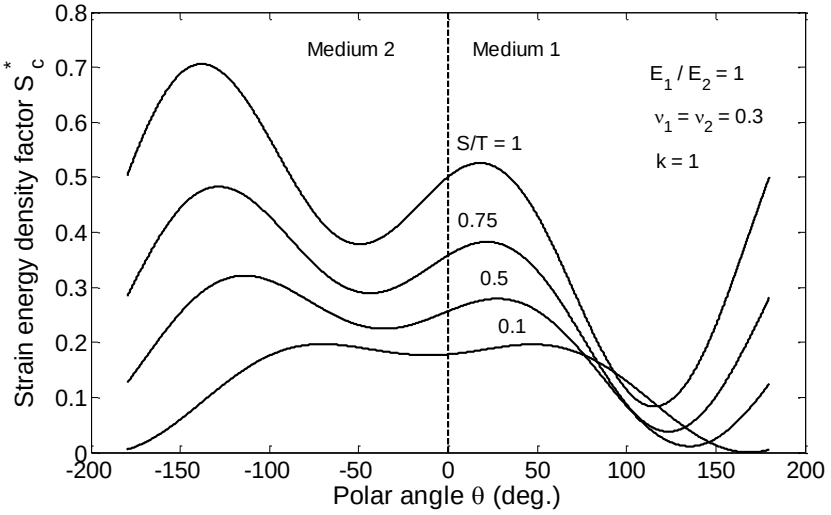

(b)

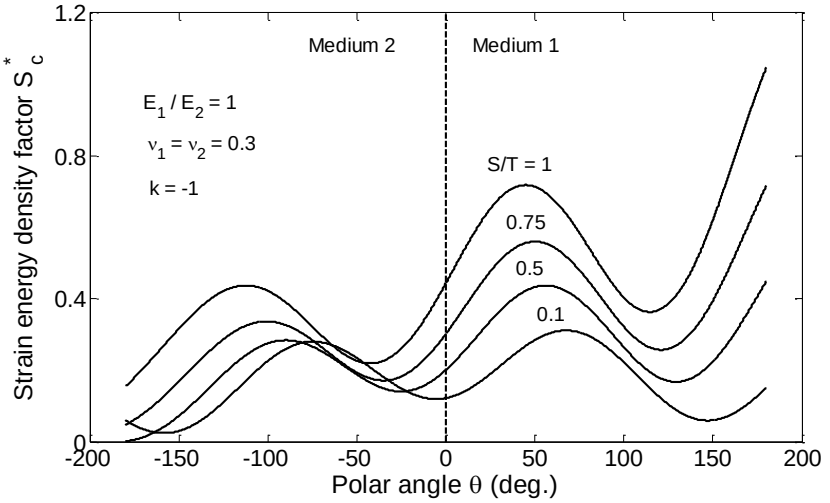

(c)

Fig. 6.6. Dimensionless strain energy density factor versus polar angle in homogenous material under loading ratio of $S/T = 0.1, 0.5, 0.75$ and 1 for (a) $k = 0$; (b) $k = 1$; (c) $k = -1$.

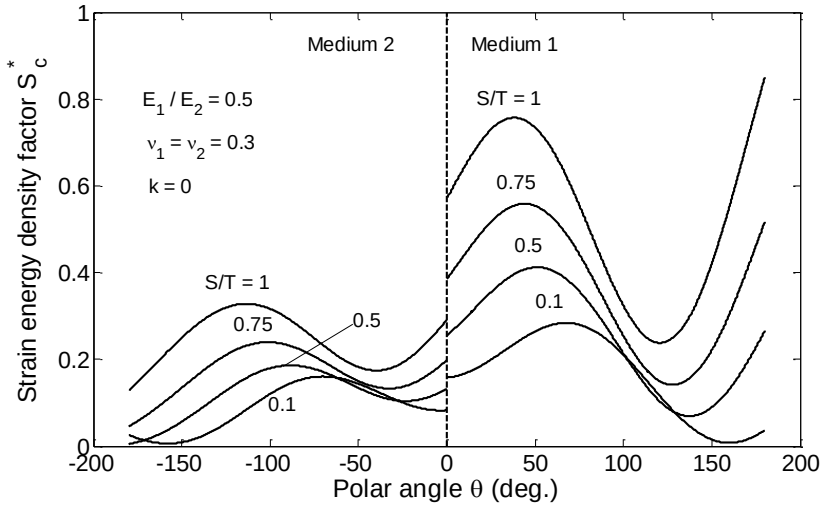
Medium 2
Medium 1
$E_1 / E_2 = 0.5$
$\nu_1 = \nu_2 = 0.3$
k = 0
S/T = 1
0.75
0.5
0.1
Strain energy density factor S_c^*
Polar angle θ (deg.)

(a)

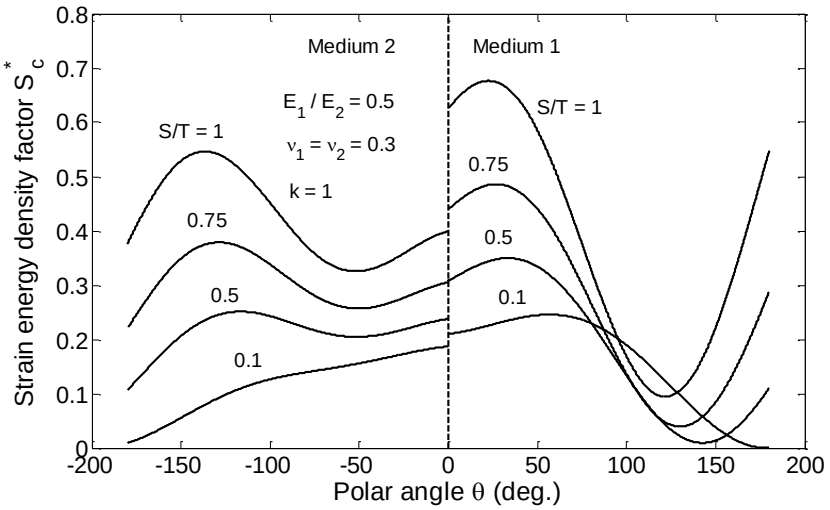
Medium 2
Medium 1
$E_1 / E_2 = 0.5$
$\nu_1 = \nu_2 = 0.3$
k = 1
S/T = 1
0.75
0.5
0.1
Strain energy density factor S_c^*
Polar angle θ (deg.)

(b)

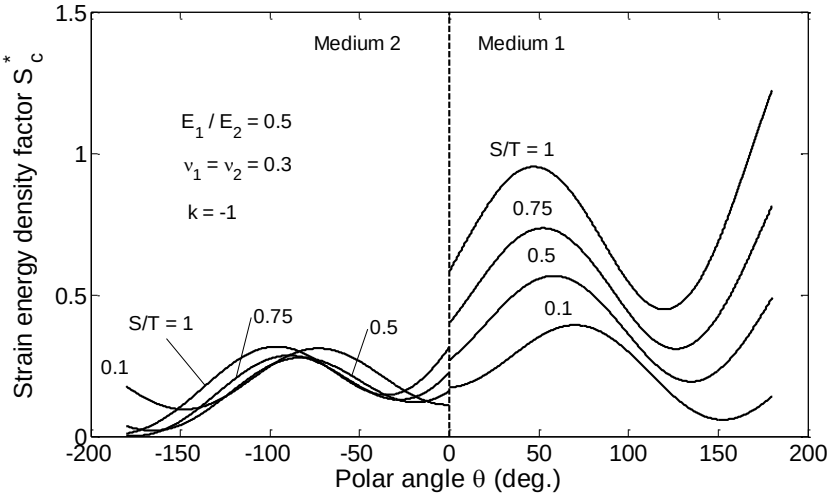
Medium 2
Medium 1
$E_1 / E_2 = 0.5$
$\nu_1 = \nu_2 = 0.3$
k = -1
S/T = 1
0.75
0.5
0.1
Strain energy density factor S_c^*
Polar angle θ (deg.)

(c)

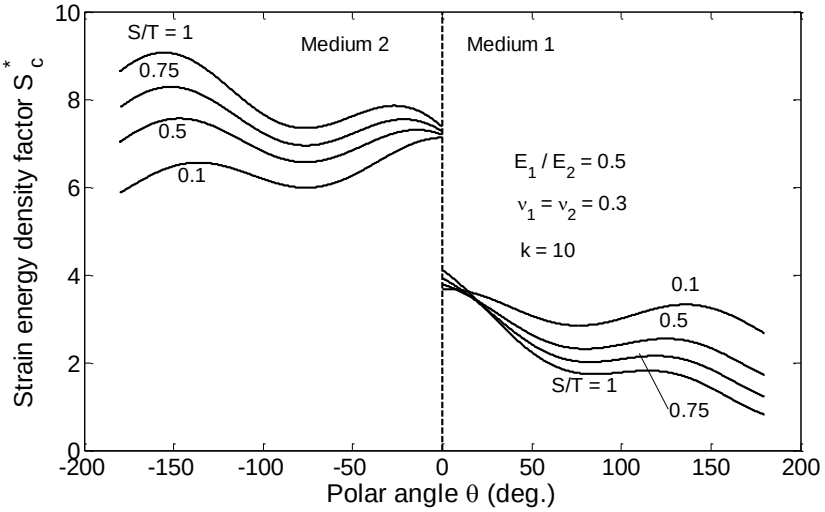

(d)

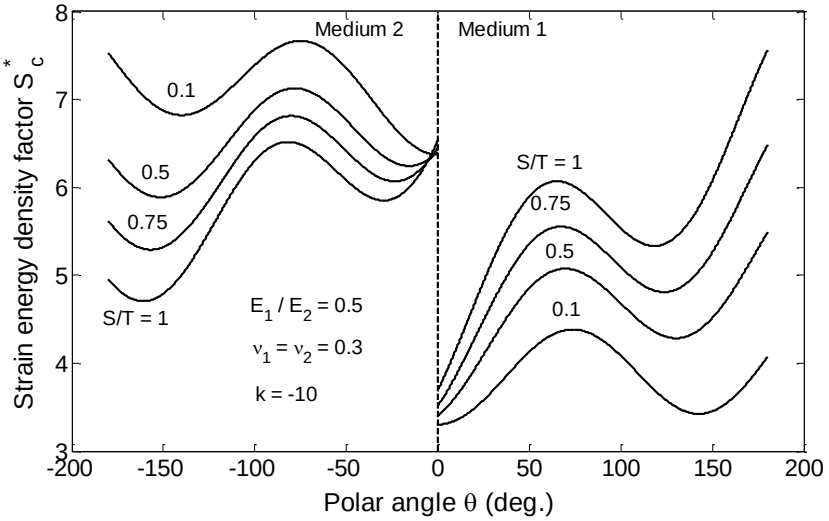

(e)

Fig. 6.7. Dimensionless strain energy density factor versus polar angle in dissimilar media under loading ratio of $S/T = 0.1, 0.5, 0.75$ and 1 for (a) $k = 0$; (b) $k = 1$; (c) $k = -1$; (d) $k = 10$; (e) $k = -10$.

Fig 6.7 shows the dimensionless strain energy density factor against polar angle centered on the crack tip of dissimilar materials combination $E_1/E_2 = 0.5$ for various biaxial load parameter $k = -10, -1, 0, 1, 10$ and force ratio $S/T = 0.1, 0.5, 0.75, 1$. As mentioned above, the strain energy density factor curves are continuous in both material 1 and material 2, but discontinuous across the interface. This characteristic of strain energy density factor curves also appears in the next figures 6.8-6.11 for different variables. In Fig 6.8-6.10, it can be found that only when the materials in the both sides are the same, the strain energy density factor is continuous across the bond line. This characteristic corresponds to Fig 6.6.

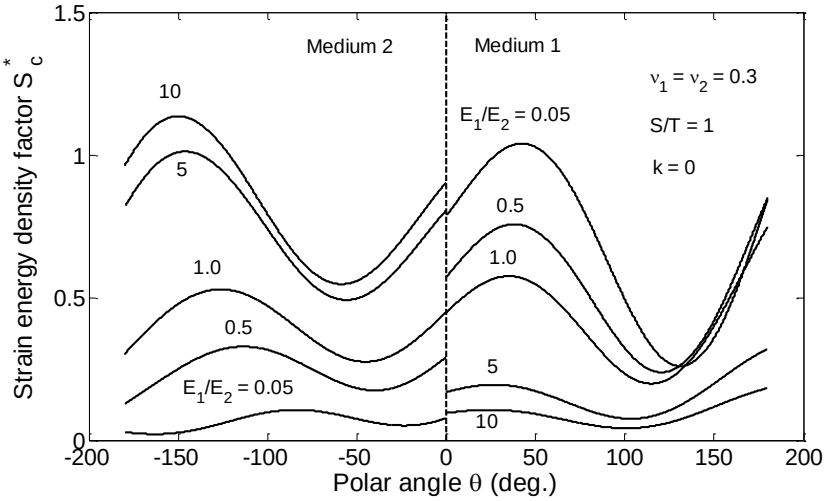

(a)

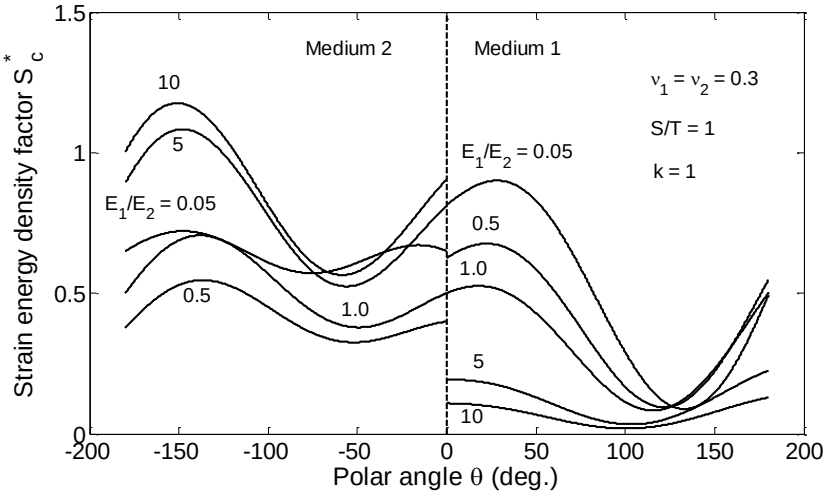

(b)

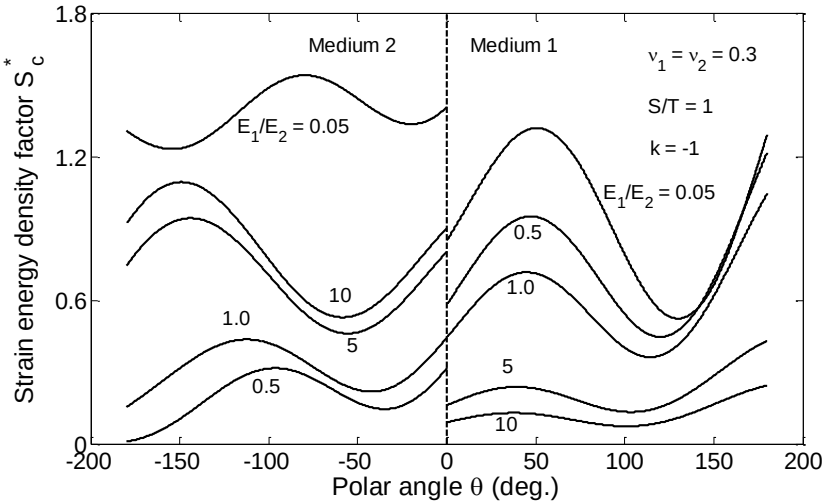

(c)

Fig. 6.8. Dimensionless strain energy density factor versus polar angle in different material combination $E_1/E_2 = 0.05, 0.5, 1.0, 5$ and 10, under loading ratio of $S/T = 1$ for biaxial loading parameter (a) $k = 0$; (b) $k = 1$; (c) $k = -1$.

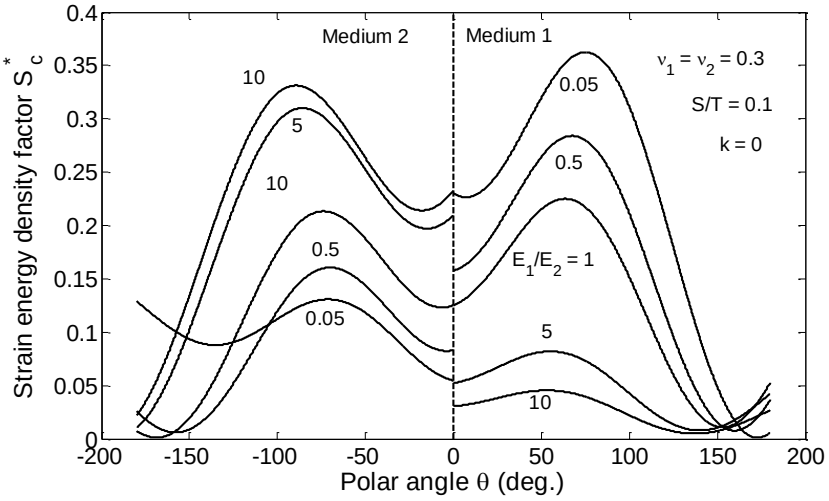

(a)

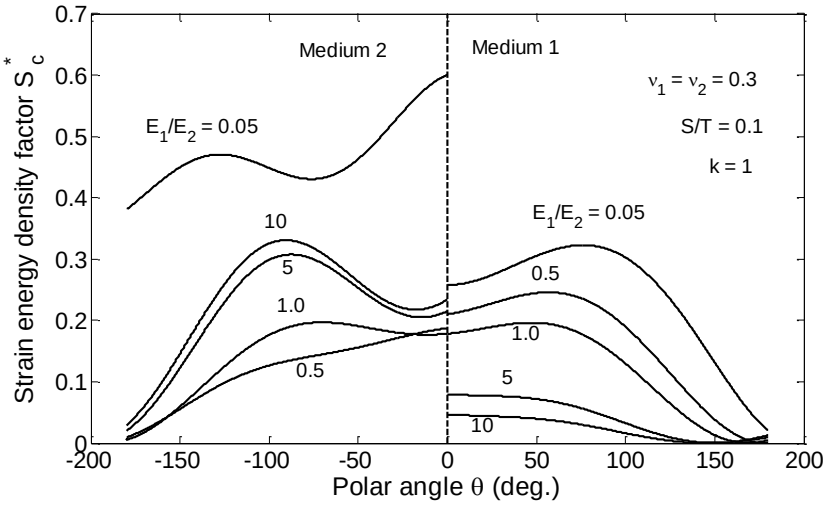

(b)

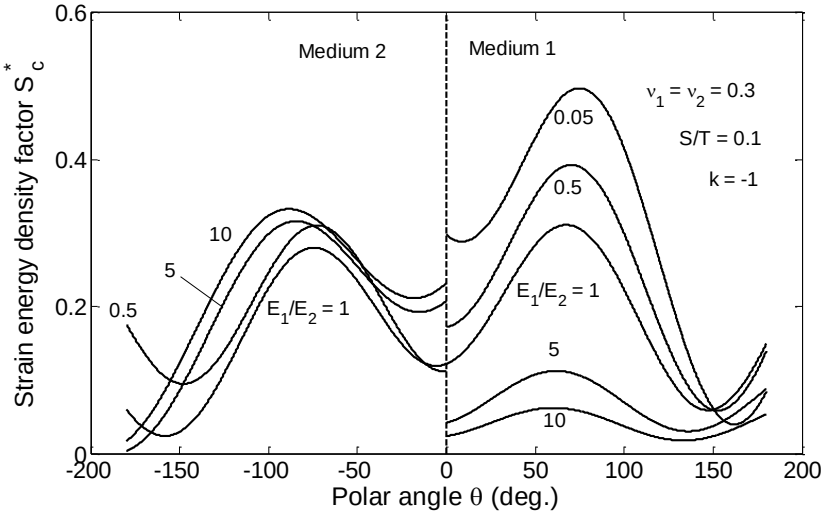

(c)

Fig. 6.9. Dimensionless strain energy density factor versus polar angle in different material combination $E_1/E_2 = 0.05, 0.5, 1.0, 5$ and 10, under loading ratio of $S/T = 0.1$ for biaxial loading parameter (a) $k = 0$; (b) $k = 1$; (c) $k = -1$.

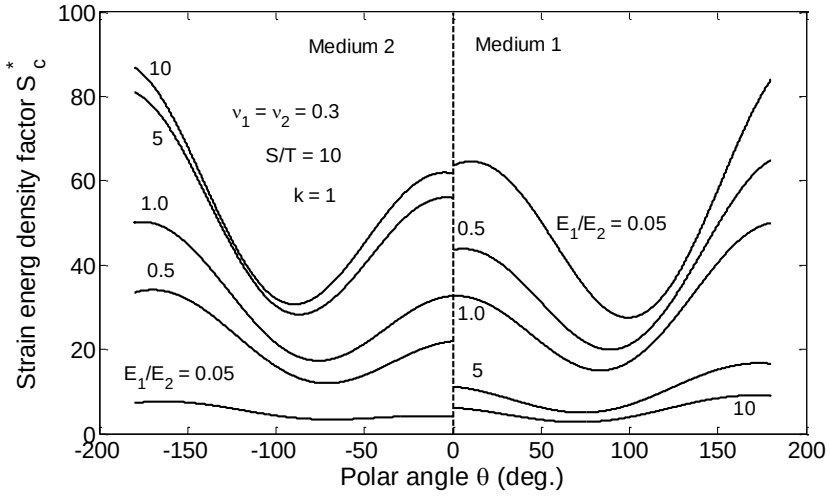
Medium 2
Medium 1
$\nu_1 = \nu_2 = 0.3$
S/T = 10
k = 1
$E_1/E_2 = 0.05$
10
5
1.0
0.5
$E_1/E_2 = 0.05$
0.5
1.0
5
10
Strain energ density factor S_c^*
Polar angle θ (deg.)

(a)

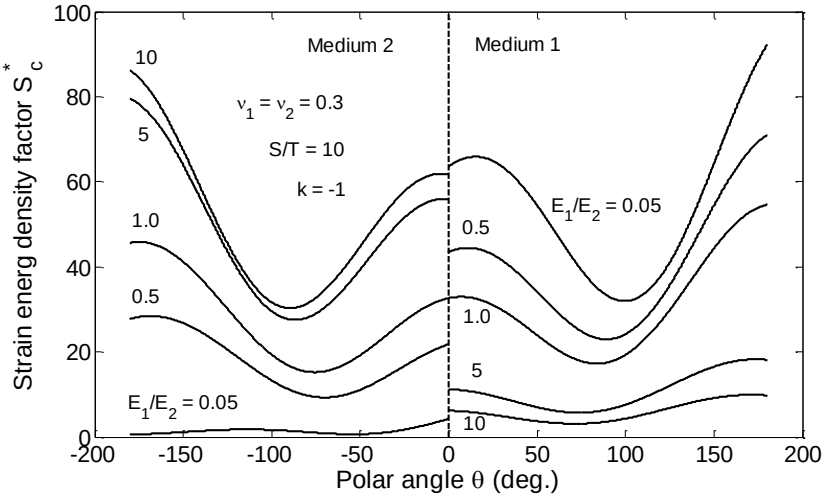
Medium 2
Medium 1
$\nu_1 = \nu_2 = 0.3$
S/T = 10
k = -1
$E_1/E_2 = 0.05$
10
5
1.0
0.5
$E_1/E_2 = 0.05$
0.5
1.0
5
10
Strain energ density factor S_c^*
Polar angle θ (deg.)

(b)

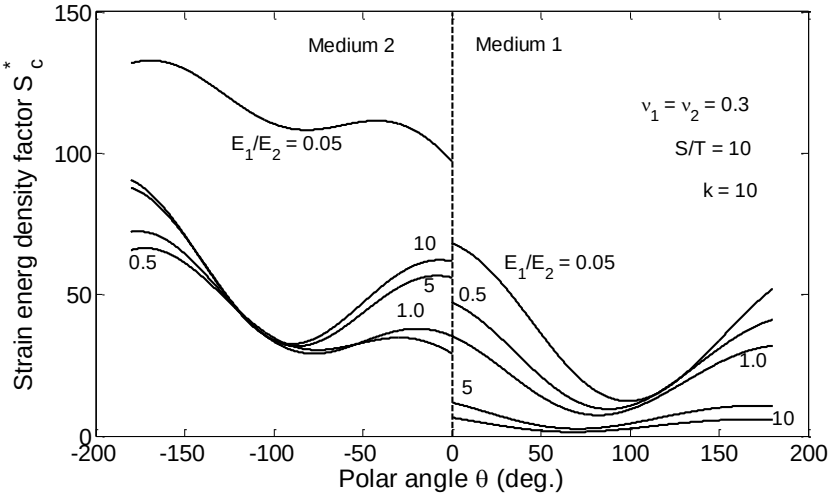
Medium 2
Medium 1
$\nu_1 = \nu_2 = 0.3$
S/T = 10
k = 10
$E_1/E_2 = 0.05$
$E_1/E_2 = 0.05$
0.5
10
5
1.0
0.5
1.0
5
10
Strain energ density factor S_c^*
Polar angle θ (deg.)

(c)

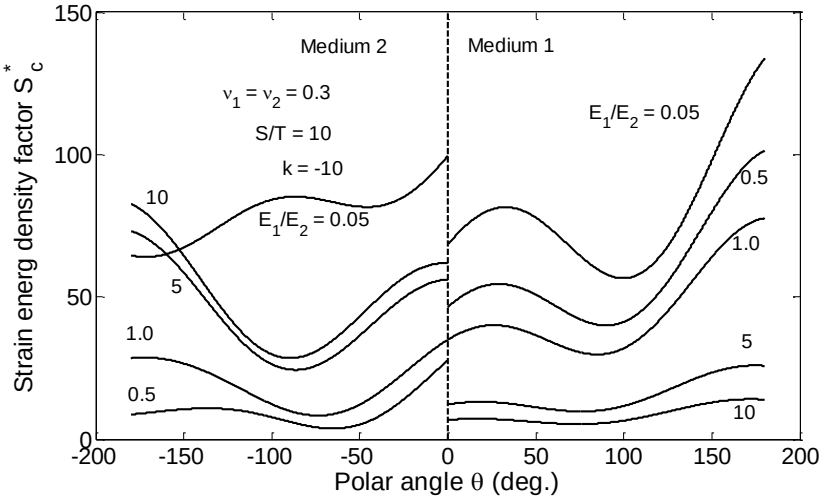

(d)

Fig. 6.10. Dimensionless strain energy density factor versus polar angle in different material combination $E_1/E_2 = 0.05, 0.5, 1.0, 5$ and 10, under loading ratio of $S/T = 10$ for biaxial loading parameter (a) $k = 1$; (b) $k = -1$; (c) $k = 10$; (c) $k = -10$.

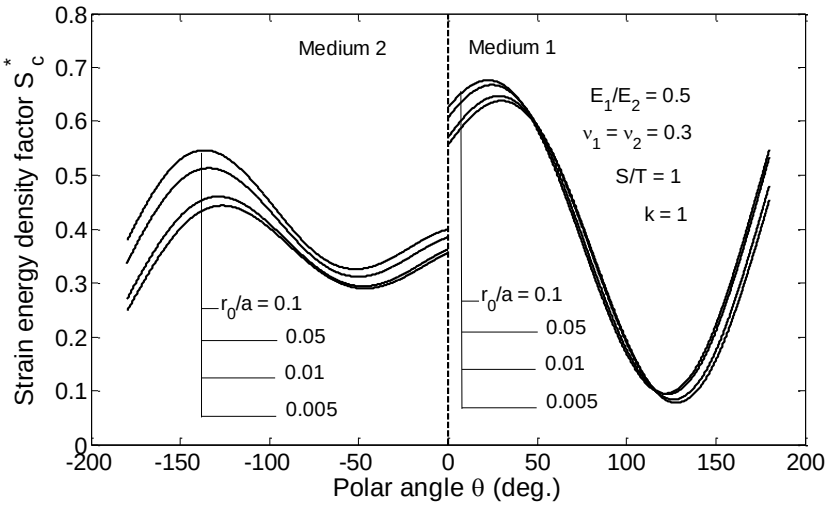

(a)

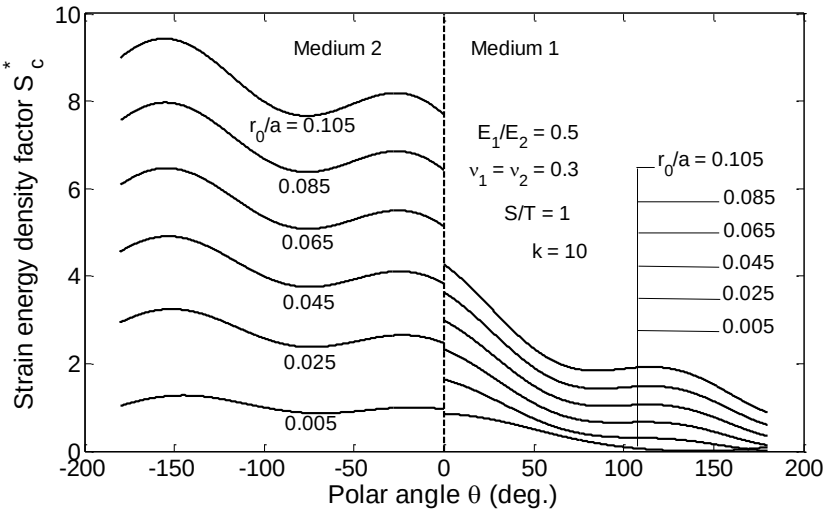

(b)

Fig. 6.11. Dimensionless strain energy density factor versus polar angle in the same material combination $E_1/E_2 = 0.5, \upsilon = 0.3$ at different distance from crack tip r_0/a under loading ratio of $S/T = 1$ for biaxial loading parameter (a) $k = 1$; (b) $k = 10$.

6.4 Conclusions

As the widely application of the composite, the strength quantity of composite has became more and more important, especially the strength of composite with flaws. The cohesion failure is the most possible damage of composite. In this chapter, an interfacial crack along the bond line between two dissimilar materials subjected to general loading is investigated. The explicit solutions of stresses around the interfacial crack tip are obtained by complex variable technique of Muskhelishvili and the superposition principle. The circumferential stress, maximum shear stress and the dimensionless strain energy density factor around the crack tip are presented graphically.

References

[1] Williams M.L. The stress around a fault or crack in dissimilar media. Bull. Seism. Soc. America, 1959, 49: 199-204.

[2] England A.H. A crack between dissimilar media. Journal of Applied Mechanics. 1965, 32: 400-402.

[3] Erdogan F. Stress distribution in bonded dissimilar material with cracks. Journal of Applied Mechanics. 1965, 32: 403-410.

[4] Rice J.R., Sih G.C. Plane problems of cracks in dissimilar media. Journal of Applied Mechanics. 1965, 32: 418-423.

[5] Gotoh H. Some problems of bonded anisotropic plates with cracks along the bond. International Journal of Fracture. 1967, 3: 253-265.

[6] Bogy D.B. The plane solution for anisotropic elastic wedges under normal and shear loading. Journal of Applied Mechanics. 1972, 39: 1103-1109.

[7] Kuo M.C., Bogy D.B. Plane solutions for the displacement and traction-displacement problems for anisotropic elastic wedges. Journal of Applied Mechanics. 1974, 41: 197-202.

[8] Ting T.C.T. Explicit solution and invariance of the singularities at an interface crack in anisotropic composites. International Journal of Solids and Structures, 1986, 22: 965-983.

[9] Ting T.C.T. Interface cracks in anisotropic biomaterials. Journal of Mechanics and Physics of Solids, 1990, 38: 505-513.

[10] Atkinson C. On stress singularities and interfaces in linear elastic fracture mechanics. Int. J. Fract. Mech. 1977, 13: 807-820.

[11] Comninou M. The interface crack. J. Appl. Mech. 1977, E44: 634-636.

[12] Comninou M. Interface crack with friction in the contact zone. J. Appl. Mech. 1977, E44: 780-781.

[13] Comninou M.The interface crack in a shear field. J. Appl. Mech. 1978, E45: 287-290.

[14] Ma C.C., Luo J.J. Plane solutions of interface cracks in anisotropic dissimilar media. Journal of Engineering Mechanics, ASCE, 1996, 122: 30-38.

[15] Piva A, Viola E. Biaxial load effects on a crack between dissimilar media. Engng. Fract. Mech. 1980; 13(1):143-174.

[16] Viola E, Piva A. Plane strain interfacial fracture analysis of a bimaterial incompressible body. Engng. Fract. Mech. 1981; 15(1-2):131-142.

[17]Salganik R.L. The brittle fracture of cemented bodies. Prikl. Mat. Mekh. 1963, 27: 1468-1478.

[18]Sih. G.C. and Rice. J.R, The bending of plates of dissimilar materials with cracks, J. Appl. Mech, 1964, 31: 477-482.

[19]Malyshev B, Salganik R. The strength of adhesive joints using the theory of cracks. Int. Fract. Mech., 1965, 1: 114-119.

[20]Efits J., Subramonian N. and Liebowitz H., Crack border stress and displacement equations revisited. Engng Fract Mech, 1977, 9: 189-210.

[21]Efits J., Subramonian N. and Liebowitz H., Biaxial load effects on the crack border elastic strain energy and strain energy rate. Engng Fract Mech, 1977, 9: 753-764.

[22]Sih GC. Some basic problems in fracture mechanics and new concepts. Engng Fract Mech 1973; 5(2): 365-77.

Appendix

Substituting eqs. (6.8) and (6.9) to eq. (6.7a) and (6.7b), the Cartesian coordinate stress components in medium 1 are obtained as following

$$\sigma_{xx}^{(1)} = (k+1)T - \frac{4T}{1+\alpha} + \frac{\sqrt{\pi a \alpha}}{(1+\alpha)\sqrt{2\pi r}}\left\{3e^{\epsilon(\theta-\pi)}\left[(T-2\epsilon S)\cos\left(\epsilon log\frac{r}{l}+\frac{\theta}{2}\right)-(2\epsilon T+S)\sin\left(\epsilon log\frac{r}{l}+\frac{\theta}{2}\right)\right]-e^{-\epsilon(\theta-\pi)}\left[(T-2\epsilon S)\cos\left(\epsilon log\frac{r}{l}-\frac{\theta}{2}\right)-(2\epsilon T+S)\sin\left(\epsilon log\frac{r}{l}-\frac{\theta}{2}\right)\right]\right\}-\frac{\sqrt{\pi a \alpha}e^{\epsilon(\theta-\pi)}}{(1+\alpha)\sqrt{2\pi r}}(1+4\epsilon^2)sin\theta\left[Tsin\left(\epsilon log\frac{r}{l}+\frac{3\theta}{2}\right)+Scos\left(\epsilon log\frac{r}{l}+\frac{3\theta}{2}\right)\right] \quad \text{(AI.1)}$$

$$\sigma_{yy}^{(1)} = \frac{\sqrt{\pi a \alpha}}{(1+\alpha)\sqrt{2\pi r}}\left\{e^{\epsilon(\theta-\pi)}\left[(T-2\epsilon S)cos\left(\epsilon log\frac{r}{l}+\frac{\theta}{2}\right)-(2\epsilon T+S)sin\left(\epsilon log\frac{r}{l}+\frac{\theta}{2}\right)\right]+e^{-\epsilon(\theta-\pi)}\left[(T-2\epsilon S)cos\left(\epsilon log\frac{r}{l}-\frac{\theta}{2}\right)-(2\epsilon T+S)sin\left(\epsilon log\frac{r}{l}-\frac{\theta}{2}\right)\right]\right\}+\frac{\sqrt{\pi a \alpha}e^{\epsilon(\theta-\pi)}}{(1+\alpha)\sqrt{2\pi r}}(1+4\epsilon^2)sin\theta\left[Tsin\left(\epsilon log\frac{r}{l}+\frac{3\theta}{2}\right)+Scos\left(\epsilon log\frac{r}{l}+\frac{3\theta}{2}\right)\right] \quad \text{(AI.2)}$$

$$\sigma_{xy}^{(1)} = \frac{\sqrt{\pi a \alpha}}{(1+\alpha)\sqrt{2\pi r}}\left\{e^{\epsilon(\theta-\pi)}\left[(T-2\epsilon S)sin\left(\epsilon log\frac{r}{l}+\frac{\theta}{2}\right)+(2\epsilon T+S)cos\left(\epsilon log\frac{r}{l}+\frac{\theta}{2}\right)\right]+e^{-\epsilon(\theta-\pi)}\left[(T-2\epsilon S)sin\left(\epsilon log\frac{r}{l}-\frac{\theta}{2}\right)+(2\epsilon T+S)cos\left(\epsilon log\frac{r}{l}-\frac{\theta}{2}\right)\right]\right\}+\frac{\sqrt{\pi a \alpha}e^{\epsilon(\theta-\pi)}}{(1+\alpha)\sqrt{2\pi r}}(1+4\epsilon^2)sin\theta\left[Tcos\left(\epsilon log\frac{r}{l}+\frac{3\theta}{2}\right)-Ssin\left(\epsilon log\frac{r}{l}+\frac{3\theta}{2}\right)\right] \quad \text{(AI.3)}$$

Substituting eqs. (6.8) and (6.9) to eqs. (6.7c) and (6.7d), the stress components in medium 2 are obtained as following

$$\sigma_{xx}^{(2)} = \mu\left[(k+1)T - \frac{4T}{1+\alpha}\right] + \frac{\sqrt{\pi a\alpha}}{(1+\alpha)\sqrt{2\pi r}}\left\{3e^{\epsilon(\theta+\pi)}\left[(T-2\epsilon S)\cos\left(\epsilon log\frac{r}{l}+\frac{\theta}{2}\right) - (2\epsilon T + S)\sin\left(\epsilon log\frac{r}{l}+\frac{\theta}{2}\right)\right] - e^{-\epsilon(\theta+\pi)}\left[(T-2\epsilon S)\cos\left(\epsilon log\frac{r}{l}-\frac{\theta}{2}\right) - (2\epsilon T+S)\sin\left(\epsilon log\frac{r}{l}-\frac{\theta}{2}\right)\right]\right\} - \frac{\sqrt{\pi a\alpha}e^{\epsilon(\theta+\pi)}}{(1+\alpha)\sqrt{2\pi r}}(1+4\epsilon^2)sin\theta\left[Tsin\left(\epsilon log\frac{r}{l}+\frac{3\theta}{2}\right) + Scos\left(\epsilon log\frac{r}{l}+\frac{3\theta}{2}\right)\right] \text{(AI.4)}$$

$$\sigma_{yy}^{(2)} = \frac{\sqrt{\pi a\alpha}}{(1+\alpha)\sqrt{2\pi r}}\left\{e^{\epsilon(\theta+\pi)}\left[(T-2\epsilon S)cos\left(\epsilon log\frac{r}{l}+\frac{\theta}{2}\right) - (2\epsilon T+S)sin\left(\epsilon log\frac{r}{l}+\frac{\theta}{2}\right)\right] + e^{-\epsilon(\theta+\pi)}\left[(T-2\epsilon S)cos\left(\epsilon log\frac{r}{l}-\frac{\theta}{2}\right) - (2\epsilon T+S)sin\left(\epsilon log\frac{r}{l}-\frac{\theta}{2}\right)\right]\right\} + \frac{\sqrt{\pi a\alpha}e^{\epsilon(\theta+\pi)}}{(1+\alpha)\sqrt{2\pi r}}(1+4\epsilon^2)sin\theta\left[Tsin\left(\epsilon log\frac{r}{l}+\frac{3\theta}{2}\right) + Scos\left(\epsilon log\frac{r}{l}+\frac{3\theta}{2}\right)\right] \text{(AI.5)}$$

$$\sigma_{xy}^{(2)} = \frac{\sqrt{\pi a\alpha}}{(1+\alpha)\sqrt{2\pi r}}\left\{e^{\epsilon(\theta+\pi)}\left[(T-2\epsilon S)sin\left(\epsilon log\frac{r}{l}+\frac{\theta}{2}\right) + (2\epsilon T+S)cos\left(\epsilon log\frac{r}{l}+\frac{\theta}{2}\right)\right] + e^{-\epsilon(\theta+\pi)}\left[(T-2\epsilon S)sin\left(\epsilon log\frac{r}{l}-\frac{\theta}{2}\right) + (2\epsilon T+S)cos\left(\epsilon log\frac{r}{l}-\frac{\theta}{2}\right)\right]\right\} + \frac{\sqrt{\pi a\alpha}e^{\epsilon(\theta+\pi)}}{(1+\alpha)\sqrt{2\pi r}}(1+4\epsilon^2)sin\theta\left[Tcos\left(\epsilon log\frac{r}{l}+\frac{3\theta}{2}\right) - Ssin\left(\epsilon log\frac{r}{l}+\frac{3\theta}{2}\right)\right] \text{(AI.6)}$$

The polar stress components can be obtained by substituting eqs. AI(1-6) to eq. (6.10) as following

$$\sigma_{\theta\theta}^{(1)} = T\left(\frac{k+1}{2}-\frac{2}{1+\alpha}\right)(1-cos2\theta) + \frac{\alpha\sqrt{\pi a}e^{-\epsilon\theta}}{(1+\alpha)\sqrt{2\pi r}}\left[(T-2\epsilon S)cos\left(\epsilon log\frac{r}{l}+\frac{3\theta}{2}\right) - (2\epsilon T + S)sin\left(\epsilon log\frac{r}{l}+\frac{3\theta}{2}\right)\right] + \frac{\sqrt{\pi a}e^{\epsilon\theta}}{(1+\alpha)\sqrt{2\pi r}}\left\{(T-2\epsilon S)\left[2cos\left(\epsilon log\frac{r}{l}+\frac{\theta}{2}\right) - cos\left(\epsilon log\frac{r}{l}-\frac{3\theta}{2}\right)\right] - (2\epsilon T+S)\left[2sin\left(\epsilon log\frac{r}{l}+\frac{\theta}{2}\right) - sin\left(\epsilon log\frac{r}{l}-\frac{3\theta}{2}\right)\right]\right\} - \frac{\sqrt{\pi a}e^{\epsilon\theta}(1+4\epsilon^2)}{2(1+\alpha)\sqrt{2\pi r}}\left\{T\left[cos\left(\epsilon log\frac{r}{l}+\frac{\theta}{2}\right) - cos\left(\epsilon log\frac{r}{l}-\frac{3\theta}{2}\right)\right] - S\left[sin\left(\epsilon log\frac{r}{l}+\frac{\theta}{2}\right) - sin\left(\epsilon log\frac{r}{l}-\frac{3\theta}{2}\right)\right]\right\} \text{(AI.7)}$$

$$\sigma_{r\theta}^{(1)} = -T\left[\frac{k+1}{2}-\frac{2}{1+\alpha}\right]sin2\theta + \frac{\sqrt{\pi a}e^{\epsilon\theta}}{(1+\alpha)\sqrt{2\pi r}}\left[(T-2\epsilon S)sin\left(\epsilon log\frac{r}{l}-\frac{3\theta}{2}\right) + (2\epsilon T+S)cos\left(\epsilon log\frac{r}{l}-\frac{3\theta}{2}\right)\right] + \frac{\alpha\sqrt{\pi a}e^{-\epsilon\theta}}{(1+\alpha)\sqrt{2\pi r}}\left[(T-2\epsilon S)sin\left(\epsilon log\frac{r}{l}+\frac{3\theta}{2}\right) + (2\epsilon T+S)cos\left(\epsilon log\frac{r}{l}+\frac{3\theta}{2}\right)\right] + \frac{\sqrt{\pi a}e^{\epsilon\theta}(1+4\epsilon^2)}{(1+\alpha)\sqrt{2\pi r}}sin\theta\left[Tcos\left(\epsilon log\frac{r}{l}-\frac{\theta}{2}\right) - Ssin\left(\epsilon log\frac{r}{l}-\frac{\theta}{2}\right)\right] \text{(AI.8)}$$

for medium 1.

$$\sigma_{\theta\theta}^{(2)} = \mu T\left(\frac{k+1}{2}-\frac{2}{1+\alpha}\right)(1-cos2\theta) + \frac{\sqrt{\pi a}e^{-\epsilon\theta}}{(1+\alpha)\sqrt{2\pi r}}\left[(T-2\epsilon S)cos\left(\epsilon log\frac{r}{l}+\frac{3\theta}{2}\right) - (2\epsilon T + S)sin\left(\epsilon log\frac{r}{l}+\frac{3\theta}{2}\right)\right] + \frac{\alpha\sqrt{\pi a}e^{\epsilon\theta}}{(1+\alpha)\sqrt{2\pi r}}\left\{(T-2\epsilon S)\left[2cos\left(\epsilon log\frac{r}{l}+\frac{\theta}{2}\right) - cos\left(\epsilon log\frac{r}{l}-\frac{3\theta}{2}\right)\right] - (2\epsilon T+S)\left[2sin\left(\epsilon log\frac{r}{l}+\frac{\theta}{2}\right) - sin\left(\epsilon log\frac{r}{l}-\frac{3\theta}{2}\right)\right]\right\} - \frac{\alpha\sqrt{\pi a}e^{\epsilon\theta}(1+4\epsilon^2)}{2(1+\alpha)\sqrt{2\pi r}}\left\{T\left[cos\left(\epsilon log\frac{r}{l}+\frac{\theta}{2}\right) - cos\left(\epsilon log\frac{r}{l}-\frac{3\theta}{2}\right)\right] - S\left[sin\left(\epsilon log\frac{r}{l}+\frac{\theta}{2}\right) - sin\left(\epsilon log\frac{r}{l}-\frac{3\theta}{2}\right)\right]\right\} \text{(AI.9)}$$

$$\sigma_{r\theta}^{(2)} =$$

$$-\mu T\left[\frac{k+1}{2}-\frac{2}{1+\alpha}\right]sin2\theta+\frac{\alpha\sqrt{\pi a}e^{\epsilon\theta}}{(1+\alpha)\sqrt{2\pi r}}\left[(T-2\epsilon S)sin\left(\epsilon log\frac{r}{l}-\frac{3\theta}{2}\right)+(2\epsilon T+S)cos\left(\epsilon log\frac{r}{l}-\right.\right.$$

$$\left.\left.\frac{3\theta}{2}\right)\right]+\frac{\sqrt{\pi a}e^{-\epsilon\theta}}{(1+\alpha)\sqrt{2\pi r}}\left[(T-2\epsilon S)sin\left(\epsilon log\frac{r}{l}+\frac{3\theta}{2}\right)+(2\epsilon T+S)cos\left(\epsilon log\frac{r}{l}+\frac{3\theta}{2}\right)\right]+$$

$$\frac{\alpha\sqrt{\pi a}e^{\epsilon\theta}(1+4\epsilon^2)}{(1+\alpha)\sqrt{2\pi r}}sin\theta\left[Tcos\left(\epsilon log\frac{r}{l}-\frac{\theta}{2}\right)-Ssin\left(\epsilon log\frac{r}{l}-\frac{\theta}{2}\right)\right] \text{(AI.10)}$$

for medium 2.

Chapter 7

Fracture criteria and crack propagation of the interfacial crack

7.1 Introduction

In chapter 3, most criteria are introduced for crack propagation in isotropic homogenous elastic material. Among those criteria, strain energy density factor criterion (SEDF) [1], maximum tangential stress criterion (MTS) [2] and the maximum energy release rate criterion (MERR) [3, 4] are most popular due to these simple formulae and easy use. However, the difficulties always arise in the interfacial crack propagation. Due to asymmetry in loading and elastic properties across the interface, many interfacial fracture problems are inherently mixed mode. In mixed mode, both normal and shear stresses act across the interface ahead of the tip of the interfacial crack, and both opening and shearing displacements occur on the crack faces behind the tip. Thus interfacial fracture in two-dimensional geometries involves mode 1 (opening) and mode 2 (shearing) stress intensity factors, and one must allow for a toughness characterization which, in general, is a function of the relative amounts of mode 1 and mode 2. This is one of the main differences between interfacial fracture mechanics and fracture mechanics for isotropic homogenous materials in which mode I toughness receives predominant emphasis. As regards the fracture criteria for a crack at interface between dissimilar materials, Piva and Viola [5] proposed a fracture criterion based on the MTS criterion, that can be used to assess whether an interface crack will extend along the interface or into one of the two adjacent materials in the plane perpendicular to the direction of maximum circumferential stress evaluated at a small distance from the crack tip. A slight different version, to take account of the shear loading was proposed by Viola and Piva [6]. He and Hutchinson [7] suggested a criterion based on the energy release rate for predicting the kinking angle. They showed that the competition between crack advance within the interface and kinking depended on relative toughness of the interface to that of the joining material. Moreover, the kinking occured in the direction where the energy release rate was maximum. Yuuki and Xu [8] and Yuuki et al [9] carried out fracture tests of aluminum epoxy dissimilar materials with an interface crack under comprehensive mixed mode conditions. Using the brazil-nut-sandwich compression tests, they showed that the fracture angles were well predicted by the criterion proposed by the authors themselves. Ayatollahi and Mirsayar [10] developed a fracture criterion, referred to as the modified maximum tangential stress criterion, which took into account the effect of T-stress in addition to the stress intensity factors for predicting

the kinking angle in the interface cracks. Rudraraju et al. [11] presented a variational multi-scale approach to predict mixed mode in-plane cohesive crack propagation. A comparative study of numerical results with the corresponding experimental observations of crack propagation in laminate fiber reinforced composite panel was also presented. A criterion based on the relative minimum plastic zone radius (MPZR) was investigated for prediction of fatigue crack initiation angles of mixed mode by Bian and Kim [12]. Based on the complex stress state at the crack tip, a maximum ratio criterion was developed to determine the crack propagation for a given inclination angle by means of an opening mode theory by Bian and Taheri [13]. It assumed that the crack began to propagate then the maximum value of ratio approached its critical value, and the direction of crack propagation coinciding with the direction of maximum ratio was defined.

Furthermore, there are some experimental and special researches that deserve to be mentioned. Theocaris and Andrianopoulos [14] introduced the Mises elastic-plastic boundary to define the core region. They used the minimum value of the radium of the elastic-plastic boundary for defining the direction of crack propagation. Spyropoulos [15] constructed the zone of yield initiation for the interface crack problem using the Mieses yield criterion according to the two-term stress solution reported in [5]. In [16] the strain energy density criterion was applied to determine the direction of crack initiation for various biaxial load factors and material combinations. Buyukozturk and Hearing [17] investigated fracture of two-phase composites in terms of parameters that influence the cracking scenarios in the interfacial regions and affect the fracture behavior of the concrete. Numerical and physical model tests were performed to study the influence of constituent fracture properties on the behavior of concrete composites. A series of interfacial crack experiments were conducted by Choi and Chai [18] using biaxial loading device for various mixed modes. Lee et al. [19] revisited the criterion to prevent kink of a crack out of a bi-material interface under the presence of in-plane residual stresses. They predicted that in-plane residual stresses control the energetic conditions to prevent crack kinking out of the interface. The change in the stress state near the crack tip due to its own contribution to the singular stress field like globally applied loadings was required. In other words, the problem at issue cannot be handled in purely local terms, but a global approach should be adopted. Kayupov and Dzenis [20] modeled the crack propagating under quasi-static loading and in fatigue life by nonlinear finite element analysis. Goyal et al. [21] proposed a new strength-fracture model for decohesion elements, which includes the geometric nonlinearity of the adherends and adhesive. The initiation and progression of interfacial cracks and/or cohesive cracks were simulated by positioning decohesion elements, at the adherent-adhesive interface and between bulk adhesive element. At an earlier date, the authors had postulated an irreversible cohesive-decohesive constitutive law for modeling the delamination process using interfacial surface discon-

tinuities [22]. Yang et al. [23] calculated the critical stresses, taking into account the influence of the adjacent ply angle and the crack size, for the initiation of crack propagation in the transverse direction and in the tunneling direction of a crack embedded in the central layer of a composite laminate. They showed that transverse cracking was a more possible fracture mode in composite laminates with initial crack-like defects. Kaminski [24] pointed a mathematical model and its numerical realization of the composite materials with stochastic interface defects. The composite was discretized using the Boundary Element Method.

For each material pair, a universal singular crack tip field exists at the crack tip according to linear elasticity theory for a traction-free line crack. For the plane problems, the normal and shear stresses of the singular field acting on the interface is distance r ahead of the tip, and it can be written in the compact "complex" form [25]

$$\sigma_{22} + i\sigma_{12} = \frac{(K_1 + iK_2)r^{i\epsilon}}{\sqrt{2\pi r}} \tag{7.1}$$

where $i = \sqrt{-1}$ and the oscillation index ϵ is the bi-material constant depending on β according to

$$\epsilon = \frac{1}{2\pi}\ln\left(\frac{1-\beta}{1+\beta}\right) \tag{7.2}$$

From the above equation, we note that the dimension of complex stress intensity factor $K = K_1 + iK_2$ is $[\text{stress}][\text{length}]^{1/2-i\epsilon}$, whereas that of its amplitude $|K|$ is the familiar $[\text{stress}][\text{length}]^{1/2}$.

In plane condition, the crack face displacements a distance r behind the tip are given by

$$\delta_2 + i\delta_1 = \frac{4}{\sqrt{2\pi}}\frac{1/\overline{E_1} + 1/\overline{E_2}}{(1+2i\epsilon)cosh(\pi\epsilon)}(K_1 + iK_2)\sqrt{r}r^{i\epsilon} \tag{7.3}$$

where

$$\overline{E_\iota} = \begin{cases} E_i & plane\ stress \\ \dfrac{E_i}{1-\nu_i^2} & plane\ strain \end{cases} \quad (i = 1,2)$$

The amplitude factors, K_1 and K_2, depending linearly on the applied loads and on the details of the full geometry of the body, will be illustrated below. These stress intensity factors are defined to be consistent with corresponding stress intensity factors for cracks in homogeneous problems. The energy release rate per unit length of extension of the crack in the interface is related to the stress intensity factors by

$$\mathcal{G} = \frac{1/\overline{E_1} + 1/\overline{E_2}}{2cosh^2(\pi\epsilon)}(K_1^2 + K_2^2) \tag{7.4}$$

which is the generalization of Irwin's famous result for a homogeneous isotropic material.

When $\epsilon = 0$, $r^{i\epsilon} = 1$, and then K_1 and K_2 are conventionally interpreted as mode 1 and mode 2 stress intensity factors measuring the singularity of normal and shear stresses, respectively, on the interface ahead of the tip.

When $\epsilon \neq 0$, the relative proportion of normal and shear stresses on the interface in the singular field varies slowly according to $r^{i\epsilon} = \cos(\epsilon \ln r) + i \sin(\epsilon \ln r)$, and this feature complicates the implementation of interfacial mechanics in several respects. When $\epsilon \neq 0$, the traction-free line crack solution is not fully consistent since the solution of displacement implies that the crack faces interpenetrate behind the tip. Although seemingly troublesome, this inconsistency will usually be inconsequential since the distance of the contact region behind the tip is generally exceedingly small compared to the zone of nonlinear deformation or fracture processes. More problematic is the fact that K_1 and K_2 cannot be interpreted in a straightforward way as mode 1 and mode 2 intensity factors directly linked to normal and shear stresses.

In the following sections, two fracture criteria about interfacial crack are introduced in detail. The first criterion is proposed by He and Hutchinson [7] (for simplicity, hereafter designated by HH-criterion) which based on the competition between the ratios of the energy release rate of interface cracking, substrate cracking, the interface and substrate toughness. The second failure criterion is proposed by Piva and Viola [5] (for simplicity, hereafter designated by PV-criterion) combining the maximum normal stress criterion with the phenomenological criterion. It can be considered as an extension of MTS criterion for interfacial crack propagation.

7.2 HH-criterion [7]

Analyzed by He and Hutchinson [7], a plane strain crack is kinked out of the interface between two dissimilar isotropic elastic solids. The focus is on the initiation of kinking and thus the segment of the crack leaving the interface is imagined to be short compared to the segment in the interface. Accordingly, the analysis provides the stress intensity factors and energy release rate of the kinked crack in terms of the corresponding quantities for the interface crack prior to kinking. Roughly speaking, the energy release rate is enhanced if the crack heads into the more compliant material and is diminished if it kinks into the stiff material. The results suggest a tendency for a crack to be trapped in the interface irrespective of the loading when the compliant material is tough and the stiff material is at least as tough as the interface.

A fracture mechanics of interfacial separation is starting to emerge, although there are still conceptual difficulties to be overcomed associated with the nonstandard oscillatory square root singularity

of some interface cracks. He and Hutchinson analyzed a crack kinking out of an interface which is carried out with the aim of providing the crack mechanics needed to assess whether an interface crack will tend to propagation in the interface or whether it will advance by kinking out of the interface. The geometry analyzed is shown in Fig. 7.1. The parent interface crack lies on the interface between two semi-infinite blocks of isotropic elastic solids with differing elastic moduli. A straight crack segment of length a and angle ω (positive clockwise) kinks downward into material 2. The length a is assumed to be small compared to the length of the parent interface segment of the crack, and thus the asymptotic problem for the semi-infinite parent crack is analyzed. The stress field prior to kinking ($a \to 0$) is therefore the singularity field of an interface crack characterized by a complex intensity factor, $K = K_1 + iK_2$, to be specified precisely. The crack tip field at the end of the kinked crack is characterized by a combination of standard mode I and mode II stress intensity factors, K_I and K_{II}. The analysis provides the relationship among K_I and K_{II} for the kinked crack and K_1 and K_2 for the interface crack as dependent on the kink angle ω and the material moduli. The energy release rate of the kinked crack is also related to the energy release rate of the interface crack.

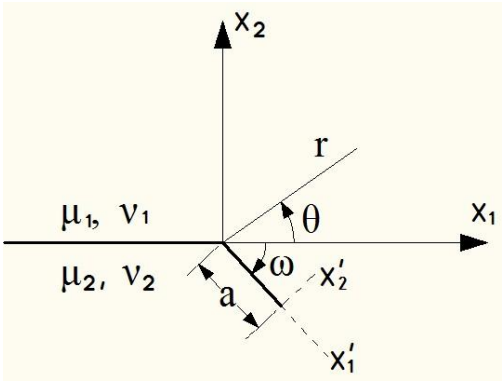

Fig. 7.1 Geometry of kinked crack

The stress field for the semi-infinite interface crack ($a = 0$) has the form

$$\sigma_{\alpha\beta} = Re\{K(2\pi r)^{-1/2} r^{i\epsilon} \bar{\sigma}_{\alpha\beta}(\theta)\} \tag{7.5}$$

where $i = \sqrt{-1}$, r and θ are planar-polar coordinates centered at the origin, $K = K_1 + iK_2$ is the complex interface stress intensity factors, and oscillation index ϵ is in eq. (7.2). The angular dependence $\bar{\sigma}_{\alpha\beta}(\theta)$ is complex in general, but universal for a given material pair. On the interface ahead of the tip the tractions are reduced as eq. (7.1).

The results for the kinked crack proposed by He and Hutchinson can be used to assess whether an interface crack will propagate in the interface or whether it will kink out of the interface. The simplest approach is to assume that the condition for propagation in the interface is $\mathcal{G}_0 = \mathcal{G}_{0c}$ and that for propagation in material 2 is $\mathcal{G} = \mathcal{G}_{2c}$. If $\mathcal{G}_{2c}$ is sufficiently large, compared to $\mathcal{G}_{0c}$, the crack will

never kink into material 2. When $\mathcal{G}_{2c}$ is comparable to $\mathcal{G}_{0c}$ there will still be a loading range, i.e., $0 \leq \psi < \psi_{max}$, (ψ is the phase angle will be defined in next section) such that the crack stays in the interface, while for $\psi > \psi_{max}$, the interface crack will kink into material 2. The interface toughness will be discussed in the next section.

In plane strain, the energy release rate eq. (7.4) can be written as

$$\mathcal{G}_0 = \frac{[(1-\nu_1)\mu_1 + (1-\nu_2)\mu_2]K\overline{K}}{(4cosh^2\pi\epsilon)} \tag{7.6}$$

in the new normalization. The energy release rate $\mathcal{G}$ of the kinked crack $a > 0$ is given by

$$\mathcal{G} = [(1-\nu_2)/(2\mu_2)](K_I^2 + K_{II}^2) \tag{7.7}$$

A similar analysis can be carried out when $\mathcal{G}_{0c}$ depends on ψ. This can be expected when the fractured interface has some roughness, as $\mathcal{G}_{0c}$ increasing with ψ. The important point is that the level of $\mathcal{G}_{2c}$ required to prevent kinking out of the interface will depend on the interface toughness $\mathcal{G}_{0c}$ at the loading angle ψ applied. When there is no dissimilarity in the elastic properties of the materials across the interface, the directions of kinking associated with the maximum energy release rate and with $K_{II} = 0$ are virtually the same.

This criterion is modified simplify the analysis for effective simulation using the finite element method by Yang [26], thus making the simulation acceptable engineering purposes. The modification is described as: if $\Gamma(\psi) \ll \Gamma_1, \Gamma_2$, the crack is assumed to remain at the interface for an arbitrary phase angle of loading, as the flaw meets the condition for continuing advance in the interface at an applied load lower than that necessary to advance the crack into the substrate. On the other hand, if $\Gamma(\psi) \approx \Gamma_2$ and $\Gamma_2 \ll \Gamma_1$, the crack is assumed to remain at the interface for $\psi < 0$; the crack will kink out of the interface and propagate in material 2 for $\psi \geq 0$ and $\Gamma(\psi)/\Gamma_2 \leq 1 - \rho(\psi)$. The function $\rho(\psi)$ can be expressed approximately as

$$\rho(\psi) = \begin{cases} 0.0, \psi \in [0, \pi/8] \\ 0.2, \psi \in [\pi/8, \pi/4] \\ 0.4, \psi \in [\pi/4, \pi/2] \end{cases} \tag{7.8}$$

The value of interface toughness, $\Gamma(\psi)$, depending on the phase angle of loading and will be discussed later. The definition of $\rho(\psi)$ doesn't have any physical meaning or experimental support. It's just for making numerical analysis conveniently.

7.3 PV-criterion [5]

Generally, for a crack in a planar anisotropic medium the crack extension conditions are established by comparison of the elastic stress vector $\bar{S}$ and the strength vector $\bar{R}$ [27]. It is assumed that crack extension occurs when the stress vector, calculated at a small radial distance from the crack tip as a function of external loading, coincides with or exceeds the strength vector which is a function of material of material properties. Referring to Fig. 7.2(a), where the polar contours $\mathfrak{R}$ and $\mathcal{F}$ of the strength and stress vectors respectively are represented, we observe that failure will occur along with the direction θ_0 which does not coincide with the direction of the maximum stress vector.

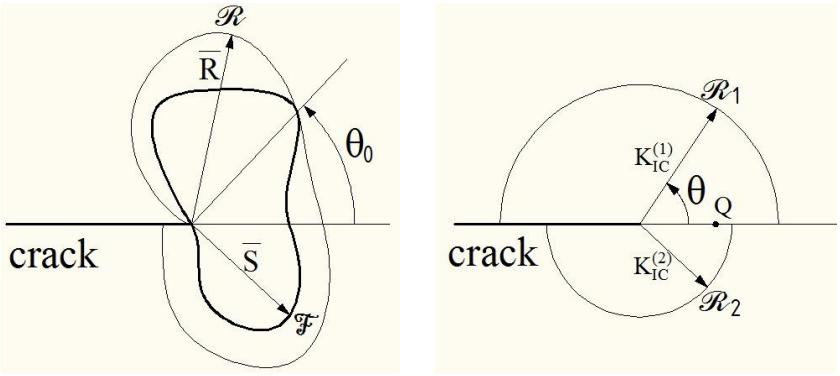

(a) (b)

Fig. 7.2 (a) Fracture criterion for an anisotropic material; (b) Strength regions for an interfacial crack between dissimilar materials.

For a fixed system of applied loads, it has been observed that the stress distribution around the tip of the interfacial crack depends on the elastic properties of the two media through the Young's moduli E_i and Poisson's ratios ν_i. Now, for a known tensional state, fracture initiation and propagation depend on the critical stress intensity factors $K_{IC}^{(1)}$ and $K_{IC}^{(2)}$ of the two media and on the adhesive strength of the bond through the critical parameter K_b which is associated with the propagation of tensile bond cracks.

Owing to the fact that both materials are assumed, separately, linearly elastic, homogeneous and isotropic, the critical stress intensity factors $K_{IC}^{(1)}$ and $K_{IC}^{(2)}$ are independent of the radial direction from the crack tip. Consequently, the strength region assumes the appearance shown in Fig. 7.2(b), if, for example, $K_b < K_{IC}^{(2)} < K_{IC}^{(1)}$. The boundary $\mathfrak{R}_1 \cup \mathfrak{R}_2 \cup Q$ is discontinuous along the axis of the crack where the point Q is representative of the interfacial strength strictly connected with K_b. Moreover, as far as the stress region is connected, we shall assume that the quantity controlling the fracture initiation is the circumferential stress evaluated at a small radial distance from the crack tip.

In view of the particular anisotropy involved in the interfacial crack problem, a failure criterion is proposed combining the maximum normal stress criterion with the phenomenological criterion

mentioned above. The following assumptions are made referring to a right polar coordinate system with the origin at the crack tip:

(1) The crack extension occurs along the maximum tangential stress direction or in to one of the two adjacent materials in the plane perpendicular to the direction of maximum circumferential stress evaluated at a small distance r_0 from the crack tip. (2) The initiation of the crack extension occurs as soon as one of the following conditions is satisfied:

$$\sqrt{2\pi r_0}\sigma_{\theta\theta}^{(1)}|_{\theta_0^{(1)},r_0} = K_{IC}^{(1)}, \qquad 0 < \theta_0^{(1)} \leq \pi \tag{7.9}$$

$$\sqrt{2\pi r_0}\sigma_{\theta\theta}^{(2)}|_{\theta_0^{(2)},r_0} = K_{IC}^{(2)}, \qquad -\pi \leq \theta_0^{(2)} < 0 \tag{7.10}$$

$$\sqrt{2\pi r_0}\sigma_{\theta\theta}|_{\theta_0,r_0} = K_b\ , \quad \theta_0 = 0 \tag{7.11}$$

where $\theta_0^{(1)}$, $\theta_0^{(2)}$ are the angles corresponding to the crack initial propagation direction in the two media, and $K_{IC}^{(1)}$, $K_{IC}^{(2)}$ and K_b are the critical stress intensity factors of the two media and the bonding face, respectively.

The first assumption states the possibilities of the crack to extend into one material or the other or along the interface for any system of external loading. The second assumption stating which of the above possibilities is chosen by the crack and the corresponding values of the critical load and of the biaxial parameter k allowing the initiation of the extension. As soon as one of the conditions of eqs. (7.9-7.11) is satisfied among the others, the crack extension initiates along the direction $\theta_0^{(1)}$ or $\theta_0^{(2)}$ in the corresponding medium, or along $\theta = 0$ at the interface. These various possibilities are indicated, for example, in Fig.7.3 where the failure criterion is shown in a plane polar representation.

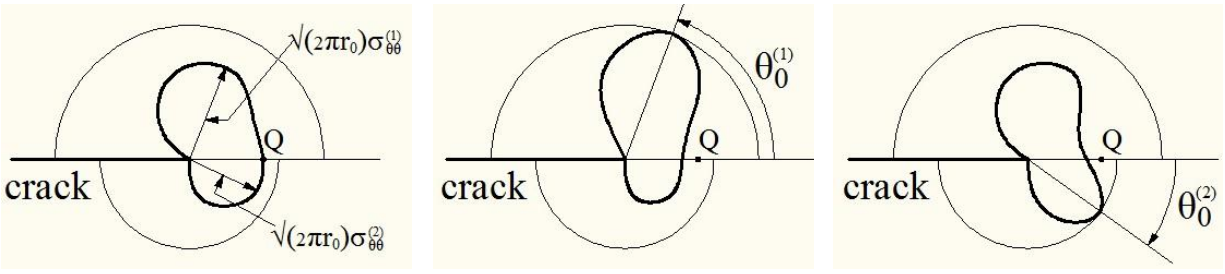

(a) (b) (c)

Fig. 7.3 Representation of the fracture criterion

The polar expression of $\sigma_{\theta\theta}$, calculated at the radial distance r_0/a, is proportionally influenced by the applied loads. Then, an increase of k at a fixed value of T, and vice versa, causes a proportional increase of the stress region up to some point of the boundary of the strength region and at this point fracture initiation occurs.

The configuration of Fig. 7.3(a) corresponds to the interfacial crack propagation, whereas the configurations of Figs. 7.3(b) and (c) correspond to the crack extension into the medium 1 or 2 with directions of extension $\theta_0^{(1)}$, $\theta_0^{(2)}$, respectively.

According to the analysis above, it is possible to know whether the crack extension occurs along the interface or into one material, and, in the second case, the angle of incipient fracture. The procedure for obtaining the crack extension previsions can be illustrated by the following schematic representation. Let K_b, $\bar{E}_i$, $\bar{K}_{IC}^{(i)}$, $i = 1, 2$ be known quantities, then, the curves corresponding to the ratios

$$K_*^{(i)} = \frac{\bar{K}_{IC}^{(i)}}{K_b}, E^* = \frac{\bar{E}_1}{\bar{E}_2} \tag{7.12}$$

can be drawn, for example, as is show in Fig. 7.4.

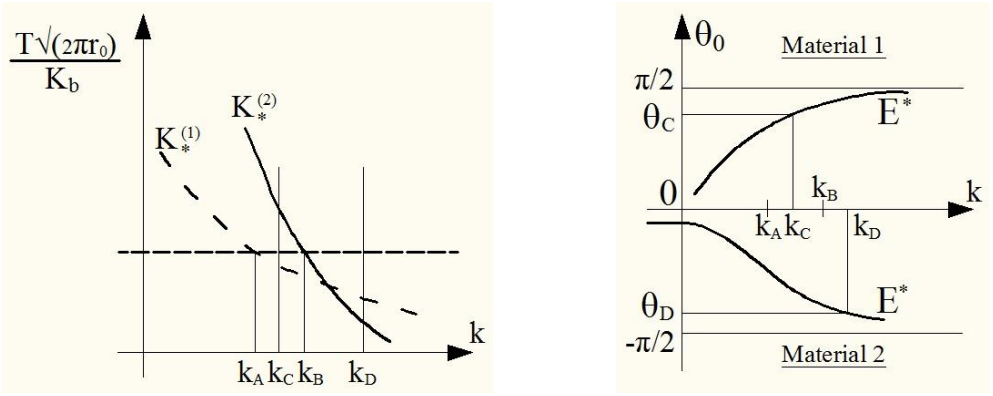

(a) (b)

Fig. 7.4 Explanation of the procedure to obtain the previsions of the fracture criterion.

From Fig. 7.4 (a) it follows that when $k < k_A$ the condition eq. (7.10) is satisfied before all the others and the crack extension occurs along the interface. When $k = k_C$ with $k_A < k_C < k_B$, the vertical line $k = k_C$ meets first the curve $K_*^{(1)}$, then the condition eq. (7.8) is satisfied before all the others and crack extends in the medium 1 along the direction θ_C obtained from Fig. 7.4(b). In the same way, when $k = k_D$, for example, the crack extension occurs in the medium 2 along the direction θ_D.

When $k = k_A$ the two conditions eq. (7.9) and eq. (7.11) are contemporaneously satisfied, but it seems that the crack will not grow along the interface. In fact, for the extension of the crack along the interface a constant $\bar{T}$ is needed while the extension of the crack in the medium 1 requires a decreasing tension. In the same way, when $k = k_B$ the extension occurs in the medium 2.

Two other cases in addition to those shown in Fig. 7.4 may occur. It is possible that for any value of k and for a fixed ratio $K_*^{(i)}, i = 1, 2$ the corresponding curve is above or below the debonding line. In these cases the extension occurs along the interface and the medium i, respectively. In the fore-

going description the particular importance of the contribution due to the non-singular terms depending on the biaxial parameter has been shown in order to explain the deviation of the crack into one material or the other. The singular solution alone is generally insufficient to account for the behavior of the crack tip. In fact, in the case which is shown in Fig. 7.4(a), for example, we can see that, if the effect due to the biaxial parameter is neglected, the crack should extend only at the interface.

In order to summarize the main results concerned with the above criterion we reiterate the following points. Principally, it is important to note that for a fixed state of stress the behavior of the crack tip is strictly dependent on the ratio $\overline{K}_{IC}^{(1)}/K_b$ and $\overline{K}_{IC}^{(2)}/K_b$. If the adhesive strength of the bond is not sufficiently strong, i.e. $\overline{K}_{IC}^{(i)}/K_b$ are very high, it is possible that the crack extension takes place at the interface even though the angle corresponding to the maximum value $\sigma_{\theta\theta}$, for a fixed r_0/a, does not occur at the bond line $\theta = 0$. In addition, if the bonding strength of the interface is great enough, depending on the fracture properties of the adjacent materials, the fracture propagation can occur into one of the two media, even though the circumferential stress has its maximum in the other medium. Practically, the availability of the foregoing method is submitted to the knowledge of the quantities E_i, ν_i, $K_{IC}^{(i)}$ $(i = 1, 2)$ and K_b.

A slightly different version is, to take account of the shear loading, the PV-criterion modified by the authors [6] by only changing eq. (7.11) to

$$\sqrt{2\pi r_0}[\sigma_{\theta\theta}^2(0, r_0) + \sigma_{r\theta}^2(0, r_0)]^{1/2} = K_b \tag{7.13}$$

K_b is the critical parameter taking account of the adhesive strength of the bond and associated with the co-planar crack propagation. It should be pointed out that the debonding condition eq. (7.13) is valid in the absence of frictional effects, i.e. when $\sigma_{\theta\theta} > 0$.

7.4 Interface toughness

One common characteristic in the two criteria is the strength of the interface, specifically in HH-criterion is the energy release rate of the interface and in PV-criterion is the critical stress intensity factor of the interface. For a crack between two dissimilar materials difficulty always arises, i.e. the interface toughness. Efforts to measure interfacial toughness under mixed mode conditions, as reviewed by Liechti and Hanson [28] and Volinsky et al [29]. Parallel efforts have also been under way to develop mixed mode fracture specimens designed to measure the delamination toughness associated with ply separation in polymermatrix composites [30]. A series of experiments [31-33] have focused on the interface between epoxy and glasses, metals and plastics. Thouless [34] has

carried out mixed mode toughness experiments for crack propagation in the interface between a brittle wax and glass. In all these systems, the interface toughness is not a single material parameter rather it is a function of the relative amount of mode 2 to mode 1 acting on the interface.

The toughness $\Gamma(\psi)$ of the interface can be thought of as an effective surface energy that depends on the mode of loading. An overview of various mechanisms responsible for the strong dependence of interfaced toughness on mixed mode is given by Evans et al. [35]. Two primary mechanisms are asperity contact and plasticity. Asperities on the fracture surfaces will tend to make contact for some distance behind the tip when mode 2 is present along with mode 1. A micro-mechanics model of shielding of the tip due to asperity interaction was presented by Evans and Hutchinson [36]. That model led to a prediction of $\Gamma(\psi)$ in terms of a non-dimensional measure of fracture surface toughness. Crack tip plasticity also depends on ψ, with the plastic zone in plane strain increasing in size as $|\psi|$ increases, with $\mathcal{G}$ held fixed [37]. The approach for the time being is that the interface has zero thickness and is modeled by the toughness function $\Gamma(\psi)$ which, in general, must be determined by experiment.

A simple, one parameter family of mixed mode fracture criteria is

$$E_*^{-1}(K_1^2 + \lambda K_2^2) = \mathcal{G}_1^c \tag{7.14}$$

The parameter λ adjusts the influence of the mode 2 contribution in the criterion. The limit $\lambda = 1$ is the "ideally brittle" interface with initiation occurring when $\mathcal{G} = \mathcal{G}_1^c$ for all mode combinations. This limit coincides with the classical surface energy criterion. When $\lambda = 0$, crack advance only depends on the mode 1 component. λ is equal to 0.3 for the plexiglas/epoxy system [32]. For any value of λ, $\mathcal{G}_1^c$ is the pure mode 1 interface fracture toughness. The strain energy release rate criterion can be cast in the form where the mixed mode toughness function is

$$\Gamma(\psi) = \mathcal{G}_1^c[1 + (\lambda - 1)\sin^2\psi]^{-1} \tag{7.15}$$

The toughness is plotted as a function of ψ for various values of λ in Ref [25].

Other phenomenological criteria have been proposed to characterize mixed mode toughness data for interlaminate fracture, e.g., Kinloch [30]. Two alternatives to eq. (7.15) are given which have qualitative features that may more realistically reproduce data trends for interfacial fracture

$$\Gamma(\psi) = \mathcal{G}_1^c\{1 + \tan^2[(1 - \lambda)\psi]\} \tag{7.16}$$

and

$$\Gamma(\psi) = \mathcal{G}_1^c\{1 + (1 - \lambda)\tan^2\psi\} \tag{7.17}$$

Both coincide with eq. (7.15) in the limit $\lambda = 0$, i.e., they reduce to a criterion based on a critical value of K_1, independent of K_2. Both are ideally brittle with $\lambda = 1$. According to eq. (7.16), the toughness increases sharply as $\psi \to 90°$. Eq. (7.17) models the toughness leveling off as $\psi \to 90°$ for all $\lambda < 1$. While this feature should not be taken literally, it did emerge in the simple model of mixed mode interface toughness due to asperity contact of Evans and Hutchinson [36]. Of the three formulas for $\Gamma(\psi)$, eq. (7.17) reflects the trends of that model most accurately.

Eqs. (7.15) and (7.17) are two-parameter criteria for non-oscillatory materials. But since these criteria assuming that the toughness has a minimum at $\psi = 0$, these criteria should be modified in oscillatory bi-materials as [38]

$$\Gamma(\psi) = \mathcal{G}_1^c[1 + (\lambda - 1)\sin^2(\psi - \psi_0)]^{-1} \tag{7.18}$$

and

$$\Gamma(\psi) = \mathcal{G}_1^c\{1 + (1 - \lambda)\tan^2(\psi - \psi_0)\} \tag{7.19}$$

where ψ_0 is a phase shift. These are three-parameter models [39] $\mathcal{G}_1^c$, λ and ψ_0 must be determined from experimental data. Charalambides *et al*. [40] has proposed a similar model with three parameters.

When $\beta \neq 0$, the notion of a mode 1 or a mode 2 crack tip field must be defined precisely, and the possibility of contact of the crack face within the region dominated by the near tip *K*-fields must be considered. As noted by Rice [41], a generalized interpretation of the mode measure is the most important complication raised by the oscillatory singularity. First, a definition of a measure of the combination of modes is made that generalizes eq. (7.16).

The phase angle ψ is a measure of the relative proportion of shear to normal tractions at a characteristic distance l ahead of the crack tip. The phase angle ψ is an important parameter in the characterization of interfacial fracture toughness. Let l be a reference length whose choice will be discussed later. Noting the stress distribution on the interface from the *K*-field, define ψ through the relation [41] as

$$\psi = \tan^{-1}\left[\frac{Im\left(Kl^{i\epsilon}\right)}{Re(Kl^{i\epsilon})}\right] \tag{7.20}$$

where $K = K_1 + iK_2$ is the complex stress intensity factor. For a choice of l within the zone of dominance of the *K*-field, eq. (7.20) is equivalent to

$$\psi = \tan^{-1}\left[\left(\frac{\sigma_{12}}{\sigma_{22}}\right)_{r=l}\right] \tag{7.21}$$

Moreover, the definition reduces to $\psi = \tan^{-1}(K_2/K_1)$ when $\beta = 0$, since $l^{i\epsilon} = 1$ when $\epsilon = 0$. When $\epsilon \neq 0$, a mode 1 crack is one with zero shear traction on the interface a distance l ahead of the tip, and a mode 2 crack has zero normal traction at that point. The measure of the proportion of "mode 2" to "mode 1" in the vicinity of the crack tip requires the specification of some length quantity since the ratio of the shear traction to normal traction varies (very slowly) with distance to the tip when $\beta \neq 0$.

The choice of reference length l is somewhat arbitrary. It is useful to distinguish between a choice based on an in-plane length L of the specimen geometry, such as crack length, and a choice based on a material length scale, such as the size of the fracture process zone or a plastic zone at fracture. The former is useful for discussing the mixed mode character of a bi-material crack solution, independent of material fracture behavior, while the latter is advantageous in interpreting mixed mode fracture data.

7.5 Crack propagation of interfacial cracks

A crack lying in the interface between two brittle elastic solids can advance either by continued growth in the interface, see Fig. 7.5 (b), or by kinking out of the interface into one of the adjoining materials, see Fig. 7.5 (c) and (d). The competition can be assessed by comparing the ratio of the energy release rates for interface cracking and for kinking out of the interface to the ratio of interface toughness to substrate toughness [7], or depending on the ratios of substrate toughness to the interfacial toughness $K_{IC}^{(i)}/K_b$ [5].

The most likely path is along the interface because the bonding strength of the interface is weaker than the strength of the homogeneous material, in general. However, the crack sometimes kinks into either material out of the interface: (i) if the bonding strength of the interface is strong enough and the crack is subjected to shear stresses [6], and (ii) depending on the state of stress near the crack tip i.e. even though the interface bond is weak, the crack may kink into the adjoining material under mixed mode loading [5].

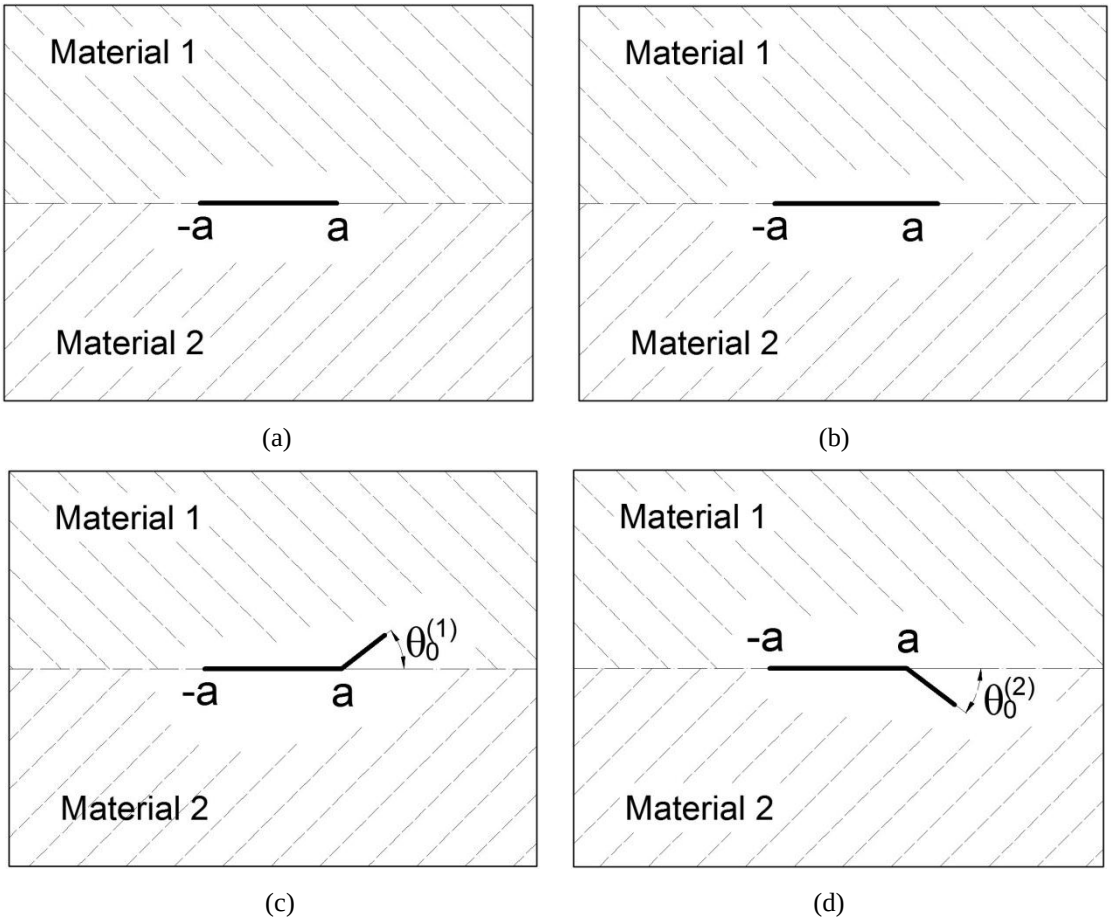

Fig. 7.5 (a) Three distinct possibilities for the interface crack between two bonded dissimilar materials, (b) extension along the interface, (c) deviation into material 1, (d) penetration into material 2.

7.5.1 Interfacial crack under biaxial loading

In the first situation, the interface assumed very well bonded. In another word, the crack will not extend along the interface. PV-criterion is used here and the angles at the maximum values of the circumferential stresses are obtained in both media, as a function of the biaxial loading factor k for various values of the dimensionless radial distance r_0/a from the right-hand tip of the crack are showed in Fig. 7.6. As mentioned in [5] the angle of maximum circumferential stress in the weaker of the two bonded materials can be well above the value of zero also for negative values of biaxial force factor k. For the stronger material the angle at the maximum circumferential stress occurs is, on the other hand, zero when biaxial force factor k is negative and can be greater than zero for positive value of k. We note that the angular position of the maximum circumferential stress is in general highly influenced by the small distance r_0 from the crack tip at which the circumferential stresses are evaluated. The shorter the radium distance, the smaller the crack extension angle in material 2, as well as in material 1 for $k > k_s$ as shown in Fig. 7.6. k_s is a threshold, in Fig. 7.6 it is about 2. Moreover, as $k \to \infty$, the angle of maximum circumferential stress occurs for $\theta \to \pm 90°$. The different shapes pointed in Fig 7.6 are obtained from Chapter 5 by ABAQUS of the mode

$L/a = 20$ and the same material combination with the analysis mode. An excellent agreement between the numerical results and the analytical calculations is observed for the different biaxial force factor and distance from the crack tip in both materials.

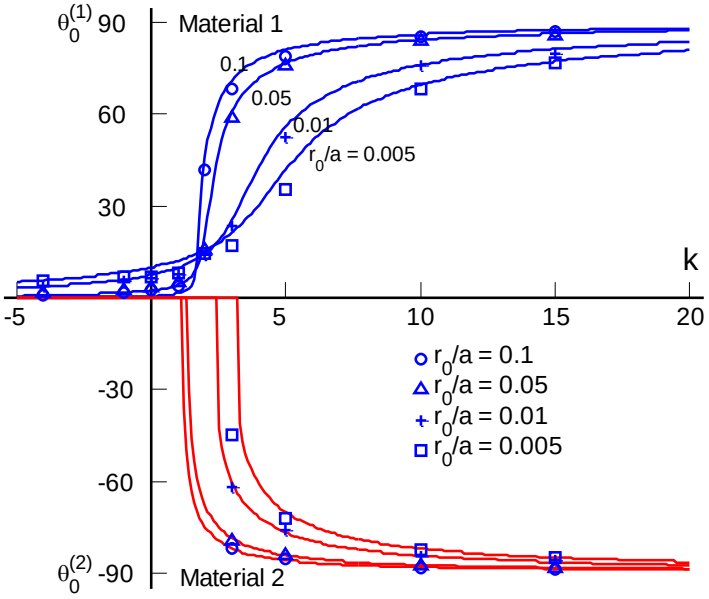

Fig. 7.6 Comparisons of crack propagation angles in both media for $L/a = 20$. Solid curves are analytical results.

Moreover, as the crack propagation angle is strongly depended on the value of r_0/a, which is a very small distance from the crack tip but is unknown, also some researchers declared that the distance is not a circular curve but can be improved by the bounds of the plastic zone. But most of the criteria have been proposed [42] are calculated from the linear elastic theory based on continuum mechanics analysis.

Moreover, there are numerous studies [43, 44] demonstrating that including the nonsingular terms T-stress effect into the fracture criterion can improve the accuracy of the proposed crack growth orientation. As shown in the Cartesian coordinate stress components, the T-stress is

$$T_\sigma = T\left[(k+1) - \frac{4}{1+\alpha}\right] \tag{7.22}$$

From the circumferential stress expression, the biaxial factor effects on the crack initiation angle just and only according to T-stress and the span approximating to 90 degrees can't be ignored.

For the most popular material combination aluminum-epoxy [45, 46], the mechanical properties are presented in Table 7.1.

Table. 7.1 Material properties for epoxy and aluminum

Materials	Young's modulus (GPa)	Poisson's ratio
Material 1 : Epoxy	1.52	0.33
Material 2 : Aluminum	68.9	0.33

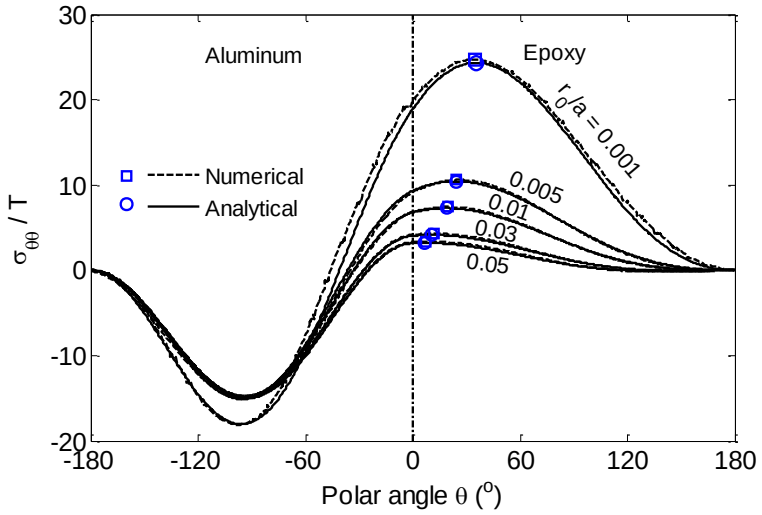

Fig. 7.7 Circumferential stresses and crack extension angles for A-E combination

Table. 7.2 Crack initiation angles in epoxy θ_0 for various dimensionless radial distances

r_0/a	Wang et al. [46] Experimental	Spyropoulos [45] MTS	Spyropoulos [45] SED	Present Analytical	Present Numerical
0.001	35^O	29^O	36^O	35.5^O	34.5^O
0.005	---	19^O	27^O	24^O	24^O
0.01	---	15^O	23^O	19^O	19.5^O
0.03	---	9^O	17^O	10.5^O	11.5^O
0.05	---	6^O	14.5^O	6.5^O	7.5^O

Table. 7.3 Crack initiation angles in epoxy θ_0 for various k

k	-10	-5	-1	0	1	5	10
Spyropoulos [45] SED	33^O	34.5^O	35.5^O	36^O	36.5^O	39.5^O	45^O
Present Analytical	21.5^O	27^O	33.5^O	35.5^O	37.5^O	46.5^O	57^O
Present Numerical	22^O	27^O	33.5^O	34.5^O	37^O	46^O	57^O

Fig. 7.7 shows the circumferential stresses obtained by analytical and numerical methods and the crack extension angles according to the criterion are mentioned above. In Table 7.2 the results are presented for different methods of the dissimilar materials in Table 7.1, uniaxial loading ($k = 0$), various radium distances and $L/a = 20$ for numerical method. It shows the Spyropoulos [45] SED method and the present results have very good agreement with experimental result for $r_0/a = 10^{-3}$. Furthermore, the present results are very similar to Spyropoulos [45] SED results for $r_0/a \leq 10^{-2}$, but to Spyropoulos [45] MTS results for $r_0/a > 10^{-2}$. The crack extension angles in epoxy computed by different methods for various biaxial factors k are presented in Table 7.3. This table shows that the present crack initiation angles are yield to Spyropoulos [45] SED only for $|k| \leq 1$. From Table 7.2 and 7.3, the crack initiation angles increase, as radium distance decreased and biaxial factor increased. The present analytical and numerical results always have excellent agreement with each other.

In the previous analysis, the interface between the two substrates is supposed perfect bonded in any material combinations and loading conditions. In fact, for bi-material system or composite materials, the damage generally occurs in the interface firstly due to the interface is always weaker than any other substrates. Therefore, the interface debonding can't be omitted in the fracture criterion and in the crack propagation analysis.

The PV-criterion is used to obtain the crack extension angle for the perfect bonded interface crack penetrating into one of the two substrates. When the criterion is applied to the interface crack that the interface could be debonded, the limitation of the PV-criterion is the interface critical stress intensity factor K_b which is unknown. For the mode for the time being is that the interface has zero thickness even the interface between a bi-material system is actually a very thin layer of a third phase and is difficult to define and measure the critical intensity factor. Fortunately, the global fracture criteria are essentially based on the energy balance, i.e., HH-criterion, and are generally applicable under the conditions that crack propagates along an interface. Even more, some extensions of the energy balance criterion have been reported to study the mixed mode crack problems. The HH-criterion is used here for the crack extends along the interface. However, the assumption of constant interface toughness $\mathcal{G}_c$ does not seem to be realistic in the mode for the crack onset, specially mixed effects obviously, the fracture mode mixity at the tip of the crack situated along the interface significantly depends on the phase angle. It is well known that such variations of fracture mode mixity in an interface crack are usually associated to relevant variations of interface fracture toughness.

As described in HH-criterion, the initiation of crack advance in the interface when the crack tip is loaded in mixed mode characterized by ψ, the critical condition is

$$\mathcal{G} = \Gamma(\psi) \tag{7.23}$$

The toughness of the interface, $\Gamma(\psi)$, can be thought of as an effective surface energy that depends on the mode of loading. The condition eq. (7.23) is also assumed to hold for quasi-static crack advance when crack growth resistance effects can disregarded.

The energy release rate of the crack advance in the interface is defined by Malyshev and Salganik as [47]

$$\mathcal{G} = \frac{1-\beta^2}{E^*}(K_1^2 + K_2^2) \tag{7.24}$$

where $\frac{1}{E^*} = \frac{1}{2}\left(\frac{1}{\overline{E_1}} + \frac{1}{\overline{E_2}}\right)$, as $\overline{E_\iota}$ is defined in eq. (7.3). Eq. (7.24) will reduce to classical Irwin's relationship in the absence of mismatch. Eq. (7.24) and eq. (7.4) can be re-expressed using the connection $1-\beta^2 = 1/cosh^2(\pi\epsilon)$.

The toughness of interface is discussed in section 7.4, eq. (7.18) will be used here as the critical crack onset value. Special attention should be paid to several material parameters in the interface toughness definition. Firstly, the phase angle ψ is defined as

$$\psi = tan^{-1}\left(\frac{k_2}{k_1}\right) \tag{7.25}$$

Secondly, the pure mode 1 interface toughness $\mathcal{G}_1^c$, in general, must be determined by experiment. Actually, DCB (double cantilever beam) test specimen is usually used to determine the pure mode 1 toughness as in Fig 7.8. There is a crack lies on one side of interface of DCB specimen. The load applied to the cracked side according to the two rigid blocks attached in the substrates. The corresponding curve between the applied load and the displacement in several iterations is recorded, as that shown in Fig. 7.9. The corresponding crack extension length with the applied loading is also needed to record.

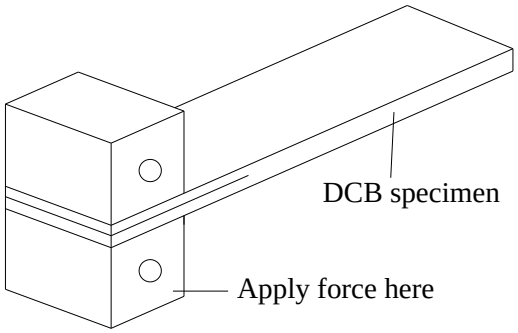

Fig. 7.8 Double cantilever beam (DCB) test specimen.

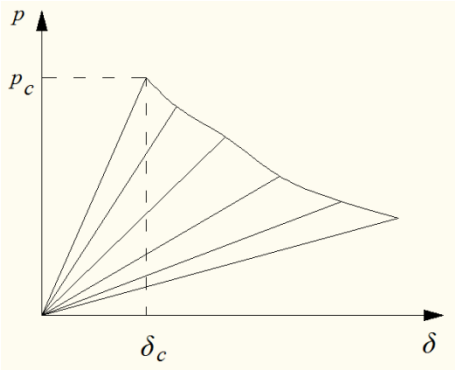

Fig. 7.9 Typical $P-\delta$ curve of the interfacial mode I fracture toughness test.

Based on LEFM, the pure mode I interfacial toughness of DCB specimen can be calculated as [25]:

$$\mathcal{G}_1^c = \frac{P_c}{2B}\frac{\partial C}{\partial a} \tag{7.26}$$

where P_C is the critical loading of the interface; a is the crack length; B is the width of the DBC specimen; and C is the flexibility of the DBC specimen, which can be determined to use the following formula

$$C = \frac{\delta}{P} \tag{7.27}$$

where δ is the displacement corresponding to load P.

Here we introduce three methods for calculating the pure mode I toughness.

Beam theory method, the DCB, considered as two cantilever beam together with crack tips are coincide. Basing on beam theory,

$$C = \frac{2a^3}{3EI} = \frac{8a^3}{BEH^3} \tag{7.28}$$

where E is bending modulus, $I = BH^3/12$is the second moment of inertia, H is the half thickness of DCB. According to eqs. (7.26) and (7.28),

$$\mathcal{G}_1^c = \frac{3P_c\delta_C}{2Ba} \tag{7.29}$$

where δ_C is the displacement corresponding to the critical loading P_c.

But for the situations of big displacement, shear deformation and the crack tip rotation, the eq. (7.29) should be modified by changing the crack length as $a + \Delta$ [48]. Δ can be determined by the approximate line of $\sqrt[3]{C} - a$. The value is the same with the intercept of the approximate line on the a-axis, therefore, the pure mode I interface toughness changes as

$$\mathcal{G}_1^c = \frac{3P_c\delta_C}{2B(a+\Delta)} \tag{7.30}$$

The second method is flexibility method proposed by Berry [49], supposing the flexibility can be expressed as

$$C = Ra^n \tag{7.31}$$

Eq. (7.26) can be determined as

$$\mathcal{G}_1^c = \frac{nP_c\delta_C}{2Ba} \tag{7.32}$$

where n and R can be determined by fitting $C - a$ relationship.

The third method is area method, which the pure mode I toughness is determined by area of the load-displacement curve. After one iteration, a crack length changes from a to $a + \Delta a$, the stain

energy decrease due to crack propagation can be expressed by the area of the load-displacement curve ΔA, so the critical strain energy release rate can be calculated as

$$\mathcal{G}_1^c = \frac{\Delta A}{B\Delta a} \tag{7.33}$$

So the new interface fracture criterion is produced, the crack propagation will take place along the interface or into one of the two adjacent materials along the direction $\theta_0^{(j)}(j = 1,2)$, for which the normal stress, evaluated at a small distance r_0 from the crack tip, is maximum. And the crack propagation along the interface will occur when the following condition satisfied

$$\mathcal{G} = \Gamma(\psi), \theta_0 = 0 \tag{7.34}$$

If the condition eq. (7.34) is not satisfied, the crack will kink out of the interface as soon as one of the following conditions is satisfied:

$$\sqrt{2\pi r_0}\sigma_{\theta\theta}^{(1)}|_{\theta_0^{(1)},r_0} = K_{IC}^{(1)}, \qquad 0 < \theta_0^{(1)} \leq \pi \tag{7.35}$$

$$\sqrt{2\pi r_0}\sigma_{\theta\theta}^{(2)}|_{\theta_0^{(2)},r_0} = K_{IC}^{(2)}, \qquad -\pi \leq \theta_0^{(2)} < 0 \tag{7.36}$$

where $K_{IC}^{(1)}$, $K_{IC}^{(2)}$ are the critical stress intensity factors of the material 1 and material 2. Therefore, the crack propagation angle can be determined once the stress state and material toughness, i.e. $K_{IC}^{(1)}$, $K_{IC}^{(2)}$ and $\Gamma(\psi)$, are obtained. It is important to note that, the critical distance r_0 is small compared to crack size but exceeds oscillatory zone and/or contact zone and for different materials the r_0 is different. Rice [41] claimed that the critical distance was given by finding the largest r for which the opening gap of crack surface behind the crack tip vanishes. On the other side, for the uniaxial loading conditions, on comparing the crack extension angle with experimental results, a good agreement was found for $10^{-2} \leq r_0/a \leq 10^{-1}$ [50]. This new criterion will be used in the next chapter in numerical modeling of an interfacial crack propagation after a little bit of modification for simplifying the numerical analysis.

7.5.2 Interfacial crack under general loading

According to PV- criterion, furtherly we suppose the interface is perfectly bonded too, the crack extension angle of different material combinations against to biaxial loading factor under general loading but shear loading $S = 0$ is illustrated in Fig. 7.10. The results illustrated here are the same with that in a published paper by authors previous [5].

As the material combinations change the crack extension angles in both media are changed. However, comparing Fig. 7.10 (a) to (b), it's easy to find that the effect of biaxial loading parameter to

the crack extension angle in the soft material is much prominent than in the stiff one, especially in the rage of $k > 0$. In the stiff material, the crack extension angle increases as the biaxial loading parameter increase for every fixed material combination E_1/E_2 and trends to $\pi/2$, the normal direction of interface. The value of crack extension angle is very close to each other for different material combination E_1/E_2 at all the value of biaxial loading parameter except $k \in [0,3]$. The most different focus on the rage of $0 < k < 3$. It is named process zone of biaxial parameter for stiff material.

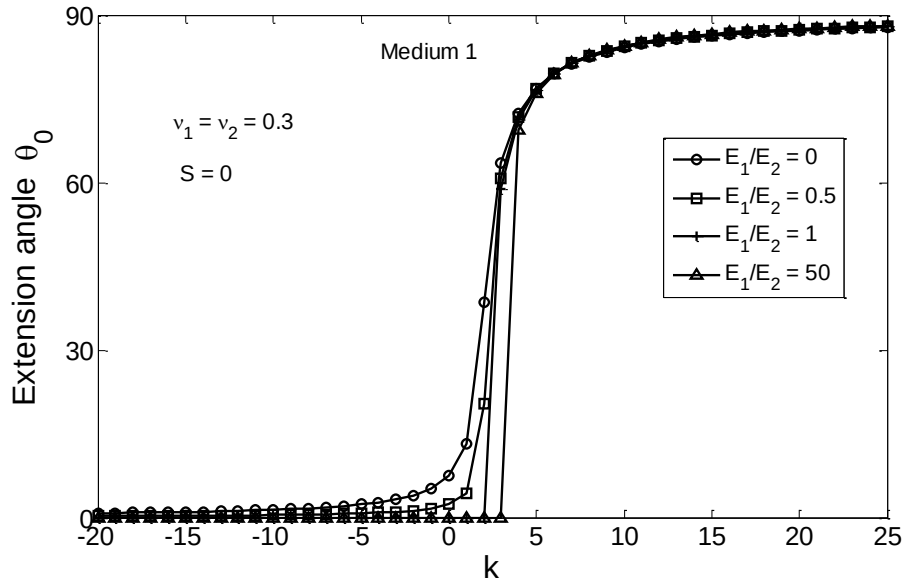

(a)

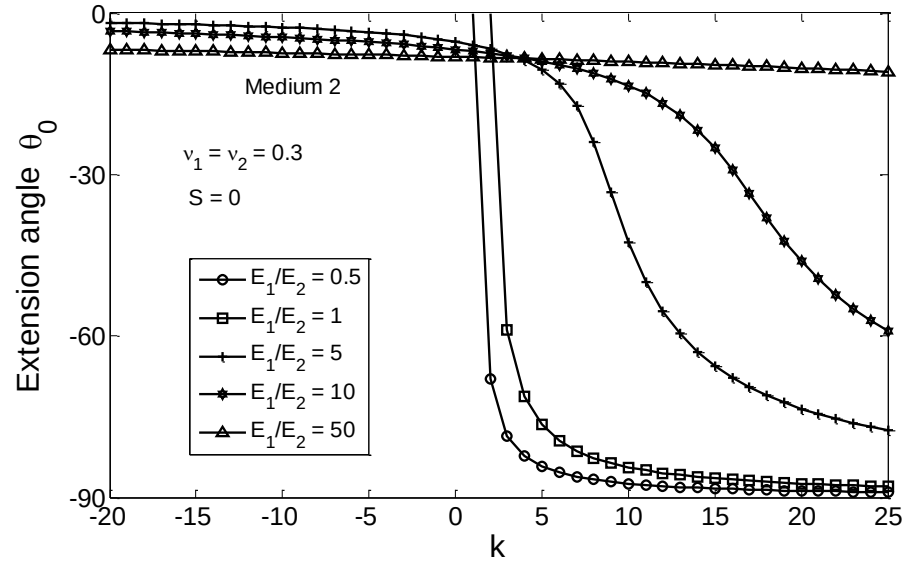

(b)

Fig. 7.10 Crack extension angle of different material combinations against to biaxial loading factor for shear loading $S = 0$ of (a) medium 1, (b) medium 2

In the side of the soft material, the relationship among crack extension angle and material combination and biaxial parameter is showed in Fig. 7.10 (b). The crack extension angles increase as the bi-

axial loading parameter increase for all the material combinations. The additions are very gradual in the rage of $k < 0$ and obvious in $k > 0$. Furthermore, different with that in stiff material, there is a process zone of biaxial parameter for soft material only in the material combination $E_1/E_2 \leq 1$. The influence of material combination to the crack propagation angle is obvious, the bigger the material combinations E_1/E_2 are, the more gradual the crack propagation angle curves.

It's worth to note that the absolute values of all the crack extension angles in both materials are not exceed $\pi/2$. This character will change if the shearing loading S is considered, and that will be discussed in the following.

For the dissimilar material combination $E_1/E_2 = 1$, the model degenerates to homogeneous material. Fig.7.11 shows the shear loading and biaxial loading factor effect on the crack propagation angle in a homogenous material and dissimilar material. Comparing Fig. 7.11(a) with Fig. 7.11(c), the crack propagation angle curves are symmetric in both sides in homogenous material, but not in dissimilar material, if only change the shear loading to opposite direction. From Fig. 7.11(b), it's clear to see that when $\frac{S}{T} = 0$ the crack extension angle curves in both media are symmetric due to the model is in the symmetric material and loading. Further, the crack extends along the interface when $k < 3$, but kinks into the injected materials as soon as $k \geq 3$. This is also can be found in Fig. 7.10.

Different from the interface crack propagation in bi-material system under biaxial loading, when force ratio S/T exceeds one and biaxial factor k exceeds a threshold value, the crack propagation angles are exceed $\pi/2$. This is because when biaxial factor k reaches to the threshold value, the load parallels to interface crack transfers to the dominating force in the biaxial loading, and the phase angle of the bi-material system has been changed by $\pi/2$.

The interface debonding can't be ignored in the bi-material interface fracture process. For the crack extending along the interface, the circumferential stresses are

$$\sigma_{\theta\theta}^{(1)}|_{\theta=0} = \sigma_{\theta\theta}^{(2)}|_{\theta=0} = \sqrt{\frac{a}{2r}}\left[(T - 2\epsilon S)cos\left(\epsilon log\frac{r}{l}\right) - (2\epsilon T + S)sin\left(\epsilon log\frac{r}{l}\right)\right] \quad (7.37)$$

$$\sigma_{r\theta}^{(1)}|_{\theta=0} = \sigma_{r\theta}^{(2)}|_{\theta=0} = \sqrt{\frac{a}{2r}}\left[(T - 2\epsilon S)sin\left(\epsilon log\frac{r}{l}\right) + (2\epsilon T + S)cos\left(\epsilon log\frac{r}{l}\right)\right] \quad (7.38)$$

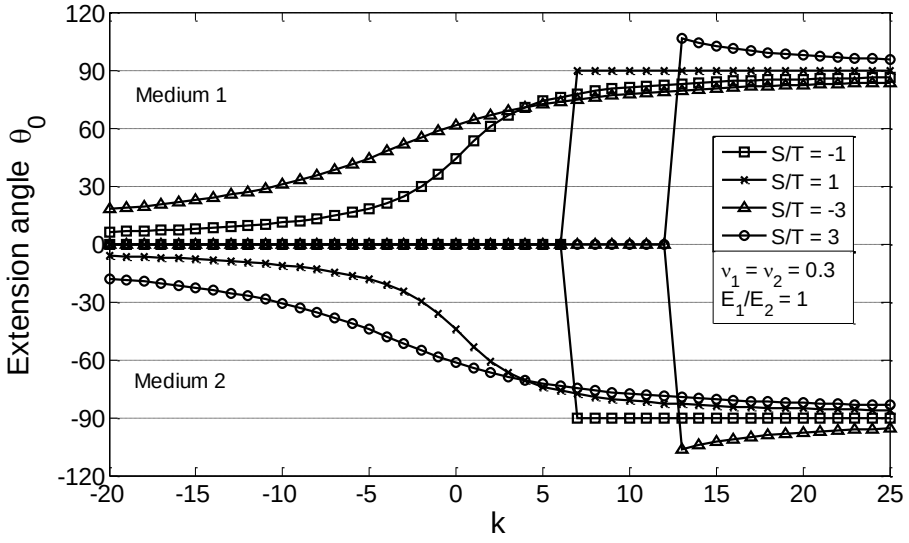

(a)

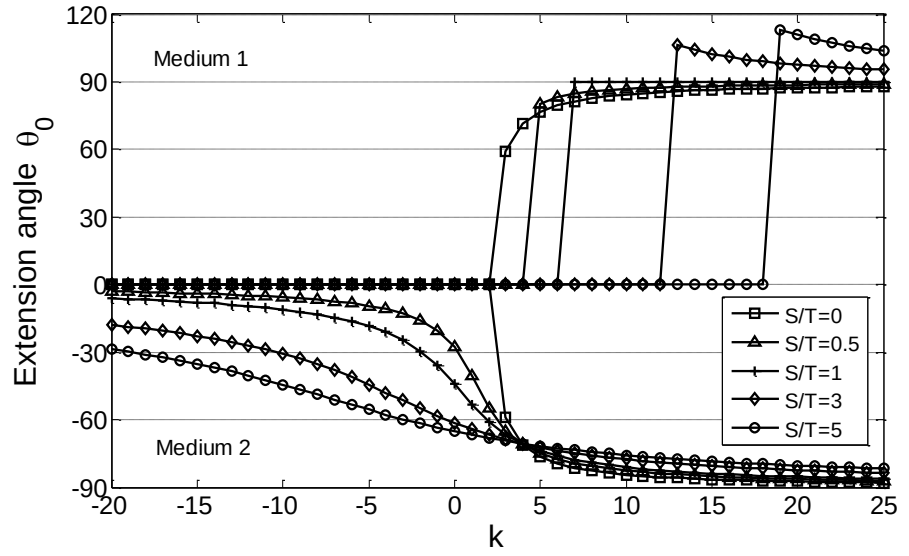

(b)

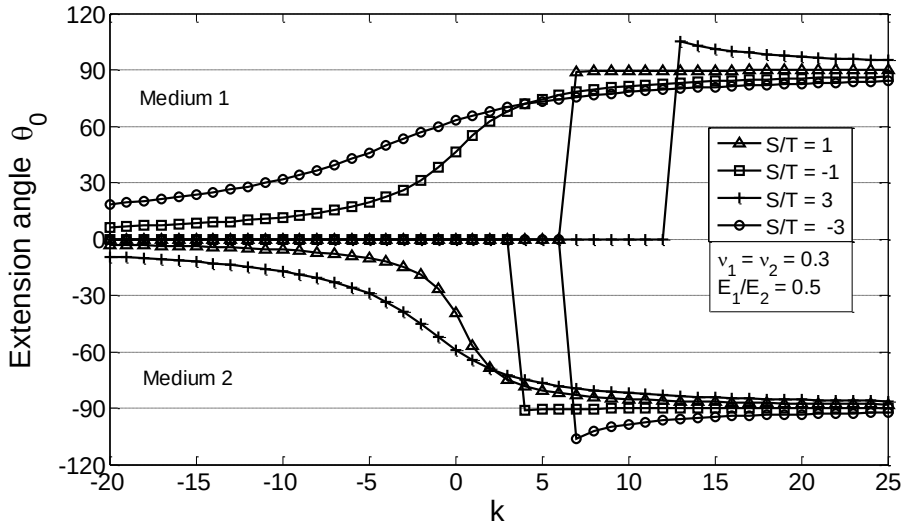

(c)

Fig. 7.11. Crack extension angle against to biaxial loading factor for loading ratio $S/T = -3; -1; 0; 0.5; 1; 3 \; and \; 5$ of dissimilar material $E_1/E_2 = 0.5 \; and \; 1; \upsilon_1 = \upsilon_2 = 0.3$.

Substituting the stress above into extension condition eq. (7.13), the criterion can be written as

$$\frac{T\sqrt{2\pi r_0}}{K_b} = \sqrt{\frac{2}{(1-2\epsilon S/T)^2 + (2\epsilon + S/T)^2}\frac{r_0}{a}} \tag{7.39}$$

This condition represents a global criterion and its dependence on the process zone size is only fictitious. In fact, it also can be written as

$$[(T-2\epsilon S)^2 + (2\epsilon T + S)^2]^{1/2}\sqrt{\pi a} = K_b \tag{7.40}$$

Because the critical stress intensity factor of the interface crack is unknown, a dimensionless applied critical force is defined as $T^* = T\sqrt{2\pi r_0}/K_b$. The dimensionless applied critical tension is represented as a function of the biaxial parameter k and various material combinations based on the assumption that $K_{IC}^{(1)} = K_{IC}^{(2)} = K_b$, $S/T = 0$ and $r_0/a = 0.05$ in Fig. 7.12. The solid line in Fig. 7.12 corresponds to the value $T^* = \sqrt{2r_0/\mathrm{a}(1+4\epsilon^2)}$ of the dimensionless force allowing the bond failure for the material combination $E_1/E_2 = 10$. The debonding dimensionless critical tension is depending on the crack length, the distance from the crack tip r_0 and the bi-material oscillatory index ϵ. This value is the same with that in [6] for incompressible material if the oscillatory index ϵ is neglected. The other curves corresponding to the initiation condition that the crack extends into the medium M1 or M2, respectively. The dashed line refers to two media are the same, the combination $E_1/E_2 = 1$, the bi-material system degenerated as an isotropic homogenous material. The coincidence of the curves with the solid line up to some positive value k_d of k means that the maximum value of $\sigma_{\theta\theta}$ occurs at $\theta = 0$ just up to the value $k = k_d$, which increases with the ratio E_1/E_2.

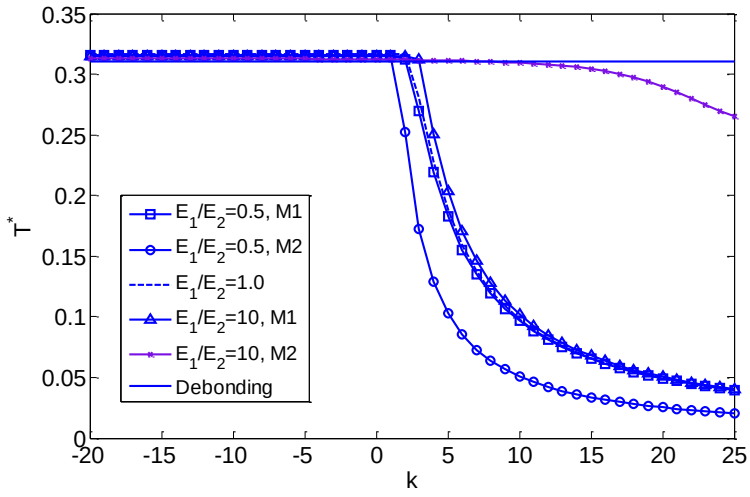

Fig. 7.12 Critical values of the applied tension vs k for various material combination and $S/\mathrm{T} = 0$

In Fig. 7.13, the critical values of applied tension as a function of biaxial force factor k for $S/\mathrm{T} = 0$ and $S/\mathrm{T} = 1$ are presented for $E_1/\mathrm{E}_2 = 10$. The critical stress intensity factor of two media is as-

sumed as $K_{IC}^{(1)} = 2.5K_b$ and $K_{IC}^{(2)} = 2.0K_b$, due to that the interface toughness generally smaller than the toughness of media. It clearly to see, that the applied dimensionless critical value for interface debonding of $S/\mathrm{T} = 0$ is bigger than the value of $S/\mathrm{T} = 1$, this situation also happens in material 2. The critical dimensionless applied load that the interface crack kinking into material 1 of $S/\mathrm{T} = 0$ is smaller than the value of $S/\mathrm{T} = 1$. Comparing the two figures in Fig. 7.13, the easiest initiation of the interface crack for biaxial factor k less than a threshold value k_s ($k_s = 8$ for $S/\mathrm{T} = 0$, $k_s = 15$ for $S/\mathrm{T} = 1$) is extending along the interface. After biaxial factor exceeding the threshold value, the crack will kink into material 1 due to the critical dimensionless applied force is the smallest value.

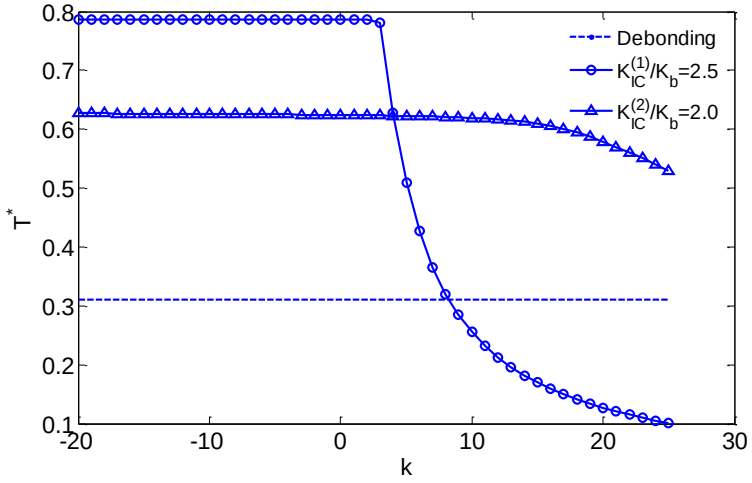

(a)

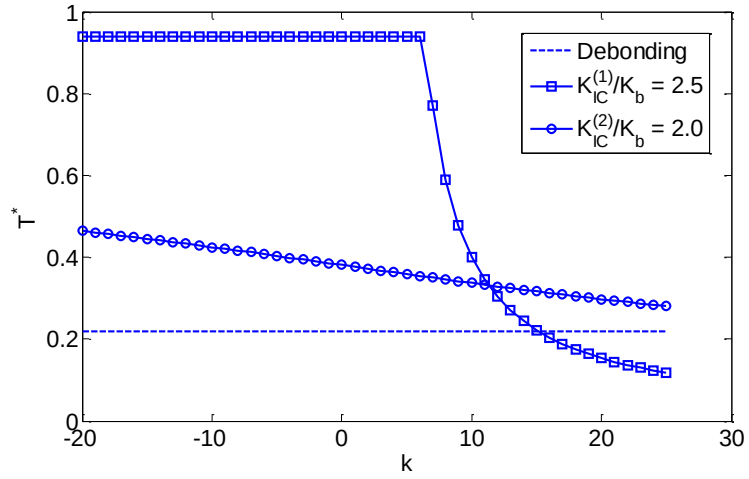

(b)

Fig. 7.13 Critical values of the applied tension for $E_1/\mathrm{E}_2 = 10$ and (a) $S/\mathrm{T} = 0$, (b) $S/\mathrm{T} = 1$

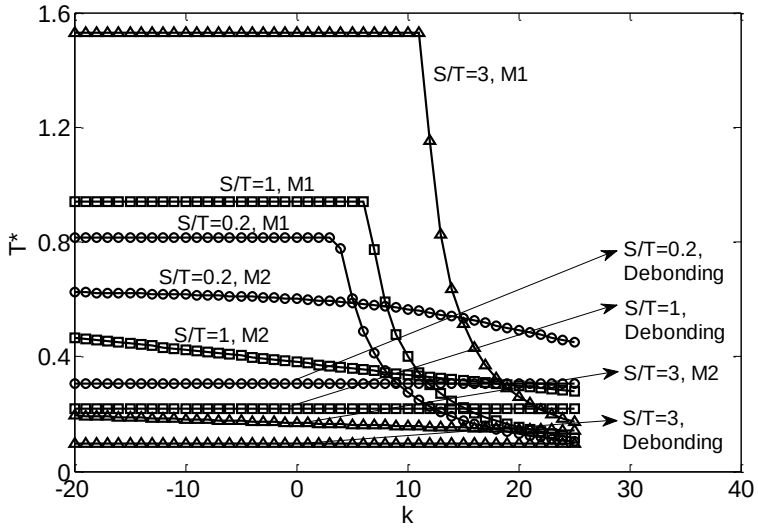

Fig. 7.14 Critical values of the applied tension vs k for various stress ratios with $E_1/\mathrm{E}_2 = 10$, $K_{IC}^{(1)} = 2.5K_b$, $K_{IC}^{(2)} = 2K_b$

In Fig 7.14, the critical values of the applied tension T^* against biaxial factor k, for various stress ratios S/T are represented. As far as the critical load level is concerned, it can be seen that the stress ratio S/T affects the two media in different ways. The critical values of applied tension are increased with the increase of stress ratios S/T in medium1. The situations are opposite in medium 2 and for interface debonding. It also can be inferred that when the loading factor S/T and biaxial force ratio k arrive to a threshold, the interface crack will be kinked into material 2 first.

References

[1] Sih GC. Some basic problems in fracture mechanics and new concepts. Engng Fract Mech 1973; 5(2): 365-77.

[2] Erdogan F, Sih GC. On the crack extension in plates under plane loading and transverse shear. J Basic Engng 1963; 85:519-525.

[3] Hussain MA, Pu SL, Underwood J. Strain energy release rate for a crack under combined mode I and mode II. Fract Anal ASTM STP 1974;560:2-28.

[4] Wu CH. Fracture under combined loads by maximum-energy-release-rate-criterion. J. Appl. Mech. 1978; 45(3):553-558.

[5] Piva A, Viola E. Biaxial load effects on a crack between dissimilar media. Engng. Fract. Mech. 1980; 13(1):143-174.

[6] Viola E, Piva A. Plane strain interfacial fracture analysis of a bi-material incompressible body. Engng Fract Mech, 1981, 15(1-2):131-142.

[7] He MY, Hutchinson JW. Kinking of a crack out of an interface. J. Appl. Mech. 1989; 56(2):270-278.

[8] Yuuki R, Xu JQ. Stress based criterion for an interface crack kinking out of the interface in dissimilar materials. Engng Fract Mech 1992; 41(5): 635-644.

[9] Yuuki R, Liu JQ, Xu JQ, Ohira T, Ono T. Mixed mode fracture criteria for an interface crack. Engng Fract Mech 1994; 47(3): 367-377.

[10] Ayatollahi MR, Mirsayar MM. Kinking angles for interface cracks. Procedia Engng 2011; 10:325-329.

[11] Rudraraju S, Salvi A, Garikipati K, Waas AM. Predictions of crack propagation using a variational multiscale approach and its application to fracture in laminated fiber reinforced composites. Compos Struct 2012; 94(11): 3336-3346.

[12] Lichun Bian, Kwang soo Kim. The minimum plastic zone radius criterion for crack initiation direction applied to surface cracks and through-cracks under mixed mode loading, Int. J. Fatigue, 2004, 26:b1169-1178.

[13] Lichun Bian, Farid Taheri. A proposed maximum ratio criterion applied to mixed mode fatigue crack propagation, Materials and Design, 2011, 32: 2066-2072.

[14] Theocaris PS, Andrianopoulos NP. The Mises elastic-plastic boundary as the core region in fracture criteria. Engng Fract Mech 1982; 16(3):425-432.

[15] Spyropoulos CP. An improved determination of the zones of yield initiation for the interface crack problem. Engng Frac Mech 1990; 36(2): 287-295.

[16] Spyropoulos CP. Crack initiation direction from interface of bonded dissimilar media. Theor Appl Fract Mech 2003; 39(1): 99-105.

[17] Buyukozturk O, Hearing B. Crack propagation in concrete composites influenced by interface fracture parameters. Int J Solids Struct 1998; 35(31-32):4055-4066.

[18] Choi BS, Chai YS. Interfacial crack propagation under various mode-mixes, KSME Int. J. 2002; 16(1):39-45.

[19] Lee W, Shin H, Yoo YH. Revisited criterion to present kinking of a crack out of a bi-material interface under the presence of in-plane residual stresses -- a global approach. Int. J. Engng Sci 2004; 42(3): 257-270.

[20] Kayupov M, Dzenis YA. Stress concentrations caused by bond cracks in single-lap adhesive composite joints. Compos Struct 2001;54(2-3):215-220.

[21] Goyal VK, Johnson ER., Goyal VK. Predictive strength fracture model for composite bonded joints. Compos Struct 2008;82(3):434-446.

[22] Goyal VK, Johnson ER, Davila CG. Irreversible constitutive law for modeling the delamination process using interfacial surface discontinuities. Compos Struct 2004;65(3-4):289-305.

[23] Yang TL, Liu YB, Wang J. A study of the propagation of an embedded crack in a composite laminate of finite thickness. Compos Struct 2003;59(4):473-479.

[24] Kaminski M. Stochastic boundary element method analysis of the interface defects in composite materials. Compos Struct 2012;94(2):394-402.

[25] Suo Z, Hutchinson JW. Mixed mode cracking in layered materials. Advances in applied mechanics, 1992, 29: 63-191.

[26] Yang QS, Qin QH. Numerical simulation of cracking processes in dissimilar media. Composite Structures, 2001,53: 403-407.

[27] E Wu, RL Thomas. Interfacial fracture phenomena. Proc. 5th Int. Cong. Rheol. University Park P ress, Baltimore, 1969, 1: 127-137.

[28] Liechti KM, Hanson EC, Nonlinear effects in mixed-mode interfacial delaminations, Int J Fracture, 1988, 36: 199-217.

[29] Volinsky AA, Moody NR, Gerberich WW. Interfacial toughness measurements for thin films on substrates. Acta Materialia, 2002; 50: 441-466.

[30] Kinloch AJ, Adhesion and Adhesives, Chapman and Hall, London, 1987.

[31] Cao HC, Evans AG, An experimental study of the fracture resistance of biomaterial interface, Mechanics of Material, 1989, 7: 295-305.

[32] Wang JS, Suo Z. Experimental determination of interfacial toughness using Brazil-nut-sandwich, Aca Met, 1990, 38: 1279-1290.

[33] Liechti KM, Chai YS. Asymmetric shielding in interfacial fracture under inplane shear. J. Appl. Mech. 1992, 59: 295-304

[34] Thouless MD. Crack spacing in brittle films on elastic substrates. J. Am. Ceram. Soc, 1990, 73: 2144-2146.

[35] Evans AG, Ruhle M, Dalgleish BJ, Charalambides PG. The fracture energy of biomaterial interfaces. Mater. Sci. Engng. A, 1990, 126:53-64.

[36] Evans AG, Hutchinson JW, Effects of non-planarity on the mixed mode fracture resistance of biomaterial interfaces. Acta Metal Mater, 1989; 37:909-916.

[37] Shih CF, Asaro RJ, Elastic-plastic analysis of cracks on biomaterial interfaces: Part I Small scale yielding. J. Appl. Mech., 1988; 55: 299-316.

[38] Kim JH. Non-orthogonal stress modes for interfacial fracture based on local plastic dissipation, Engng. Fract. Mech. 2003, 70: 625-642.

[39] Banks-sills L, Ashkenazi D. A note on fracture criteria for interface fracture. Int J Fract, 2000; 103: 177-88.

[40] Charalambides M, Kinloch AJ, Wang Y, Williams JG. On the analysis of mixed-mode failure. Int J Fract, 1992; 54: 269-91.

[41] Rice JR. Elastic fracture concepts for interfacial cracks. J. Appl. Mech. 1988, 55: 98-103.

[42] Mróz KP, Mróz Z. On crack path evolution rules. Engng Fract Mech 2010; 77(11):1781-1807.

[43] Ayatollahi MR, Mirsayar MM. Kinking angles for interface cracks. Procedia Engng 2011; 10:325-329.

[44] Ayatollahi MR, Sedighiani K. A T-stress controlled specimen for mixed mode fracture experiments on brittle materials. Eur J Mech A-Solid 2012; 36:83-93.

[45] Spyropoulos CP. Crack initiation direction from interface of bonded dissimilar media. Theor Appl Fract Mech 2003; 39(1): 99-105.

[46] Wang TT, Kwei TK, Zupko HM. Tensile strength of butt-joined epoxy-aluminum plates. Int. J. Fract. Mech. 1970; 6(2):127-137.

[47] Malyshev BM and Salganik RL. The strength of adhesive joints using the theory of cracks. Int. J. Fract. Mech. 1965(5): 114-128.

[48] Hashemi S, Kinloch AJ, Williams JG. The effects of geometry, rate and temperature on the mode I, mode II and mixed-mode I/II interlaminar fracture of carbon-fibre/poly (ether-ether ketone) composites. J Comp. Mater, 1990, 24:918-956.

[49] Berry JP. Determination of fracture surface energies by the cleavage technique. J. Appl. Phys, 1983, 34: 62-66.

[50] E Viola, Influenza delle tensioni non singolari sulla direzione di diramazione di un crack dominante in regime biassiale. Gior Genio Civile

Chapter 8

Crack propagation trajectory using XFEM

8.1 Introduction

The extended finite element method (XFEM) is a numerical method that enables a local enrichment of approximation spaces. The method is useful for the approximation of solutions with pronounced non-smooth characteristics in small parts of the computational domain, for example near discontinuities and singularities. In these cases, standard numerical methods such as the FEM or FVM often exhibit poor accuracy. The main advantage is that XFEM offers significant advantages by enabling optimal convergence rates for these applications.

The basic idea and the mathematical foundation of XFEM are the partition of unity finite element method (PUFEM) which was discussed by Melenk and Babuska [1] and Duarte and Oden [2]. Later Belytschko and Black [3] presented a minima remeshing finite element method by adding discontinuous enrichment functions to the finite element approximation to account for the presence of a crack. The method was then improved by Moes *et al*. [4] and Dolbow [5] and called the eXtended Finite Element Method (XFEM). The new methodology allowed for the entire crack to be represented independently of the mesh and constructed the enriched approximation from the interaction of the crack geometry with the mesh. More contributions from Dolbow *et al*. [6-8], Daux *et al*. [9] and Sukumar *et al*. [10] extended the method for three-dimensional crack modeling and arbitrary branched and intersecting cracks. The use of level set methods to represent the crack location was studied by Stolarska *et al*. [11], Belyschko *et al.* [12], Sukumar *et al*. [13], Moes *et al.* [14].

Fracture of composite structures constitutes a major part of recent studies related to LEFM and EPFM. Dolbow and Nadeau [15] employed the extended finite element method to simulate behaviour of micro-structured materials with a focus on functionally graded materials. Then Dolbow and Gosz [16] described a new interaction energy integral method for the computation of mixed mode stress intensity factors at the tip of arbitrarily oriented cracks in functionally graded materials. In a related contribution, Remmers *et al.* [17] presented a new formulation for the simulation of delamination growth in thin-layered composite structures.

Interface crack propagation is rapidly gaining wide attention. Such a crack growth is exceedingly important for delamination and debonding analysis in composite materials, and can be extended to other brittle and semi-brittle materials such as concrete and rock crack interfaces. Study of bi-

material interface cracks was performed by Sukumar *et al.* [18] by developing partition of unity enrichment techniques. Nagashima *et al.* [19] and Nagashima and Suemasu [20] described the application of XFEM to stress analysis of structures containing interface cracks between dissimilar materials. This chapter is dedicated to describing the applications of the XFEM in bi-material interface crack. Fundamental aspects of the extended finite element method were reviewed mainly for crack propagation problems. Then it was further extended to simulate other localization problems in solid mechanics, especially in bi-material and composite applications.

8.2 Basic theory

8.2.1 Standard finite element method

Isoparametric finite elements are the mostly used element in standard finite element method. In this section the basic knowledge of isoparametric finite elements is reviewed. Consider a domain in the state of equilibrium discretized by a four-node quadrilateral finite element mesh, as depicted in Fig. 8.1. According to the finite element methodology, the coordinates $\mathbf{x}^{\mathrm{T}} = (\mathrm{x}, \mathrm{y})$ are interpolated from the nodal values $\bar{\mathbf{x}}^{\mathrm{T}} = (\bar{\mathrm{x}}, \bar{\mathrm{y}})$

$$\mathbf{x} = \sum_{\mathrm{j}=1}^{4} \boldsymbol{N}_j \bar{\mathbf{x}}_j \tag{8.1}$$

where **N** is the matrix of finite element shape functions.

$$\boldsymbol{N}_j = \begin{bmatrix} N_j & 0 \\ 0 & N_j \end{bmatrix} \tag{8.2}$$

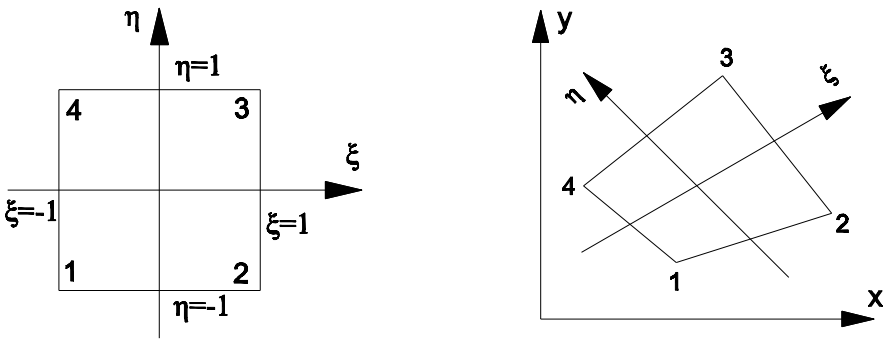

(a) (b)

Fig. 8.1 An isoparametric finite element (a) Bilinear element in the Natural Coordinate; (b) Bilinear element in the Physical Coordinate

In an isoparameteric finite element representation, displacement fields $\mathrm{u}^{\mathrm{T}} = (\mathrm{u_x}, \mathrm{u_y})$ are similarly interpolated from the nodal displacements values $\bar{\mathbf{u}}^{\mathrm{T}} = (\bar{\mathrm{u}}_{\mathrm{x}}, \bar{\mathrm{u}}_{\mathrm{y}})$:

$$\mathbf{u} = \sum_{j=1}^{4} \boldsymbol{N}_j \bar{\mathbf{u}}_j \tag{8.3}$$

The strain field is computed directly from above equation

$$\boldsymbol{\varepsilon} = \sum_{j=1}^{4} \mathbf{B}_j \bar{\mathbf{u}}_j \tag{8.4}$$

where the matrix **B** is defined in terms of derivatives of the shape functions N_j

$$\boldsymbol{B}_j = \begin{bmatrix} \dfrac{\partial N_j}{\partial x} & 0 \\ 0 & \dfrac{\partial N_j}{\partial y} \\ \dfrac{\partial N_j}{\partial y} & \dfrac{\partial N_j}{\partial x} \end{bmatrix} \tag{8.5}$$

And the chain rule is invoked to determine the coefficients of $\mathbf{B}_j$

$$\begin{bmatrix} \dfrac{\partial N}{\partial x} \\ \dfrac{\partial N}{\partial y} \end{bmatrix} = \mathbf{J}^{-1} \begin{bmatrix} \dfrac{\partial N}{\partial \xi} \\ \dfrac{\partial N}{\partial \eta} \end{bmatrix} \tag{8.6}$$

where **J** is the Jacobian matrix

$$\mathbf{J} = \begin{bmatrix} \dfrac{\partial x}{\partial \xi} & \dfrac{\partial y}{\partial \xi} \\ \dfrac{\partial x}{\partial \eta} & \dfrac{\partial y}{\partial \eta} \end{bmatrix} \tag{8.7}$$

$$\mathbf{J}^{-1} = \frac{1}{\det \mathbf{J}} \begin{bmatrix} \dfrac{\partial y}{\partial \eta} & \dfrac{\partial y}{\partial \xi} \\ -\dfrac{\partial x}{\partial \eta} & \dfrac{\partial x}{\partial \xi} \end{bmatrix} \tag{8.8}$$

Finally, the following discrete system of linear equations is obtained:

$$\mathbf{K}\mathbf{d} = \mathbf{f} \tag{8.9}$$

where **d** is the vector of nodal unknows, and **K** and **f** are the global stiffness matrix and external force vector, respectively. The stiffness matrix and the force vector are computed on an element-by-element basis and assembled into their global counterparts through the usual assembly procedure.

The stiffness matrix $\mathbf{K}_e$ of an element Ω_e can be determined from

$$\mathbf{K}_{\mathrm{e}} = \int_{\Omega_{\mathrm{e}}} \mathbf{B}^{\mathbf{T}}\mathbf{D}\mathbf{B}\mathrm{d}\Omega \tag{8.10}$$

where **D** is the material stress-strain or constitutive matrix ($\boldsymbol{\sigma} = \mathbf{D}\mathbf{B}\overline{\mathbf{u}}_{\mathrm{i}}$). Eq. (8.10) can be rewritten in local curvilinear coordinates ξ, η:

$$\mathbf{K} = \int_{-1}^{1}\int_{-1}^{1} \mathbf{B}(\xi,\eta)^{\mathrm{T}}\mathbf{D}\mathbf{B}(\xi,\eta)(\det\mathbf{J})\, d\xi d\eta \tag{8.11}$$

8.2.2 Partition of unity finite element method

As mentioned before, the global solution of partition of unity finite element method (PUFEM) has been the theoretical basis of the extended finite element method (XFEM). The basic mathematical foundation of the PUFEM was discussed by Melenk and Babuska [1]. A partition of unity is defined as a set of m functions $f_k(x)$ within a domain Ω_{pu} such that

$$\sum_{k=1}^{m} f_k(x) = 1 \tag{8.12}$$

It can easily be shown that by selection of any arbitrary function $\Upsilon(x)$, the following property is automatically satisfied:

$$\sum_{k=1}^{m} f_k(x)\Upsilon(x) = \Upsilon(x) \tag{8.13}$$

This is equivalent to the definition of the reproducing condition or completeness. The set of isoparametric finite element shape functions N_j also satisfy the condition of partition of unity

$$\sum_{j=1}^{n} N_j(x) = 1 \tag{8.14}$$

where n is the number of nodes for each finite element. The concept of partition of unity provides a mathematical framework for the development of an enriched solution.

8.2.3 Interaction integral method

The stress intensity factor plays a very important role in fracture mechanics. The most accurate method for calculating SIFs of mixed mode is interaction integral method. In the interaction integral method, auxiliary fields are introduced and superimposed onto the actual fields satisfying the boundary value problem [21]. Stresses and strains for the auxiliary state should be chosen so as to satisfy both the equilibrium equation and the traction free boundary condition on the crack surface

in the A^* area. These auxiliary fields are suitable selected in order to find a relationship between the mixed mode stress intensity factors and the interaction integrals. The contour J integral for the sum of the two states can be defined as

$$\mathrm{J} = \mathrm{J}^{\mathrm{act}} + \mathrm{J}^{\mathrm{aux}} + \mathrm{M} \tag{8.15}$$

where $\mathrm{J}^{\mathrm{act}}$ and $\mathrm{J}^{\mathrm{aux}}$ are associated with the actual and auxiliary states, respectively, and M is the interaction integral

$$J^{\mathrm{act}} = \int_{A^*} \left[\sigma_{ij}\frac{\partial u_i}{\partial x_1} - W_s\delta_{1i}\right]\frac{\partial q}{\partial x_i}\,\mathrm{d}\Gamma \tag{8.16}$$

$$J^{\mathrm{aux}} = \int_{A^*} \left[\sigma_{ij}^{\mathrm{aux}}\frac{\partial u_i^{\mathrm{aux}}}{\partial x_1} - W^{\mathrm{aux}}\delta_{1i}\right]\frac{\partial q}{\partial x_i}\,\mathrm{d}\Gamma \tag{8.17}$$

$$\mathrm{M} = \int_{A^*} \left[\sigma_{ij}\frac{\partial u_i^{\mathrm{aux}}}{\partial x_1} + \sigma_{ij}^{\mathrm{aux}}\frac{\partial u_i}{\partial x_1} - W^{\mathrm{M}}\delta_{1i}\right]\frac{\partial q}{\partial x_j}\,\mathrm{d}\Gamma \tag{8.18}$$

with the actual, auxiliary and interaction works defined as

$$W_s = \sigma_{ij}\varepsilon_{ij} \tag{8.19}$$

$$W^{\mathrm{aux}} = \sigma_{ij}^{\mathrm{aux}}\varepsilon_{ij}^{\mathrm{aux}} \tag{8.20}$$

$$W^{\mathrm{M}} = \frac{1}{2}\left(\sigma_{ij}\varepsilon_{ij}^{\mathrm{aux}} + \sigma_{ij}^{\mathrm{aux}}\varepsilon_{ij}\right) \tag{8.21}$$

One of the choices for the auxiliary state is the displacement and stress fields in the vicinity of the crack tip. From the relation of the J integral and mode I and II stress intensity factors,

$$J = \frac{1}{E'}(K_I^2 + K_{II}^2) \tag{8.22}$$

The following relationship is obtained

$$M = \frac{2}{E'}(K_I K_I^{\mathrm{aux}} + K_{II}K_{II}^{\mathrm{aux}}) \tag{8.23}$$

Therefore, the mode I and II stress intensity factors can be obtained from

$$K = \frac{E'}{2}M \tag{8.24}$$

by choosing $K_I^{\mathrm{aux}} = 1$, $K_{II}^{\mathrm{aux}} = 0$ for mode I and $K_I^{\mathrm{aux}} = 0$, $K_{II}^{\mathrm{aux}} = 1$ for mode II.

Finally, application of the finite element method for evaluation of the J_M integral by the interaction integral method is

$$J_M = \int_{A^*} \left[\sigma_{ij} \frac{\partial u_i^{aux}}{\partial x_1} + \sigma_{ij}^{aux} \frac{\partial u_i}{\partial x_1} - \sigma_{ij} \varepsilon_{ij}^{aux} \delta_{1i} \right] \frac{\partial q}{\partial x_j} d\Gamma \tag{8.25}$$

or in a discretized form is obtained through a Gauss integration scheme

$$J_M = \sum_{A^*} \left(\sum_{g=1}^{ng} \left\{ \left[\left(\sigma_{ij} \frac{\partial u_i^{aux}}{\partial x_1} + \sigma_{ij}^{aux} \frac{\partial u_i}{\partial x_1} - \sigma_{ij} \varepsilon_{ij}^{aux} \delta_{1i} \right) \frac{\partial q}{\partial x_j} \right] detJ \right\}_g W_g \right) \tag{8.26}$$

where W_g is the Gauss weighting factor, ng is the order of integration.

8.3 Extended finite element method (XFEM)

8.3.1 Governing equations

Considering **x**, a point in an elastic finite element body Ω shown in Fig. 8.2. The boundary Γ is composed of the segments Γ_t, Γ_u and Γ_c. Γ_t is the force boundary which is imposed tractions t_0, Γ_u is displacement boundary which is imposed displacements $\bar{u}$, while Γ_C is the traction free crack surface.

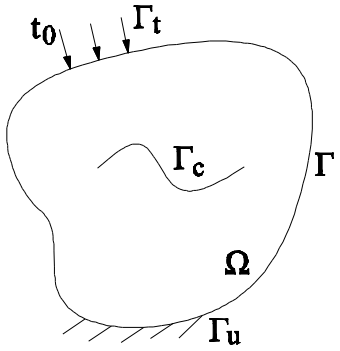

Fig. 8.2. A cracked body subjected to prescribed boundary tractions and displacements.

We consider small deformation elastostatics, which is governed by the equation of equilibrium

$$\nabla \cdot \boldsymbol{\sigma} + \mathbf{b} = 0 \text{ in } \Omega \tag{8.27}$$

accompanying with the constitutive law $\boldsymbol{\sigma} = \mathbf{D}: \boldsymbol{\varepsilon}$ and the geometry equation $\boldsymbol{\varepsilon} = \nabla^s \boldsymbol{u}$, where $\boldsymbol{\sigma}$ is the Cauchy stress tensor, $\boldsymbol{\varepsilon}$ is the small strain tensor, **b** is the body force, **D** denotes the elastic material moduli matrix, $\boldsymbol{u}$ is the displacement. ∇ is the gradient operator and ∇^s is the symmetry gradient operator.

$$\mathbf{u} = \bar{\mathbf{u}} \text{ on } \Gamma_u \tag{8.28a}$$

$$\mathbf{n} \cdot \boldsymbol{\sigma} = \mathbf{t_0} \text{ on } \Gamma_t \tag{8.28b}$$

$$\mathbf{n} \cdot \boldsymbol{\sigma} = \mathbf{0} \text{ on } \Gamma_{c+} \tag{8.28c}$$

$$\mathbf{n} \cdot \boldsymbol{\sigma} = \mathbf{0} \text{ on } \Gamma_{c-} \tag{8.28d}$$

$\mathbf{n}$ is the unit normal vector, Γ_{c+} and Γ_{c-} are the surfaces of the crack Γ_c, respectively.

The variational formulation of the boundary value problem can be defined as

$$W^{\text{int}} = W^{\text{ext}} \tag{8.29}$$

The virtual work equation without body forces is given by

$$\int_{\Omega} \sigma(\mathbf{u}) : \nabla^s \mathbf{v} \mathrm{d}\Omega = \int_{\Gamma_t} \mathrm{v} \cdot t_0 \mathrm{d}\Gamma \tag{8.30}$$

8.3.2 Discretization

Assume the arbitrary domain Ω discretized into some n node finite elements. In the extended finite element method, the following approximation is utilized to calculate the displacement for the point $\mathbf{x}$ locating within the domain [22]

$$\mathbf{u}^h(\mathbf{x}) = \mathbf{u}^{\text{FE}} + \mathbf{u}^{\text{enr}} = \sum_{j=1}^{n} N_j(\mathbf{x})\mathbf{u}_j + \sum_{h=1}^{m} N_h(\mathbf{x})\psi(\mathbf{x})\mathbf{a}_h \tag{8.31}$$

where $\mathbf{u}_j$ is the vector of regular degrees of nodal freedom in the standard finite element method, $\mathbf{a}_h$ is the added set of degrees of freedom to the standard finite element model and $\psi(\mathbf{x})$ is the discontinuous enrichment function defined for the set of nodes that the discontinuity has in its influence (support) domain.

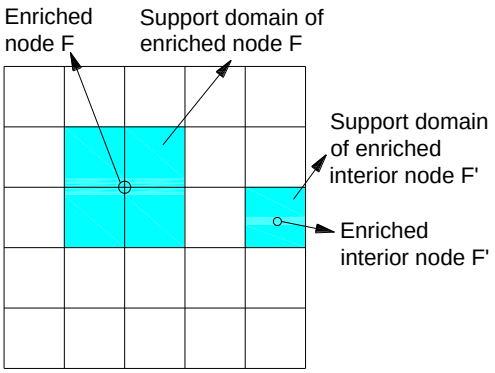

Fig. 8.3 Support domains of an edge node and an interior node in a finite element mesh.

The support domain associated to a node, located on an edge, consists of the elements containing that node, whereas for an interior node (in higher order elements) it is the element surrounding the node. Fig 8.3 illustrates definitions of the influence domain for a node located on edges of elements as well as an internal node.

The enrichment function $\psi(\mathbf{x})$ can be chosen by applying appropriate analytical solutions according to the type of enrichment functions within an XFEM procedure can be expressed as the following:

1. Reproducing the singular field around a crack tip.

2. Continuity in displacement between adjacent finite elements.

3. Independent strain fields in two different sides of a crack surface.

4. Other features according to the specific discontinuity problem.

The first term on the right-hand side of eq. (8.31) is the classical finite element approximation to determine the displacement field, while the second term is the enrichment approximation which takes into account the existence of any discontinuities. The second term utilizes additional degrees of freedom to facilitate modeling the existence of any discontinuous field, such as a crack, without modeling it explicitly in the finite element mesh.

Moes *et al.* [4] proposed that eq. (8.31) be rearranged in order to model crack surfaces and tips in the extended finite element method as below

$$\mathbf{u}^h(\mathbf{x}) = \mathbf{u}^{\mathrm{FE}} + \mathbf{u}^{\mathrm{enr}} = \sum_{j=1}^{n} N_j(\mathbf{x})\mathbf{u}_j + \sum_{h=1}^{m} N_h(\mathbf{x})\psi(\mathbf{x})\mathbf{a}_h + \sum_{k=1}^{t} N_k(\mathbf{x})\varphi(\mathbf{x})\mathbf{b}_k \tag{8.32}$$

where m is the set of nodes that have the crack face (but not the crack tip) in their support domain, while t is the sets of nodes associated with crack tip in their influence domain; $\mathbf{u}_j$ are the nodal displacements (standard degrees of freedom). $\mathbf{a}_h$ and $\mathbf{b}_k$ are vectors of additional degrees of nodal freedom for modeling crack faces and crack tip, respectively; and $\varphi(\mathbf{x})$ represent crack tip enrichment functions.

Discretization of eq. (8.30) using the XFEM procedure eq. (8.32), results in a discrete system of linear equilibrium equations:

$$\mathbf{K}\mathbf{u}^h = \mathbf{f} \tag{8.33}$$

where $\mathbf{K}$ is the stiffness matrix, $\mathbf{u}^h$ is the vector of degrees of nodal freedom (for both classical and enrichment ones) and $\mathbf{f}$ is the vector external force. The global matrix and vectors are calculated by assembling the matrix and vectors of each element. $\mathbf{K}$ and $\mathbf{f}$ for each element e are defined as

$$\mathbf{K}_{ij}^{e} = \begin{bmatrix} \mathbf{K}_{ij}^{\mathbf{uu}} & \mathbf{K}_{ij}^{\mathbf{ua}} & \mathbf{K}_{ij}^{\mathbf{ub}} \\ \mathbf{K}_{ij}^{\mathbf{au}} & \mathbf{K}_{ij}^{\mathbf{aa}} & \mathbf{K}_{ij}^{\mathbf{ab}} \\ \mathbf{K}_{ij}^{\mathbf{bu}} & \mathbf{K}_{ij}^{\mathbf{ba}} & \mathbf{K}_{ij}^{\mathbf{bb}} \end{bmatrix} \tag{8.34}$$

$$\mathbf{f}_i^{e} = \left\{ \mathbf{f}_i^{\mathbf{u}} \quad \mathbf{f}_i^{\mathbf{a}} \quad \mathbf{f}_i^{\mathbf{b}1} \quad \mathbf{f}_i^{\mathbf{b}2} \quad \mathbf{f}_i^{\mathbf{b}3} \quad \mathbf{f}_i^{\mathbf{b}4} \right\}^{\mathrm{T}} \tag{8.35}$$

and $\mathbf{u}^h$ is the vector of nodal parameters

$$\mathbf{u}^h = \{\mathbf{u} \quad \mathbf{a} \quad \mathbf{b}_1 \quad \mathbf{b}_2 \quad \mathbf{b}_3 \quad \mathbf{b}_4\}^{\mathrm{T}} \tag{8.36}$$

with

$$\mathbf{K}_{ij}^{rs} = \int_{\Omega^{\mathrm{e}}} (\mathbf{B}_i^r)^{\mathrm{T}} \mathbf{D} \left(\mathbf{B}_j^s\right) \mathrm{d}\Omega \quad (r, s = \mathbf{u}, \mathbf{a}, \mathbf{b}) \tag{8.37}$$

$$\mathbf{f}_i^{\mathbf{u}} = \int_{\Gamma_t} N_i \mathbf{f}^t \mathrm{d}\Gamma + \int_{\Omega^{\mathrm{e}}} N_i \mathbf{f}^{\mathrm{b}} \mathrm{d}\Omega \tag{8.38}$$

$$\mathbf{f}_i^{\mathbf{a}} = \int_{\Gamma_t} N_i H \mathbf{f}^t \mathrm{d}\Gamma + \int_{\Omega^{\mathrm{e}}} N_i H \mathbf{f}^{\mathrm{b}} \mathrm{d}\Omega \tag{8.39}$$

$$\mathbf{f}_i^{\mathbf{b}\alpha} = \int_{\Gamma_t} N_i F_\alpha \mathbf{f}^t \mathrm{d}\Gamma + \int_{\Omega^{\mathrm{e}}} N_i F_\alpha \mathbf{f}^{\mathrm{b}} \mathrm{d}\Omega \quad (\alpha = 1,2,3 \text{ and } 4) \tag{8.40}$$

In the stiffness matrix, **B** is the matrix of shape function derivatives,

$$\mathbf{B}_i^{\mathbf{u}} = \begin{bmatrix} N_{i,x} & 0 \\ 0 & N_{i,y} \\ N_{i,y} & N_{i,x} \end{bmatrix} \tag{8.41}$$

$$\mathbf{B}_i^{\mathbf{a}} = \begin{bmatrix} (N_i\psi)_{,x} & 0 \\ 0 & (N_i\psi)_{,y} \\ (N_i\psi)_{,y} & (N_i\psi)_{,x} \end{bmatrix} \tag{8.42}$$

$$\mathbf{B}_i^{\mathrm{b}} = \begin{bmatrix} \mathbf{B}_i^{\mathrm{b}1} & \mathbf{B}_i^{\mathrm{b}2} & \mathbf{B}_i^{\mathrm{b}3} & \mathbf{B}_i^{\mathrm{b}4} \end{bmatrix} \tag{8.43}$$

$$\mathbf{B}_i^{\alpha} = \begin{bmatrix} (N_i\varphi_\alpha)_{,x} & 0 \\ 0 & (N_i\varphi_\alpha)_{,y} \\ (N_i\varphi_\alpha)_{,y} & (N_i\varphi_\alpha)_{,x} \end{bmatrix} (\alpha = 1,2,3 \text{ and } 4) \tag{8.44}$$

The rest of the computation depends on the definition of the enrichment function.

8.3.3 Discontinuous enrichment

We now describe the construction of the discontinuous function $\psi(x)$ in two dimensions. The Heaviside function $H(x)$ is the mostly used in the literatures.

The distance d from a point **x** to an interface Γ is defined as

$$d = \|\mathbf{x} - \mathbf{x}_\Gamma\| \tag{8.45}$$

where $\mathbf{x}_\Gamma$ is the normal projection of **x** on Γ, as shown in Fig. 8.4.

The signed distance function $\xi(x)$ can be defined as

$$\xi(x) = \min_{\mathbf{x}_\Gamma \in \Gamma} \|\mathbf{x} - \mathbf{x}_\Gamma\| \, sign(\mathbf{n} \cdot (\mathbf{x} - \mathbf{x}_\Gamma)) \tag{8.46}$$

where **n** is the unit normal vector.

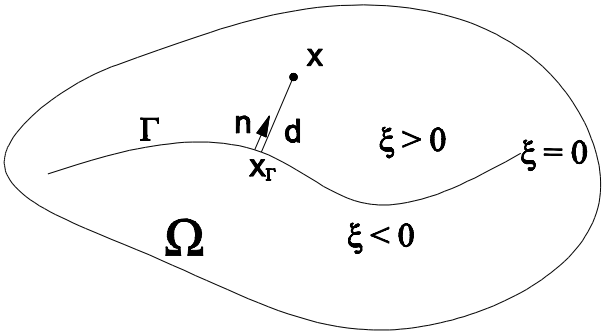

Fig. 8.4. Difinition of the signed distance function.

The Heaviside enrichment function is assumed to be the signed function

$$H(\xi) = \text{sign}(\xi) = \begin{cases} 1 & \forall\, \xi > 0 \\ -1 & \forall\, \xi < 0 \end{cases} \tag{8.47}$$

Approximation of the discontinuous which is the second term in eq. (8.32), the displacement rewritten as

$$\mathbf{u}^h(\mathbf{x}) = \sum_{j=1}^{n} N_j(\mathbf{x})\mathbf{u}_j + \sum_{h=1}^{m} N_h(\mathbf{x})H(\xi)\mathbf{a}_h + \sum_{k=1}^{t} N_k(\mathbf{x})\varphi(\mathbf{x})\mathbf{b}_k \tag{8.48}$$

A simple one-dimensional representation of the step function is depicted in Fig. 8.5(a). Fig. 8.5(b) illustrates the way the step function simulations the discontinuity.

It's easily found that, suppose the crack tip enrichment is accurate enough, the approximation eq. (8.32) is no longer an interpolation and the value of the field variable $\mathbf{u}^h(\mathbf{x})$ on an enriched node *j* is not equal to the nodal value $\mathbf{u}_j$

$$\mathbf{u}^h(\mathbf{x}_j) = \mathbf{u}_j + H(\xi_j)\mathbf{a}_j \neq \mathbf{u}_j \tag{8.49}$$

A simple shifting procedure guarantees the interpolation

$$\mathbf{u}^h(\mathbf{x}) = \sum_{j=1}^{n} N_j(\mathbf{x})\mathbf{u}_j + \sum_{h=1}^{m} N_h(\mathbf{x})\big(H(\xi) - H(\xi_h)\big)\mathbf{a}_h + \sum_{k=1}^{t} N_k(\mathbf{x})\varphi(\mathbf{x})\mathbf{b}_k \tag{8.50}$$

Fig. 8.5(c) illustrates the effect of the modified approximation on the one-dimensional crack problem. The overall jump in the displacement field can be obtained from

$$\langle \mathbf{u}^h(\mathbf{x}) \rangle = \mathbf{u}^h(\mathbf{x}^+) - \mathbf{u}^h(\mathbf{x}^-) = \cdots = 2\sum_{h=1}^{m} N_h(\mathbf{x})\mathbf{a}_h \tag{8.51}$$

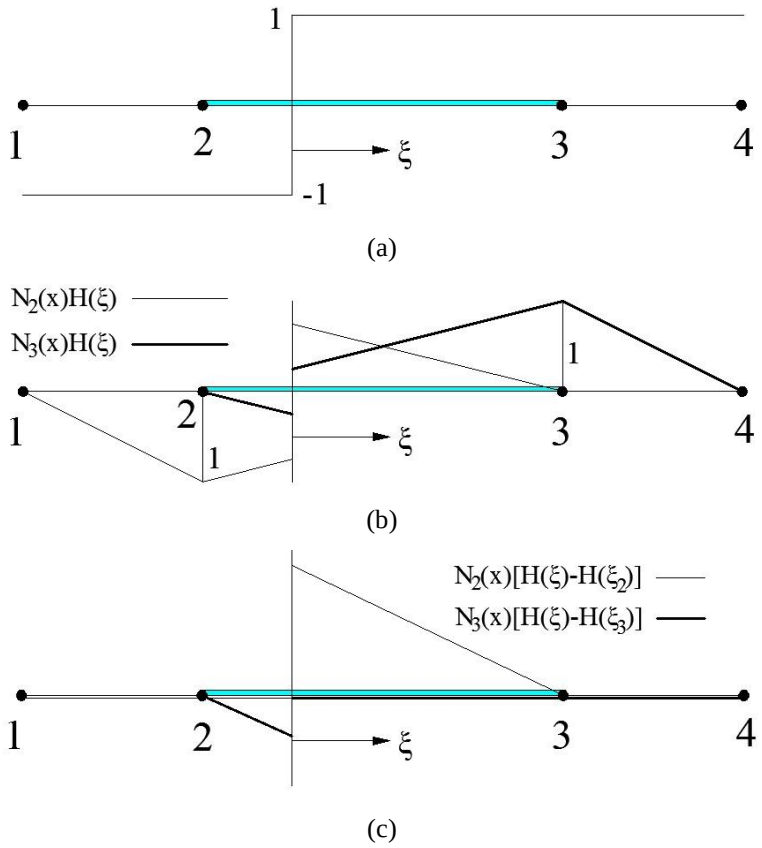

Fig. 8.5 (a) Sign function; (b) Effect of the sign function on shape functions; (c) Effect of shifting on shape functions

Derivative of the Heaviside function is the Dirac delta function:

$$H_{,i}(\xi) = \delta(\xi) \tag{8.52}$$

which vanishes except at the position of the crack interface:

$$H_{,i}(\xi) = \begin{cases} 1 \text{ at crack tip} \\ 0 \quad \text{otherwise} \end{cases} \tag{8.53}$$

As a result eq. (8.42) can be rewritten as

$$\mathbf{B}_i^{\mathbf{a}} = \begin{bmatrix} N_{i,x}H & 0 \\ 0 & N_{i,y}H \\ N_{i,y}H & N_{i,x}H \end{bmatrix} \tag{8.54}$$

To include the effects of interpolation, $H(\xi)$ should be replaced by $[H(\xi) - H(\xi_i)]$, the following shifting amendments are required

$$\mathbf{B}_i^{\mathbf{a}} = \begin{bmatrix} (N_i[H(\xi) - H(\xi_i)])_{,x} & 0 \\ 0 & (N_i[H(\xi) - H(\xi_i)])_{,y} \\ (N_i[H(\xi) - H(\xi_i)])_{,y} & (N_i[H(\xi) - H(\xi_i)])_{,x} \end{bmatrix} \tag{8.55}$$

8.3.4 Crack tip enrichment functions

8.3.4.1 Crack in isotropic

The near tip enrichment functions have already been defined in terms of the local crack tip coordination system (r,θ), The crack-tip enrichment functions in isotropic elasticity are [23]

$$\varphi_\alpha(r,\theta)=\left\{\sqrt{r}\sin\frac{\theta}{2},\sqrt{r}\cos\frac{\theta}{2},\sqrt{r}\sin\theta\sin\frac{\theta}{2},\sqrt{r}\sin\theta\cos\frac{\theta}{2}\right\} \tag{8.56}$$

where r and θ are polar coordinates in the local crack-tip coordinate system. Note that the first function in the above equation is discontinuous across the crack.

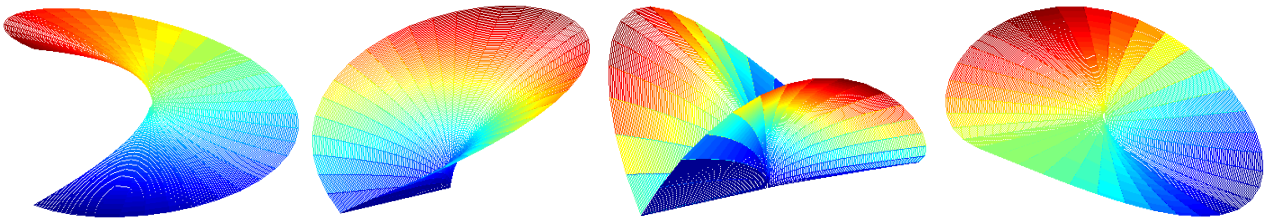

(a) φ_1 (b) φ_2 (c) φ_3 (d) φ_4

Fig. 8.6 Crack tip enriched functions in isotropic

Similar to the discontinuous enrichment function, to include the effects of interpolation, the following shifting amendments are required,

$$\mathbf{B}_i^\alpha=\begin{bmatrix}(N_i[\varphi_\alpha-\varphi_{\alpha i}])_{,x} & 0\\ 0 & (N_i[\varphi_\alpha-\varphi_{\alpha i}])_{,y}\\ (N_i[\varphi_\alpha-\varphi_{\alpha i}])_{,y} & (N_i[\varphi_\alpha-\varphi_{\alpha i}])_{,x}\end{bmatrix}\ (\alpha=1,2,3\text{ and }4) \tag{8.57}$$

The shifting amendments will be required in all the enrichment. To keep it simple, we will not mentioned again in the following description.

Derivatives of $\varphi_\alpha(r,\theta)$ with respect to the crack tip polar coordinates (r,θ) become

$$\varphi_{1,r}=\frac{1}{2\sqrt{r}}\sin\frac{\theta}{2};\ \varphi_{1,\theta}=\frac{\sqrt{r}}{2}\cos\frac{\theta}{2} \tag{8.58a}$$

$$\varphi_{2,r}=\frac{1}{2\sqrt{r}}\cos\frac{\theta}{2};\ \varphi_{2,\theta}=-\frac{\sqrt{r}}{2}\sin\frac{\theta}{2} \tag{8.58b}$$

$$\varphi_{3,r}=\frac{1}{2\sqrt{r}}\sin\frac{\theta}{2}\sin\theta\ ;\ \varphi_{3,\theta}=\sqrt{r}\left(\frac{1}{2}\cos\frac{\theta}{2}\sin\theta+\sin\frac{\theta}{2}\cos\theta\right) \tag{8.58c}$$

$$\varphi_{4,r}=\frac{1}{2\sqrt{r}}\cos\frac{\theta}{2}\sin\theta\ ;\ \varphi_{4,\theta}=\sqrt{r}\left(-\frac{1}{2}\sin\frac{\theta}{2}\sin\theta+\cos\frac{\theta}{2}\cos\theta\right) \tag{8.58d}$$

and the derivatives of $\varphi_\alpha(r,\theta)$ with respect to the local crack coordinate system (x',y') can then be defined as

$$\varphi_{1,x'} = -\frac{1}{2\sqrt{r}}\sin\frac{\theta}{2};\ \varphi_{1,y'} = \frac{1}{2\sqrt{r}}\cos\frac{\theta}{2} \tag{8.59a}$$

$$\varphi_{2,x'} = \frac{1}{2\sqrt{r}}\cos\frac{\theta}{2};\ \varphi_{2,y'} = \frac{1}{2\sqrt{r}}\sin\frac{\theta}{2} \tag{8.59b}$$

$$\varphi_{3,x'} = -\frac{1}{2\sqrt{r}}\sin\frac{3\theta}{2}\sin\theta;\ \varphi_{3,y'} = \frac{1}{2\sqrt{r}}\left(\sin\frac{\theta}{2} + \sin\frac{3\theta}{2}\cos\theta\right) \tag{8.59c}$$

$$\varphi_{4,x'} = -\frac{1}{2\sqrt{r}}\cos\frac{3\theta}{2}\sin\theta;\ \varphi_{4,y'} = \frac{1}{2\sqrt{r}}\left(\cos\frac{\theta}{2} + \cos\frac{3\theta}{2}\cos\theta\right) \tag{8.59d}$$

Finally, the derivatives in the global coordinates system are obtained,

$$\varphi_{\alpha,x} = \varphi_{\alpha,x'}\cos\alpha - \varphi_{\alpha,y'}\sin\alpha \tag{8.60a}$$

$$\varphi_{\alpha,y} = \varphi_{\alpha,x'}\sin\alpha + \varphi_{\alpha,y'}\cos\alpha \tag{8.60b}$$

where α is the angle of crack path with respect to the x axis.

8.3.4.2 Interfacial crack in bi-material

To model interfacial cracks as shown in Fig. 8.7 within the X-FEM setting, Sukumar *et al*. [18] use the generalized Heaviside functions $H(x)$ to model the crack interior Γ_c, and the asymptotic crack-tip function $[\varphi_\alpha(x), \alpha = 1{\sim}12]$ to model the crack tip for an interface crack. According to the displacement solution of an interface crack, the near-tip crack enrichment functions are written as

$$[\varphi_\alpha(x), \alpha = 1{\sim}12] = \left\{\begin{array}{l} \sqrt{r}\cos(\epsilon log r)\, e^{-\epsilon\theta}\sin\frac{\theta}{2},\ \ \sqrt{r}\cos(\epsilon log r)\, e^{-\epsilon\theta}\cos\frac{\theta}{2} \\ \sqrt{r}\cos(\epsilon log r)\, e^{\epsilon\theta}\sin\frac{\theta}{2},\ \ \sqrt{r}\cos(\epsilon log r)\, e^{\epsilon\theta}\cos\frac{\theta}{2} \\ \sqrt{r}\cos(\epsilon log r)\, e^{\epsilon\theta}\sin\frac{\theta}{2}\sin\theta, \sqrt{r}\cos(\epsilon log r)\, e^{\epsilon\theta}\cos\frac{\theta}{2}\sin\theta \\ \sqrt{r}\sin(\epsilon log r)\, e^{-\epsilon\theta}\sin\frac{\theta}{2}, \sqrt{r}\sin(\epsilon log r)\, e^{-\epsilon\theta}\cos\frac{\theta}{2} \\ \sqrt{r}\sin(\epsilon log r)\, e^{\epsilon\theta}\sin\frac{\theta}{2}, \sqrt{r}\sin(\epsilon log r)\, e^{\epsilon\theta}\cos\frac{\theta}{2} \\ \sqrt{r}\sin(\epsilon log r)\, e^{\epsilon\theta}\sin\frac{\theta}{2}sin\theta, \sqrt{r}\sin(\epsilon log r)\, e^{\epsilon\theta}\cos\frac{\theta}{2}sin\theta \end{array}\right\} \tag{8.61}$$

where r and θ are polar coordinates in the local crack-tip coordinate system, ϵ is the bi-material index.

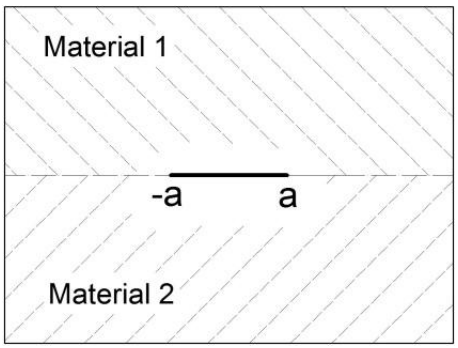

Fig. 8.7 Interfacial crack

If the bi-material constant $\epsilon = 0$ (isotropic material), the span of the enrichment functions given above is degenerated as that for a crack in isotropic material, eq. (8.56).

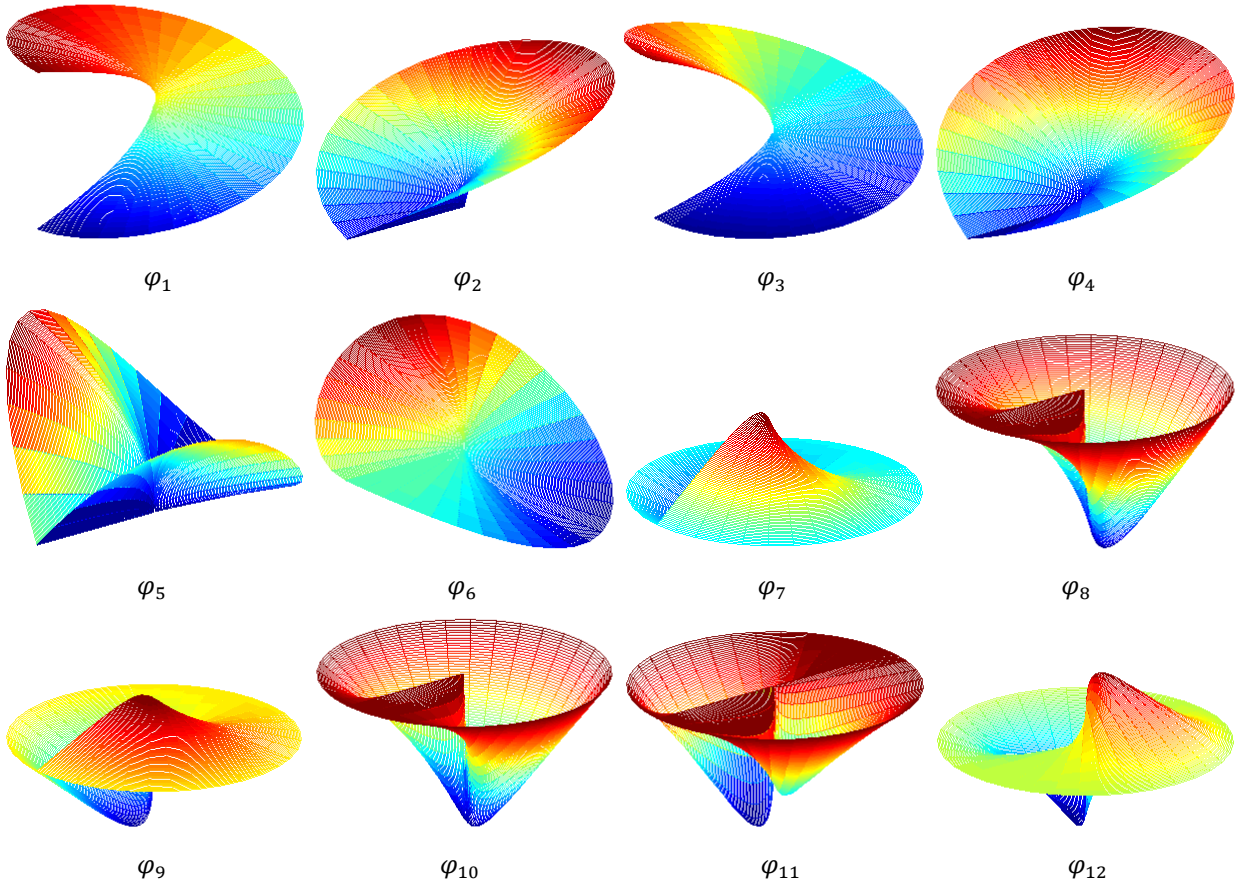

Fig. 8.8 Enrichment functions for interfacial crack

The enrichment functions are graphically shown in Fig 8.8. It's very clearly that the functions φ_1 and φ_3 are not continue across the crack. Derivatives of $\varphi_\alpha(r,\theta)$ with respect to the crack tip polar coordinates (r,θ) and local coordinate can be found in reference [18].

8.3.4.3 Interfacial crack perpendicular to the interface

Consider a bi-material with a crack perpendicular to the interface and the crack terminates at the interface. The near-tip asymptotic field for this problem has been studied by many researchers [24-26]. The elastic mismatch between the two elastic materials is characterized by Dundurs parameters [27] α and β. The asymptotic displacement field near the tip of a plane crack in a bi-material takes the form [26]

$$u_i(r,\theta) = r^{1-\lambda}\{a_i sin\lambda\theta + b_i cos\lambda\theta + c_i sin(\lambda-2)\theta + d_i cos(\lambda-2)\theta\} \qquad (8.62)$$

where $\lambda(0<\lambda<1)$, which is the stress singularity exponent, is a function of the Dundurs parameters and is given by the root of the transcendental equation [24].

$$cos(\lambda\pi) - 2\frac{\alpha-\beta}{1-\beta}(1-\lambda)^2 + \frac{\alpha-\beta^2}{1-\beta^2} = 0 \qquad (8.63)$$

The value λ as a function of α and β is tabulated in Beuth [28]. In the case of no mismatch ($\alpha = \beta = 0$) the stress singularity reduces to the classical inverse $\sqrt{r}$ stress singularity $\lambda = 1/2$ for homogeneous linear elastic materials. When material 2 is stiffer than material 1 ($\alpha < 0$), the singularity is weaker ($\lambda < 1/2$), and if material 2 is more compliant that material 1 ($\alpha > 0$), the singularity is stronger ($\lambda > 1/2$).

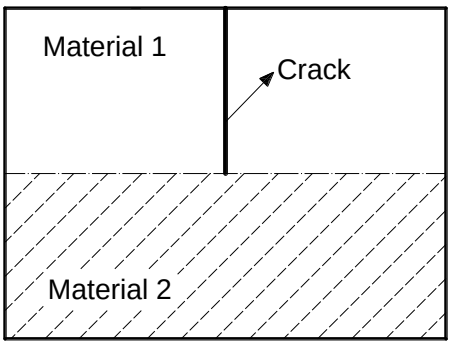

Fig. 8.9 Bi-material with a crack perpendicular to the interface

The crack tip enrichment functions for the bi-material crack problem are [29]

$$[\varphi_\alpha(x), \alpha = 1\sim4] = r^{1-\lambda}[sin\lambda\theta, cos\lambda\theta,\ sin(\lambda-2)\theta, cos(\lambda-2)\theta\ ] \qquad (8.64)$$

where the above functions span the asymptotic crack-tip displacement expansion given in eq.(8.62). Note that in this instance the first function and the third function in the above equation are discontinuous across the crack $\theta = \pm\pi$.

8.3.4.4 Interfacial crack terminates to the interface [30]

For a crack terminates at the interface, the order of the stress singularity is characterized by the solution of the equation

$$[\alpha+\beta^2-(1-\beta)(\alpha-\beta)(1-\cos 2\theta_0)\lambda^2+(1-\beta^2)\cos\lambda\pi\cos\lambda(\pi-2\theta_0)]^2$$
$$+(1-\beta^2)\sin^2\lambda(\pi-2\theta_0)\,[(1-\beta^2)\cos^2\lambda\pi+\beta^2-\alpha^2]=0 \quad (8.65)$$

where α and β are the Dundurs bi-material parameters; θ_0 is the arbitrary angle between crack and interface.

The enrichment functions are considered separately the case where the characteristic exponent λ is real and the case where it is complex.

Real characteristic exponent:

$$\varphi_{\alpha=1,\dots,4\times k}(r,\theta)=r^{\lambda_k}\{\sin(\lambda_k+1)\theta\,,\cos(\lambda_k+1)\theta\,,\sin(\lambda_k-1)\theta\,,\cos(\lambda_k-1)\theta\,\} \quad (8.66)$$

where k is the number of the characteristic exponents: $k=1$ in case where $\lambda=\lambda_1$ is real single, and $k=2$ in case where $\lambda=(\lambda_1,\lambda_2)$ is real double.

Imaginary characteristic exponent:

In case of imaginary characteristic exponents, both $\lambda=\lambda_R+\mathrm{i}\lambda_I$ and its conjugate $\bar{\lambda}=\lambda_R-\mathrm{i}\lambda_I$ are solutions of the eq. (8.65). The enrichment functions in case of a complex characteristic exponent for a crack tip terminating at a bi-material interface are given by:

$$\varphi_{\alpha=1,\dots,16}(r,\theta)=\begin{Bmatrix} r^{\lambda_R}e^{\lambda_I\theta}[cos(\lambda_I\log(r))\cos(\lambda_R+1)\,,cos(\lambda_I\log(r))\sin(\lambda_R+1)\,,\\ sin(\lambda_I\log(r))\cos(\lambda_R+1)\,,sin(\lambda_I\log(r))\sin(\lambda_R+1)\,,\\ cos(\lambda_I\log(r))\cos(\lambda_R-1)\,,cos(\lambda_I\log(r))\sin(\lambda_R-1)\,,\\ sin(\lambda_I\log(r))\cos(\lambda_R-1)\,,sin(\lambda_I\log(r))\sin(\lambda_R-1)],\\ r^{\lambda_R}e^{-\lambda_I\theta}[cos(\lambda_I\log(r))\cos(\lambda_R+1)\,,cos(\lambda_I\log(r))\sin(\lambda_R+1)\,,\\ sin(\lambda_I\log(r))\cos(\lambda_R+1)\,,sin(\lambda_I\log(r))\sin(\lambda_R+1)\,,\\ cos(\lambda_I\log(r))\cos(\lambda_R-1)\,,cos(\lambda_I\log(r))\sin(\lambda_R-1)\,,\\ sin(\lambda_I\log(r))\cos(\lambda_R-1)\,,sin(\lambda_I\log(r))\sin(\lambda_R-1)] \end{Bmatrix} \quad (8.67)$$

8.4 Level set method

8.4.1 Level set functions

The level set method is a versatile method for computing and analyzing the evolution of an interface Γ_c in two or three dimensions, which was introduced by Osher and Sethian [31, 32], and investigated by many researchers [11, 13, 33]. The interface bounds an open region Ω. The velocity of the evolving interface can depend on position, time, interface geometry and the physics of the underlying problem. The level set function will be used for representing the material interface between the fiber and matrix as well as the geometry of a crack. The level set function $\psi(x,t)$ is a continuous function, where x is a point in the domain Ω. The level set function has the following properties

$$\psi(x,t) < 0, for\ x \in \Omega \tag{8.68a}$$

$$\psi(x,t) > 0, for\ x \notin \Omega \tag{8.68b}$$

$$\psi(x,t) = 0, \text{for } x \in \Gamma \tag{8.68c}$$

Therefore, the boundary of interest at any given time t can be located by finding x that satisfies the following equation

$$\psi(x,t) = 0 \tag{8.69}$$

the boundary is commonly referred to as the zero level set of ψ which can be abbreviated as ψ_0. Equation is commonly referred to the level set equation. The typical approach to using the level set equation to propagate a moving front over time is to differentiate with respect to time which yields

$$\frac{\partial \psi}{\partial t} + \frac{\partial \psi}{\partial x}\frac{\partial x}{\partial t} = 0 \tag{8.70}$$

The equation can be rewritten as

$$\psi_{,t} + \vec{V} \cdot \nabla\psi = 0 \tag{8.71}$$

where $\vec{V}$ is the velocity field. This partial differential equation can then be solved numerically by discretizing and using a finite difference approach to approximate the gradient of ψ. The derivative of ψ with respect to the time t can be approximated using the forward difference method as

$$\frac{\psi^{n+1} - \psi^n}{\Delta t} + \vec{V}^n \cdot \nabla\psi^n = 0 \tag{8.72}$$

Which can be rewritten into a more convenient form for updating ψ in two-dimensions are

$$\psi^{n+1} = \psi^n - \Delta t\left(u^n \cdot \psi_{,x}^n + v^n \cdot \psi_{,y}^n\right) \tag{8.73}$$

where u and v are the x and y components of the evolving interface velocity. The time step Δt is governed by the Courant-Friedrichs-Lewy (CFL) condition. The CFL condition ensures that the approximation of the solution to the partial differential equation given in eq. (8.70) is convergent. The limiting parameter for the time step in two-dimensions can be written as

$$\Delta t < \frac{\max(\Delta x, \Delta y)}{\max(u, v)} \tag{8.74}$$

where $(\Delta x, \Delta y)$ represent the grid spacing in the x and y-directions.

For modeling a composite material, a fiber in matrix will be considered. The level set function associated with a cylindrical fiber in the composite is denoted as $\zeta(x)$and calculated as

$$\zeta(\mathrm{x}) = \sqrt{(x_i - x_0)^2 + (y_i - y_0)^2} - r_0 \tag{8.74}$$

where x_i and y_i are the coordinates of the i^{th}node in the domain, x_0 and y_0 are the coordinates of the center of the fiber and r_0 is the fiber radius.

The analytical form of the level set function as in eq. (8.73) is limited for simple geometries. In addition, when the interface moves according to $\psi(\mathrm{x},\mathrm{t}) = 0$, the new interface will not have a simple analytical expression. Stolarska *et al.* [11] introduced an extension of the level set method for modeling the evolution of one-dimensional curve in a piecewise linear fashion with a particular focus on representing the evolution of a crack. Instead of having analytical expression of the level set function, a discrete value is assigned at each node of finite elements, and the location of zero level set is found using interpolation. Sukumar [13] proposed additional enrichment via the level set method for the modeling of holes and inclusions. Two level set functions ϕ and ψ are needed to track the growth of an open curve in this case, one for the crack path and the other for the crack tip. In this extension the crack path is represented as the zero level set of $\psi(\mathrm{x},\mathrm{t})$. The ψ level set is oriented such that its zero level set passes through the current crack tip and is oriented in the direction of the crack tip speed function. The zero level set of $\phi(\mathrm{x},\mathrm{t})$ is then given by the line intersecting the current crack tip and orthogonal to the zero level set of ψ.

For the level functions ϕ and ψ, each grid point is assigned a distance from that point to the nearest point of function's zero level set. The sign of the distance for the ψ level set function is positive on the side counter-clockwise from the direction of the crack tip speed function and negative on the clockwise side. The sign of the distance function for the ϕ function is positive on the side in the direction of crack growth and negative on the opposite side. The crack is defined to the locations where the following conditions are true

$$\phi(\mathrm{x},\mathrm{t}) \leq 0 \tag{8.75a}$$

$$\psi(\mathrm{x},\mathrm{t}) = 0 \tag{8.75b}$$

8.4.2 Level set algorithm for modeling crack growth

Modeling one-dimensional crack growth in a level set framework by representing the crack as the zero level set function $\psi(\mathrm{x},\mathrm{t})$. An endpoint of the crack is represented as the intersection of the zero level set of ψ with an orthogonal zero level set of the function $\phi_i(\mathrm{x},\mathrm{t})$, where i is the number of tips on a given crack. For cracks that are entirely in the interior of the bulk of a material, two functions are used ϕ_1 and ϕ_2, one for each crack tip. For edge cracks only on function ϕ is necessary. The values of the level set functions are stored only at the nodes. The functions are interpolated over the mesh by the same shape functions as the displacement. Thus,

$$\phi_i(\mathrm{x},\mathrm{t}) = \sum_{\mathrm{j}\in\mathrm{J}} \phi_{ij}(\mathrm{t})\mathrm{N_j}(\mathrm{x}) \tag{8.76a}$$

$$\psi(\mathrm{x},\mathrm{t}) = \sum_{\mathrm{j}\in\mathrm{J}} \psi_j(\mathrm{t})\mathrm{N_j}(\mathrm{x}) \tag{8.76b}$$

Since the shape functions are C^0, the crack representation is also C^0.

The level set function representing the initial crack is constructed by computing the signed distance function for the crack. A difficulty in doing this arises from the fact that, although the crack tip lies within the domain, the level set function representing the crack must initially be constructed on the entire domain. To circumvent this problem, the initial crack is extended tangentially from its tip and the signed distance function $\phi(\mathrm{x},\mathrm{t}) = \pm\min_{x_\Gamma\in\Gamma(\mathrm{t})}\|x - x_\Gamma\|$ is constructed from this extended crack.

The level set functions that represent the crack tip are initially defined by

$$\phi_\mathrm{i}(\mathrm{x},0) = (\mathrm{x} - \mathrm{x_i})\cdot\hat{\mathrm{t}} \tag{8.77}$$

where $\hat{\mathrm{t}}$ is a unit vector tangent to the crack at its tip and $\mathrm{x_i}$ is the location of the ith crack tip. Given the construction described by above eq. the planar function ϕ_i has a zero level set which is orthogonal to ψ at the crack tip. The initial level set function, ψ and ϕ_i, and the representation of the crack are shown in Fig. 8.10.

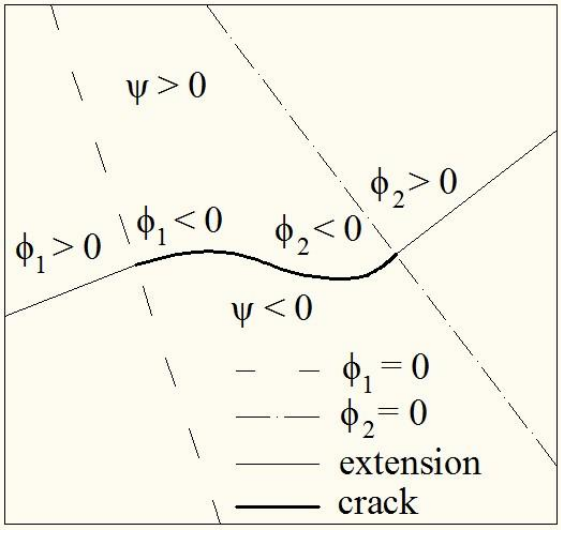

Fig. 8.10 Construction of initial level set functions

An important consideration is that, although the actual crack is embedded inside a domain, the zero level set of ψ cuts through the entire domain. In the level set framework, the crack is considered to be the zero level set of ψ, where both $\phi_1 \le 0$ and $\phi_2 \le 0$ in the case of an interior crack. In the

case of an edge crack $\phi_1 \leq 0$. This is consistent with the initial conditions and will continue to be so as the level set functions are updated.

For the case of more than one crack tip, it is convenient to define a single function $\phi(x,t)$ for the crack tip level set representation by

$$\phi(x,t) = \max_i(\phi_i) \tag{8.78}$$

The function ϕ allows us to define the location of the crack using only one function whether a crack has one or two tips. In other words, a crack is defined as the set

$$\{x: \psi(x,t) = 0 \text{ and } \phi(x,t) \leq 0\} \tag{8.79}$$

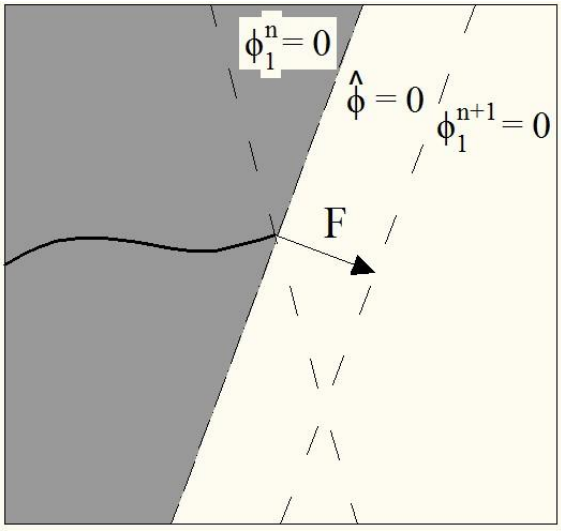

Fig. 8.11 Level set function update. Gray region is $\Omega^{\text{no update}}$. Non-gray region is Ω^{update}.

Since only considering one-dimensional curve crack, we can confine the level set representation to a narrow band of elements around the crack. In addition we assume that once a part of a crack has formed, that part will no longer change shape or move. Therefore, the ψ, ϕ_i and ϕ functions need only be updated on a small region of elements surrounding each crack tip. This narrow band is built by surrounding the crack tip by a predetermined layer of elements. The number of surrounding elements is chosen so that it is larger than the incremental growth length of the crack.

Crack growth is modeled by appropriately updating the ϕ_i and ψ functions, then reconstructing the updated ϕ function. A crack is extended at each tip in the same manner, regardless of the number of cracks and the number of crack tips on a given crack. The evolution of ϕ_i and ψ is determined by the crack growth direction, θ_c. In each step, the displacement of the crack tip is given by the prescribed vector $F = (F_x, F_y)$. The magnitude of crack extension $\|F\|$ depends on the crack growth law. The current location of the crack tip, $\mathbf{x}_i = (x_i, y_i)$ is also used in the equations of evolution.

Let the current values of ϕ_i and ψ at step n be ${\phi_i}^n$ and ψ^n. The algorithm for evolution of the level set functions ϕ_i and ψ is as follows:

1. ${\phi_i}^n$ is updated using Equation $\phi_t + F\|\nabla\phi\| = 0$. F is always the speed normal to the interface. However, F is not necessarily orthogonal to the zero level set of ${\phi_i}^n$. For this reason, we must first rotate ${\phi_i}^n$ so that F is orthogonal. ${\phi_i}^n$ after rotation is referred to as $\widehat{\phi}_i$ and given by

$$\widehat{\phi}_i = (x - x_i)\frac{F_x}{\|F\|} + (y - y_i)\frac{F_y}{\|F\|} \tag{8.80}$$

2. The crack is extended by computing new values of ψ^{n+1} only where $\widehat{\phi}_i > 0$, which is referred to as Ω^{update}. Let the region where $\widehat{\phi}_i \le 0$ be $\Omega^{\text{no update}}$

$$\psi^{n+1} = \psi^n \text{ in } \Omega^{\text{no update}} \tag{8.81}$$

$$\psi^{n+1} = \pm|(\mathbf{x} - \mathbf{x}_i)| \times \frac{\mathbf{F}}{\|\mathbf{F}\|} = \pm\left|(x - x_i)\frac{F_x}{\|\mathbf{F}\|} + (y - y_i)\frac{F_y}{\|\mathbf{F}\|}\right| \; in\; \Omega^{\text{update}} \tag{8.82}$$

The sign of ψ^{n+1} in Ω^{update} is chosen so that it is consistent with the current sign on a given side of the crack in $\Omega^{\text{no update}}$.

3. ${\phi_i}^{n+1}$ is computed using $\phi_t + F\|\nabla\phi\| = 0$ so that is represents the updated location of the crack tip.

$${\phi_i}^{n+1} = \widehat{\phi} - \Delta t\|\mathbf{F}\| \tag{8.83}$$

where by construction, $\nabla\|\phi\| \equiv 1$ at all times. The rotated level set function $\widehat{\phi}_i$ is calculated exactly in eq($\widehat{\phi}_i = (x - x_i)\frac{F_x}{\|F\|} + (y - y_i)\frac{F_y}{\|F\|}$). Since ${\phi_i}^{n+1}$ is calculated from $\widehat{\phi}_i$, it is important to note that ${\phi_i}^{n+1}$ is also recalculated in each step rather than updated from the previous values of ϕ_i. the recalculate of ${\phi_i}^n$ and ${\phi_i}^{n+1}$ is illustrated in Fig 8.11.

4. Once all ${\phi_i}^{n+1}$'s corresponding to a crack are updated, ${\phi_i}^{n+1}$ is updated using

$$\phi(x, t) = \max_i(\phi_i) \tag{8.84}$$

The location of the new crack tip i can now be determined by finding the intersection of the zero level set of ${\phi_i}^{n+1}$ and the newly extended ψ^{n+1}. The updated tip is used to determine a new region of elements over which the level set computation will take place.

8.4.3 Coupling the level set method and the extended finite element method

The LSM and XFEM couple naturally to model crack growth. The value of ψ, ϕ_i and ϕ are stored at nodes. Any information needed for crack growth, such as the location of the crack tip, can be obtained from these nodal values, making it unnecessary to store any other information pertaining to the crack. The XFEM algorithm is an efficient finite element scheme that solves the elliptical problem which determines the evolution of a crack on a mesh. The mesh is unchanged throughout the computation of the evolution of the crack. For these reasons, the LSM and XFEM work quite well together.

Moreover, the level set representation of the work facilitates the computation of the enrichment. The enrichment function is defined so that the discontinuity is coincident with the crack. Because the crack is represented as the zero level set of ψ, all values above or below the crack are either positive or negative. From Heaviside function

$$H(y) = H^*(\psi(x,t)) = \begin{cases} 1 \text{ for } \psi(x,t) > 0 \\ -1 \text{ for } \psi(x,t) < 0 \end{cases} \tag{8.85}$$

Therefore, to determine the location of a point relative to the crack, one merely has to determine the sign of ψ as that point.

The crack tip enrichment functions are defined in coordinates local to the crack tip. These coordinates can be determined by the level set function representing the tip. The function associated with the tips ϕ is always planar with $\|\nabla\phi\| = 1$, and its zero level sets makes a natural coordinate system. The direction of the local x-axis is determined by $\nabla\phi$. The direction of the local y-axis is then simply $\boldsymbol{n}_z \times \nabla\phi$. In this local coordinate system, the arguments of the branch function can be expressed by the level set functions. That is, at point x, the radius from the crack tip and the angle of the deviation from the tangent to the crack tip is given by

$$r = \sqrt{\phi^2(x,t) + \psi^2(x,t)} \; and \; \theta = \frac{\psi(x,t)}{\phi(x,t)} \tag{8.86}$$

The nodes chosen for enrichment can be determined from the nodal values of ψ and ϕ. In a given element, let ψ_{min} and ψ_{max}, respectively, be the minimum and maximum nodal values of ψ on the nodes of that element. If $\phi < 0$ and $\psi_{min}\psi_{max} \leq 0$, then the crack cuts through the element and the nodes of the element are to be enriched with Heaviside function. Similarly, let ϕ_{min} and ϕ_{max}, respectively, be the minimum and maximum nodal values of ϕ on the nodes of that element. If in that element $\phi_{min}\phi_{max} \leq 0$ and $\psi_{min}\psi_{max} \leq 0$ then the crack tip lies within that element, and its nodes are to be enriched with crack tip function.

The coupling of the LSM and XFEM is illustrated in next figure. For a given crack, each iteration begins by examining the level set functions at each node of each element in the narrow band and

choosing the nodes which require enrichment from the nodal values of these functions. These nodes are then enriched by the appropriate function and the stress field is determined by XFEM. Once the stress field is determined, the stress intensity factors are computed, and from these factors the direction of crack growth θ_c is computed. The angle θ_c is then used in updating the level set functions. Once the level set functions are updated, the process is repeated.

8.5 Interfacial crack growth

8.5.1 Fatigue crack growth criteria

Three essential factors should be carefully considered for the successful simulation of mixed crack growth in composite relate to the criteria. First factor is the initiation of the crack growth. The second factor is the rate of crack growth. Paris's law [34] must be extended to the mixed-mode case, usually by replacing the Mode I stress intensity factor range ΔK_I with an effective stress intensity factor range ΔK_{eff} [35]. The third factor is the direction of crack growth. The maximum principal stress criterion [36, 37] and the minimum strain energy density criterion [38-40] are commonly used. However, it was reported [41] that the difference between these two criteria is negligible.

The Paris' Law is expressed as

$$\frac{da}{dN} = c(\Delta K_I)^m \tag{8.87}$$

where a is the crack length, N is the number of fatigue loading cycles. The two constants c and m are material parameters. ΔK_I is the Mode I stress intensity factor range. For extension to the mixed-mode case, it is replaced by ΔK_{eff}.

The equivalent Mode I stress intensity factor is calculated using the growth angle θ_c in the expression for the circumferential stress. We write

$$\sigma_{\theta\theta}(r, \theta_c) = \frac{K_{eff}}{\sqrt{2\pi r}} \tag{8.88}$$

which after a few manipulations yields

$$K_{eff} = K_I \cos^3\left(\frac{\theta_c}{2}\right) - K_{II} \cos\left(\frac{\theta_c}{2}\right) \sin(\theta_c) \tag{8.89}$$

Tanaka [35] derived the following formula for evaluating ΔK_{eff} in 3D case

$$\Delta K_{eff} = \left(\Delta K_I^4 + 8\Delta K_{II}^4 + \frac{8\Delta K_{III}^4}{1-\upsilon}\right)^{1/4} \tag{8.90}$$

$$\Delta \mathrm{K} = \mathrm{K}_{max} - \mathrm{K}_{min} \tag{8.91}$$

where K_{max} and K_{min} are the SIFs corresponding to a maximum (σ_{max}) and minimum (σ_{min}) applied loads, respectively. For static elastic crack propagation, researchers used to suppose a constant crack growth rate.

After setting the crack growth angle and rate, at each stage the equivalent stress intensity factor K_{eff} is calculated. This can then be compared to the critical value for the material (if available), and crack growth is said to occur if

$$\mathrm{K}_{eff} \geq \mathrm{K}_c \tag{8.92}$$

where K_c is the critical stress intensity factor, or fracture toughness of the material.

Stable fracture is characterized by a decreasing K_{eff} with increasing crack length, in which eventual crack arrest in expected. (for unstable fracture, in which either the equivalent stress intensity factor remains above the critical value with increasing crack length or increasing applied load.)

8.5.2 Improved PV-criterion

For sake of clearly, the improved PV-criterion proposed in Chapter 7 is reintroduced here. The crack propagation will take place along the interface or into one of the two adjacent materials along the direction $\theta_0^{(j)} (j = 1,2)$ for which the normal stress, evaluated at a small distance r_0 from the crack tip, is maximum. Preferentially, the crack propagation along the interface will occur when the following condition satisfied

$$\mathcal{G} = \Gamma(\psi), \theta_0 = 0 \tag{8.93}$$

If the condition eq. (8.93) is not satisfied, the crack will kink out of the interface as soon as one of the following conditions is satisfied:

$$\sqrt{2\pi r_0}\sigma_{\theta\theta}^{(1)}|_{\theta_0^{(1)}, r_0} = K_{IC}^{(1)}, \qquad 0 < \theta_0^{(1)} \leq \pi \tag{8.94}$$

$$\sqrt{2\pi r_0}\sigma_{\theta\theta}^{(2)}|_{\theta_0^{(2)}, r_0} = K_{IC}^{(2)}, \qquad -\pi \leq \theta_0^{(2)} < 0 \tag{8.95}$$

where $K_{IC}^{(1)}$, $K_{IC}^{(2)}$ are the critical stress intensity factors of the material 1 and material 2. Therefore, the crack propagation angle can be determined once the stress state and material toughness, i.e. $K_{IC}^{(1)}$, $K_{IC}^{(2)}$ and $\Gamma(\psi)$, are obtained.

8.6 Test in homogenous material

8.6.1 Test 1 Edge-cracked plate under shear

Consider an edge-cracked plate, as shown in Fig. 8.12(a), fixed at the bottom and subjected to a uniform shear stress $\sigma_{12} = 1$ applied at the top. The plate has the length H = 16 units, width W = 7 units, and the crack length is a = 3.5 units. Plane strain conditions are assumed. Poisson's ratio is taken as 0.3 and Young's modulus is chosen as 100 units. [42] Four kinds of the FE discretization are chosen: Mesh 1 as 99×199 elements, Mesh 2 as 47×95 elements, Mesh 3 as 35×81 elements and Mesh 4 as 23×47 elements, as shown in Fig 8.12(b). The tip enrich range is $r_0 = 0.2, 0.6, 1.0$, using branch enrichment. The deformed geometry is shown in Fig. 8.12(c). The mixed mode SIFs K_I and K_{II} are investigated. The analytical stress intensity factors of the plane strain solution solved by Wilson [43] are $K_I = 34.0$ and $K_{II} = 4.55$. Comparison between analytical SIFs and XFEM numerical solutions is listed in Table 1.

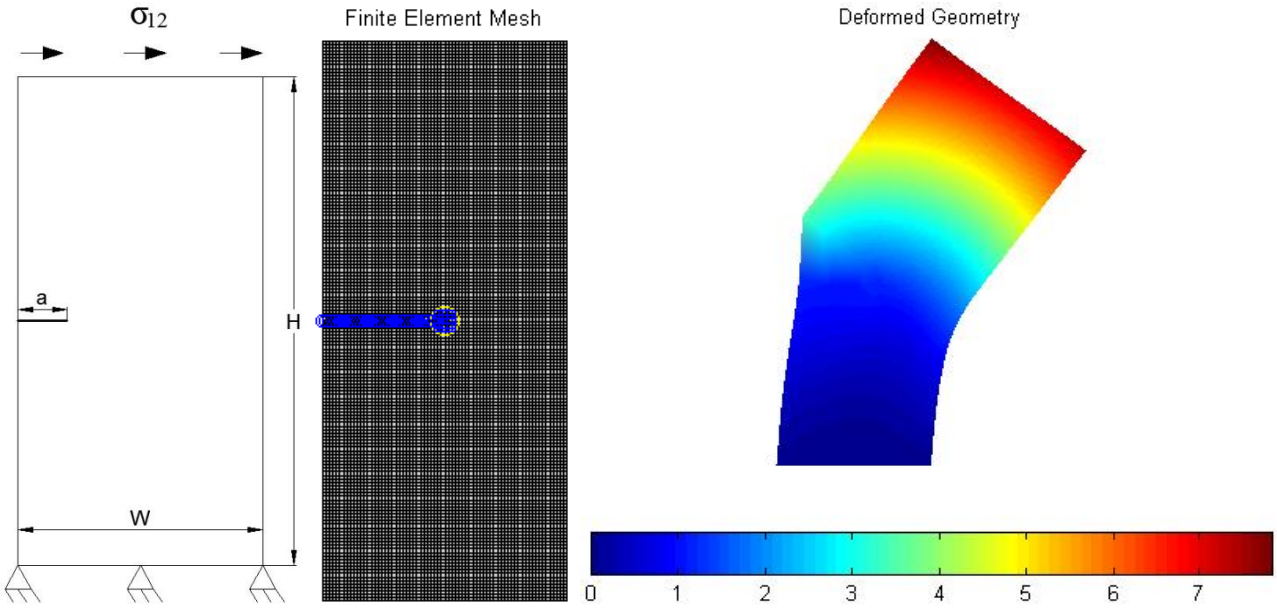

Fig. 8.12. Edge-cracked plate under shear: (a) Geometry and load; (b) FE Mesh; (c) Deformed geometry

Table 1. SIFs for different meshes.

	Analytical	Mesh 1 / r_0			Mesh 2 / r_0			Mesh 3 / r_0			Mesh 4 / r_0		
		0.2	0.6	1.0	0.2	0.6	1.0	0.2	0.6	1.0	0.2	0.6	1.0
K_I	34.0	33.966	33.991	33.990	33.662	33.820	33.806	33.316	33.687	33.674	34.150	33.166	33.081
K_{II}	4.55	4.519	4.534	4.534	4.429	4.526	4.525	4.373	4.519	4.517	4.630	4.486	4.493

8.6.2 Test 2 Central-cracked plate under uniaxial tension

A crack lying on the center of a homogenous and isotropic infinite plate subjected to a remote uniaxial tension is considered. Only a half of the plate is modeled due to the symmetry. The geometry model with boundary condition and loading condition is shown in Fig. 8.13(a), which the plane strain condition is used and the width is $W = 10$, the length is $H = 19.9$, the half crack length is $a = 1$. The left edge is symmetry boundary that is fixed in the x-direction, the right-hand edge is fixed in the x-direction and the right-bottom corner is fixed also y-direction the edge singularity. The uniaxial loading is applied in the top and bottom edges with the magnitude is $\sigma_{22} = 1$. The model is divided into 100×199 elements with the element size $LE = 0.1$ as shown in Fig. 8.13(b). The material constants include Young's module $E = 100$ and Poisson's ratio $\nu = 0.3$.

The calculated stress intensity factor of the crack is $K_I = 1.7861$ and $K_{II} = -3.1670 \times 10^{-10}$.

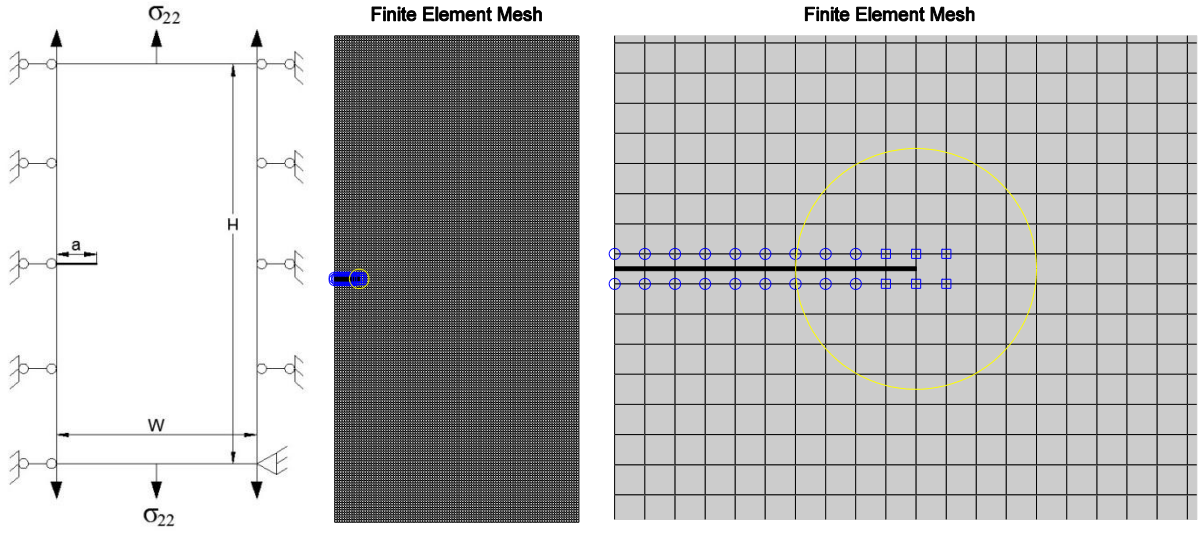

(a) (b) (c)

Fig. 8.13. (a) Geometry; (b) Mesh of the whole model; (c) Crack enrichment nodes (circle nodes), crack tip enrichment nodes (square nodes) and the J-integral (orange circle).

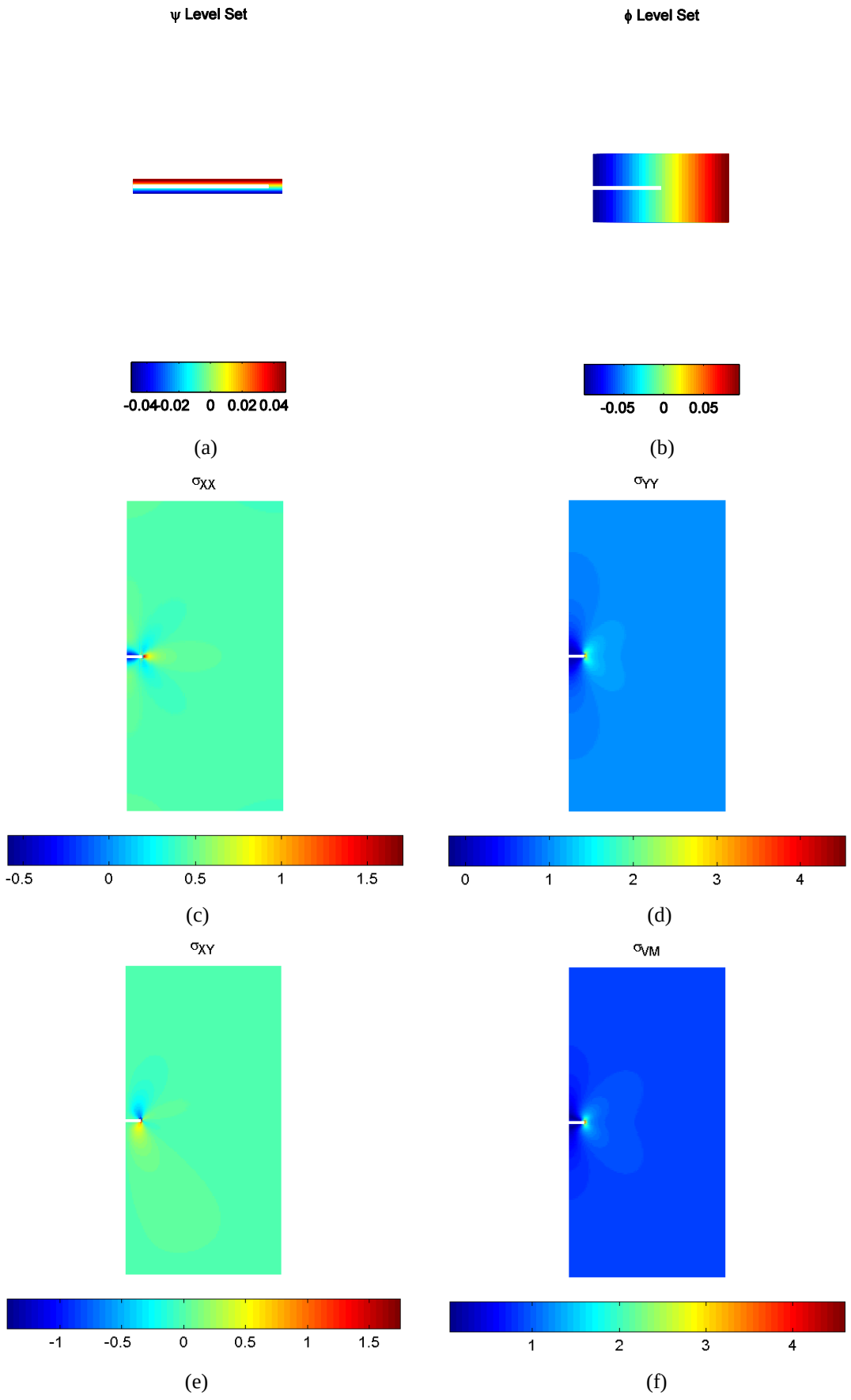

Fig. 8.14. (a) Heaviside level set function; (b) Level set function for crack tip; (c) Horizontal stress σ_{xx}; (d) Vertical stress σ_{yy}; (e) Shear stress σ_{xy}; (f) Mises stress σ_{VM}.

8.6.3 Test 3 Crack extension of test 2

In order to investigate the process of crack extension, the model of test 1 is analyzed con MTS criterion. The crack increment is assumed one element length and the extensional steps are assumed 10. In Fig 8.15, the crack trajectory and enriched nodes are shown. It is clearly seen that the crack extends straight along ahead due to only Mode I appears. Fig. 8.15(b) and Fig .8.16 show the deformed geometry, ϕ and ψ level set functions, stress distributions of the plate.

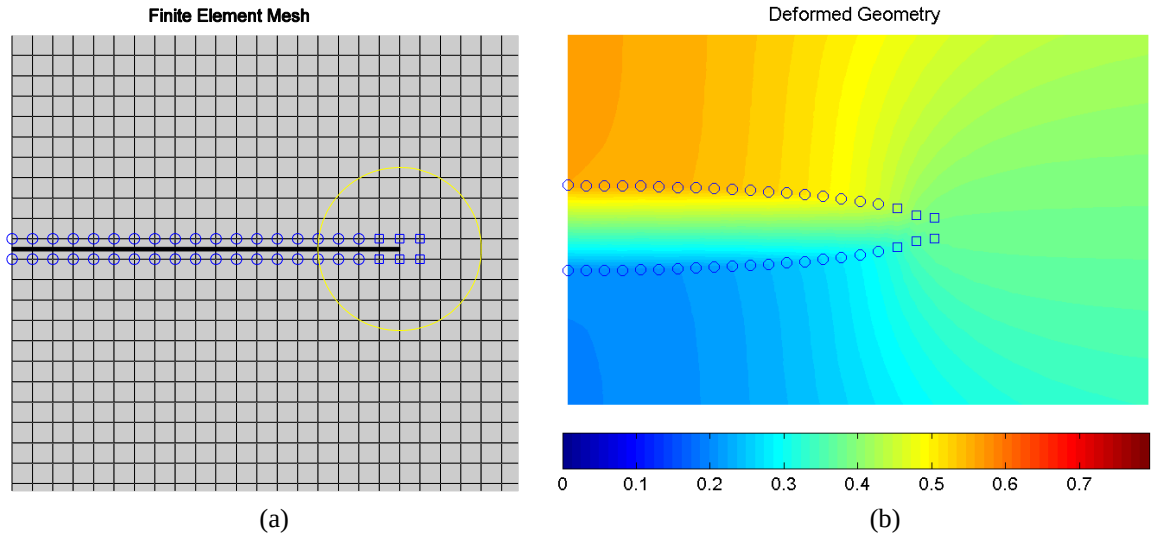

Fig. 8.15. (a) Finite element mesh and enriched nodes; (b) Deformed geometry near crack tip

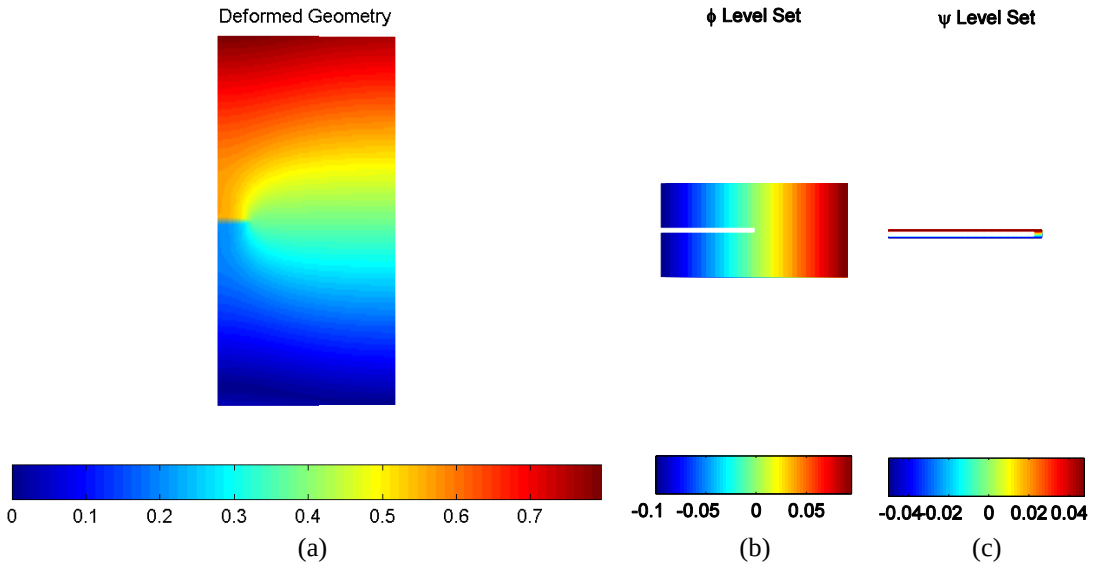

Fig. 8.16. (a) Deformed geometry; (b) Level set function ϕ; (c) Level set function ψ

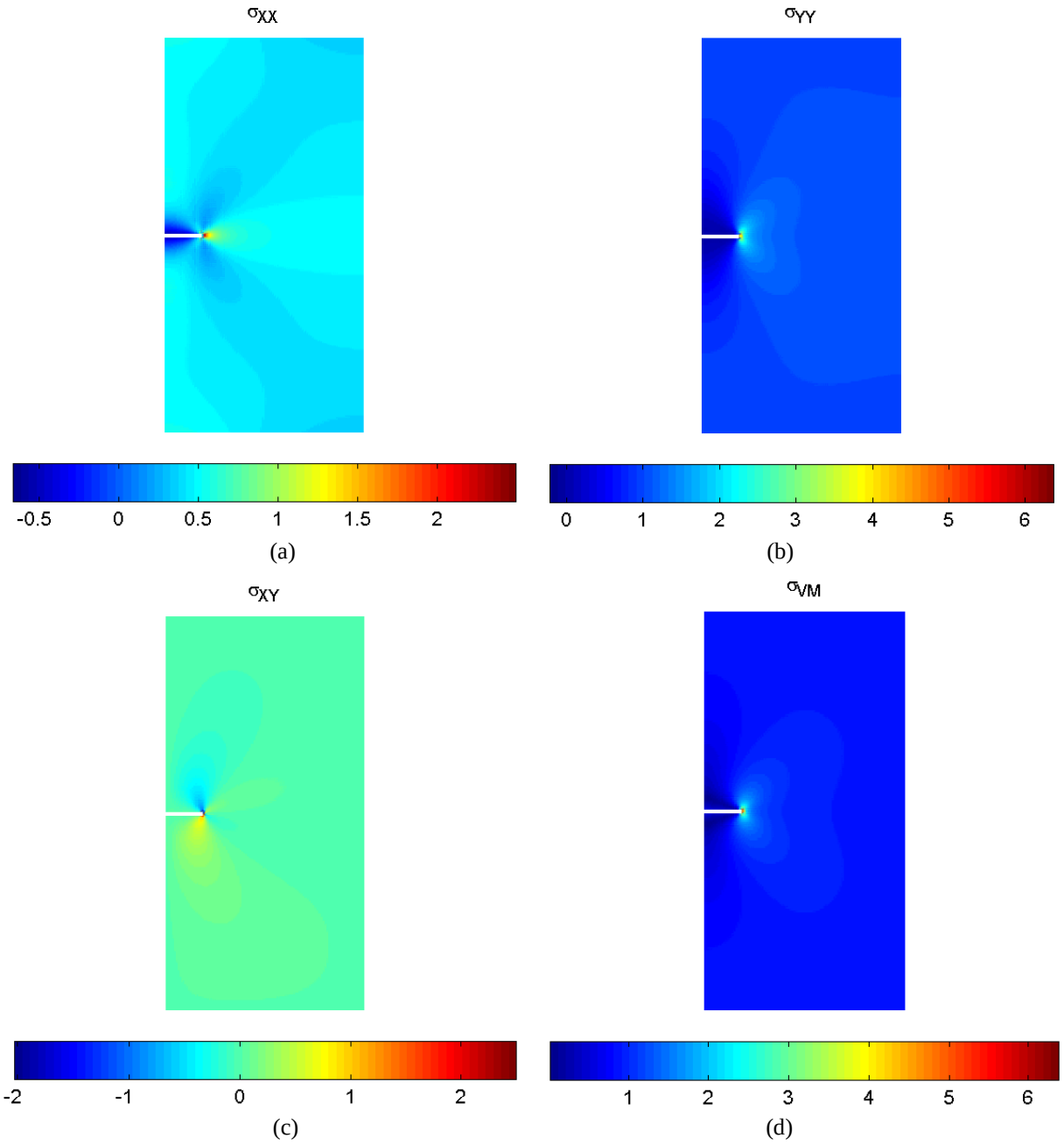

Fig. 817. The stresses distribution (a) Horizontal stress σ_{xx}; (b) Vertical stress σ_{yy}; (c) Shear stress σ_{xy}; (d) Mises stress σ_{VM}.

8.6.4 Test 4 Crack extension of edge-cracked plate

This model is almost the same with that in Test 1. Only the dimension of the plate is changed as height H = 20, width W = 10, and the crack length is a = 1. The plate is divided into 100×200 elements. The crack extension parameters assumed as: the crack increment is half of element length ($LE/2$) and the increased steps are 20. The Maximum Tangential Stress (MTS) criterion is used. The crack trajectory, ψ level set function and deformed geometry are graphically shown in Fig. 8.18. The stress distributions of the plate after crack extension terminates are shown in Fig. 8.19.

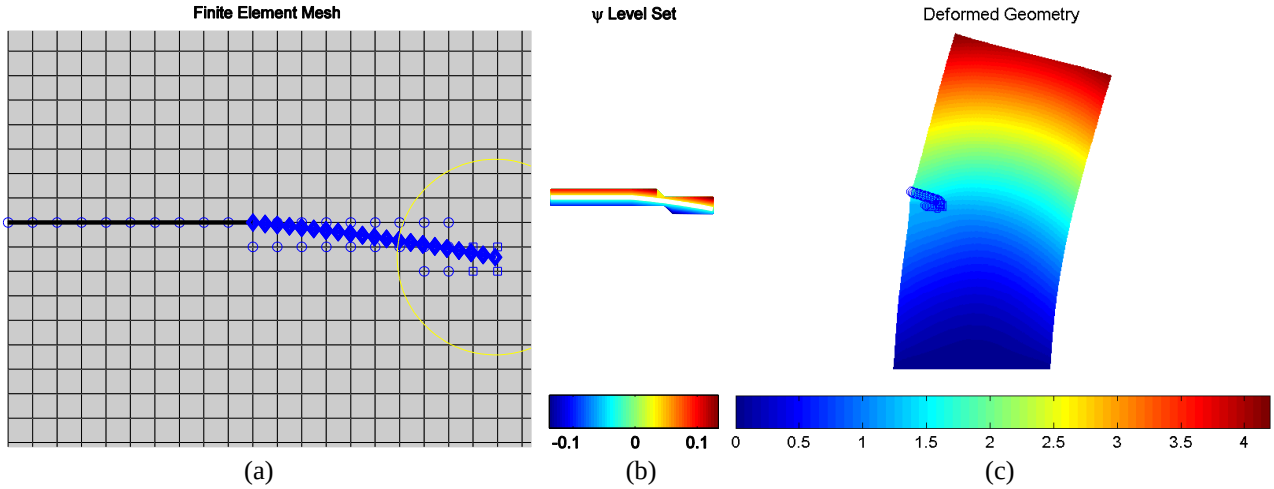

Fig. 8.18. (a) Crack trajectory and enriched nodes; (b) Level set function ψ; (c) Deformed geometry

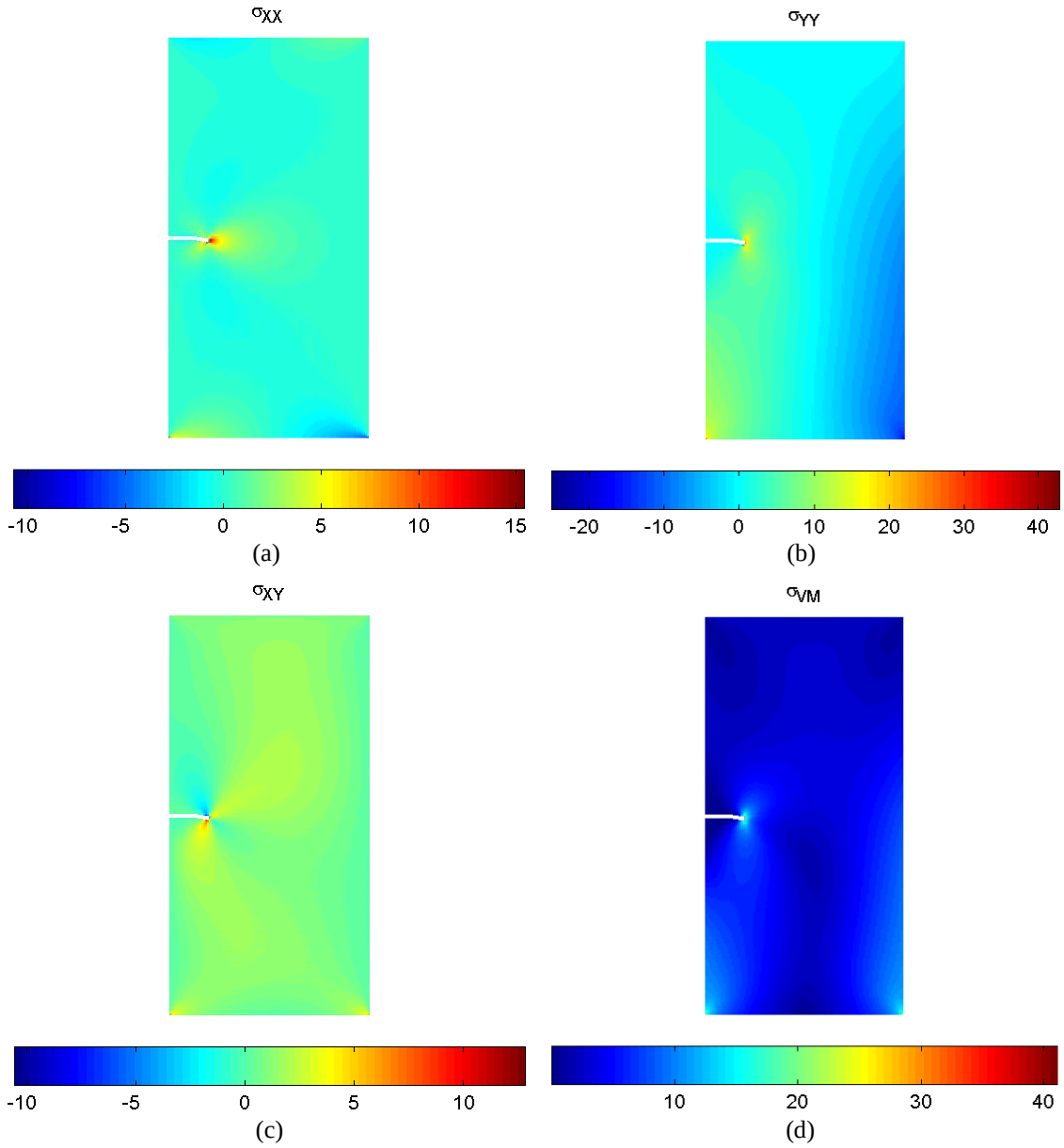

Fig. 8.19. The stresses distribution (a) Horizontal stress σ_{xx}; (b) Vertical stress σ_{yy}; (c) Shear stress σ_{xy}; (d) Mises stress σ_{VM}

8.6.5 Test 5 Edge crack propagation under compress-shear loading

In many experiments, a specimen under compress-shear force, as shown in Fig. 8..20(a) which the top and bottom edge is fixed in y-direction and the lower half of right-edge is fixed in the x-direction under a pressure on the upper half of left-edge, is always applied.

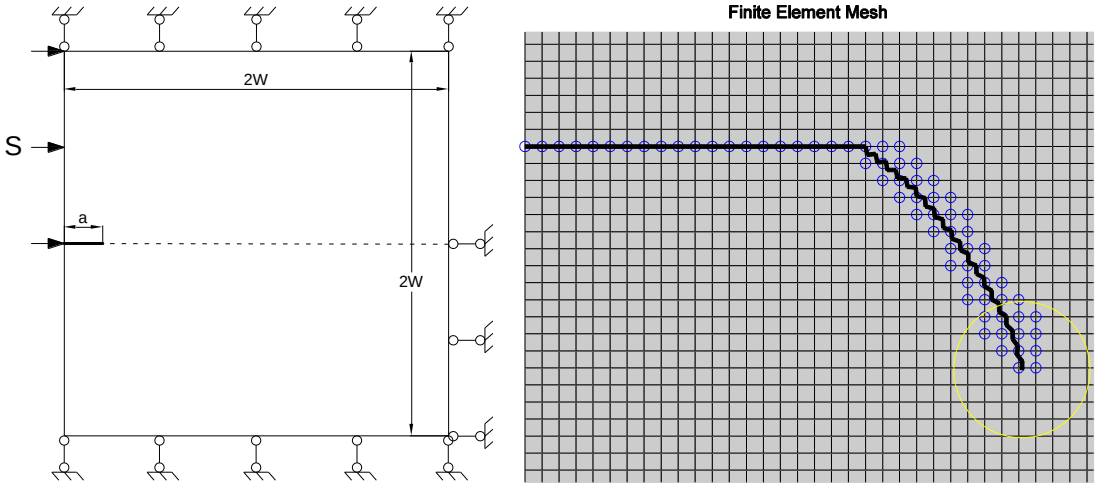

(a) (b)

Fig. 8.20. (a) Model geometry; (b) Crack trajectory and enriched nodes.

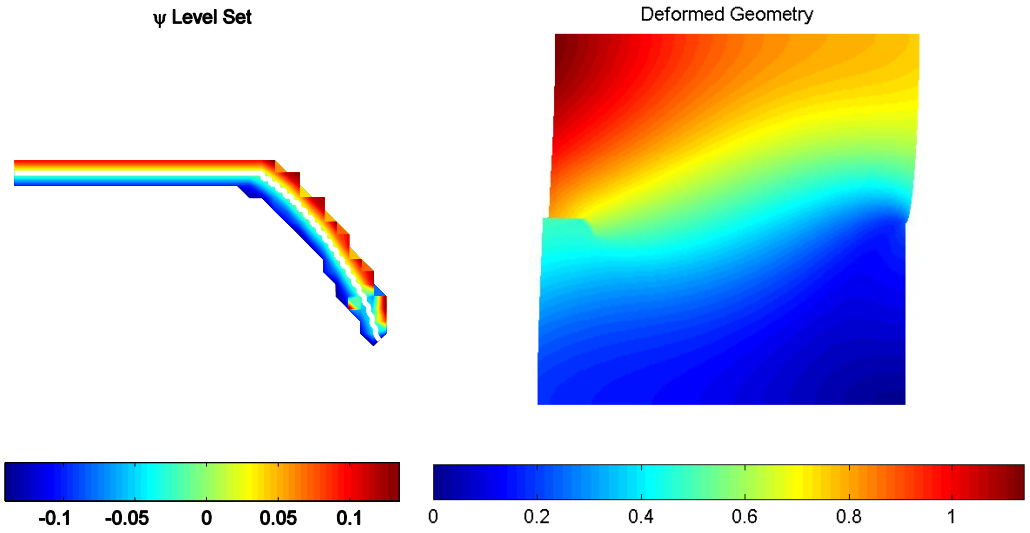

(a) (b)

Fig. 8.21. (a) Level set function ψ; (b) Deformed geometry

The plate is a square with the length $2W = 20$ and crack length $a = 2$ and divided into 200×200 elements of plane strain condition. The material properties are $E = 100$ and $\nu = 0.3$. The crack extension parameters assumed as: the crack increment is half of element length ($LE/2$) and the increased steps are 40. The Maximum Tangential Stress (MTS) criterion is used. The crack trajectory, enriched nodes and J-integral are shown in Fig.20 (b). Dissimilar to the trajectory in Test 3 and Test 4, the trajectory in this model is not smoothly but roughly. The crack extension angles are different from step by step, but the extension tendency is continue and clear. The ψ level set function and de-

formed geometry are graphically shown in Fig. 8.21. The stress distributions of the plate after crack extension terminates are shown in Fig. 8.22. From Fig. 8.22, it can be seen that there are two stress concentration in this plate, one is the crack tip undoubtedly, and another one lies to the middle of right edge due to the singularity of the boundary condition.

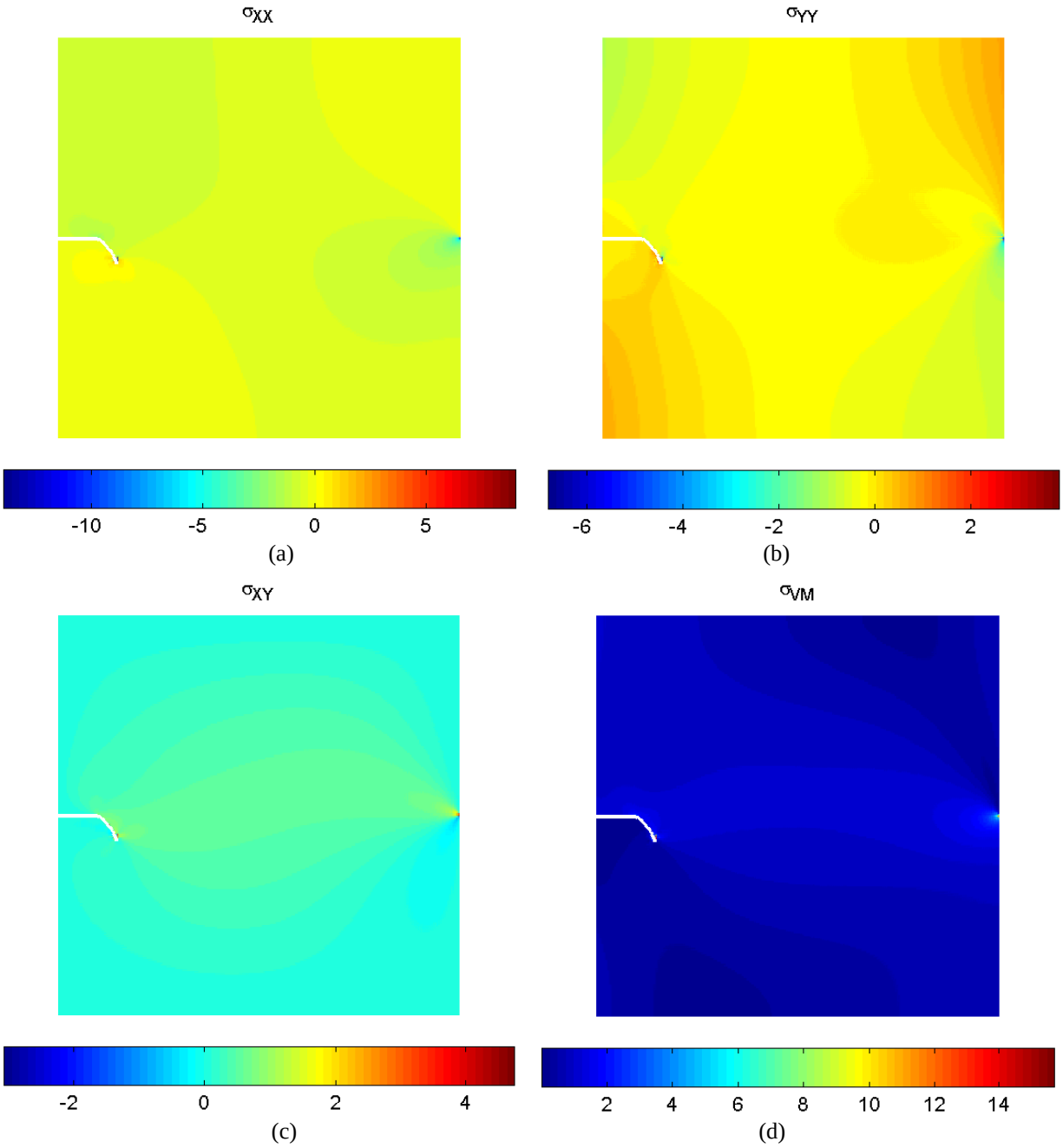

Fig. 8.22. The stresses distribution (a) Horizontal stress σ_{xx}; (b) Vertical stress σ_{yy}; (c) Shear stress σ_{xy}; (d) Mises stress σ_{VM}

8.7 Numerical results of an interfacial crack in bi-material plate

8.7.1 Stress intensity factors of a central crack in an infinite bi-material plate

An isolated crack of length $2a$ lying on the interface in a bi-material solid subjected to the remote traction $\sigma_0^\infty + i\tau_0^\infty$ is considered. The exact solution for the mixed-mode SIFs at the right crack tip is given by [44-46] as

$$K_1 + iK_2 = (\sigma_{22} + i\sigma_{12})(1 + 2i\epsilon)\sqrt{\pi a}(2a)^{-i\epsilon} \tag{8.96}$$

Only the case of pure tension loading is considered. In the numerical model, the symmetry and only half of the specimen is used with the boundary condition as Fig. 8.23. The plane strain condition is assumed in the model. The material constants used in the numerical computations are: $E_1/E_2 = 22$, $\nu_1 = 0.2571$ and $\nu_2 = 0.3$. According to eq. (5.7), the second Dundurs parameter $\beta = 0.2584$ and the bi-material constant $\epsilon = -0.0842$. To obtain an in-depth numerical investigation of the number of elements effects the accuracy and the location of crack, there are four sample sizes and element length chosen as

1) $W \times H = 10 \times 20$, $a = 1$ and element length is $LE = 0.1$, the total element is 100×200;
2) $W \times H = 10 \times 20$, $a = 1$ and element length is $LE = 0.2$, the total element is 50×100;
3) $W \times H = 10 \times 19.9$, $a = 1$ and element length is $LE = 0.1$, the total element is 100×199;
4) $W \times H = 10 \times 19.8$, $a = 1$ and element length is $LE = 0.2$, the total element is 50×99.

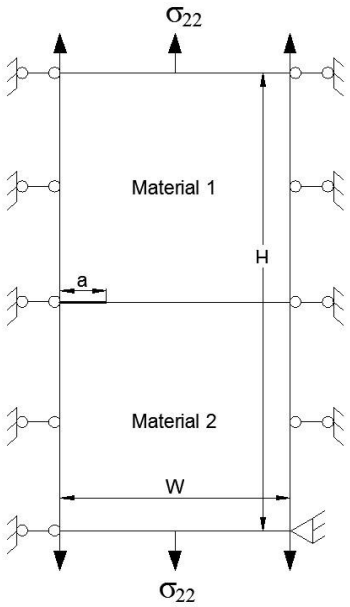

Fig. 8.23 Interfacial crack under uniaxial tension

According to eq. (8.96) and considering the material parameters used in the present model, the theoretical solution of stress intensity factors for central crack in an bi-material plate are $K_1 = 1.7868$, $K_2 = -0.1945$. The stress intensity factors of the four meshes are obtained as shown in Table 2.

The excellent agreement between the numerical results and the exact solutions is observed. The maximum relative errors of K_1 and K_2 are only 1.33% and 2.88%, respectively.

Table 2. The stress intensity factors of exact solutions and numerical results.

	Analytical	Mesh 1		Mesh 2		Mesh 3		Mesh 4	
		value	error	value	error	value	error	value	error
K_1	1.7868	1.7783	0.48%	1.7710	0.88%	1.8105	1.33%	1.8045	0.99%
K_2	-0.1945	-0.1944	0.00%	-0.1921	1.23%	-0.1986	2.11%	-0.2001	2.88%

To obtain the stress intensity factors of various crack length and estimate the accuracy of the numerical solution, the comparison between numerical solutions and analytical results for different crack length are presented in Table 3 and Fig. 8.24, the mode of mesh 1 is used.

Table 3. Stress intensity factors for various crack length.

	a=0.5		a=0.8		a=1.1		a=1.4		a=1.7		a=2.0	
	Ans	Num	Ans	Num	Ans	Num	Ans	Num	Ans	Num	Ans	Num
K_1	1.2533	1.2349	1.5946	1.6071	1.8756	1.8965	2.1199	2.1568	2.3387	2.3963	2.5387	2.6229
K_2	-0.2110	-0.1980	-0.2039	-0.1947	-0.1890	-0.1843	-0.1702	-0.1734	-0.1493	-0.1523	-0.1273	-0.1287

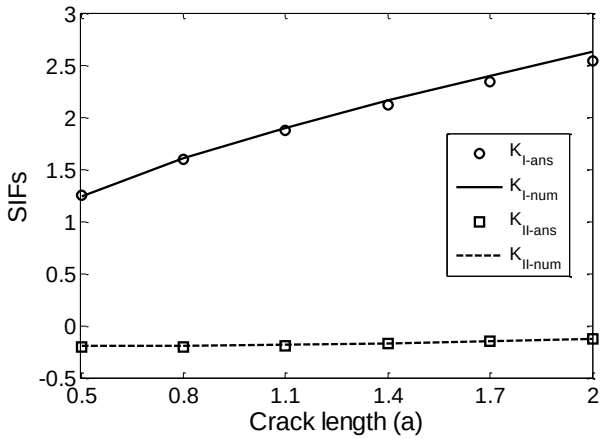

Fig. 8.24 Stress intensity factors of central interface crack

8.7.2 Crack trajectory of an interfacial crack

8.7.2.1 Example 1:

In the first example, the model of mesh 1 is used. The crack extension parameters assumed as: the crack increment is half element length ($LE/2$) and the increased 20 steps. The Maximum Tangential Stress (MTS) criterion is used for both of the interfacial crack extension and crack tip in isotropic material. For the main aim of this example which is the trajectory of interface crack propagation, the initial condition of crack extending in MTS-criterion is assumed to be satisfied in all the steps.

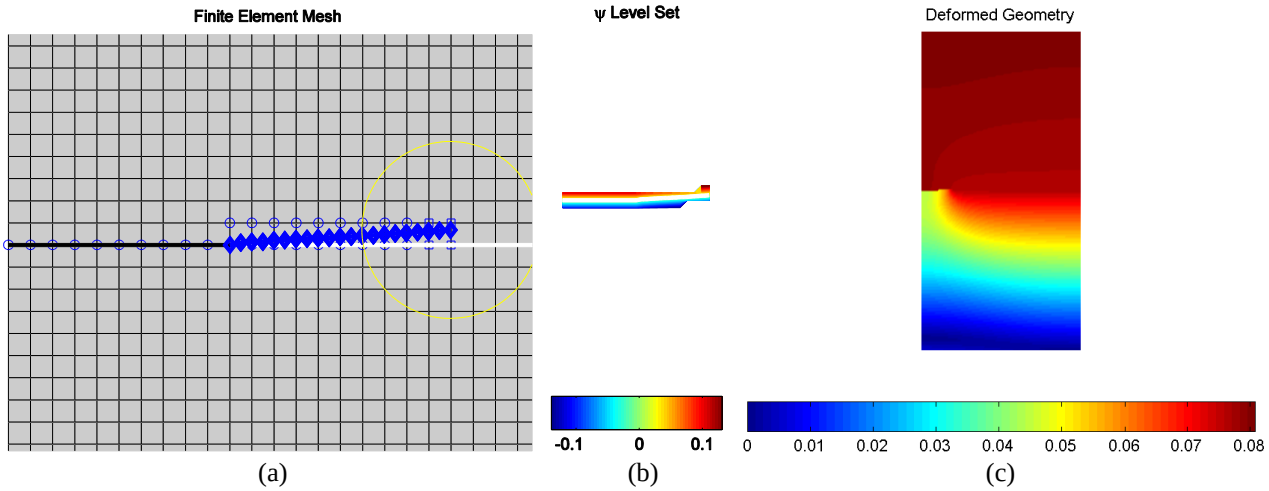

Fig. 8.25. (a) Crack trajectory; (b) The crack enrichment level set function ψ; (c) The mode deformation.

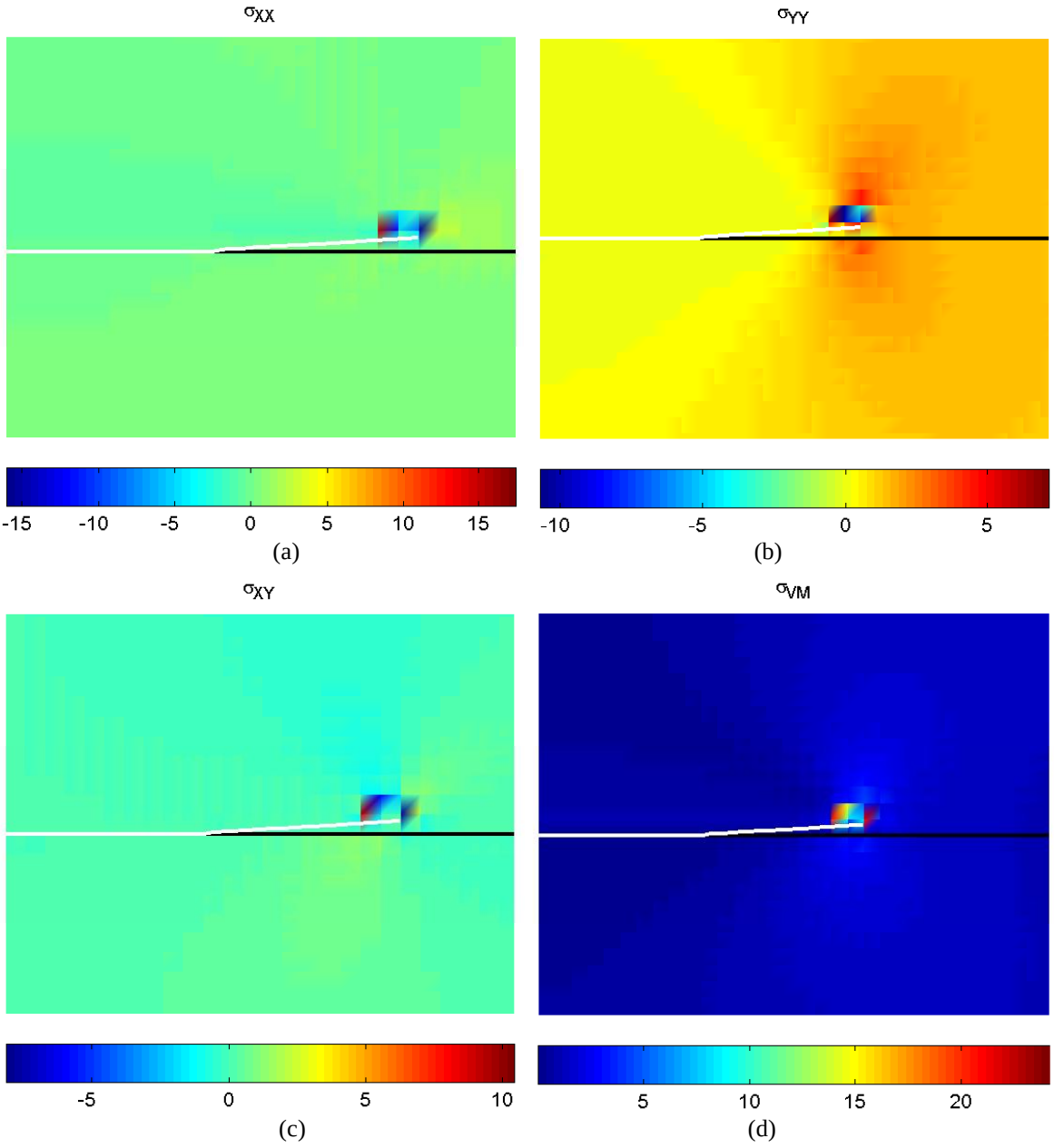

Fig. 8.26. The stresses (a) horizontal stress σ_{xx}; (b) vertical stress σ_{yy}; (c) shear stress σ_{xy}; (d) Mises stress σ_{VM}.

In Fig 8.25, the crack trajectory, the crack enrichment level set function and geometry deformation are shown. The numerical stress distributions near the crack are shown in Fig 8.26. Simply application of MTS-criterion without considering the effect of interface, the interfacial crack kinks out of the interface and extends into material 1 which is the stiff material. But the interface does affect the stress distribution in both of the materials. As the evidence, all the stress distributions and concentration around crack tip are not symmetry and the crack trajectory in material 1 is not horizontal.

8.7.2.2 Example 2:

Considering the interface affects crack propagation, the improved PV-criterion proposed in Chapter 7 is used in this example. The numerical mode is the same with that used in example 1 except the crack criterion improved and the crack extension step increased to 40.

In the improved PV-criterion, $r_0 = 0.4$, the energy release rate calculated by eq. (7.4), the interface toughness is given in eq. (7.15) in which the phase angle defined in eq. (7.20), $l = a/2$ is used. The other two parameters $\mathcal{G}_1^c$ and λ must be determined from experimental data. As an analytical investigation, in the present example assumed

$$\lambda = 0.1 \tag{8.97a}$$

$$\mathcal{G}_1^c = \frac{K_1^2}{\cosh^2(\pi\epsilon)E^*} \tag{8.97b}$$

where K_1 is Mode 1 stress intensity factor, ϵ is the bi-material index, $\frac{1}{E^*} = \frac{1}{2}\left(\frac{1}{E_1} + \frac{1}{E_2}\right)$.

After the interfacial crack kinking into one of the substrate materials, the general MTS-criterion is used as the failure criterion as usually.

Crack trajectory, ψ level set function and the model deformation are shown in Fig. 8.27. Though the simulated model is the same with example one, the crack trajectories are quite different. The crack extends along the interface in the first 22 steps, but kinks into material 2 (the complaint one) at the 23th step.

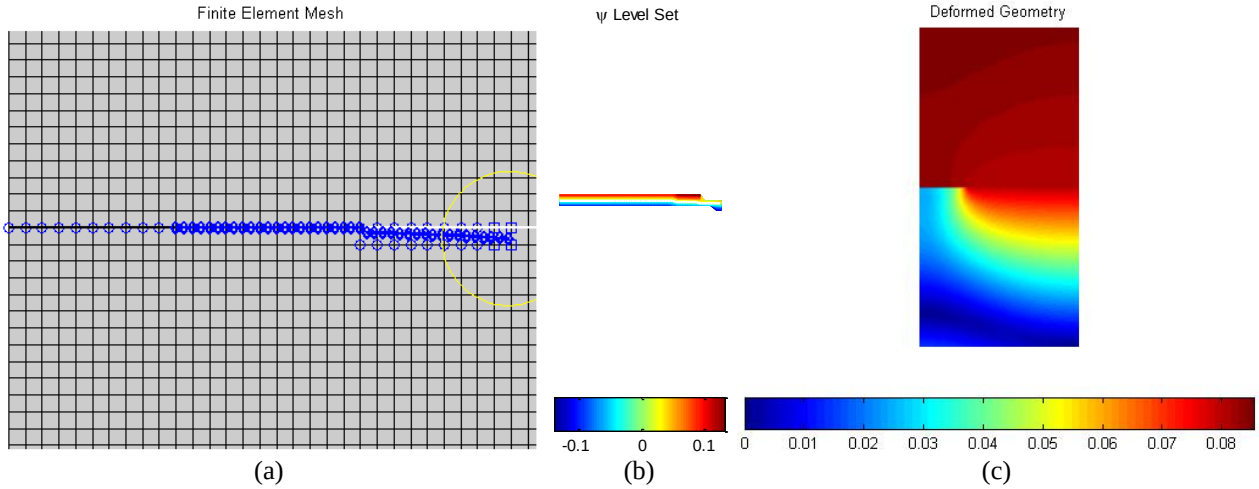

Fig. 8.27. (a) Crack trajectory; (b) The crack enrichment level set function ψ; (c) The model deformation.

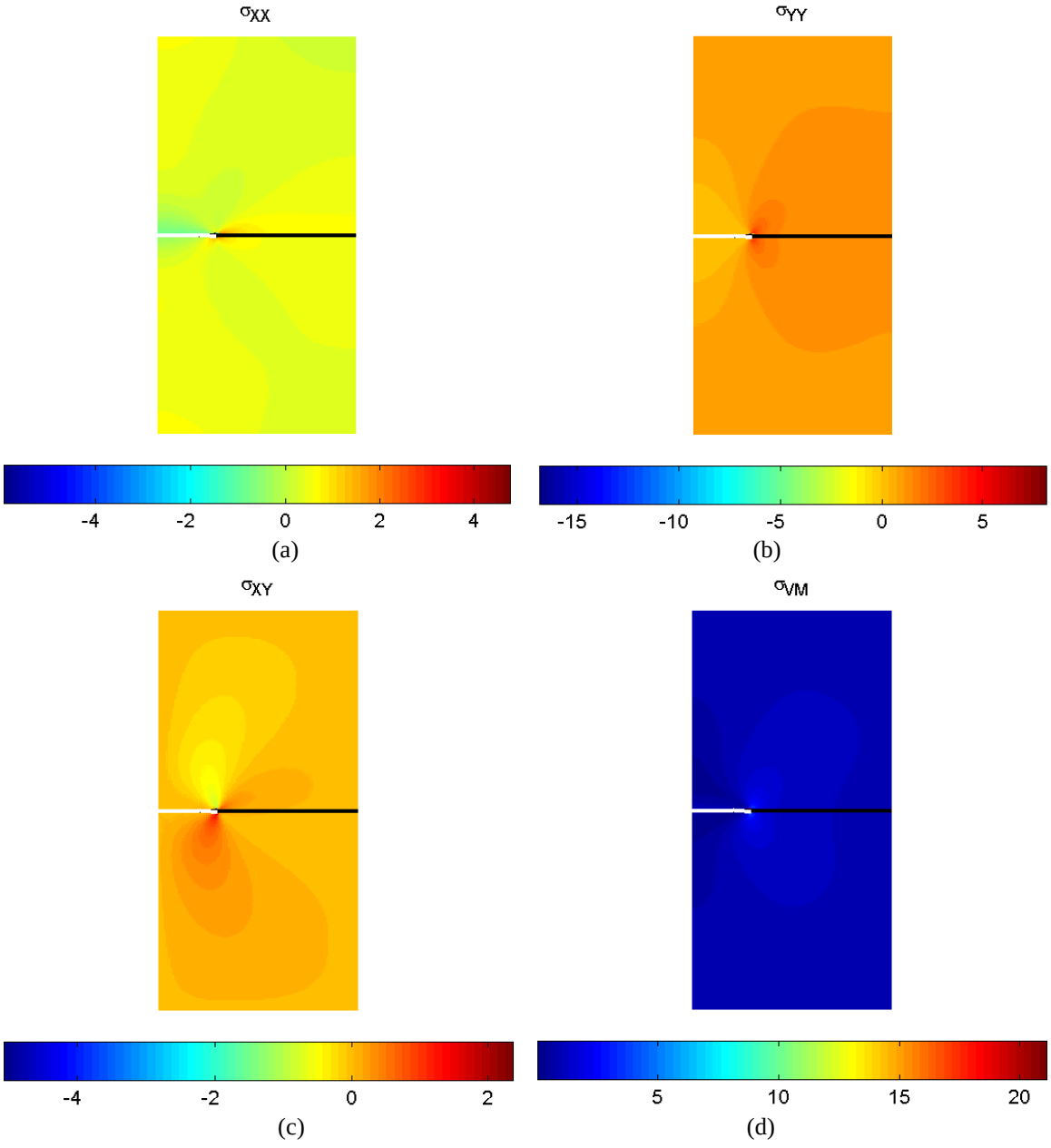

Fig. 8.28. The stresses (a) horizontal stress σ_{xx}; (b) vertical stress σ_{yy}; (c) shear stress σ_{xy}; (d) Mises stress σ_{VM}.

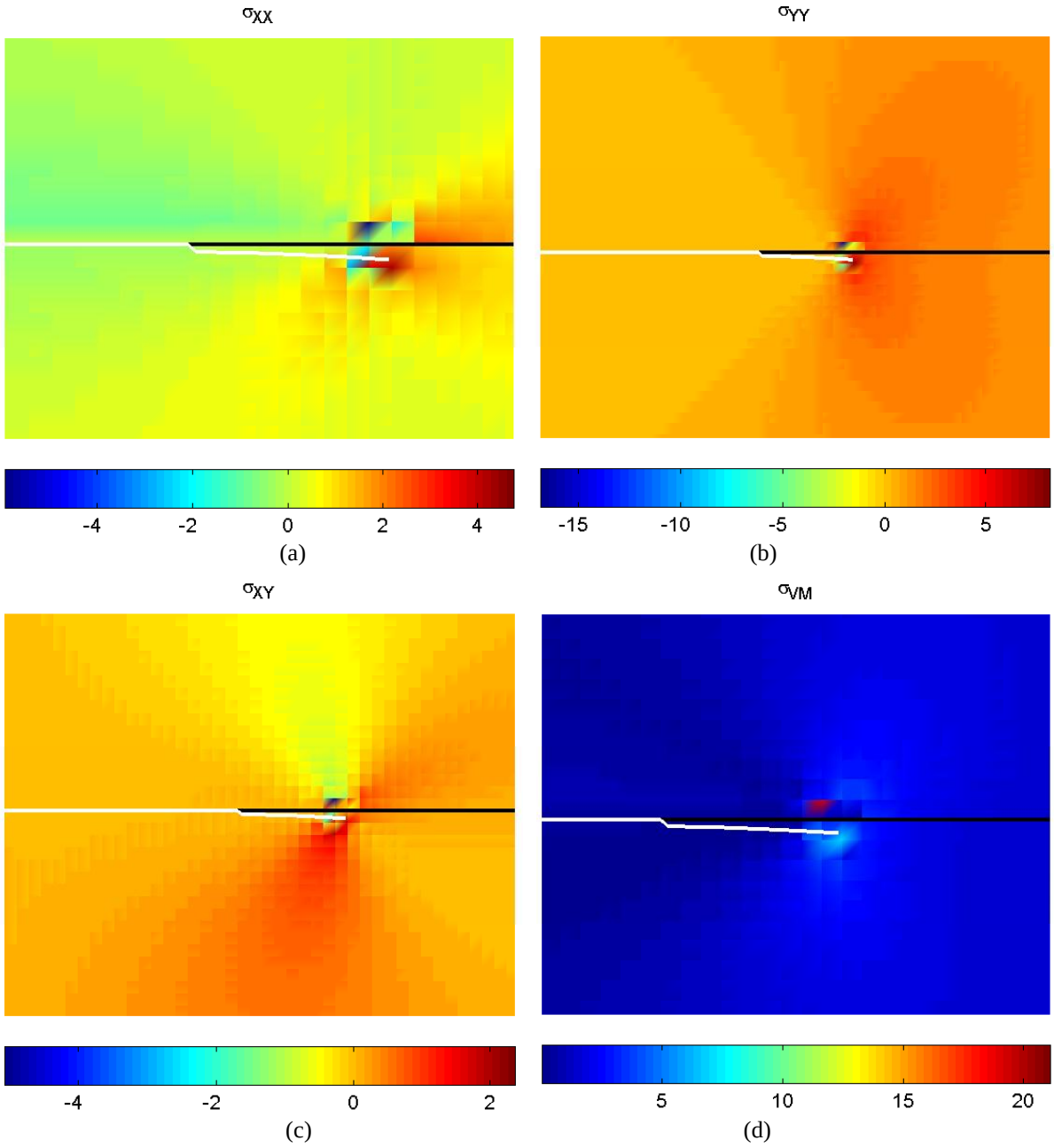

Fig. 8.29. The stresses concentration (a) horizontal stress σ_{xx}; (b) vertical stress σ_{yy}; (c) shear stress σ_{xy}; (d) Mises stress σ_{VM}.

8.7.2.3 Example 3:

The last example is an edged-interfacial-crack in a plate subjected shear traction on the top edge and fixed the bottom edge, as shown in Fig. 8.30(a). The material constants, the model dimension, crack length and crack propagation parameters and criterion are the same with that in example 2.

The deformation of the plate and the stress concentration can be found in Fig. 8.30(b) and Fig. 8.32. The crack trajectory is the most important result shown in Fig. 8.31(a). It can be seen that the inter-facial crack extends along the interface in the first four steps and then kinks into material 2.

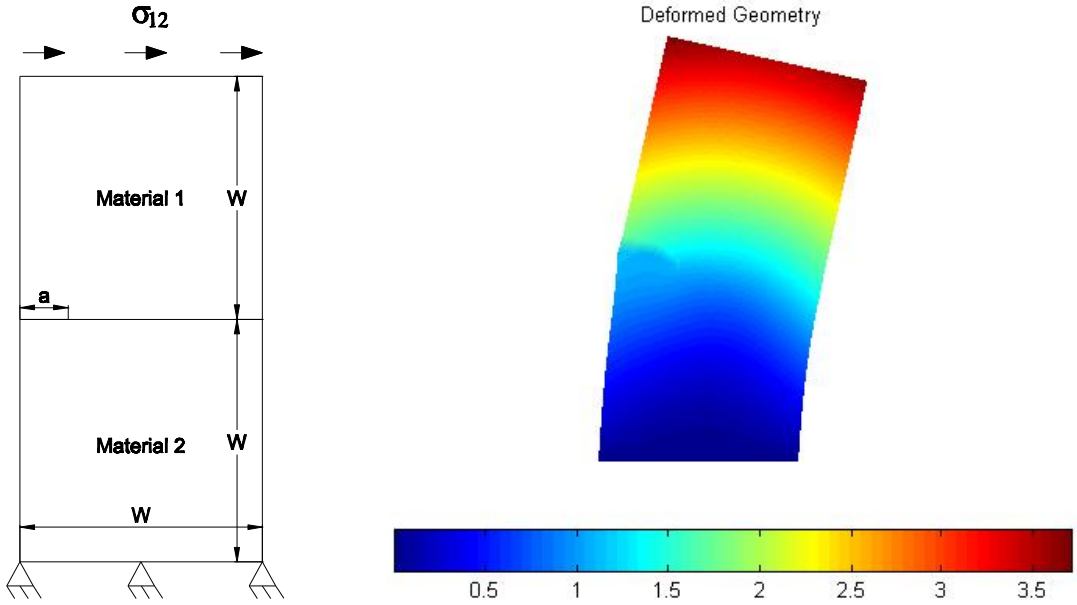

(a) (b)

Fig. 8.30. (a) Geometry model; (b) The mode deformation.

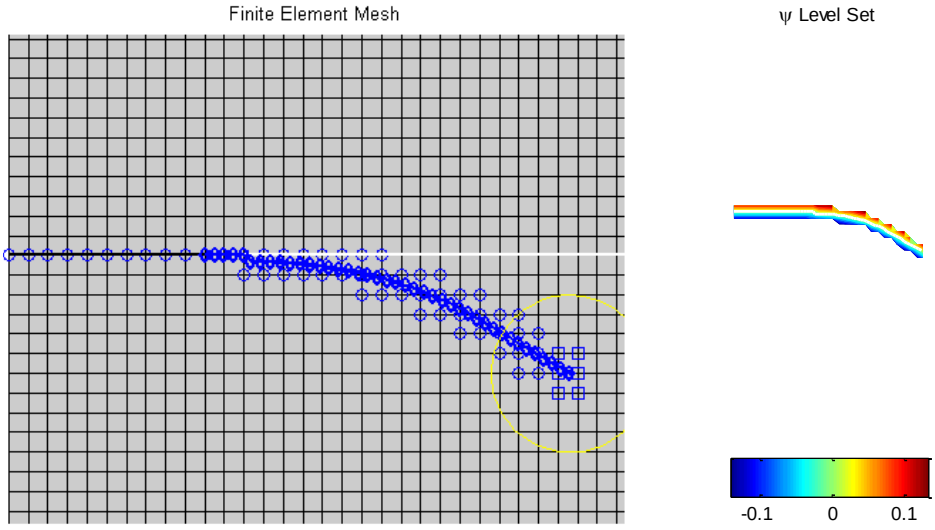

(a) (b)

Fig. 8.31. (a) Crack trajectory and enrichment nodes; (b) The crack enrichment level set function ψ

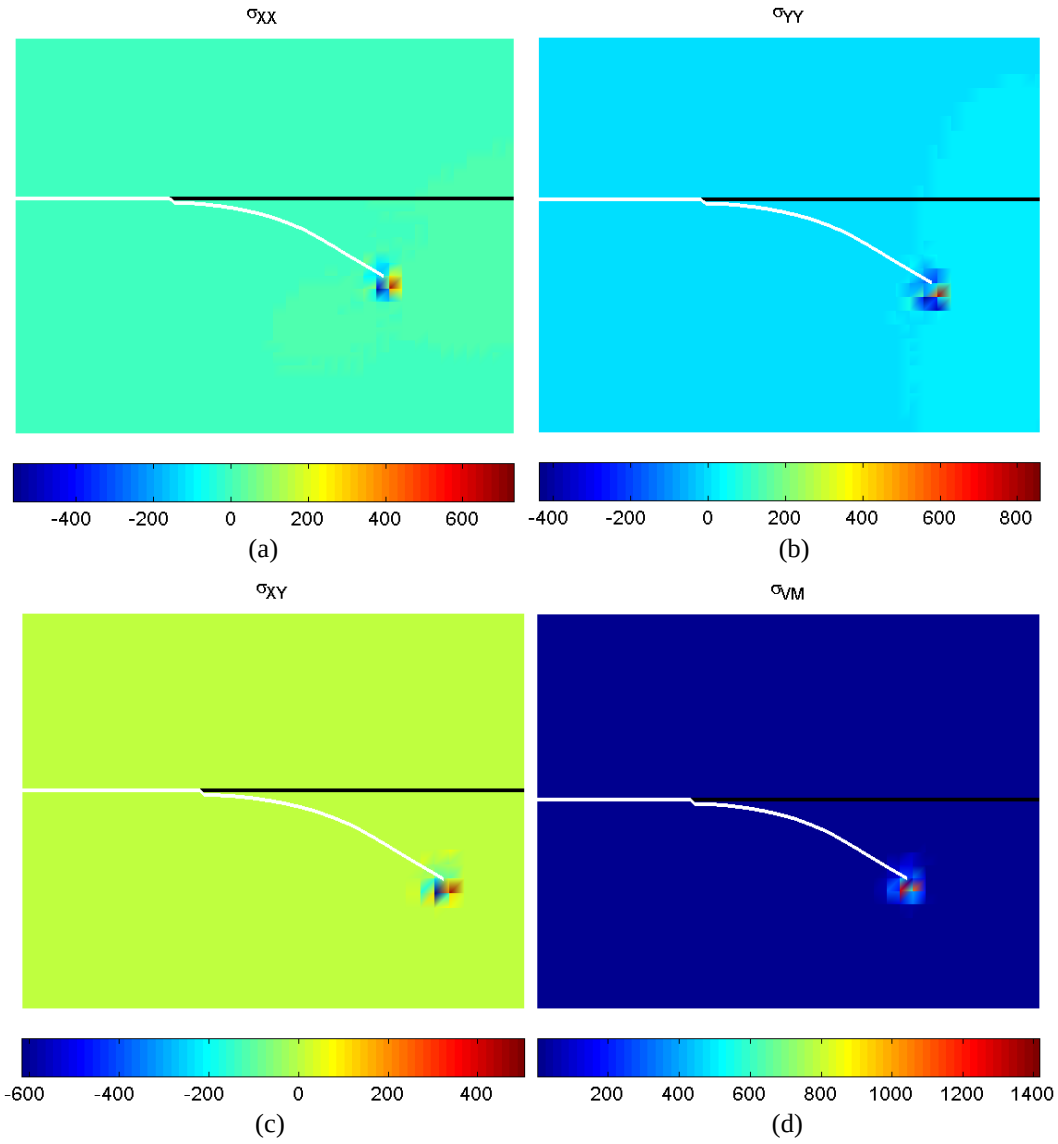

Fig. 8.32. The stresses concentration (a) horizontal stress σ_{xx}; (b) vertical stress σ_{yy}; (c) shear stress σ_{xy}; (d) Mises stress σ_{VM}.

References

[1] Melenk JM, Babuska I. The partition of unity finite element method: Basic theory and applications. Semina fur anewandte mathematic, Eidgenossische technische hochschule, Research report No.96-01, January 1996, CH-8092 Zurich, Swizerland.

[2] Duarte CA, Oden JT. An H-p adaptive method using clouds. Computer Methods in Applied Mechanics and Engineering, 1996; 139: 237-262.

[3] Elastic crack growth in finite elements with minimal remeshing. International Journal of Fracture Mechanics, 1999; 45: 601-620.

[4] Moes N, Dolbow J, Belytschko T. A finite element method for crack growth without remeshing. International Journal for Numerical Methods in Engineering, 1999; 46:131-150.

[5] Dolbow JE. An extended finite element method with discontinuous enrichment for applied mechanics. PhD dissertation, Theoretical and Applied Mechanics, Northwestern University, 1999, USA.

[6] Dolbow J, Moes N, Belytschko T. Discontinuous enrichment in finite elements with a partition of unity method. Finite Elements in Analysis and Design, 2000a, 36: 235-260.

[7] Dolbow J, Moes N, Belytschko T. Modeling fracture in Mindlin-Reissneer plates with extended finite element method, International Journal of Solids and Structures, 2000b; 37: 7161-7183.

[8] Dolbow J, Moes N, Belytschko T. An extended finite element method for modeling crack growth with frictional contact. Finite Elements in Analysis and Design. 2000c; 36(3):235-260.

[9] Daux C, Moes N, Dolbow J, Sukumark N, Belytschko T. Arbitrary branched and intersecting cracks with the extended finite element method. International Journal for Numerical Methods in Engineering, 2000; 48:1741-1760.

[10] Sukumar N, Moes N, Moran B, Belytschko T. Extended finite element method for three-dimensional crack modeling. International Journal for Numerical Methods in Engineering, 2000; 48: 1549-1570.

[11] Stolarska M, Chopp DL, Moes N, Belytschko T. Modeling crack growth by level sets in the extended finite element method. International Journal for Numerical Methods in Engineering, 2001; 51: 943-960.

[12] Belytschko T, Moes N, Usui S, Parimik C. Arbitrary discontinuities in finite elements. International Journal for Numerical Methods in Engineering, 2001; 50:993-1013.

[13] Sukumar N, Chopp DL, Moes N, Belytschko T. Modeling holes and inclusions by level sets in the extended finite element method. Computer Method in Applied Mechanics and Engineering, 2001; 190: 6181-6200.

[14] Moes N, Gravouil A, Belytschko T. Non-planar 3D crack growth by the extended finite element and level sets-Part I: Mechanical model. International Journal for Numerical Methods in Engineering, 2002; 53: 2549-2568.

[15] Dolbow JE, Nadeau JC. On the use of effective properties for the fracture analysis of microstructured materials. Engineering Fracture Mechanics, 2002; 69:1607-1634.

[16] Dolbow JE, Gosz M. On the computation of mixed-mode stress intensity factors in functionally graded materials. International Journal of Solids and Structures, 2002; 39:2557-2574.

[17] Remmers JJC, Wells GN, de Borst R. A solid-like shell element allowing for arbitrary delaminations. International Journal for Numerical Methods in Engineering, 2003; 58: 2013-2040.

[18] Sukumar N, Huang Z, Prevost JH, Suo Z. Partition of unity enrichment for biomaterial interface cracks. International Journal for Numerical Methods in Engineering, 2004; 59:1075-1102.

[19] Nagashima T, Omoto Y, Tani S. Stress intensity factor analysis of interface cracks using X-FEM. International Journal for Numerical Methods in Engineering, 2003; 56:1151-1173.

[20] Application of extended finite element method to fracture of composite materials European Congress on Computational Methods in Applied Sciences and Engineering (ECCOMAS), 2004 Jyvaskyla, Finland.

[21] Sih G.C., Paris P., Irwin G. On cracks in rectilinearly anisotropic bodies. International Journal of Fracture Mechanics, 1965, 1(3):189-203.

[22] Belytschko, T. and Black, T. (1999) Elastic crack growth in finite elements with minimal remeshing. *International Journal of Fracture Mechanics*, 45, 601–620.

[23] Fleming M, Chu YA, Moran B, Belyschko T. Enriched element-free Galerkin methods for singular fields. Int J Num Meth Engng, 1997; 40:1483-1504.

[24] Zak AR, Williams ML. Crack point singularities at a bimaterial interface. *Journal of Applied Mechanics* 1963; 30: 142–143.

[25] Cook TS, Erdogan F. Stresses in bonded materials with a crack perpendicular to the crack. *International Journal of Engineering Science* 1972; 10:677– 697.

[26] Chen DH. A crack normal to and terminating at a biomaterial interface. Engineering Fracture Mechanics 1994;49(4):517–32.

[27] Dundurs J. Edge-bonded dissimilar orthogonal elastic wedges. *Journal of Applied Mechanics* 1969; **36**:650–652.

[28] Beuth JL, Klingbeil NW. Cracking of thin bonded films in residual tension. Int J Solid & Struc, 1992; 29(13): 1657-1675.

[29] Huang R, Sukumar N, Prévost J.-H. Modeling quasi-static crack growth with the extended finite element method. Part II: Numerical applications. *International Journal of Solids and Structures* 2003; 40(26): 7539–7552

[30] L. Bouhala, Q. Shao, Y. Koutsawa, A. Younes, et al. An XFEM crack-tip enrichment for a crack terminating at a bi-material interface. Engng Fract Mech, accepted article.

[31] Osher S, Sethian JA. Fronts propagation with curvature-dependent speed: Algorithms based on Hamilton-Jacobi formulations. Journal of computational physics, 1988; 79(1):12-49.

[32] Sethian JA. Level set methods and fast marching methods: evolving interfaces in computational geometry, fluid mechanics, computer vision, and materials science on applied and computational mathematics, Cambridge University Press, 2nd, 1999.

[33] Pais MJ, Kim NH. Modeling failure in composite materials with extended finite element and level set methods. Structural Dynamics, and Materials Conference, 17th, 4-7 May 2009, Palm Springs, California.

[34] Paris PC, Gomez RE, Anderson WE. A rational analytic theory of fatigue. Trend Engng 1961;13:9–14.

[35] Tanaka K. Fatigue crack propagation from a crack inclined to the cyclic tensile axis. Engng Fracture Mech 1974;6:493–507.

[36] Grestle WH. Finite and boundary element modeling of crack propagation in two- and three-dimensions using interactive computer graphics. PhD Thesis. Cornell University, Ithaca, NY; 1986.

[37] Erdogan F, Sih GC. On the crack extension in plates under plane loading and transverse shear. J Basic Engng Transition ASME 1963; 85:519–27.

[38] Mi Y, Aliabadi MH. Three-dimensional crack growth simulation using BEM. Int J Comput Struct 1994;52:871–8.

[39] Mi Y, Aliabadi MH. Automatic procedure for mixed-mode crack growth analysis. Commun Numer Meth Engng 1995;11:167–77.

[40] Sih GC, Cha BCK. A fracture criterion for three-dimensional crack problems. Engng Fracture Mech 1974;6:699–732.

[41] Bowness D, Lee MMK. Fatigue crack curvature under the weld toe in an offshore tubular joint. Int J Fatigue 1998;20:481–90.

[42] Liu XY, Xiao QZ, Karihaloo BL. XFEM for direct evaluation of mixed mode SIFs in homogeneous and bi-materials. Int J Numer Meth Engng, 2004; 59:1103-1118.

[43] Wilson WK. Combined mode fracture mechanics. *Ph.D. Thesis*, University of Pittsburgh, 1969.

[44] Rice JR, Sih GC. Plane of cracks in dissimilar media. Journal of Applied Mechanics 1965; 32: 418-423.

[45] Rice JR. Elastic fracture mechanics concepts for interfacial cracks. J. Appl Mech. 1988; 55: 98-103.

[46] Hutchinson JW, Suo Z. Mixed mode cracking in layered materials. In Advances in Applied Mechanics, vol 29, Hutchinson JW, Wu TY (eds), Academic Press: San Diego, CA, 1991; 63-191.